

# **CP Violation in $B^\pm \rightarrow Dh^\pm$ Decays**

## **where $D \rightarrow K_S^0 h'^+ h'^-$**

*A measurement of the CKM angle  $\gamma$  at LHCb and understanding  
the impact of neutral kaon CP violation*



Mikkel Bjørn  
St. Anne's College  
University of Oxford

A thesis submitted for the degree of  
*Doctor of Philosophy*  
Trinity 2020

# Abstract

This thesis presents a measurement of the Cabibbo-Kobayashi-Maskawa angle  $\gamma$  using  $B^\pm \rightarrow DK^\pm$  and  $B^\pm \rightarrow D\pi^\pm$  decays, where the  $D$  meson decays to one of the final states  $K_S^0\pi^+\pi^-$  and  $K_S^0K^+K^-$ . The measurement relies on the distribution of signal decays over the phase space of the  $D$  decay, analysed using a model-independent method based on strong-phase measurements by the CLEO and BESIII collaborations. The measurement is performed using proton-proton collision data collected by the LHCb experiment during the full Run 1 and 2 of the Large Hadron Collider, corresponding to a total integrated luminosity of  $8.7\text{ fb}^{-1}$  at centre-of-mass energies of  $\sqrt{s} = 7, 8,$  and  $13\text{ TeV}$ . The measurement determines that  $\gamma = (68.7^{+5.2}_{-5.1})^\circ$ , with an alternative solution corresponding to  $\gamma + 180^\circ$ . This is the most precise stand-alone measurement of  $\gamma$  to date, and achieves a precision that is comparable to all earlier measurements of  $\gamma$  combined.

The thesis also presents a phenomenological study of the impact of neutral kaon  $CP$  violation and material interaction on  $\gamma$  measurements with  $B^\pm \rightarrow (K_S^0h^+h^-)_D h'^\pm$  decays. The existing literature at the outset of the thesis work had estimated the potential bias to be  $\mathcal{O}(1^\circ)$  in  $B^\pm \rightarrow DK^\pm$  decays and to scale with  $1/r_B$ . This suggests potentially large biases for a measurement with  $B^\pm \rightarrow D\pi^\pm$  decays, since  $r_B^{D\pi} \simeq 0.005$  is much smaller than  $r_B^{DK} \simeq 0.1$ . However, the thesis argues that the actual impact is an order of magnitude smaller, as long as the  $CP$ -violation observables are determined based on the phase-space distribution of signal decays. This is demonstrated in a number of numerical studies that take the geometries of the LHCb and Belle II detectors into account.

# Acknowledgements

First of all, I want to thank my supervisor, Sneha Malde, for four years of invaluable, always-honest guidance, and for teaching me the ropes of being an experimental particle physicist. I could not have asked for a better, more involved supervisor and colleague, and I am very proud of the work that we have done together. I would also like to thank Guy Wilkinson for his supervision while Sneha was on maternity leave. Finally, I want to thank Nathan Jurik for his countless pieces of advice, insights, and ideas while cooperating on my first analysis, and for at least as many celebratory pints afterwards.

I am grateful to the many organisations that have funded my research degree: first and foremost the Royal Society for providing my main funding, and to Aage & Johanne Louis-Hansens Fond, St. Anne's College, Knud Højgaards Fond, Augustinusfonden, Hery Shaws Legat, and the Anglo-Danish Society for generous additional scholarships that made my stays in Oxford and Geneva possible.

My time in Oxford would certainly not have been the same without the many friends I've made here. I feel lucky to have shared the LHCb offices in Oxford and at CERN with an ever-changing, always-friendly bunch of fellow students (including at least one ATLAS infiltrator), with whom I've shared many enjoyable breaks, Monday push-ups, diplomatic schemes, plug-related memes, `ROOT`-induced frustrations, and warm English ales. The same can be said for the wider group of Particle Physics students, and especially Santiago, the most trusty table-football and beer-brewing buddy anyone could wish for. Likewise, the St. Anne's College MCR and boat club have brought me many good memories, of formal dinners and second desserts, of icy sunrises on the Isis, and of the sweet iron taste of a well-earned bump. Last but not least, as an expat, it has been an absolute pleasure to keep my Danish fluent by showing the University to visitors from home, trying to teach my house mates the word *brød* for 1.5 years, and sharing a *juleøl* or two with other Danes in Oxford.

Finally, I'm grateful to my family for their life-long love and for their trust that I can manage not to do too many stupid things; and I am eternally in debt to Anne Liv for her patience when I do just that, for her love and support during the last few years, and for the many adventures yet to come.

# Contents

|  |            |
|--|------------|
| <b>Preface</b>   | <b>vii</b> |
| <b>1 Introduction</b>  | <b>1</b>   |
| <b>2 Theoretical background</b>  | <b>4</b>   |
| 2.1 The C, P and T symmetries and their violation . . . . .                      | 4          |
| 2.2 CP violation in the Standard Model . . . . .                                 | 6          |
| 2.2.1 The CKM matrix and the Unitarity Triangle . . . . .                        | 7          |
| 2.2.2 Measuring $\gamma$ in tree level decays . . . . .                          | 11         |
| 2.3 Measuring $\gamma$ using multi-body D final states . . . . .                 | 14         |
| 2.3.1 Dalitz plots and the phase space of multi-body decays . . . . .            | 15         |
| 2.3.2 The BPGGSZ method to measure $\gamma$ . . . . .                            | 16         |
| 2.3.3 A model-independent approach . . . . .                                     | 19         |
| 2.3.4 Measuring strong-phase inputs at charm factories . . . . .                 | 21         |
| 2.3.5 Global CP asymmetry and the relation to GLW and ADS measurements . . . . . | 27         |
| 2.4 Strategy for the LHCb measurement . . . . .                                  | 29         |
| <b>3 The LHCb experiment</b>   | <b>34</b>  |
| 3.1 The LHCb subdetectors . . . . .  | 36         |
| 3.1.1 The VELO . . . . .   | 37         |
| 3.1.2 Magnet and tracking stations . . . . .                                     | 39         |
| 3.1.3 The RICH detectors . . . . .   | 42         |
| 3.1.4 Calorimeters . . . . .   | 43         |
| 3.1.5 Muon detectors . . . . .   | 45         |
| 3.2 Reconstruction . . . . .   | 46         |
| 3.2.1 Track reconstruction . . . . .   | 47         |
| 3.2.2 Particle identification . . . . .  | 48         |
| 3.3 The LHCb trigger system . . . . .  | 50         |
| 3.3.1 The level-0 hardware trigger . . . . .                                     | 51         |
| 3.3.2 High-level triggers . . . . .  | 52         |
| 3.3.3 Offline data filtering: the LHCb stripping . . . . .                       | 53         |
| 3.4 Simulation . . . . .   | 53         |
| 3.5 Data-taking conditions . . . . .   | 54         |

|  |           |
|--|-----------|
| <b>4 Neutral kaon <math>CP</math> violation and material interaction in BPGGSZ measurements</b>        | <b>56</b> |
| 4.1 CP violation and material interaction of neutral kaons . . . . .                                   | 57        |
| 4.1.1 A first look at the impact on $\gamma$ measurements . . . . .                                    | 60        |
| 4.2 Impact on BPGGSZ measurements of $\gamma$ :<br>principles . . . . .                                | 62        |
| 4.2.1 Modified symmetry relations . . . . .  | 62        |
| 4.2.2 Relationship between the $K_S^0$ and $K_L^0$ amplitudes . . . . .                                | 63        |
| 4.2.3 Modification of the BPGGSZ yield equations . . . . .   | 64        |
| 4.3 Impact on BPGGSZ measurements of $\gamma$ :<br>LHCb and Belle II measurements . . . . .            | 67        |
| 4.3.1 Detector geometries . . . . .  | 68        |
| 4.3.2 Kaon momentum distributions . . . . .  | 69        |
| 4.3.3 Experimental time acceptance . . . . .   | 71        |
| 4.3.4 Detector material budget . . . . .   | 71        |
| 4.3.5 Calculation procedure . . . . .  | 73        |
| 4.3.6 Results . . . . .  | 75        |
| 4.3.7 Coupled $B^\pm \rightarrow DK^\pm$ and $B^\pm \rightarrow D\pi^\pm$ measurements . . . . .       | 77        |
| 4.4 Concluding remarks . . . . .   | 78        |
| <b>5 A BPGGSZ measurement of <math>\gamma</math> with <math>B^\pm \rightarrow Dh^\pm</math> decays</b> | <b>80</b> |
| 5.1 Candidate reconstruction and selection . . . . .   | 80        |
| 5.1.1 Initial requirements . . . . .   | 81        |
| 5.1.2 Boosted decision tree . . . . .  | 83        |
| 5.1.3 Particle-identification requirements . . . . .   | 88        |
| 5.1.4 Final requirements . . . . .   | 89        |
| 5.1.5 Selected candidates . . . . .  | 91        |
| 5.2 Signal selection efficiencies . . . . .  | 92        |
| 5.2.1 Efficiency of the PID requirements . . . . .   | 94        |
| 5.2.2 Efficiency profile over the Dalitz plot . . . . .  | 95        |
| 5.3 Background studies . . . . .   | 99        |
| 5.3.1 Charmless decays . . . . .   | 100       |
| 5.3.2 Background from four-body $D$ decays . . . . .   | 101       |
| 5.3.3 Semi-leptonic backgrounds . . . . .  | 102       |
| 5.3.4 Cross-feed from other $D \rightarrow K_S^0 h^+ h^-$ decays . . . . .                             | 109       |
| 5.3.5 Swapped-track backgrounds . . . . .  | 110       |
| 5.4 Signal and background mass shapes . . . . .  | 112       |
| 5.4.1 Signal decays . . . . .  | 113       |
| 5.4.2 Cross-feed between $B^\pm \rightarrow Dh^\pm$ channels . . . . .                                 | 114       |

|                     |  |            |
|---------------------|--|------------|
| 5.4.3               | Partially reconstructed backgrounds . . . . .                                    | 117        |
| 5.4.4               | Combinatorial background . . . . .   | 122        |
| 5.4.5               | Fit results . . . . .  | 122        |
| 5.5                 | Measurement of the CP-violation observables . . . . .                            | 128        |
| 5.5.1               | Fit setup . . . . .  | 128        |
| 5.5.2               | Main results . . . . .   | 137        |
| 5.5.3               | Cross checks . . . . .   | 141        |
| 5.6                 | Systematic uncertainties . . . . .   | 150        |
| 5.6.1               | Strong phase uncertainties . . . . .   | 150        |
| 5.6.2               | Efficiency-profile-related systematic uncertainties . . . . .                    | 151        |
| 5.6.3               | Mass shapes . . . . .  | 155        |
| 5.6.4               | $CP$ violation and material interaction of the $K_S^0$ . . . . .                 | 161        |
| 5.6.5               | Impact of $D$ mixing . . . . .   | 161        |
| 5.6.6               | PID efficiencies . . . . .   | 161        |
| 5.6.7               | Dalitz-coordinate resolution . . . . .   | 162        |
| 5.6.8               | The fixed yield fractions . . . . .  | 163        |
| 5.6.9               | Systematic uncertainty due to backgrounds that are not modelled in fit . . . . . | 163        |
| 5.6.10              | Bias correction . . . . .  | 165        |
| 5.6.11              | Charmless backgrounds . . . . .  | 166        |
| 5.6.12              | Summary of systematic uncertainties . . . . .                                    | 166        |
| 5.7                 | Obtained constraints on $\gamma$ . . . . .                                       | 168        |
| 5.7.1               | Statistical approach . . . . .   | 168        |
| 5.7.2               | Interpretation results . . . . .   | 171        |
| 5.7.3               | Compatibility with other measurements . . . . .                                  | 174        |
| <b>6</b>            | <b>Summary and outlook</b>   | <b>178</b> |
| 6.1                 | A look towards the future . . . . .  | 180        |
| <b>Appendices</b>   |  |            |
| <b>A</b>            | <b>Projections of the main fit to data</b>                                       | <b>183</b> |
| <b>B</b>            | <b>Contributions for the LHCb collaboration</b>                                  | <b>189</b> |
| <b>Bibliography</b> |  | <b>191</b> |

# Preface

The work presented in this thesis has resulted in two papers, either to be submitted to or published in the Journal of High Energy Physics. These are

- [1] *Measurement of the CKM angle  $\gamma$  using  $B^\pm \rightarrow DK^\pm$  and  $B^\pm \rightarrow D\pi^\pm$  with  $D \rightarrow K_S^0 h^+ h^-$  decays*, arxiv:2010.08483, submitted to JHEP.

This paper describes a measurement of the CKM angle  $\gamma$  using  $pp$  collision data taken with the LHCb experiment during the Run 1 of the LHC, in 2011 and 2012, and during the full Run 2, in 2015–2018. The measurement uses the decay channels  $B^\pm \rightarrow Dh^\pm$  where  $D \rightarrow K_S^0 h'^+ h'^-$ , in which  $h$  and  $h'$  denotes pions or kaons. It obtains a value of  $\gamma = (68.7^{+5.2}_{-5.1})^\circ$ , which constitutes the World’s best single-measurement determination of  $\gamma$ . The work is the main focus of this thesis and is described in detail in Chapter 5.

- [2] *CP violation and material interaction of neutral kaons in measurements of the CKM angle  $\gamma$  using  $B^\pm \rightarrow DK^\pm$  decays where  $D \rightarrow K_S^0 \pi^+ \pi^-$* , JHEP 19 (2019) 106.

This paper describes a phenomenological study of the impact of neutral-kaon  $CP$  violation and material interaction on measurements of  $\gamma$ . With the increased measurement precision to come in the near future, an understanding of these effects is crucial, especially in the context of  $B \rightarrow D\pi$  decays; however no detailed study had been published at the start of this thesis. The study is the subject of Chapter 4. Some text excerpts and figures from the paper have been reproduced in the thesis.

All of the work described in the thesis is my own, except where clearly referenced to others. Furthermore, I contributed significantly to an analysis of  $B^\pm \rightarrow DK^\pm$  decays with LHCb data taken in 2015 and 2016, now published in

- [3] *Measurement of the CKM angle  $\gamma$  using  $B^\pm \rightarrow DK^\pm$  with  $D \rightarrow K_S^0 \pi^+ \pi^-$ ,  $K_S^0 K^+ K^-$  decays*, JHEP 08 (2018) 176.

I was responsible for the selection and analysis of the signal channel, studies of systematic uncertainties, and the interpretation of the measured observables in terms of underlying physics parameters. The measurement is superseded by that of Ref. [1] and is not described in detail in the thesis.

Beyond my data analysis and phenomenology work, I have made numerous other contributions to the LHCb experiment. I took part in the preparation for Run 3 by working as a *migration coordinator* for the *B-decay-to-open-charm* (B2OC) physics working group, responsible<sup>1</sup> for the development of the working group's centralised selections in the software trigger framework being developed for the LHCb Upgrade.<sup>2</sup> With more than 800 lines in the current B2OC selection module this is a major task. The new B2OC selection framework was redesigned and written from scratch, and I took a leading role in the initial design and testing, and in helping the first analysts implement their selections within it. I have also undertaken shift work as RICH piquet and Data Manager, and acted as the liason between the B2OC physics working group and the *particle-identification* performance working group. This work is described in more detail in Appendix B.

---

<sup>1</sup>Along with Alessandro Bertolin and Shunan Zhang.

<sup>2</sup>The current software trigger and centralised selection framework is presented in Section 3.3.

*Le roi est mort, vive le roi!*

— Traditional French proclamation at the death  
of one monarch and the ascension of a new

# 1

## Introduction

*"The King is dead, long live the King!"*. These words, traditionally proclaimed by the Duke of Uzès, marked the death of French monarchs from 1498 until Louis XVII lost the throne (presumably the current duke had other things on his mind during the winter 1792–93). In the original setting, the words express the fundamental premise of hereditary monarchy: at the last breath of the king, the god-given sovereignty of the crown passes to the oldest, living heir. In an altogether different sense, the words fittingly summarise the situation in the field of particle physics.

In the sub-atomic world, the Standard Model rules supreme in spite of everyone agreeing that it is in fact quite dead: while the successes of the model are numerous, it leaves several phenomena that have been observed in the world completely unexplained. Most famously, *gravity* is not included in the model, and no mathematically consistent unification of general relativity and the Standard Model has been found. A related short coming is the lack of an explanation of *dark matter* and *dark energy*: the Standard Model describes only 5 % of the energy content of modern cosmological models of the universe. Of special relevance to this thesis is the matter-antimatter asymmetry in our matter-dominated universe, for which there is no explanation in the Standard Model. Furthermore, there are a number of theoretical issues, such as the (relatively) low mass of the Higgs boson requiring extreme fine tuning of parameter values, and the absence of an explanation for the hierarchy of masses that the Higgs mechanism gives rise to. When the Standard Model continues to live long in spite of these shortcomings, it is not for want of tries at murder: thousands of physicists at dozens of experiments spend their days looking for physics effects that are *Beyond the Standard Model* (BSM), but so

far no (statistically significant) experimental results have been obtained that point to a suitable successor, able to resolve the fundamental issues with the existing theory.<sup>1</sup>

These efforts take place at two complimentary frontiers. At the vanguard of the *energy frontier* is the Large Hadron Collider, where protons are collided at energies never reached before in any experimental settings. The CMS and ATLAS experiments look for new, heavy particles produced in these unprecedented circumstances. However, so far it has only been possible to *rule out* alternative theories, excluding regions of (infinite) phase space in a multitude of possible standard model extensions.<sup>2</sup>

The other frontier is the *precision frontier*, which seeks to exploit that the (potential) existence of heavy particles can cause or influence phenomena at energies that are orders of magnitude smaller than required for their direct production. The canonical example is that of weak decays that occur in atom nuclei at rest, but are mediated by the  $W$  boson, which can only be directly produced in powerful particle accelerators. Thus, by way of precise measurements of processes at a low energy, characteristics of high energy physics can be derived. The field of flavour physics, which concerns itself with processes that distinguish the different generations of quarks and leptons in the Standard Model, plays a significant role at the precision frontier. Good historical examples are provided by the charm and third-generation quarks, the existence of which were predicted well before the particles could be produced, in order to explain lower energy phenomena (the lack of flavour-changing neutral currents and  $CP$  violation, respectively). Furthermore, the possible  $c$  and  $t$  quark masses could be constrained before their discoveries by measurements of mixing in neutral kaons and  $B$  mesons [4]. With regards to constraints on *new*, as-of-yet unknown physics effects, impressive results have been achieved in flavour physics experiments, where meson mixing and  $CP$  violation measurements provide bounds on BSM physics at energy scales of the order  $\Lambda \gtrsim 10^4$  TeV; a much higher energy scale than what can be directly probed in current and potential, near-future particle colliders [4].<sup>3</sup>

This thesis places itself at the forefront of the latter efforts, presenting the World's most precise measurement of the  $CP$ -violating phase  $\gamma$ ; a fundamental

<sup>1</sup>Neutrino masses have been experimentally observed to be different from zero. This can be accounted for by several possible extensions of the Standard Model, which cannot be differentiated given current data (but potentially in the near future). However, such extensions are not expected to resolve the issues outlined above.

<sup>2</sup>The, obviously extremely important, observation of the Higgs boson and the determination of its couplings and properties all agree with the Standard Model expectations.

<sup>3</sup>These bounds do not rule out new physics lower energy scales, but they do impose stringent constraints on the possible flavour structure of any new physics model at the  $< 10^4$  TeV scale.

parameter in the Standard Model, in which it describes the sole source of matter-antimatter asymmetry. The measurement is based on samples of  $B^\pm \rightarrow DK^\pm$  and  $B^\pm \rightarrow D\pi^\pm$  decays, where the  $D$  meson is reconstructed in one of the final states  $K_S^0\pi^+\pi^-$  and  $K_S^0K^+K^-$ . The role of  $CP$  violation in the Standard Model and the methodology used to probe it in the thesis are described in detail in Chapter 2.

The measurement is based on data taken with the LHCb experiment during Run 1 and 2 of the Large Hadron Collider. The detector and software used to obtain the data set are described in Chapter 3.

It is the first time that  $B^\pm \rightarrow D\pi^\pm$  decays are used to measure  $\gamma$  with the approach taken in the thesis; therefore, a number of effects had to be considered that were not important in measurements based solely on  $B^\pm \rightarrow DK^\pm$  decays. The most important such effect is due to  $CP$  violation and material interaction of the neutral kaon in the final state. At the outset of the work presented in the thesis, existing literature suggested that the impact could potentially be significant. Therefore, these phenomena had to be analysed in detail to establish the feasibility of the main measurement of the thesis. Chapter 4 describes such an analysis, and shows that the existing literature overestimated the potential effect by an order of magnitude; in fact the impact on the measurement is negligible.

The main results of the thesis are presented in Chapter 5, where the measurement of  $\gamma$  is described in detail. The approach differs from earlier measurements in LHCb due to the inclusion of  $B^\pm \rightarrow D\pi^\pm$  as a signal channel; therefore, a series of feasibility studies that lead to the specific approach being chosen is also presented.

Naturally, the work presented here is far from the last word to be said on the value of  $\gamma$ . In the very near future, several important results will be updated by the LHCb collaboration, based on the full data set collected during Run 2 of the Large Hadron Collider. In the coming 10–15 years, both the LHCb and Belle II experiments will record data samples of  $B$  decays that are orders of magnitudes larger than those collected before, pushing the obtainable precision on  $\gamma$  towards, even below, one degree. An outlook towards this ultra-high-precision era of  $CP$ -violation measurements is given in Chapter 6, along with a summary of the contributions made in the thesis.

# 2

## Theoretical background

This chapter lays out the theoretical framework of the thesis. Section 2.1 introduces charge and parity symmetry violation in general, while Section 2.2 covers the description in the Standard Model and the general theory behind charge-parity symmetry violation measurements in charged  $B$  decays. Section 2.3 focuses on the theory of measurements using  $B^\pm \rightarrow Dh^\pm$  decays with multi-body  $D$  final states, after which the specific analysis strategy for the measurement described in the thesis is outlined out in Section 2.4.

### 2.1 The C, P and T symmetries and their violation

The concept of symmetry plays a fundamental role in modern physics. By Noether's theorem [5], the simple assumption of invariance of our physical laws under temporal and spatial translations leads to the very non-trivial prediction of conserved energy and momentum; within the field of particle physics, the interactions and dynamics of the Standard Model (SM) follow completely simply from requiring the fundamental particle fields to satisfy a local  $U(1) \times SU(2) \times SU(3)$  gauge symmetry [6]; and one of the short-comings of the SM, is that it fails to explain the apparent *lack* of symmetry in our matter-dominated universe [7]. Indeed, it is important to experimentally establish the symmetries of our world at a fundamental level, and the degree to which they are broken.

Three discrete symmetries of importance are the symmetries under

1. The charge operator  $C$ , which conjugates all internal quantum numbers of a quantum state and thus converts particles into their anti-particle counter parts. For example,  $C$  transforms the electric charge of a particle state  $Q \rightarrow -Q$ .
2. The parity operator  $P$ , which inverts the spatial dimensions of space time:  $\vec{x} \rightarrow -\vec{x}$ . As such, it transforms left-handed particle fields into right-handed particle fields and vice versa.
3. The time-inversion operator  $T$ , which inverts the temporal dimension of space time:  $t \rightarrow -t$ .

These are fundamentally related by the *CPT* theorem [8], which states that any Lorentz-invariant Quantum Field Theory (QFT) must be symmetric under the simultaneous application of *all* three operators. However, any one of the symmetries can be broken individually, and experiments have shown the physical laws of our world to violate each of the  $C$ ,  $P$ , and  $T$  symmetries.

Such a symmetry-breaking effect was established for the first time in 1956, when Chien-Shiung Wu observed parity violation in weak decays of Co-60 nuclei [9], after carrying out an experiment that was proposed by Yang Chen-Ning and Tsung-Dao Lee [10]. While this experiment established the breaking of  $P$  symmetry, it left open the possibility that the physical laws are invariant under a combination of a charge-and parity inversion; that they are  $CP$  symmetric. However, this was disproved in 1964 when Cronin and Fitch observed that long-lived kaons, which predominantly decay to the  $CP$ -odd  $3\pi$  state, could decay to the  $CP$ -even  $\pi\pi$  states [11].

Since then,  $CP$  violation has been found in the  $B^0$  system by the BaBar and Belle collaborations during the early 2000's [12, 13]; the  $B$  factories also saw evidence for  $CP$  violation in  $B^\pm$  decays [14, 15] later confirmed by LHCb [16], and  $CP$  violation was measured in the  $B_s^0$  system by LHCb in 2013 [17]; within the last year and a half, the first observation of  $CP$ -violation in  $D^0$  decays has also been made by the LHCb collaboration [18], and most recently evidence for  $CP$ -violation in the neutrino sector has been reported by the T2K collaboration [19]. The observed effects can be divided into distinct classes. The conceptually simplest case is

1.  *$CP$ -violation in decay*, where  $|A/\bar{A}| \neq 1$  for some decay amplitude  $A$ , and the amplitude  $\bar{A}$  of the  $CP$ -conjugate decay. The result is different decay rates in two  $CP$ -conjugate decays

$$\Gamma(M \rightarrow f) \neq \Gamma(\bar{M} \rightarrow \bar{f}). \quad (2.1)$$

This type of  $CP$  violation was not seen until the late 1980's [20, 21], more than 20 years after the first observation of  $CP$  violation, and only finally established around the year 2000 [22, 23]. This discovery was also made in  $K \rightarrow \pi\pi$  decays.

$CP$ -violation in decay is the only type possible for charged initial states, and it is thus the main focus of the thesis. Two additional  $CP$ -violating effects are possible for neutral initial states (a situation that will be the main focus of Chapter 4). These effects are

2.  $CP$ -violation in mixing, which denotes the case where the mixing rates between two  $CP$ -conjugate states,  $M^0$  and  $\bar{M}^0$ , differ

$$\Gamma(M^0 \rightarrow \bar{M}^0) \neq \Gamma(\bar{M}^0 \rightarrow M^0). \quad (2.2)$$

The  $CP$  violation first observed by Cronin and Fitch in the neutral kaon sector [11] is (dominantly) of this type.

3.  $CP$ -violation in interference between mixing and decay, which can be present for a neutral initial state,  $M^0$ , decaying into a final state  $f$  common to both  $M^0$  and the  $CP$ -conjugate state  $\bar{M}^0$ . The decay rate includes an interference term between two amplitudes: the amplitude for a direct  $M^0 \rightarrow f$  decay and the amplitude for a decay after mixing:  $M^0 \rightarrow \bar{M}^0 \rightarrow f$ . Even in the absence of the two aforementioned effects, the rates  $\Gamma(M^0 \rightarrow f)$  and  $\Gamma(\bar{M}^0 \rightarrow \bar{f})$  can differ due to the interference term. Such  $CP$  asymmetries have been measured in eg.  $B^0 \rightarrow J/\psi K$  decays by LHCb and the  $B$  factories, and in  $B_s^0 \rightarrow J/\psi \phi$  decays by the LHC and Tevatron experiments [24].

$CP$  violation measurements thus have a long, rich, and still-developing history.

## 2.2 CP violation in the Standard Model

All existing measurements of  $CP$  violation in the quark sector are naturally explained in the SM. Indeed, the need to explain the observation  $CP$  violation in neutral kaons was a driving force in the development of the model in the first place, when it lead Kobayashi and Maskawa to predict the existence of then-unknown particles in 1973 [25] (now known to be the third generation quarks).

### 2.2.1 The CKM matrix and the Unitarity Triangle

The SM contains three generations of quarks, each consisting of an up-type quark ( $u$ ,  $c$ , and  $t$ ) and a down-type quark ( $d$ ,  $s$ , and  $b$ ). The charged weak interaction of the  $W^\pm$  boson couples up and down-type quarks. The quark states that couple to the  $W$  are not (a priori) identical to the mass eigenstates, and can be denoted  $(u', c', \text{ and } t')$  and  $(d', s', \text{ and } b')$ . A basis for the quark states can be chosen such that the weakly coupling up-quark states are identical to the propagating quark states,  $u = u'$ , but then the down-type quark states are different:  $d' \neq d$ . The two bases of the down-type quarks are related via the Cabibbo-Kobayashi-Maskawa (CKM) matrix [25, 26]<sup>1</sup>

$$\begin{pmatrix} d' \\ s' \\ t' \end{pmatrix} = V \begin{pmatrix} d \\ s \\ t \end{pmatrix} = \begin{pmatrix} V_{ud} & V_{us} & V_{ub} \\ V_{cd} & V_{cs} & V_{cb} \\ V_{td} & V_{ts} & V_{tb} \end{pmatrix} \begin{pmatrix} d \\ s \\ t \end{pmatrix}. \quad (2.3)$$

Thus the Lagrangian terms representing the coupling of a  $W^\pm$  boson with a  $u$ - and a  $d$ -type quark is

$$\mathcal{L}_{W^+} = -\frac{g}{\sqrt{2}} V_{ud} (\bar{u} \gamma^\mu W_\mu^+ d) \quad \mathcal{L}_{W^-} = -\frac{g}{\sqrt{2}} V_{ud}^* (\bar{d} \gamma^\mu W_\mu^- u) \quad (2.4)$$

where  $g$  is the weak coupling constant,  $\gamma_u$  are the Dirac matrices, and  $u$  and  $d$  represent the left-handed components of the physical quark states.

The CKM matrix is a unitary complex  $3 \times 3$  matrix, and hence has  $3^2 = 9$  independent, real parameters. However, five of these can be absorbed into non-physical phases of the quark states (both mass and weak eigenstates) and hence the matrix has four real, physical parameters: three mixing angles and a single phase. Chau and Keung [27] proposed the parameterisation

$$\begin{aligned} V &= \begin{pmatrix} 1 & 0 & 0 \\ 0 & c_{23} & s_{23} \\ 0 & -s_{23} & c_{23} \end{pmatrix} \begin{pmatrix} c_{13} & 0 & s_{13}e^{-i\delta_{CP}} \\ 0 & 1 & 0 \\ -s_{13}e^{-i\delta_{CP}} & 0 & c_{13} \end{pmatrix} \begin{pmatrix} c_{12} & s_{12} & 0 \\ -s_{12} & c_{12} & 1 \\ 0 & 0 & 1 \end{pmatrix} \\ &= \begin{pmatrix} c_{12}c_{13} & s_{12}c_{13} & s_{13}e^{-i\delta_{CP}} \\ -s_{12}c_{23} - c_{12}s_{23}s_{13}e^{i\delta_{CP}} & c_{12}c_{23} - s_{12}s_{23}s_{13}e^{i\delta_{CP}} & s_{23}c_{13} \\ s_{12}s_{23} - c_{12}c_{23}s_{13}e^{i\delta_{CP}} & -c_{12}s_{23} - s_{12}s_{23}s_{13}e^{i\delta_{CP}} & c_{23}c_{13} \end{pmatrix} \end{aligned} \quad (2.5)$$

which is the preferred standard by the *Particle Data Group* (PDG) [28]. Here,  $s_{ij} \equiv \sin \theta_{ij}$  and  $c_{ij} \equiv \cos \theta_{ij}$  denote the sine and cosine of three rotation angles in quark space;  $\theta_{12} = \theta_C$  being the usual Cabibbo angle [26].

---

<sup>1</sup> A basis for the quarks can of course be chosen, such that neither the up-quarks or the down-quarks are expressed in their mass eigenstates. In that case the CKM matrix is recovered as  $V = U_u U_d^\dagger$ , where  $U_{u/d}$  is the unitary transformation matrices that transform the  $u/d$  quarks from the weak eigenbasis to their mass eigenstates.

The presence of the complex phase  $\delta_{CP}$  in the Lagrangian term of the  $W$  coupling causes  $CP$  violation because, as evident from Eq. (2.4), if  $\delta_{CP}$  enters the amplitude for some decay mediated by a  $W$  boson,  $A = |A|e^{i(\delta_0 + \delta_{CP})}$ , then it will enter the  $CP$  conjugate decay amplitude with the opposite sign:  $\bar{A} = |A|e^{i(\delta_0 - \delta_{CP})}$ . In these expressions,  $\delta_0$  denotes a  $CP$  conserving phase that is not caused by complex terms in the Lagrangian, but arises due to potential intermediate states in the decay amplitude. Usually the underlying mechanism is due to QCD effects, and these  $CP$  conserving phases are therefore generally dubbed *strong* phases, as opposed to the  $CP$  violating *weak* phase of the  $W$  coupling [28]. This terminology will be applied throughout the thesis.

The absolute values of all nine elements of the CKM matrix have been measured individually, and the PDG average values are [28]<sup>2</sup>

$$\begin{pmatrix} |V_{ud}| & |V_{us}| & |V_{ub}| \\ |V_{cd}| & |V_{cs}| & |V_{cb}| \\ |V_{td}| & |V_{ts}| & |V_{tb}| \end{pmatrix} = \begin{pmatrix} 0.97370 \pm 0.00014 & 0.2245 \pm 0.0008 & 0.00382 \pm 0.00024 \\ 0.221 \pm 0.004 & 0.987 \pm 0.011 & 0.0410 \pm 0.0014 \\ 0.0080 \pm 0.0003 & 0.0388 \pm 0.0011 & 1.013 \pm 0.030 \end{pmatrix}. \quad (2.6)$$

The CKM matrix elements along the diagonal are all approximately equal to unity, while the off-diagonal elements show a clear hierarchy of sizes that in terms of the parameterisation of Eq. (2.5) translates to  $s_{13} \ll s_{23} \ll s_{12}$ . This motivates an often used, alternative parameterisation of the matrix, where the elements are expressed as power series in  $\lambda \equiv s_{12} \simeq 0.23$  that naturally incorporates the hierarchy: the Wolfenstein parameterisation [29]. The definitions

$$\begin{aligned} s_{12} &\equiv \lambda \\ s_{23} &\equiv \lambda^2 A \\ s_{13} e^{-i\delta_{CP}} &\equiv \lambda^3 (\rho - i\eta) \end{aligned} \quad (2.7)$$

are made, after which the unitarity conditions (or Eq. 2.5) determine the remaining elements to any order in  $\lambda$ .<sup>3</sup> To  $\mathcal{O}(\lambda^5)$  the Wolfenstein parameterisation of the CKM matrix is [31, 32]

$$V = \begin{pmatrix} 1 - \frac{\lambda^2}{2} - \frac{\lambda^4}{8} & \lambda & A\lambda^3(\rho - i\eta) \\ -\lambda + \frac{\lambda^5}{2} A^2(1 - 2(\rho + i\eta)) & 1 - \frac{\lambda^2}{2} - \frac{\lambda^4}{8}(1 + 4A^2) & A\lambda^2 \\ A\lambda^3(1 - (\rho + i\eta)(1 - \frac{\lambda^2}{2})) & -A\lambda^2(1 - \frac{\lambda^2}{2}(1 - 2(\rho + i\eta))) & 1 - \frac{1}{2}A^2\lambda^4 \end{pmatrix}. \quad (2.8)$$

---

<sup>2</sup>References to the individual measurements can be found in the *CKM Quark-Mixing Matrix* review of the 2020 version of the PDG.

<sup>3</sup>Other variants of the Wolfenstein parameterisation do exist [30]. They all agree at the lowest orders of  $\lambda$ .

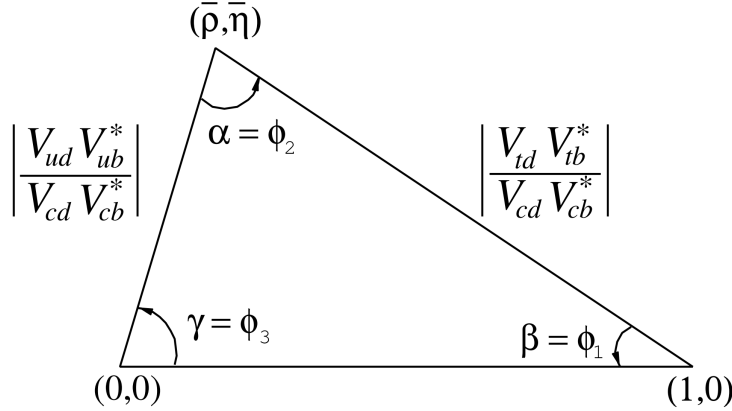


**Figure 2.1:** Definition of the lengths and sides of the Unitarity Triangle. Reproduced from the *CKM Quark-Mixing Matrix* review of the PDG [28].

The unitarity condition  $V^\dagger V = VV^\dagger = \mathbb{1}$  defines orthogonality relations between the rows and columns of the CKM matrix of the form

$$\sum_{j \in \{u,c,t\}} V_{j\alpha}^* V_{j\beta} = \delta_{\alpha\beta} \quad , \quad \alpha, \beta \in \{d,s,b\}, \quad (2.9a)$$

$$\sum_{\alpha \in \{d,s,b\}} V_{i\alpha}^* V_{j\alpha} = \delta_{ij} \quad , \quad i, j \in \{u, c, t\}. \quad (2.9b)$$

The six unique off-diagonal conditions each constrain three complex numbers to sum to zero and they can thus be visualised as triangles in the complex plane, the so-called unitarity triangles. Of these, the triangle corresponding to the first and third columns of the CKM matrix plays a special role because all three sides are of the same order of magnitude,  $\mathcal{O}(\lambda^3)$ . When expressed in the form

$$\frac{V_{ud}^* V_{ub}}{V_{cd}^* V_{cb}} + \frac{V_{td}^* V_{tb}}{V_{cd}^* V_{cb}} + 1 = 0, \quad (2.10)$$

it is often referred to as the singular Unitarity Triangle, illustrated in Fig. 2.1 where the usual names for the three angles are also given.

Over-constraining the unitarity triangle by making separate measurements of all sides and angles, in as many different decay channels as possible, is an important and non-trivial test of the SM. The current experimental constraints are in agreement with the SM predictions, as visualised in Fig. 2.2. The topic of the thesis is a measurement of the CKM angle

$$\gamma \equiv \arg(-V_{ud}V_{ub}^*/V_{cd}V_{cb}^*) = \arg(-V_{cb}V_{cd}^*/V_{ub}V_{ud}^*). \quad (2.11)$$

From the Wolfenstein parameterisation in Eq. (2.8), it is can be seen that  $\gamma$  equals

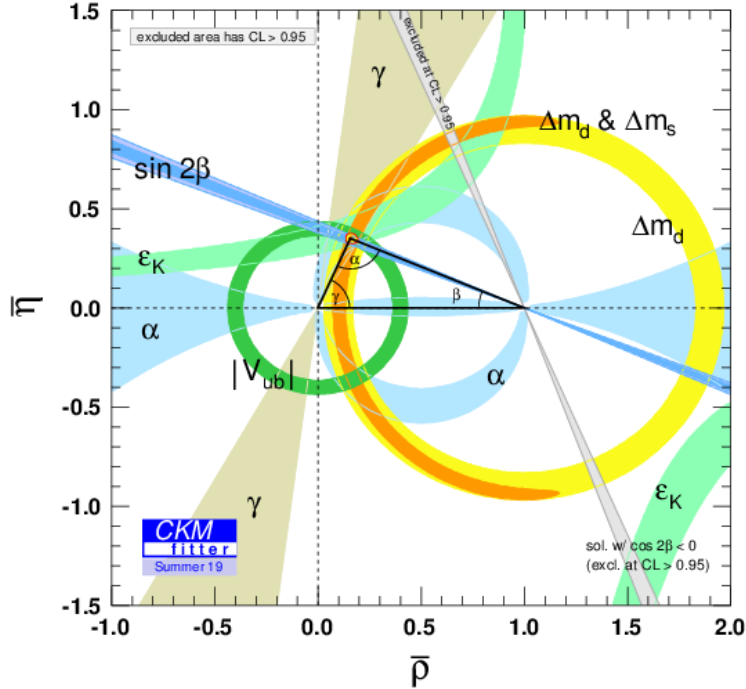


**Figure 2.2:** Current constraints on the Unitarity Triangle parameters as determined by the CKMFitter group for the EPS 2019 conference [33].

the fundamental  $CP$ -violating phase  $\delta_{CP}$  to  $\mathcal{O}(\lambda^4)$ . The angle  $\gamma$  is unique among the CKM parameters, in that it can be easily measured in tree-level processes, without significant theoretical uncertainty from lattice QCD calculations [34]. Since  $\gamma$  is (essentially) an input parameter in the SM, it is not possible to calculate a theoretical expectation that measurements can be compared to. However, tree-level processes are generally considered unlikely to be affected by Beyond-Standard-Model (BSM) effects. Therefore direct measurements of  $\gamma$  can be considered a SM benchmark, to be compared with constraints based on measurements of other CKM elements that are measured in loop-level processes, and thus are more likely to be affected by BSM effects [35]. These constraints are obtained in global fits, based on measurements of all CKM elements except  $\gamma$ , in which the unitarity of the CKM matrix is assumed to hold true. In practice,  $\gamma$  is predominantly constrained by the value of  $\beta$  and the elements defining the length of the side of the unitarity triangle opposite  $\gamma$ ; the measurement of both rely on neutral  $B$  mixing processes. If BSM physics effects enter the mixing loop, but is not accounted for in the global fit, it can result in the value of  $\gamma$  that is determined in the global fit being different to the one obtained in direct measurements. The current, worldwide combination of

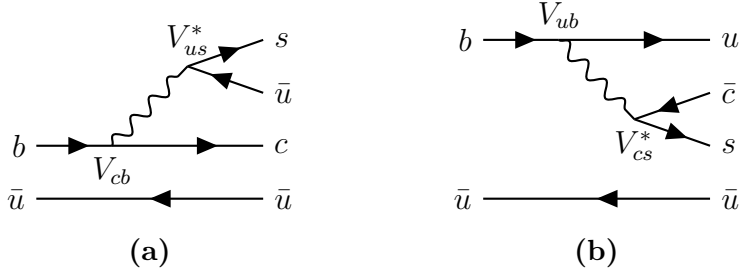


**Figure 2.3:** Tree level Feynman diagrams describing (a)  $B^- \rightarrow D^0 K^-$  and (b)  $B^- \rightarrow \bar{D}^0 K^-$  decays. The weak phase difference between the two decays is  $\Delta\phi = \arg(V_{cb}V_{us}^*/V_{ub}V_{cs}^*) \simeq \gamma$ .

direct measurements published by the CKMFitter group is  $\gamma = (72.1^{+5.4}_{-5.7})^\circ$ , to be compared with the estimate from a global fit (without any  $\gamma$  measurements) of  $\gamma = (65.66^{+0.90}_{-2.65})^\circ$  [33]. Other world averages exist [24, 36], but the overall picture is the same: the ability to constrain BSM physics is currently limited by the uncertainty of the direct measurements. Hence further precision measurements of  $\gamma$  are highly motivated. The precision is driven by time-integrated measurements of direct  $CP$ -violation in  $B^\pm \rightarrow DK^\pm$  decays; such a measurement is the topic of this thesis and the theory behind is treated in detail in the following section. It is also possible to measure  $\gamma$  in time-dependent mixing analyses of  $B_s^0 \rightarrow D_s^\mp K^\pm$ ,  $B^0 \rightarrow D^\mp \pi^\pm$ , and related decays, by measuring  $CP$  violation in interference between mixing and decay. These modes are expected to provide measurements with a precision of a few degrees in the future [37].

### 2.2.2 Measuring $\gamma$ in tree level decays

The phase  $\gamma$  can be measured in tree-level processes with interference between  $b \rightarrow c s \bar{u}$  and  $b \rightarrow \bar{c} s u$  transitions (and their  $CP$  conjugates). The canonical example, also the subject of this thesis, is based on measurements sensitive to interference between the  $B^\pm \rightarrow D^0 K^\pm$  and  $B^\pm \rightarrow \bar{D}^0 K^\pm$  decay amplitudes. As illustrated in Fig. 2.3 for the case of  $B^-$  decays, the weak phase difference between the two decays is  $\Delta\phi = \arg(V_{cb}V_{us}^*/V_{ub}V_{cs}^*)$ . While  $\Delta\phi$  is not identical to the definition of  $\gamma$  in Eq. (2.11), the ratio of the involved CKM matrix elements is [38]

$$\begin{aligned} -\frac{V_{cd}^*/V_{ud}^*}{V_{us}^*/V_{cs}^*} &= -\frac{-\lambda[1 - \frac{\lambda^4}{2}A^2(1 - 2(\rho - i\eta))](1 - \frac{\lambda^2}{2} - \frac{\lambda^4}{8}(1 + 4A^2))}{\lambda(1 - \frac{\lambda^2}{2} - \frac{\lambda^4}{4})} \\ &= 1 - \lambda^4 A^2(1 - 2(\rho - i\eta)) + \mathcal{O}(\lambda^5). \end{aligned} \quad (2.12)$$

The ratio equals unity to  $\mathcal{O}(\lambda^4) \simeq 2.6 \times 10^{-3}$ , and thus  $\Delta\phi \simeq \gamma$  is a good approximation within current experimental uncertainties. For the remainder of this

thesis the approximation will be used without further comment. The diagrams in Fig. 2.3 describe the leading order contributions to the two amplitudes

$$\begin{aligned} A[B^- \rightarrow D^0 K^-] &\equiv A_B \\ A[B^- \rightarrow \bar{D}^0 K^-] &\equiv \bar{A}_B \equiv r_B A_B e^{i(\delta_B - \gamma)}, \end{aligned} \quad (2.13a)$$

where the last equality introduces two new parameters: the amplitude magnitude ratio  $r_B \equiv |\bar{A}_B|/|A_B|$ , and  $\delta_B$ , the strong-phase difference between the decay amplitudes. Since all  $CP$ -violation is attributed to the weak phase in the SM, the  $CP$ -conjugate decay amplitudes are [39]

$$\begin{aligned} A[B^+ \rightarrow \bar{D}^0 K^+] &= A_B \\ A[B^+ \rightarrow D^0 K^+] &= \bar{A}_B = r_B A_B e^{i(\delta_B + \gamma)}. \end{aligned} \quad (2.13b)$$

In an experimental setting, the  $D^0$  and  $\bar{D}^0$  mesons are reconstructed in some final state,  $f$ , or its  $CP$ -conjugate state,  $\bar{f}$ . In analogy with the  $B^\pm$  decays, the  $D$  decay amplitude can be related<sup>4</sup>

$$\begin{aligned} A[D^0 \rightarrow f] &= A[\bar{D}^0 \rightarrow \bar{f}] = A_D \\ A[\bar{D}^0 \rightarrow f] &= A[D^0 \rightarrow \bar{f}] = r_D A_D e^{i\delta_D}. \end{aligned} \quad (2.14)$$

where the assumption has been made that  $CP$  violation in the  $D$  decays is negligible, and  $\delta_D$  denotes a  $CP$ -conserving strong-phase difference. While  $CP$ -violation in  $D$  decays has recently been measured [18], the size of the effect is small and it is considered negligible in this thesis. Based on Eqs. (2.13) and (2.14), the decay rates of  $B^+$  and  $B^-$  mesons into the possible final states can be seen to satisfy

$$\Gamma(B^- \rightarrow D(\rightarrow f) K^-) \propto 1 + r_D^2 r_B^2 + 2r_B r_D \cos [\delta_B + \delta_D - \gamma], \quad (2.15a)$$

$$\Gamma(B^+ \rightarrow D(\rightarrow \bar{f}) K^+) \propto 1 + r_D^2 r_B^2 + 2r_B r_D \cos [\delta_B + \delta_D + \gamma], \quad (2.15b)$$

$$\Gamma(B^- \rightarrow D(\rightarrow \bar{f}) K^-) \propto r_D^2 + r_B^2 + 2r_B r_D \cos [\delta_B - \delta_D - \gamma], \quad (2.15c)$$

$$\Gamma(B^+ \rightarrow D(\rightarrow f) K^+) \propto r_D^2 + r_B^2 + 2r_B r_D \cos [\delta_B - \delta_D + \gamma]. \quad (2.15d)$$

The processes in Eqs. (2.15a) and (2.15b) are  $CP$ -conjugate and it is clear how, in the general case where  $\delta_B + \delta_D \neq 0$ , a non-zero value of  $\gamma$  leads to  $CP$  violation in the form of differing decay rates. The same is true for the processes in Eqs. (2.15c) and (2.15d). Depending on the choice of  $D$  final state, these expressions can be used to relate  $\gamma$  to various observables that are experimentally accessible. This thesis concerns

---

<sup>4</sup>In this convention  $\delta_D$  is thus phase of the suppressed  $D$ -decay amplitude minus the phase of the favoured  $D$ -decay amplitude. This is the opposite convention to that used in the LHCb measurements with the ADS technique, but aligns with the phase definition used in the literature on  $\gamma$  measurements in  $D \rightarrow K_S^0 \pi^+ \pi^-$  decays.

the choice  $f = K_S^0\pi^+\pi^-$  or  $f = K_S^0K^+K^-$ , where the terms related to the  $D$  decay all have a non-trivial variation over the phase space of the decay. However, it is useful to first analyse the simpler case where  $f$  is a two-body state.

The simplest case is when  $f$  is chosen to be a  $CP$  eigenstate, so that  $f = \pm\bar{f}$  and the rate equations of (2.15a)–(2.15d) simplify, because  $r_D = 1$  and  $\delta_D \in \{0, \pi\}$ . Measurements of  $\gamma$  in such decay modes are denoted GLW measurements, after Gronau, London, and Wyler who described the approach in the early 90's [39, 40]. Experimentally it is preferable to measure yield ratios rather than absolute rates, and the observables of interest are thus the  $CP$  asymmetry

$$\begin{aligned} A_{CP=\pm 1} &= \frac{\Gamma[B^- \rightarrow D_{CP}K^-] - \Gamma[B^+ \rightarrow D_{CP}K^+]}{\Gamma[B^- \rightarrow D_{CP}K^-] + \Gamma[B^+ \rightarrow D_{CP}K^+]} \\ &= \frac{\pm r_B \sin \delta_B \sin \gamma}{1 + r_B^2 \pm 2r_B \cos \delta_B \cos \gamma}, \end{aligned} \quad (2.16a)$$

as well as the ratio

$$\begin{aligned} R_{CP=\pm 1} &= 2 \frac{\Gamma[B^- \rightarrow D_{CP}K^-] + \Gamma[B^+ \rightarrow D_{CP}K^+]}{\Gamma[B^- \rightarrow D^0K^-] + \Gamma[B^+ \rightarrow \bar{D}^0K^+]} \\ &= 1 + r_B^2 \pm 2r_B \cos \delta_B \cos \gamma. \end{aligned} \quad (2.16b)$$

In practice,  $A_{CP}$  and  $R_{CP}$  are obtained from measured yield ratios that are corrected with appropriate branching fractions. A measurement of  $A_{CP}$  and  $R_{CP}$  alone is not sufficient to determine the underlying physics parameters  $(\gamma, r_B, \delta_B)$ : even if  $r_B$  was to be known exactly, the measurements only constrain the products  $\cos \delta_B \cos \gamma$  and  $\sin \delta_B \sin \gamma$  and will always allow four solutions for  $(\gamma, \delta_B)$ . One way to break the ambiguity, first noted in the original paper [39], is to make further measurements in additional  $B$  decays, such as the  $B^\pm \rightarrow D^*K^\pm$  or  $B^0 \rightarrow DK^{*0}$  modes. These decays can also be described with the formalism derived above, but will not share the same ambiguous solutions because the  $r_B$  and  $\delta_B$  values are unique to a given  $B$  decay. Another method is to analyse  $D$  decay final states that are not  $CP$  eigenstates.

A few years after the GLW method was proposed, Atwood, Dunietz, and Soni analysed an alternative choice of  $D$  final states: a simultaneous analysis of a Cabibbo-favoured (CF) decay  $D^0 \rightarrow f$  and the doubly-Cabibbo-suppressed (DCS) decay  $D^0 \rightarrow \bar{f}$  into the  $CP$  conjugate final state [41, 42]. Their suggested method is named the ADS method after the authors. The classical example is to take  $f = K^-\pi^+$  and  $\bar{f} = K^+\pi^-$ . The relative suppression means that the  $r_D$  of Eq. (2.15) is small, typically of the same order of magnitude as  $r_B$ , and thus

the  $CP$  asymmetry of the suppressed decay is  $\mathcal{O}(1)$ :

$$\begin{aligned} A_{ADS(\bar{f})} &= \frac{\Gamma[B^- \rightarrow D(\rightarrow \bar{f})K^-] - \Gamma[B^+ \rightarrow D(\rightarrow f)K^+]}{\Gamma[B^- \rightarrow D(\rightarrow \bar{f})K^-] + \Gamma[B^+ \rightarrow D(\rightarrow f)K^+]} \\ &= \frac{r_D r_B \sin(\delta_B - \delta_D) \sin \gamma}{r_D^2 + r_B^2 + 2r_D r_B \cos(\delta_B - \delta_D) \cos \gamma}. \end{aligned} \quad (2.17a)$$

The large  $CP$  asymmetry is a prime feature of the ADS method. However, the suppressed-to-favoured yield ratio is also sensitive to the physics parameters of interest:

$$\begin{aligned} R_{ADS(\bar{f})} &= \frac{\Gamma[B^- \rightarrow D(\rightarrow \bar{f})K^-] + \Gamma[B^+ \rightarrow D(\rightarrow f)K^+]}{\Gamma[B^- \rightarrow D(\rightarrow f)K^-] + \Gamma[B^+ \rightarrow D(\rightarrow \bar{f})K^+]} \\ &= \frac{r_B^2 + r_D^2 + 2r_D r_B \cos(\delta_B - \delta_D) \cos \gamma}{1 + r_D^2 r_B^2 + 2r_D r_B \cos(\delta_B + \delta_D) \cos \gamma}. \end{aligned} \quad (2.17b)$$

The interpretation of  $A_{ADS}$  and  $R_{ADS}$  in terms of  $(\gamma, r_B, \delta_B)$  requires knowledge of the  $r_D$  and  $\delta_D$  parameters, but these can be measured independently [24]. In general, the constraints from a single set of ADS observables suffer from ambiguities similar to those in the GLW case. However, unlike the GLW case, each  $D$  decay mode provides an independent set of constraints, because the parameters related to the  $D$  decay vary.

The discussion of this section has centred on the classical case of  $B^\pm \rightarrow DK^\pm$  decays with a two-body  $D$  final state. With minor modifications the techniques have been used to make measurements sensitive to  $\gamma$  in  $B^0$  decays, with  $B$  decay final states including excited  $D$  mesons or kaons, and in  $B^\pm \rightarrow D\pi^\pm$  decays (summaries of the measurements made by the  $B$  factories and LHCb can be found in Refs. [14, 15, 43, 44]). The  $B^\pm \rightarrow D\pi^\pm$  decay is also  $CP$ -violating, although the effect is much smaller than in the  $B^\pm \rightarrow DK^\pm$  decay because  $r_B^{D\pi} \simeq 0.005$  [45], whereas  $r_B^{DK} \simeq 0.1$ . Furthermore, it is possible to use multi-body  $D$  final states. However, in some cases, a better precision can then be obtained by exploiting phase-space dependent decay rates. This is the topic of the next section.

## 2.3 Measuring $\gamma$ using multi-body $D$ final states

In multi-body  $D$  decays, the  $r_D$  and  $\delta_D$  parameters of the fundamental decay rates in Eq. (2.15) vary over the phase space of the  $D$  decay. This section describes a model-independent approach to measure  $\gamma$  in  $B \rightarrow D(\rightarrow K_S^0 \pi^+ \pi^-) h^\pm$  decays by exploiting this variation, where  $h^\pm$  denotes a kaon or a pion. The theory is identical for  $D \rightarrow K_S^0 K^+ K^-$  decays, and similar ideas have been proposed for the  $D \rightarrow K^+ \pi^- \pi^- \pi^+$  [46],  $D \rightarrow K_S^0 \pi^+ \pi^- \pi^0$  [47], and  $D \rightarrow 2\pi^+ 2\pi^-$  modes [48]. First, however, the formalism for describing amplitudes of multi-body decays is briefly reviewed.

### 2.3.1 Dalitz plots and the phase space of multi-body decays

In general, the phase space of the  $n$ -body decay  $P \rightarrow 1 + 2 + \dots + n$  consists of  $n$  four momenta, with a total of  $4n$  components. The requirement that each of the final state particles is on-shell provides  $n$  constraints on these components, and energy-momentum conservation removes a further four degrees of freedom. If the original particle  $P$  is a *scalar*, the decay is isotropic, which removes an additional three degrees of freedom, leaving the total number of degrees of freedom at  $3n - 7$ . For the specific case of three-body decays, the available phase space can thus be parameterised with only two parameters. A practical and often used choice is the invariant masses

$$s_{12} = (p_1^\mu + p_2^\mu)^2, \quad s_{13} = (p_1^\mu + p_3^\mu)^2. \quad (2.18)$$

The choice of particle pairs is arbitrary, and the coordinates easily related

$$m_P^2 + m_1^2 + m_2^2 + m_3^2 = s_{12} + s_{13} + s_{23}. \quad (2.19)$$

A scatter plot of  $(s_{12}, s_{13})$  values for a sample of particle decays is denoted a Dalitz plot [49]. It has the very useful feature that the presence of (narrow) resonances in the decay leads to visible bands in the scatter plot. Figure 2.4 illustrates how the limits of the Dalitz plot are defined by kinematic constraints, and shows an example of a Dalitz plot for  $D^0 \rightarrow K_S^0 \pi^+ \pi^-$  decays in which the  $K^*(892)^\pm$  and  $\rho(770)$  resonances are clearly visible.

In terms of the coordinates of Eq. (2.18) the differential decay rate is given by

$$d\Gamma = \frac{1}{32(2\pi)^3 m_P^3} |\mathcal{M}|^2 ds_{12} ds_{13}, \quad (2.20)$$

where  $\mathcal{M}$  is the QFT matrix element, or total decay amplitude, corresponding to the decay. In general, it is not possible to calculate  $\mathcal{M}$  from first principles. Instead, the experimental analysis of multi-body decays typically rely on an amplitude model defined with an empirically well motivated form, in which a number of free parameters must be determined experimentally. The simplest case is that of an *isobar* model, where it is assumed that the full decay can be decomposed into consecutive two-body decays of the form  $P \rightarrow R_{ij} (\rightarrow i+j) + k$ . Thus,  $\mathcal{M}$  is expressed as a non-resonant constant amplitude term,  $k_{\text{NR}}$ , plus a sum of resonance terms

$$\mathcal{M}(s_{12}, s_{13}) = k_{\text{NR}} + \sum_r k_r \mathcal{M}^r(s_{12}, s_{13}). \quad (2.21)$$

The exact form of the  $\mathcal{M}^r$  function depends on the resonance in question. An overview is given in the PDG review on resonances and references therein [28]. The

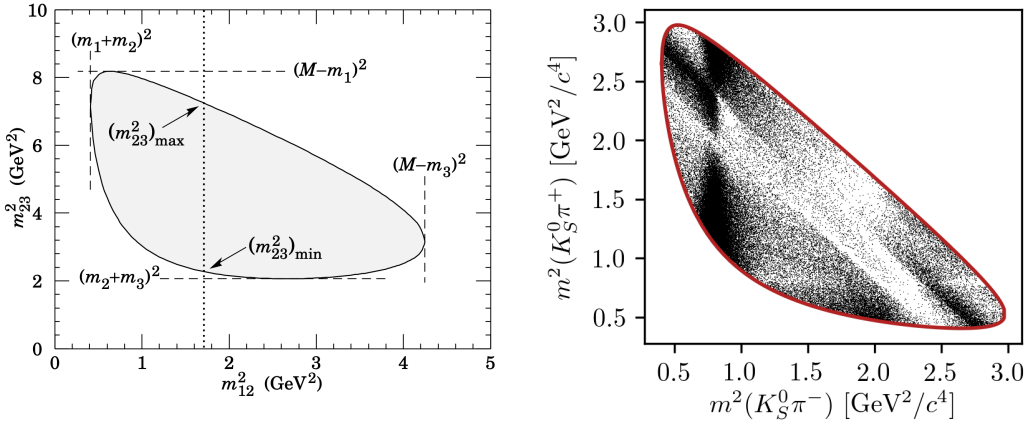


**Figure 2.4:** (Left) Schematic of a general Dalitz plot for a decay  $P \rightarrow 1 + 2 + 3$ , where the decaying particle  $P$  has the mass  $M$  and the decay products have the masses  $m_1$ ,  $m_2$ , and  $m_3$ , showing the limits of the kinematically allowed phase space. The dotted line illustrates how the possible values of  $m_{23}^2 = s_{23}$  are restricted to an interval for a given value of  $m_{12}^2 = s_{12}$ . Reproduced from the *Kinematics* review of the PDG [28]. (Right) Example of a Dalitz plot for  $D^0 \rightarrow K_S^0 \pi^+ \pi^-$  decays in an LHCb sample of flavour-tagged  $D^0$  decays. The  $K^{*-}(892)$  resonance gives rise to the vertical band of data points at  $m^2(K_S^0 \pi^-) \simeq 0.8 (\text{GeV}/c^2)^2$ , and the  $\rho^0$  resonance leads to the visible diagonal structure.

isobar formalism breaks down when resonances in the decay are not well separated in phase space. In this case, models of the form in Eq. (4.28) can still be employed, if the contribution from overlapping resonances are collected in a single term. An example of such a model, is the amplitude model for  $D^0 \rightarrow K_S^0 \pi^+ \pi^-$  decays developed by the BaBar and Belle collaborations for a measurement of the CKM angle  $\beta$  in 2018 [50] (this model is referred to as the Belle 2018 model in the thesis, because it is obtained using the Belle data set only). In this model, individual terms are included for  $D^0 \rightarrow K^*(\rightarrow K_S^0 \pi^\pm) \pi^\mp$  decays, whereas the  $\pi\pi$  and  $K\pi$   $S$ -wave contributions are modelled with the so-called  $K$ -matrix- and LASS formalisms [51, 52]. The amplitude and phase of  $\mathcal{M}$  as predicted by this model are shown in Fig. 2.5.

### 2.3.2 The BPGGSZ method to measure $\gamma$

The non-trivial phase-space dependence of the  $D \rightarrow K_S^0 \pi^+ \pi^-$  decay amplitude can be exploited to measure  $\gamma$  with  $B^\pm \rightarrow DK^\pm$  or  $B^\pm \rightarrow D\pi^\pm$  decays. This approach was proposed independently by Bondar and Poluektov [53, 54] within the Belle collaboration, and by Giri, Grossman, Soffer, and Zupan [55]. It takes the commonly used acronym BPGGSZ after all these authors.<sup>5</sup> For this specific

<sup>5</sup>The "B" and "P" are a recent addition to the BPGGSZ acronym, in recognition of the role played by Bondar and Poluektov in the development of the method. For a history of the origins of the approach, see Ref. [56].

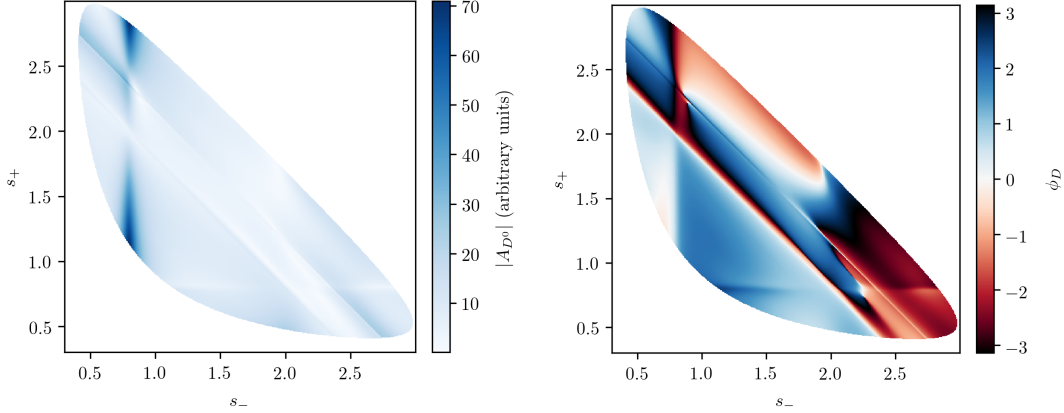


**Figure 2.5:** The (left) magnitude and (right) phase of the  $D \rightarrow K_S^0 \pi^+ \pi^-$  amplitude in the Belle 2018 model [50]. In these plots,  $s_{\pm}$  denotes the Dalitz coordinate  $m^2(K_S^0 \pi^{\pm})$ .

decay, the Dalitz coordinates are denoted

$$s_- = m^2(K_S^0 \pi^-) \quad s_+ = m^2(K_S^0 \pi^+), \quad (2.22)$$

and the  $D$  decay amplitude is a function of these coordinates

$$A_S^{\bar{D}}(s_-, s_+) = A(\bar{D}^0 \rightarrow K_S^0 \pi^+ \pi^-), \quad (2.23)$$

The magnitude and phase of  $A_S^D(s_-, s_+)$  were shown in Fig. 2.5, as predicted by the Belle 2018 amplitude model [50]. To a good approximation the  $K_S^0$  meson is a  $CP$  eigenstate, meaning that the  $K_S^0 \pi^+ \pi^-$  state is self-conjugate if the pion momenta are exchanged. Assuming this approximation to be exact, and that  $CP$  violation in the  $D$  decay is negligible, the  $D$  decay amplitudes satisfy the symmetry relation

$$A_S^{\bar{D}}(s_-, s_+) = A_S^D(s_+, s_-). \quad (2.24)$$

The impact of the  $K_S^0$  meson *not* being an exact  $CP$  eigenstate is treated in detail in Chapter 4. In order to simplify equations, the short-hand notation

$$(s_{-+}) = (s_-, s_+), \quad (s_{+-}) = (s_+, s_-) \quad (2.25)$$

will be employed for the remainder of the thesis, so that the relation in Eq. (2.24) can be expressed as  $A_S^{\bar{D}}(s_{-+}) = A_S^D(s_{+-})$ . Thus, the  $B^{\pm}$  decay rates,  $\Gamma^{\pm}$ , of Eq. (2.15) for the  $D \rightarrow K_S^0 \pi^+ \pi^-$  mode are

$$\begin{aligned} d\Gamma^-(s_{-+}) &\propto |\mathcal{A}_S^-|^2 = |A_B|^2 |A_{K_S^0}|^2 \\ &\times \left[ |A_S^D(s_{-+})|^2 + r_B^2 |A_S^D(s_{+-})|^2 + 2r_B |A_S^D(s_{-+})| |A_S^D(s_{+-})| \right. \\ &\quad \left. \times (\cos[\delta_D(s_{-+})] \cos[\delta_B - \gamma] + \sin[\delta_D(s_{-+})] \sin[\delta_B - \gamma]) \right], \end{aligned} \quad (2.26a)$$

$$\begin{aligned} d\Gamma^+(s_{-+}) &\propto |\mathcal{A}_S^+|^2 = |A_B|^2 |A_{K_S^0}|^2 \\ &\times \left[ |A_S^D(s_{-+})|^2 + r_B^2 |A_S^D(s_{+-})|^2 + 2r_B |A_S^D(s_{-+})| |A_S^D(s_{+-})| \right. \\ &\quad \left. \times (\cos[\delta_D(s_{-+})] \cos[\delta_B + \gamma] - \sin[\delta_D(s_{-+})] \sin[\delta_B + \gamma]) \right]. \end{aligned} \quad (2.26b)$$

Here,  $A_{K_S^0}$  is the decay amplitude for the  $K_S^0 \rightarrow \pi^+\pi^-$  decay, the strong phase of the  $D$  decay enters via

$$\delta_D(s_{-+}) = \phi_D(s_{-+}) - \phi_D(s_{+-}) = -\delta_D(s_{+-}), \quad (2.27)$$

where  $\phi_D(s_{-+})$  denotes the complex phase of the  $A_S^D(s_{-+})$  amplitude, and a standard trigonometric relation have been employed to factorise the terms depending on the complex phases of the  $B$  and  $D$  decays. It can be seen that in the case where  $\gamma = 0$  the  $B^+$  and  $B^-$  decay rates are symmetric if the Dalitz coordinates are exchanged:  $\Gamma^+(s_-, s_+) = \Gamma^-(s_+, s_-)$ . The presence of  $CP$  violation in the  $B$  decay breaks the symmetry. Therefore it is possible to measure  $\gamma$  (and the nuisance parameters  $r_B$  and  $\delta_B$ ) from the phase-space distribution of  $B^\pm \rightarrow D(\rightarrow K_S^0\pi^+\pi^-)h^\pm$  decays, given knowledge of  $A_S^D(s_{-+})$ .

A series of measurements of  $\gamma$  have been made that use amplitude models of the  $D$  decay [54, 57–63]. However, a model-independent approach was proposed in the original GGSZ paper [55], and developed further by Bondar and Poluektov [64, 65]. It relies on binning phase-space, in which case the necessary information on the  $D$  decay amplitude can be summarised in a small set of coefficients that can be measured in a separate experiment. That is the approach followed in this thesis, and has been used previously by the Belle [66] and LHCb collaborations [3, 67, 68]. It is described in detail in the following section.

Such a model-independent approach is favourable for two reasons. Firstly, estimating the systematic uncertainty related to the choice of parameterisation in an amplitude model is non-trivial. The BPGGSZ method relies heavily on knowledge of  $\delta_D(s_-, s_+)$ , yet the amplitude model parameters are determined in samples of flavour tagged  $D^0$  and  $\bar{D}^0$  decays, where only the magnitude of the amplitude is probed directly. Model-related uncertainties are determined by varying the model parameters within uncertainties, as well as repeating the analysis with alternative models where, for example, the included set of resonance contributions are changed, or alternative parameterisations are employed for some contributions. This is a somewhat subjective procedure, best exemplified by the fact that the BaBar and Belle collaborations assigned very different uncertainties on their legacy BPGGSZ measurements of  $\gamma$ . The BaBar collaboration assigned a model-related uncertainty on  $\gamma$  of  $3^\circ$  [59], much smaller than the  $8.9^\circ$  assigned in the Belle paper [61]. The authors of the latter paper observe that the main uncertainty contribution is precisely due the imperfect knowledge of the phase of the amplitude, even in the case where a model perfectly describes the data. In the model-independent approach described below, this uncertainty is avoided in exchange for a statistically dominated

measurement uncertainty that is trivial to determine. Secondly, in the precision era it is favourable that any experiment is easy to reinterpret in extensions of the SM. This is non-trivial for an experiment that relies on determining a set parameters in a specific  $D$ -decay model, in which the parameters are only indirectly related to physically observable quantities. On the contrary, it is non-problematic for an experiment that measures a small set of well-defined, model-independent physical observables, such as the  $c_i$  and  $s_i$  parameters. The model-independent approach described below does sacrifice some statistical performance due to the necessity of binning phase space: the statistical uncertainties on  $\gamma$  are 10–20 % larger than in unbinned, model-dependent measurements [65]. However, a slightly reduced statistical performance is preferable to a dominating, model-dependent systematic uncertainty when  $\gamma$  is to serve as a high-precision SM benchmark; this motivates the approach followed in the thesis.

An alternative model-independent approach has recently been proposed by Poluektov [69] where the externally measured input on the  $D$ -decay phase are Fourier expansion coefficients, and which therefore avoids binning phase space. The approach may have the potential to improve the obtainable precision in the future, but this has yet to be demonstrated in an experimental setting.

### 2.3.3 A model-independent approach

The phase-space distribution can be analysed in a model-independent way, if the  $D$ -decay phase space is split into regions, or bins, and the  $B$  decay yield in each bin determined experimentally. A measurement of  $\gamma$  using this approach is the main topic of the thesis. This section describes the fundamental principle, whereas the details pertaining to the exact experimental approach are delegated to Section 2.4.

The amplitude symmetry of Eq. (2.24) is exploited by defining  $2\mathcal{N}$  bins to be symmetric around the  $s_- = s_+$  diagonal of the Dalitz plot, numbered  $i = -\mathcal{N}$  to  $\mathcal{N}$  (omitting zero) such that if the point  $(s_-, s_+)$  is in bin  $i$ , then  $(s_+, s_-)$  is in bin  $-i$ , and by convention  $i > 0$  for bins where  $s_- > s_+$ . The principle is illustrated in Fig. 2.6, but the binning schemes used in actual measurements are more complicated. The decay rates in Eq. (2.26) can be integrated over such bins to calculate the yield of  $B^\pm$  decays in bin  $i$ ,  $N_i^\pm$ . These yields can be expressed

$$\begin{aligned} N_i^- &\propto h^- \left[ K_i + r_B^2 K_{-i} + 2\sqrt{K_i K_{-i}} (c_i x_- + s_i y_-) \right], \\ N_i^+ &\propto h^+ \left[ K_{-i} + r_B^2 K_i + 2\sqrt{K_i K_{-i}} (c_i x_+ - s_i y_+) \right], \end{aligned} \quad (2.28)$$

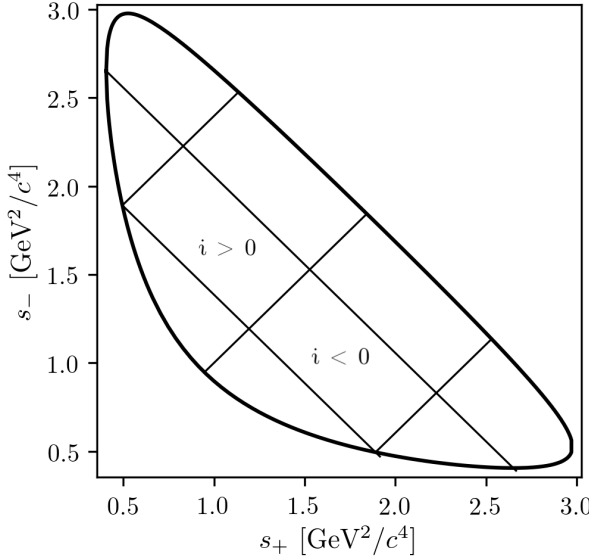


**Figure 2.6:** Illustration of the binning principle used in BPNGGSZ measurements: the bins are symmetric around the  $s_- = s_+$  diagonal, and numbered so that opposite bins have the same number, except with opposite sign.

where the parameters describing the  $B$  decay have been expressed in terms of the observables

$$x_{\pm} = r_B \cos(\delta_B \pm \gamma), \quad y_{\pm} = r_B \sin(\delta_B \pm \gamma), \quad (2.29)$$

and a number of phase-space integrated quantities related to the  $D$ -decay have been introduced. The  $K_i$  parameters denote the fractional yield of a flavour-tagged  $D^0$  decaying into bin  $i$ , defined as

$$K_i = \frac{1}{N_K} \int_i ds^2 |A_S^D(s_{-+})|^2, \quad N_K = \int ds^2 |A_S^D(s_{-+})|^2, \quad (2.30)$$

where  $\int_i ds^2$  denotes integration over bin  $i$  of the Dalitz plot. The  $c_i$  and  $s_i$  denote the amplitude-weighted average of  $\cos \delta_D(s_{-+})$  and  $\sin \delta_D(s_{-+})$  over bin  $i$

$$\begin{aligned} c_i &= \frac{\int_i ds^2 |A_S^D(s_{-+})| |A_S^D(s_{+-})| \cos[\delta_D(s_{-+})]}{\sqrt{\int_i ds^2 |A_S^D(s_{-+})|^2} \sqrt{\int_i ds^2 |A_S^D(s_{+-})|^2}}, \\ s_i &= \frac{\int_i ds^2 |A_S^D(s_{-+})| |A_S^D(s_{+-})| \sin[\delta_D(s_{-+})]}{\sqrt{\int_i ds^2 |A_S^D(s_{-+})|^2} \sqrt{\int_i ds^2 |A_S^D(s_{+-})|^2}}. \end{aligned} \quad (2.31)$$

By the symmetry properties of  $\delta_D(s_{-+})$  these parameters satisfy  $c_i = c_{-i}$  and  $s_i = -s_{-i}$ . The normalisation constants  $h^+$  and  $h^-$  are identical in the ideal case, but it is convenient to define them separately for practical reasons: depending on the experimental setup, there may be overall production and detection asymmetries that

affect the total signal yields. If an experimental analysis measures the  $CP$  observables  $(x_{\pm}, y_{\pm})$  and the normalisations  $h^{\pm}$  separately, based on the expressions in Eq. (2.28), the analysis is insensitive to these effects, because they are absorbed into the normalisation constants (as long as they are constant over the  $D$ -decay phase space). This comes at the cost that the information on  $x_{\pm}$  and  $y_{\pm}$  from the overall yield asymmetry is lost, but Section 2.3.5 will show the loss in precision to be minimal.

Thus, for a set of  $2\mathcal{N}$  bins, the bin yields of Eqs. (2.28) provide  $4\mathcal{N}$  constraints on a total of  $4\mathcal{N} + 5$  parameters:  $(h^{\pm}, K_i, c_i, s_i, x_{\pm}, y_{\pm})$ .<sup>6</sup> However, the  $K_i$ ,  $c_i$ , and  $s_i$  parameters relate only to the  $D$  decay, and can thus, in principle, be measured in independent experiments. With such external inputs, a measurement of the  $B^{\pm} \rightarrow D(\rightarrow K_S^0 \pi^+ \pi^-) h^{\pm}$  yields in a set of bins can be used to constrain  $x_{\pm}$  and  $y_{\pm}$ , and thereby  $(\gamma, r_B, \delta_B)$ . The measurement presented in this thesis determines the  $K_i$  parameters directly, but uses externally measured values of  $c_i$  and  $s_i$  as input, as measured in quantum correlated  $D$  decays by the CLEO [70] and BESIII [71, 72] collaborations. Because these measurements are the foundation of the approach, they are described in some detail in the following section. In the future, it is possible that the  $c_i$  and  $s_i$  parameters may be measured in charm-mixing measurements [73].

### 2.3.4 Measuring strong-phase inputs at charm factories

The strong-phase parameters  $c_i$  and  $s_i$  have been measured by the CLEO and BESIII collaborations using quantum correlated  $D^0 \bar{D}^0$  pairs from decays of the  $\psi(3770)$  resonance state, itself produced in  $e^+ e^-$  collisions at the resonance energy. The  $\psi(3770)$  has quantum-number  $C = -1$ , which is conserved in the strong decay into two  $D$  mesons, and thus the two  $D$  mesons are produced in an anti-symmetric wave function. By observing the decay of one  $D$  meson into a specific final state, say a  $CP$  eigenstate, the quantum state of the other  $D$  meson can be determined. The measurement is based on decays where both  $D$  decays are reconstructed, one in the  $K_S^0 \pi^+ \pi^-$  final state, the other in one of several different tag categories. The main principles are outlined below, but most experimental considerations and implementation details are left out for the sake of brevity.

The simplest case is when one  $D$  meson decays into a final state that uniquely tags the flavour, such as  $\bar{D}^0 \rightarrow K^+ e^- \bar{\nu}_e$ . In that case, the  $D$  meson decaying to  $K_S^0 \pi^+ \pi^-$  is known to be in the  $D^0$  state and the decay rate is simply determined by  $A_S^D : \Gamma(s_{-+}) \propto |A_S^D(s_{-+})|^2$ . This allows for a measurement of the  $K_i$  parameters.

---

<sup>6</sup>There are  $2\mathcal{N}$  different  $K_i$  parameters but only  $2\mathcal{N} - 1$  of them are independent, as they are constrained to sum to unity by definition.

If one  $D$  meson is reconstructed in a  $CP$ -even state, eg.  $K^+K^-$ , or a  $CP$ -odd state, eg.  $K_S^0\pi^0$ , the  $D$  meson decaying to  $K_S^0\pi^+\pi^-$  is known to be in a state of opposite  $CP$ . Thus, for a tag-decay of  $CP = \pm 1$  the decay rate has the form

$$\Gamma_{CP=\pm 1} \propto |A_S^D(s_{-+}) \mp A_S^D(s_{+-})|^2 \quad (2.32a)$$

and the bin yields will be given by

$$M_i^\pm \propto K_i + K_{-i} \mp 2\sqrt{K_i K_{-i}} c_i. \quad (2.32b)$$

Thus a simultaneous analysis of flavour and  $CP$  tagged decays allow for a determination of the  $K_i$  and  $c_i$  parameter sets.

Finally, the case where both  $D$  mesons, for now denoted  $D$  and  $D'$ , decay into the  $K_S^0\pi\pi$  final state can be considered. The total amplitudes have contributions from the case where  $D$  is in the  $D^0$  state and  $D'$  is in the  $\bar{D}^0$  state, as well as the opposite flavour assignment. Thus the decay rate satisfies

$$\Gamma_{CP=\pm 1} \propto |A_S^D(s_{-+})A_S^D(s'_{+-}) + A_S^D(s_{+-})A_S^D(s'_{-+})|^2 \quad (2.33a)$$

where  $s_{-+}$  denotes the Dalitz-plot coordinates of the  $D$  meson, and  $s'_{-+}$  those of the  $D'$  meson. Defining  $M_{ij}$  to be the yield of decays where the  $D$  decay is in bin  $i$  and the  $D'$  in bin  $j$ , the bin yields satisfy

$$M_{ij} \propto K_i K_{-j} + K_j K_{-i} - 2\sqrt{K_i K_{-i} K_j K_{-j}} (c_i c_j + s_i s_j). \quad (2.33b)$$

Thus, analysing these decays in addition to the  $CP$  and flavour tagged decays provide information on all of  $K_i$ ,  $c_i$ , and  $s_i$ . Note, however, that Eqs. (2.32) and (2.33) are invariant under the transformation  $\delta_D \rightarrow -\delta_D$ . In practice, the analysis is extended in a number of ways to enhance the statistics: using "flavour-tag" states that are not exact flavour tags, such as  $K^-\pi^+$ , using self-conjugate multi-body  $D$ -decay final states that are not exact  $CP$  eigenstates, such as  $\pi^+\pi^-\pi^0$ , and using the  $K_L^0\pi^+\pi^-$  final state as well. However, the main principles are the same as described above.

The measurements of  $c_i$  and  $s_i$  are made for a range of different binning schemes. It was noted already in Ref. [65] that a rectangular binning scheme, such as the example in Fig. 2.6, does not provide the optimal sensitivity to  $\gamma$ . It will always be the case that some statistical sensitivity is lost in a binned analysis, as compared to an unbinned, model-dependent analysis; however, the degree to which this is the case depends on the choice of binning. A better sensitivity can be obtained if the bins are defined such that  $\delta_D$  is approximately constant over a given bin. In practice, the binning scheme is defined by splitting the  $D$ -decay phase space

into quadratic *micro bins* with a width of  $0.0054 (\text{GeV}/c^2)^2$  and assigning a bin number to each micro bin depending on the decay amplitude phase, as evaluated in an amplitude model of choice. The obtained binning scheme when using an amplitude model developed by the BaBar collaboration in 2008 [58] is shown in Fig. 2.7a. In Ref [65] it was also shown that the binning can be even further optimised for sensitivity. The suggested figure of merit is

$$Q^2 = \frac{\sum_i \left( \frac{1}{\sqrt{N_i^B}} \frac{dN_i^B}{dx} \right)^2 + \left( \frac{1}{\sqrt{N_i^B}} \frac{dN_i^B}{dy} \right)^2}{\int ds^2 \left[ \left( \frac{1}{|\Gamma^B(s_{-+})|} \frac{d|\Gamma^B(s_{-+})|^2}{dx} \right)^2 + \left( \frac{1}{|\Gamma^B(s_{-+})|} \frac{d|\Gamma^B(s_{-+})|^2}{dy} \right)^2 \right]} \quad (2.34)$$

which quantifies the statistical sensitivity for a given binning, relative to the one achievable in an unbinned analysis. The CLEO collaboration defined an *optimal* binning scheme by an iterative procedure where, starting from the equal binning scheme, a micro-bin is randomly reassigned new bin numbers in each step, and a step accepted if  $Q^2$  increases. The optimisation is done for the case where  $x = y = 0$  and thus  $Q^2$  simplifies to  $Q_{x=y=0}^2 = \sum_i N_i^{x=y=0} (c_i^2 + s_i^2) / N_{total}^{x=y=0}$ . The resulting binning scheme is shown in Fig. 2.7b. An additional binning scheme is defined, denoted the *modified optimal* scheme and shown in Fig. 2.7c, where the  $Q^2$  figure of merit is modified to take into account the presence of backgrounds [70]. The modified optimal binning scheme has proven beneficial to use in measurements with small signal yields [74], but is not employed in the present thesis.

Both the CLEO [70] and BESIII [71] collaborations have measured the values of  $c_i$  and  $s_i$  for the equal, optimal, and modified optimal binning schemes. The results are also shown in Fig. 2.7, where they are compared to the expectation from the latest amplitude model [50]. The measurements presented in this thesis are based on a combination of the BESIII and CLEO results for the optimal binning scheme, made by the BESIII collaboration [71] and tabulated in Table 2.1.

While the *definition* and *optimisation* of these binning schemes depend on knowledge of  $A_S^D(s_-, s_+)$  via an amplitude model, it is important to note that no model information is needed when the binning schemes are used in the subsequent measurements of strong-phases<sup>7</sup> or *CP*-observables. Therefore the measurements will not be biased by any modelling imperfections, although the obtained precision might be lower than expected.

The preceding discussion has been focusing on the  $D \rightarrow K_S^0 \pi^+ \pi^-$  channel, however the  $D \rightarrow K_S^0 K^+ K^-$  channel can be analysed completely analogously. The

---

<sup>7</sup>With the exception of minimal model-dependence introduced when the  $K_L^0 \pi^+ \pi^-$  final state is employed to constrain the  $s_i$  parameters by the  $D$ -factories [70–72], the impact of which is well under control.

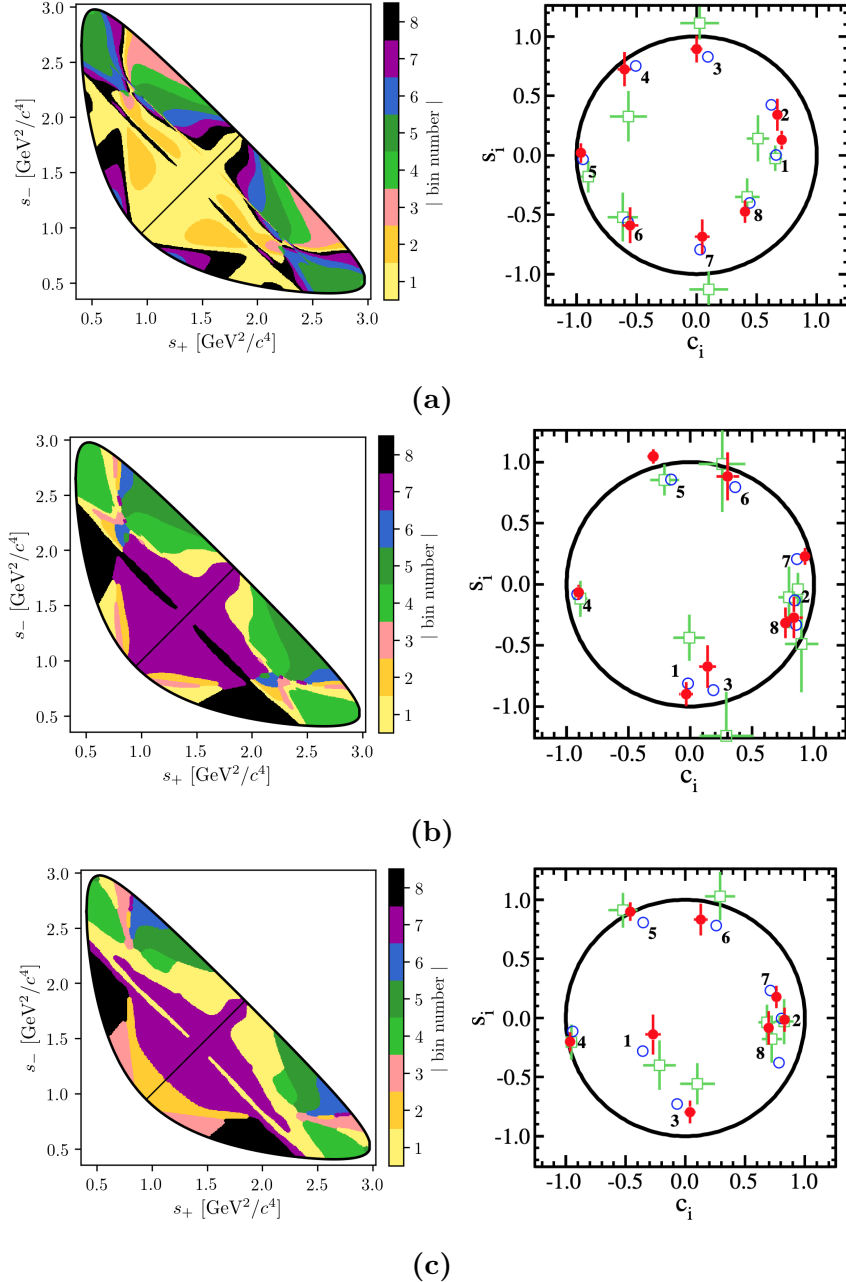


**Figure 2.7:** The (left) binning schemes and (right) measured values of  $(c_i, s_i)$  for the (a) equal, (b) optimal, and (c) modified optimal binning schemes for  $D \rightarrow K_S^0 \pi^+ \pi^-$  decays. The plots of the measured values are taken from Ref. [71] and show the results obtained by (red) BESIII, (green) CLEO, and (blue) the model expectation using the model from Ref. [50]. The measurement featured in this thesis uses the optimal binning scheme. Due to a different sign convention for the bin numbers, the  $s_i$  values shown in the BESIII figures have the opposite sign to those defined in the text.

**Table 2.1:** The experimentally measured  $c_i$  and  $s_i$  values used in the thesis. For both the  $D \rightarrow K_S^0\pi^+\pi^-$  and  $D \rightarrow K_S^0K^+K^-$  channels, the values are the combined values from the BESIII [71, 72] and CLEO [70] measurements published by BESIII in Refs. [71] and [72], respectively. Due to a different sign convention for the bin numbers, the  $s_i$  values are quoted with the opposite sign to those in the BESIII publications.

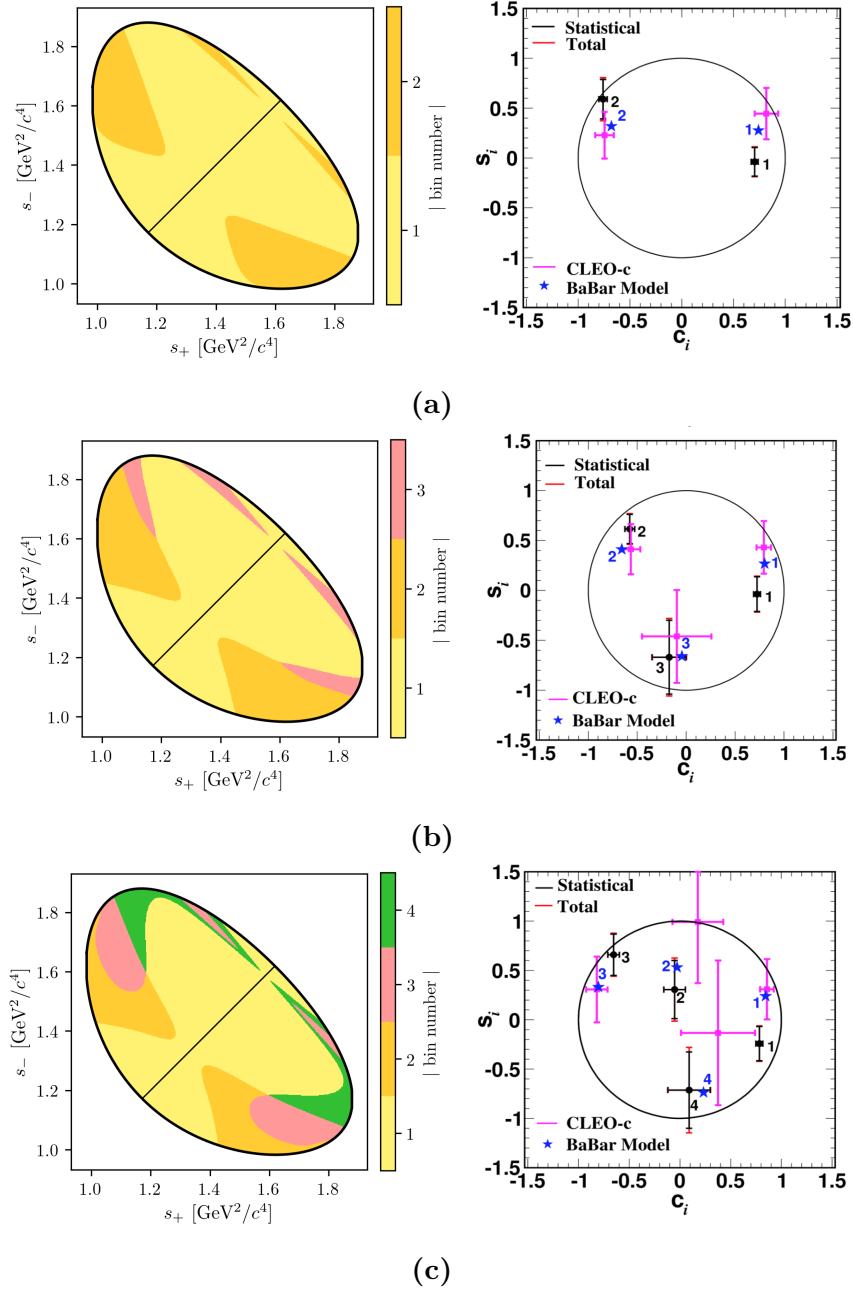
| Optimal binning scheme: $D \rightarrow K_S^0\pi^+\pi^-$ |                    |                    |
|---|--------------------|--------------------|
| Bin $i$   | $c_i$              | $s_i$              |
| 1   | $-0.037 \pm 0.049$ | $0.829 \pm 0.097$  |
| 2   | $0.837 \pm 0.067$  | $0.286 \pm 0.152$  |
| 3   | $0.147 \pm 0.066$  | $0.786 \pm 0.154$  |
| 4   | $-0.905 \pm 0.021$ | $0.079 \pm 0.059$  |
| 5   | $-0.291 \pm 0.041$ | $-1.022 \pm 0.062$ |
| 6   | $0.272 \pm 0.082$  | $-0.977 \pm 0.176$ |
| 7   | $0.918 \pm 0.017$  | $-0.184 \pm 0.065$ |
| 8   | $0.773 \pm 0.033$  | $0.277 \pm 0.118$  |

| 2-bins binning scheme: $D \rightarrow K_S^0K^+K^-$ |                    |                    |
|--|--------------------|--------------------|
| Bin $i$  | $c_i$              | $s_i$              |
| 1  | $0.713 \pm 0.032$  | $-0.107 \pm 0.132$ |
| 2  | $-0.758 \pm 0.037$ | $-0.394 \pm 0.173$ |

BESIII and CLEO collaborations have measured  $c_i$  and  $s_i$  values for this mode as well, in three binning schemes [70, 72]. These are all equal-phase binning schemes, with 2, 3, and 4 bins, respectively, shown in Fig. 2.8. The  $D \rightarrow K_S^0K^+K^-$  decay amplitude is almost completely dominated by two  $K^+K^-$  resonances, the  $CP$ -odd  $\phi(1020)$  and the  $CP$ -even  $a_0(980)$ , and this means that very little gain in sensitivity can be made by altering the equal-phase binning schemes [70]. The measured  $c_i$  and  $s_i$  values are shown in Fig. 2.8, and tabulated in Table 2.1, for the 2-bins scheme, which is used in this thesis.

The strong-phase measurements are dominated by statistical uncertainties for both the  $D \rightarrow K_S^0\pi^+\pi^-$  and  $D \rightarrow K_S^0K^+K^-$  decay channels. The current BESIII measurements are based on a data set corresponding to an integrated luminosity of  $2.9\text{ fb}^{-1}$ ; the BESIII collaboration is planning to continue to collect data at the  $\psi(3770)$  resonance energy corresponding to an additional  $17\text{ fb}^{-1}$  during 2021 and 2022 [75], and therefore significantly improved measurements can be made in the near future.



**Figure 2.8:** The (left) binning schemes and (right) measured values of  $(c_i, s_i)$  for the (a) 2-, (b) 3-, and (c) 4-bins binning schemes for  $D \rightarrow K_S^0 K^+ K^-$  decays. The plots of the measured values are taken from Ref. [72] and show the (error bars) results obtained by (black) BESIII, (pink) CLEO, and (blue) the model expectation using the model from Ref. [59]. The measurement featured in this thesis uses the 2-bins scheme. Due to a different sign convention for the bin numbers, the  $s_i$  values shown in the BESIII figures have the opposite sign to those defined in the text.

### 2.3.5 Global CP asymmetry and the relation to GLW and ADS measurements

The introduction of separate normalisation factors  $h^+$  and  $h^-$  in Eq. (2.28) hides the fact that information on  $\gamma$  (in principle) can be obtained from the asymmetry in phase-space-integrated  $B^+$  and  $B^-$  yields. In the ideal case where  $h^- = h^+$  the total yield asymmetry is

$$\begin{aligned} A_{\text{BPGGSZ}} &= \frac{\sum_{i=-N}^N N_i^- - N_i^+}{\sum_{i=-N}^N N_i^- + N_i^+} = \frac{\sum_{i=-N}^N \sqrt{K_i K_{-i}} c_i (x_- - x_+)}{1 + r_B^2 + 2 \sum_{i=-N}^N \sqrt{K_i K_{-i}} c_i (x_- + x_+)} \\ &= \frac{2 \sum_{i=1}^N \sqrt{K_i K_{-i}} c_i (x_- - x_+)}{1 + r_B^2 + 4 \sum_{i=1}^N \sqrt{K_i K_{-i}} c_i (x_- + x_+)}, \end{aligned} \quad (2.35)$$

using that  $\sum_{i=-N}^N \sqrt{K_i K_{-i}} s_i = 0$  by definition. The size of the asymmetry is governed by the factor  $2 \sum_{i=1}^N \sqrt{K_i K_{-i}} c_i$ , which is small for  $D \rightarrow K_S^0 \pi^+ \pi^-$  and  $D \rightarrow K_S^0 K^+ K^-$  decays. The underlying reason is that  $\delta_D(s_-, s_+)$  varies significantly across phase-space for these decays, as evident by the spread in the values of  $c_i$  in Table 2.1, which reduces the *average* of the asymmetry-generating  $D^0 - \bar{D}^0$  interference term to being close to zero. The value of  $2 \sum_{i=1}^N \sqrt{K_i K_{-i}} c_i$  is closely related to the *CP* content of the final state in question: for a self-conjugate *CP* even (odd) final state the  $D^0$  and  $\bar{D}^0$  decay amplitudes satisfy

$$A_{D^0}(s_-, s_+) = {}^{(+)}_{(-)} A_{\bar{D}^0}(s_-, s_+) = {}^{(+)}_{(-)} A_{D^0}(s_+, s_-), \quad (2.36)$$

meaning that  $K_i = K_{-i}$  and  $c_i = \pm 1$ ; thus  $2 \sum_{i=1}^N \sqrt{K_i K_{-i}} c_i = {}^{(+)}_{(-)} 1$ . This motivates the definition of the *CP*-even fraction of the decay

$$\mathcal{F}_+ \equiv \frac{1}{2} \left( 1 + 2 \sum_{i=1}^N \sqrt{K_i K_{-i}} c_i \right), \quad (2.37)$$

equivalent to the definition in Ref. [76] for the case  $N = 1$ . With  $\mathcal{F}_+$  in hand, the asymmetry in Eq. (2.35) can be rewritten

$$A_{\text{BPGGSZ}} = \frac{(2\mathcal{F}_+ - 1)r_B \sin \delta_B \sin \gamma}{1 + r_B^2(2\mathcal{F}_+ - 1)2r_B \cos \delta_B \cos \gamma}, \quad (2.38)$$

which is the usual form used in quasi-GLW measurements [76, 77]. The value of  $\mathcal{F}_+$  is independent of the number and shape of bins in a given binning scheme, as long as the bin definitions follow the symmetry principles outlined in Section 2.3.3. For  $D \rightarrow K_S^0 \pi^+ \pi^-$  and  $D \rightarrow K_S^0 K^+ K^-$  decays the values of  $\mathcal{F}_+$  are

$$\begin{aligned} \mathcal{F}_+(K_S^0 \pi^+ \pi^-) &= 57\% \\ \mathcal{F}_+(K_S^0 K^+ K^-) &= 51\% \end{aligned} \quad (2.39)$$

as evaluated with the Belle 2018 model [50] for  $D \rightarrow K_S^0\pi^+\pi^-$  decays and the BaBar 2010 model [59] for  $D \rightarrow K_S^0K^+K^-$  decays. In  $B^\pm \rightarrow DK^\pm$  decays  $r_B^{DK} \sim 0.1$ , and the predicted global asymmetries are thus approximately 1–2 %, which is not resolvable with the current experimental yields. As shown in Chapter 4,  $CP$  violation in the  $K_S^0$  sector leads to asymmetries of a similar size, further complicating the use of global asymmetries to constrain  $x_\pm$  and  $y_\pm$ . Thus these modes are ill-suited for quasi-GLW measurements, and ignoring global asymmetries leads to a negligible loss of information on  $\gamma$  in a BPGGSZ measurement. The reverse is true for a well-suited quasi-GLW mode, such as  $D \rightarrow \pi^+\pi^-\pi^0$ : if  $\mathcal{F}_+$  is close to either zero or unity, it means that  $(c_i, s_i)$  will be close to  $(\pm 1, 0)$  in all bins for *any* given binning scheme, and the set of bins will provide almost identical constraints on  $x_\pm$  and  $y_\pm$ . Thus, the binning of phase space leads to no significant gain in precision compared to a global analysis.

Indeed, a crucial quality of the BPGGSZ method, is that exactly because each bin-pair provides independent constraints on  $x_\pm$  and  $y_\pm$ , the method provides a single solution for  $(\gamma, r_B, \delta_B)$  that does not suffer the ambiguities of the ADS and GLW approaches. In order to illustrate this further, it is useful to make one more comparison of the model-independent BPGGSZ formalism to the ADS and GLW formalisms. In a  $CP$  symmetric world, the  $B^+$  yield in bin  $+i$  would equal the  $B^-$  yield in bin  $-i$ . Therefore the relevant  $CP$  asymmetry for a given Dalitz bin is

$$\begin{aligned} A_{BPGGSZ}^i &\equiv \frac{N_i^- - N_{-i}^+}{N_i^- + N_{-i}^+} \\ &= \frac{\sqrt{K_i K_{-i}}(c_i(x_- - x_+) + s_i(y_- - y_+))}{K_i + r_B^2 K_{-i} + 2\sqrt{K_i K_{-i}}(c_i(x_- + x_+) + s_i(y_- + y_+))}. \end{aligned} \quad (2.40)$$

This expression is identical to the ADS asymmetry in Eq. (2.17a) if the effective  $D$ -decay parameters  $r_D^i$  and  $\delta_D^i$  are defined via

$$\kappa_i \cos \delta_D^i \equiv c_i \quad , \quad \kappa_i \sin \delta_D^i \equiv s_i \quad , \quad r_D^i \equiv \sqrt{K_i / K_{-i}}, \quad (2.41)$$

and a coherence factor,  $\kappa$ , is included in the interference terms of the ADS expression, as is standard for multi-body  $D$  decays [78]. These parameters allow us to classify a given pair of bins with number  $\pm i$  as either *GLW-like*, if  $\delta_D^i$  is close to 0 or  $\pi$  and  $r_D^i$  is close to unity, or *ADS-like* if  $r_D^i \ll 1$ . The  $CP$ -even fraction of the  $D$ -decay can also be defined for a given bin-pair:

$$\mathcal{F}_+^i = \mathcal{F}_{+i}^{-i} \equiv \frac{1}{2} \left( 1 + 2c_i \frac{\sqrt{K_i K_{-i}}}{K_i + K_{-i}} \right) = \frac{1}{2} \left( 1 + 2c_i \frac{r_D^i}{1 + r_D^i} \right). \quad (2.42)$$

**Table 2.2:** Classification of the bins used in model-independent BPGGSZ measurements, in terms of whether the interplay between the  $D^0$  and  $\bar{D}^0$  amplitudes in the bin resemble typical GLW or ADS behaviour. The parameters are calculated using the 2018 Belle model [50] for  $D \rightarrow K_S^0\pi^+\pi^-$  decays and the 2010 BaBar model [59] for  $D \rightarrow K_S^0K^+K^-$  decays.

| Optimal binning scheme: $D \rightarrow K_S^0\pi^+\pi^-$ |             |                  |                 |          |               |
|---|-------------|------------------|-----------------|----------|---------------|
| Bin $i$   | $\hat{r}_D$ | $\hat{\delta}_D$ | $\mathcal{F}_+$ | $\kappa$ | Bin type      |
| 1   | 0.473       | 91.9°            | 48.97 %         | 0.81     | Odd-even      |
| 2   | 0.164       | 11.1°            | 63.38 %         | 0.85     | ADS-like      |
| 3   | 0.157       | 79.4°            | 52.50 %         | 0.89     | ADS-like      |
| 4   | 0.768       | 175.3°           | 5.85 %          | 0.92     | GLW-odd-like  |
| 5   | 0.759       | -99.9°           | 42.84 %         | 0.87     | Odd-even      |
| 6   | 0.223       | -64.5°           | 57.92 %         | 0.87     | ADS-like      |
| 7   | 0.651       | -13.3°           | 89.44 %         | 0.89     | GLW-even-like |
| 8   | 1.745       | 21.0°            | 87.08 %         | 0.92     | GLW-even-like |

| 2-bins binning scheme: $D \rightarrow K_S^0K^+K^-$ |             |                  |                 |          |               |
|--|-------------|------------------|-----------------|----------|---------------|
| Bin $i$  | $\hat{r}_D$ | $\hat{\delta}_D$ | $\mathcal{F}_+$ | $\kappa$ | Bin type      |
| 1  | 0.816       | 19.8°            | 86.14 %         | 0.78     | GLW-even-like |
| 2  | 0.775       | 154.5°           | 16.23 %         | 0.77     | GLW-odd-like  |

A GLW-even-like bin pair will have  $\mathcal{F}_+^i \simeq 1$  and a GLW-odd-like bin pair will have  $\mathcal{F}_+^i \simeq 0$ .

Table 2.2 summarises a classification of the bins for the optimal  $D \rightarrow K_S^0\pi^+\pi^-$  binning scheme and the 2-bins  $D \rightarrow K_S^0K^+K^-$  binning scheme following these principles. Two bin pairs are classified as *Odd-even*; in these bins,  $r_D^i$  is not particularly small but  $\mathcal{F}_+^i$  is close to 0.5. The name refers to the fact that for these bins  $A_{\text{BPGGSZ}}^i$ , as defined in Eq (2.40), will be positive and  $A_{\text{BPGGSZ}}^{-i}$  negative or vice versa.<sup>8</sup> The fact that multiple bin types appear for both the  $D \rightarrow K_S^0\pi^+\pi^-$  and  $D \rightarrow K_S^0K^+K^-$  modes underline that each mode benefits from being analysed in the BPGGSZ formalism.

## 2.4 Strategy for the LHCb measurement

The main topic of the thesis is a model-independent BPGGSZ measurement using  $B^\pm \rightarrow DK^\pm$  and  $B^\pm \rightarrow D\pi^\pm$  decays, with two  $D$  final states  $K_S^0\pi^+\pi^-$  and

<sup>8</sup>Neither individual asymmetry is zero, however, and these bins play an important role in constraining the  $y_\pm$  parameters. This is illustrated in Fig. 5.46 on page 148, where constraints from individual bins are evaluated as a cross checks of the measurement in Chapter 5.

$K_S^0 K^+ K^-$ . The measurement is based on the data collected by the LHCb experiment, described in detail in next chapter, during Run 1 and 2 of the Large Hadron Collider. The optimal binning scheme is used for the  $D \rightarrow K_S^0 \pi^+ \pi^-$  mode, with the combined strong-phase inputs from the BESIII [71] and CLEO [70] collaborations published in Ref. [71]. For the  $D \rightarrow K_S^0 K^+ K^-$  channel, the 2-bins scheme is used, again using a combination [72] of measurements from the CLEO [70] and BESIII [72] collaborations. The details of the analysis are presented in Chapter 5, but the overall strategy, and a few extensions of the formalism from the previous sections, are given here.

It is the first time that  $\gamma$  is measured in  $B^\pm \rightarrow D\pi^\pm$  decays with the BPGGSZ method at LHCb (although it has been used as a control channel in previous measurements with  $B^\pm \rightarrow DK^\pm$  decays [3, 67, 68]). The promotion of  $B^\pm \rightarrow D\pi^\pm$  to a signal channel has two benefits. First of all, there is a small degree of  $CP$  violation in  $B^\pm \rightarrow D\pi^\pm$  decays, and therefore a measurement of  $CP$  observables in  $B^\pm \rightarrow D\pi^\pm$  decays does provide some further information on  $\gamma$ . However, the latest LHCb combinations have generally *not* included this information, because the currently measured  $B^\pm \rightarrow D\pi^\pm$  observables allow for two solutions for  $(r_B^{D\pi}, \delta_B^{D\pi})$  [43]. One of these is almost certainly non-physical, and the presence of both makes the statistical interpretation of the results on  $\gamma$  highly non-trivial. The multiple solutions arise because the constraints on the  $B^\pm \rightarrow D\pi^\pm$  parameters come from ADS/GLW measurements. As described in Section 5.7, the situation is resolved by the measurement presented in the thesis, and therefore  $B^\pm \rightarrow D\pi^\pm$  measurements can be included in future LHCb combinations without incurring such problems. However, the  $B^\pm \rightarrow D\pi^\pm$  channel constrains  $\gamma$  much less than the  $B^\pm \rightarrow DK^\pm$  channel, and therefore the impact on the overall precision is small. The second, more significant, benefit from the promotion of  $B^\pm \rightarrow D\pi^\pm$  to a signal channel, is that the analysis avoids a significant systematic uncertainty due LHCb acceptance effects that was present in earlier analyses. This is described further below.

Due to the geometry of the LHCb detector, the signal reconstruction efficiency for  $B^\pm \rightarrow D(\rightarrow K_S^0 h^+ h^-) h'^\pm$  decays varies significantly across the  $D$ -decay phase space. This is clearly visible in Fig. 2.9, where examples of the acceptance profile for  $B^\pm \rightarrow D(\rightarrow K_S^0 h^+ h^-) K^\pm$  decays in LHCb simulation are shown, and the acceptance is seen to vary  $\pm 50\%$  relative to the average over the allowed phase space. The main feature, especially visible for  $D \rightarrow K_S^0 \pi^+ \pi^-$  decays, is a falling acceptance along the diagonal of the Dalitz plot, which is caused by the fact that a non-significant fraction of  $K_S^0$  mesons escape the LHCb tracking region before decaying, and that there is a correlation between  $m^2(h^+ h^-)$  and the  $K_S^0$  momentum

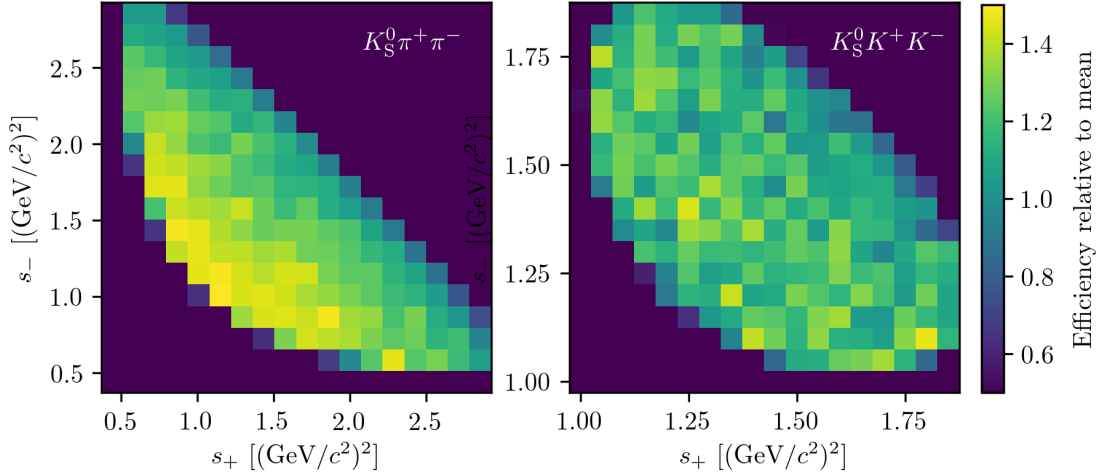


**Figure 2.9:** The LHCb acceptance in simulated  $B^\pm \rightarrow DK^\pm$  decays where (left)  $D \rightarrow K_S^0 \pi^+ \pi^-$  and (right)  $D \rightarrow K_S^0 K^+ K^-$ .

in the LHCb frame. The non-uniform acceptance results in yield equations that differ slightly from those derived in the preceding sections. Denoting the efficiency profile as  $\eta(s_-, s_+)$ , the expressions in Eq. (2.28) are modified to

$$\begin{aligned} N_i^- &= h^{B^-} \left[ F_i + r_B^2 F_{-i} + 2\sqrt{F_i F_{-i}} (c'_i x_- + s'_i y_-) \right], \\ N_i^+ &= h^{B^+} \left[ F_{-i} + r_B^2 F_i + 2\sqrt{F_i F_{-i}} (c'_i x_+ - s'_i y_+) \right], \end{aligned} \quad (2.43)$$

where the phase-space integrated quantities now include the efficiency profile

$$F_i = \frac{1}{N_F} \int_i ds^2 \eta(s_{-+}) |A_S^D(s_{-+})|^2, \quad N_F = \int ds^2 \eta(s_{-+}) |A_S^D(s_{-+})|^2, \quad (2.44)$$

$$c'_i = \frac{\int_i ds^2 \eta(s_{-+}) |A_S^D(s_{-+})| |A_S^D(s_{-+})| \cos[\delta_D(s_{-+})]}{\sqrt{\int_i ds^2 \eta(s_{-+}) |A_S^D(s_{-+})|^2} \sqrt{\int_i ds^2 \eta(s_{-+}) |A_S^D(s_{-+})|^2}}, \quad (2.45)$$

with an analogous definition of  $s'_i$ . At leading order, the strong-phase parameters are unaffected by the non-uniform efficiency, and, in addition, the bin definitions favour bins for which  $\cos[\delta_D(s_{-+})]$  and  $\sin[\delta_D(s_{-+})]$  are approximately constant across each bin. Therefore, the  $c_i$  and  $s_i$  values reported by the charm factories are used directly in the measurement. The impact on the obtained central values is negligible, as described in detail in Section 5.6 where a systematic uncertainty is assigned.

The  $F_i$  and  $K_i$  parameters are significantly different, because the experimental acceptance profile in LHCb is significantly non-uniform. Given external inputs for the strong-phase parameters, it is possible to fit the  $F_i$  parameters and  $x_\pm$  and  $y_\pm$  simultaneously in a fit to the LHCb  $B^\pm \rightarrow DK^\pm$  data set, in which case the

obtained  $F_i$  parameters incorporate the correct acceptance profile correction by construction. However, the obtainable precision for the  $CP$  observables measured by this procedure is suboptimal. As an alternative, the first LHCb measurement [67] determined acceptance-related yield corrections based on model predictions of  $K_i$ , adjusted using the relative acceptance between bins determined in  $B^\pm \rightarrow D\pi^\pm$  decays (assuming  $CP$  symmetry and that the  $K_i$  were correctly predicted by the model). However, there is  $CP$  violation present in the  $B^\pm \rightarrow D\pi^\pm$  decays, which led to a dominant systematic uncertainty. Later LHCb measurements [3, 68] instead relied on flavour tagged  $D$  mesons from  $\bar{B}^0 \rightarrow D^{*+}(\rightarrow D^0\pi^+)\mu^-\bar{\nu}_\mu X$  decays to obtain  $F_i$ , where no  $CP$  violation is possible. However, due to necessarily different triggering paths and selections, the acceptance profile is not exactly identical between semi-leptonic decays and the  $B^\pm \rightarrow Dh^\pm$  decays of interest. An efficiency correction based on (very large) samples of simulated decays was therefore applied to obtain the correct  $F_i$  values, and in this case, the uncertainty related to the correction constituted the largest systematic uncertainty on the measurement.

Both sources of systematic uncertainty can be avoided by making a simultaneous analysis of  $B^\pm \rightarrow DK^\pm$  and  $B^\pm \rightarrow D\pi^\pm$  decays, where  $CP$ -violating observables are measured in *both* channels and the  $F_i$  parameters are shared. It is a reasonable assumption that  $F_i^{DK} = F_i^{D\pi}$  to a very good approximation, given the similar kinematics of the decays. The assumption is confirmed using simulated decays in Section 5.2.2, for the candidate selection used in the measurement of the thesis. Effectively, the  $F_i$  are determined in the high statistics  $B^\pm \rightarrow D\pi^\pm$  channel, but with no systematic effect from  $CP$ -violation in that channel, since the  $CP$ -violation is incorporated in the yield description.

At the start of the work that lead to this thesis, it was not clear to what degree the measured  $CP$ -violating observables in  $B^\pm \rightarrow D\pi^\pm$  decays were affected by  $CP$  violation in the neutral kaon sector. The potential bias had been shown to be  $\sim 1^\circ$  in the  $B^\pm \rightarrow DK^\pm$  channel, a negligible effect given the past precision, but to scale with  $1/r_B$  [38] suggesting potentially large biases in the  $B^\pm \rightarrow D\pi^\pm$  channel where  $r_B$  is  $\sim 20$  times smaller. However, the dedicated analysis presented in Chapter 4 has proved the effect to be an order of magnitude smaller in BPGGSZ measurements than suggested in Ref. [38], and the simultaneous measurement is indeed viable.

The measurement in Chapter 5 is performed by making extended maximum-likelihood fits to the  $m_B$  spectra of  $B \rightarrow D(\rightarrow K_S^0 h^+ h^-)h'^\pm$  candidates split by charge and Dalitz bin. The  $B^\pm \rightarrow DK^\pm$  signal yields are parameterised using the expressions in Eq. (2.43) directly, and the fit therefore determines values for  $x_\pm^{DK}$  and  $y_\pm^{DK}$ . The Cartesian  $CP$ -violating observables  $x_\pm$  and  $y_\pm$  are employed because

they lead to better statistical behaviour than fits to data where the underlying parameters ( $\gamma, r_B^{DK}, \delta_B^{DK}$ ) are determined directly, at the cost of introducing a fourth degree of freedom. With the addition of the  $B^\pm \rightarrow D\pi^\pm$  mode as a true signal channel, two new underlying parameters are introduced,  $r_B^{D\pi}$  and  $\delta_B^{D\pi}$ . There is a choice to be made, in terms of how to define the observables that are measured. One possibility is to introduce an additional set of four observables,  $(x_-^{D\pi}, y_-^{D\pi}, x_+^{D\pi}, y_+^{D\pi})$ , that are analogous to the  $B^\pm \rightarrow DK^\pm$  parameters. As an alternative, it is possible to introduce only two Cartesian parameters [79, 80], by defining

$$\xi^{D\pi} = \left( \frac{r_B^{D\pi}}{r_B^{DK}} \right) \exp[i(\delta_B^{D\pi} - \delta_B^{DK})] \quad (2.46a)$$

and letting

$$x_\xi^{D\pi} = \text{Re}[\xi^{D\pi}] \quad y_\xi^{D\pi} = \text{Im}[\xi^{D\pi}]. \quad (2.46b)$$

In terms of these parameters, the usual Cartesian  $x_\pm$  and  $y_\pm$  are given by

$$x_\pm^{D\pi} = x_\xi^{D\pi} x_\pm^{DK} - y_\xi^{D\pi} y_\pm^{DK}, \quad y_\pm^{D\pi} = x_\xi^{D\pi} y_\pm^{DK} + y_\xi^{D\pi} x_\pm^{DK}. \quad (2.47)$$

Using this expression, the  $B^\pm \rightarrow D\pi^\pm$  yields can also be defined via Eq. (2.43) in the maximum-likelihood fit. Note that  $\xi$  does not depend on  $\gamma$ : all information on  $CP$  asymmetries in both the  $B^\pm \rightarrow DK^\pm$  and  $B^\pm \rightarrow D\pi^\pm$  channels is encoded in  $x_\pm^{DK}$  and  $y_\pm^{DK}$ . In the thesis, the latter parameterisation is chosen, because it allows for a stable fit for all six  $x$  and  $y$  parameters and the shared  $F_i$  parameters; the choice is described in much greater detail in Section 5.5.1.

As discussed, the combined analysis of  $B^\pm \rightarrow DK^\pm$  and  $B^\pm \rightarrow D\pi^\pm$  decays presents a significant step forward, because it solves the problem of obtaining  $F_i$  parameters for the appropriate acceptance profile in a manner that avoids leading systematic uncertainties, and almost all reliance on simulation. This is of great importance, if the large data samples that will be collected by LHCb in the future are to be exploited to their full potential.

# 3

## The LHCb experiment

The LHCb experiment is one of the four large experiments at the Large Hadron Collider (LHC), the World’s most powerful particle accelerator, able to accelerate protons to record centre-of-mass energies of  $\sqrt{s} = 13 \text{ TeV}$  in a 27 km long tunnel underneath Geneva. The LHCb experiment is specifically designed to study the large number of particles containing  $b$  or  $c$  quarks produced in such collisions, which has led to a number of design decisions that make the LHCb unique among the LHC experiments. The LHCb detector is not a full-solid-angle detector like the other three large LHC experiments, CMS, ATLAS, and ALICE, but a single-arm spectrometer, instrumented in the forward region where a large fraction of  $b\bar{b}$  pairs are produced. During data taking the experiment is operated at a lower instantaneous luminosity than the other experiments, leading to far fewer  $pp$  interactions. This, in combination with a vertex detector located extremely close to the interaction point, allows for excellent resolution in the reconstruction of primary and secondary vertex locations, crucial to many of the central measurements of the experiment. Finally, dedicated particle-identification detectors allow for very efficient separation of hadron species, absolutely crucial to isolate a number important signal decays (including the  $B^\pm \rightarrow D K^\pm$  decay studied in the thesis). Each of these features is described in much greater detail in the sections below.

During operation of the LHC, bunches of about  $\mathcal{O}(10^{11})$  protons are accelerated to the desired centre-of-mass energy in a series of linear and circular accelerators, the final one being the LHC itself. This is illustrated in Fig. 3.1. The bunches remain in the LHC for the duration of a *fill*, typically about 12 hours, where they are made to collide at four distinct locations, the collision points, each home to one of

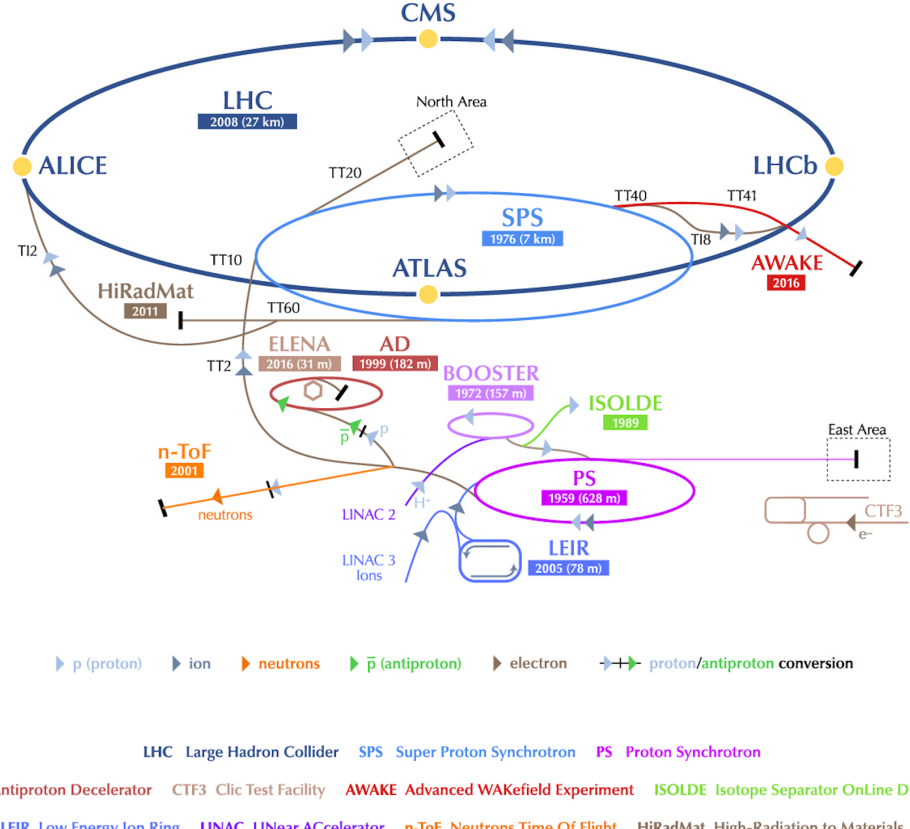


**Figure 3.1:** The CERN accelerator complex, including the length and construction year for a number of accelerators, not all of which are used in  $pp$  operations. During  $pp$  operation, the proton acceleration chain is: LINAC 2 → BOOSTER → PS → SPS → LHC. The figure is reproduced from Ref. [81].

the large experiments. The collisions occur with a frequency of up to 40 MHz. A fill ends when the beams are dumped, typically because the average number of protons in the bunches has become too low, after which the whole process begins again.

The LHC has been providing  $pp$  collisions during two periods so far: Run 1 during 2011 and 2012, where the centre-of mass energies were  $\sqrt{s} = 7$  TeV and 8 TeV, respectively, and Run 2 from 2015 to 2018, where  $\sqrt{s} = 13$  TeV. The instantaneous luminosity at the LHCb collision point has been  $4 \times 10^{32} \text{ cm}^{-2} \text{ s}^{-1}$ , and has allowed for the collection of a data set corresponding to an integrated luminosity of approximately  $3 \text{ fb}^{-1}$  during Run 1 and  $6 \text{ fb}^{-1}$  during Run 2. The full data set forms the basis of the thesis. This instantaneous luminosity is significantly lower than at other collision points, for example the peak instantaneous luminosity in the ATLAS detector was about  $20 \times 10^{33} \text{ cm}^{-2} \text{ s}^{-1}$  in 2018 [82], 50 times higher than in LHCb. The lower luminosity is necessary to limit the number of  $pp$  interactions per bunch crossing to an average of about 1.1–1.6 (depending on the data-taking period), necessary for a vertex reconstruction with the required

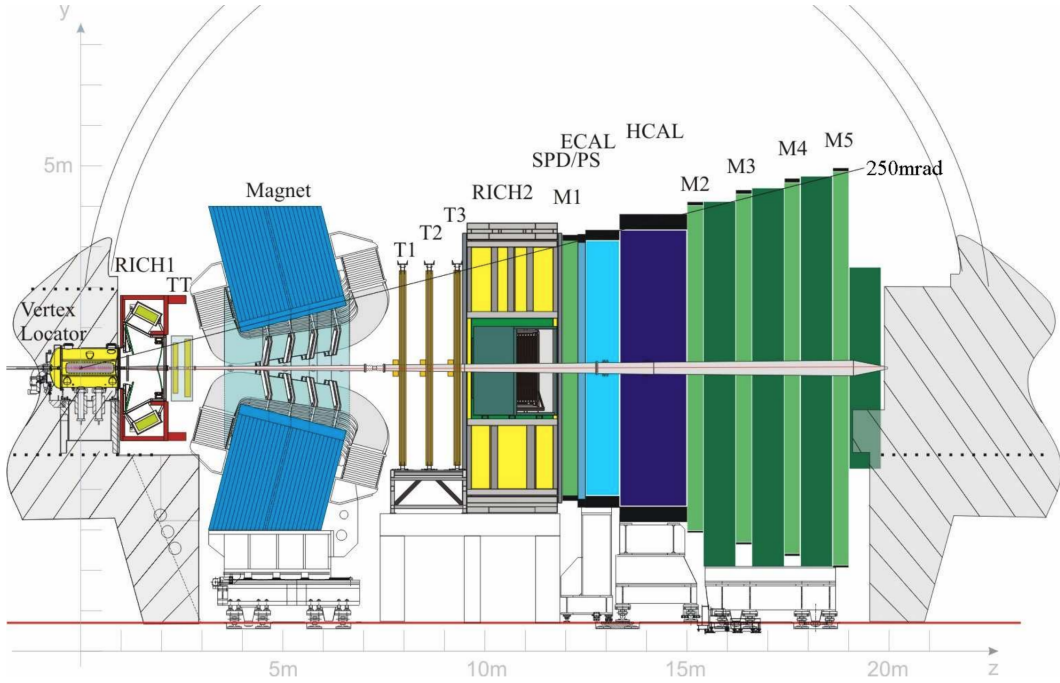


**Figure 3.2:** Overview of the LHCb detector reproduced from Ref. [83]. The individual subdetectors are described in detail in the text.

precision. The lower luminosity is achieved by colliding the proton beams with an off-set at the LHCb collision point. This has the added benefit that the offset can be continuously adjusted during a fill of the LHC, and thus all data can be taken at the same instantaneous luminosity, allowing for simpler trigger configuration, and simpler subsequent analysis because the detector occupancy is constant. The lower luminosity, of course, comes with the downside that the collected data sample is smaller.

### 3.1 The LHCb subdetectors

The LHCb detector, shown in Fig. 3.2, is able to detect particles in the forward region  $\eta \in [2, 5]$ , corresponding to an angle  $\theta$  with respect to the beam line between 15 and 300/250 mrad in the horizontal/vertical direction. As illustrated in Fig. 3.3, the  $b\bar{b}$  production cross section is very large within the LHCb acceptance: even though the acceptance covers less than 2 % of the solid angle, 24 % of all  $b\bar{b}$  pairs created at  $\sqrt{s} = 14$  TeV are within the acceptance [84] (for  $\sqrt{s} = 8$  TeV the number is 25 %). The detector is described with a coordinate system, where the  $z$ -axis is along the beam line and the  $x$  ( $y$ ) axis is in the horizontal (vertical) directions normal to the beam line. The origin is at the collision point. The experiment consists of a number

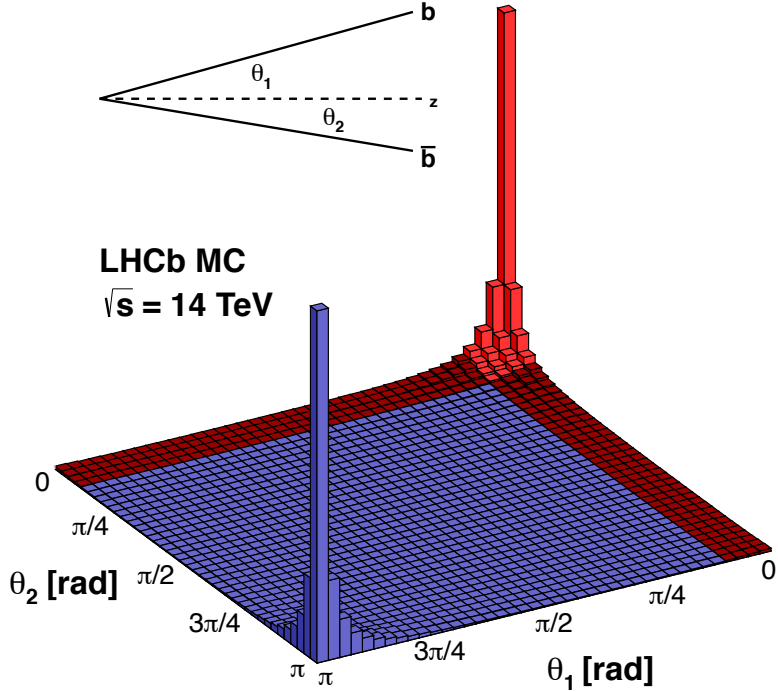


**Figure 3.3:** Production cross section of  $b\bar{b}$  pairs at a centre-of-mass energy of  $\sqrt{s} = 14 \text{ TeV}$ , as a function of  $\theta_1$  and  $\theta_2$ , the angle of the  $b$  and  $\bar{b}$  quark, respectively, with respect to the beam axis  $z$ . The LHCb acceptance is marked in red. The cross-section looks very similar for  $\sqrt{s} = 7, 8, 13 \text{ TeV}$ . The figure is taken from Ref. [84].

of subdetectors, located in the region from around the interaction point, and up to a distance of  $z = 20 \text{ m}$  along the beam line (in the following, the direction from the interaction point towards the subdetectors is denoted *downstream*, and the opposite direction *upstream*). This section describes each of the subdetectors in detail.

### 3.1.1 The VELO

The VErtex LOcator (VELO) [85] is a silicon detector located immediately around the collision point, used to provide precise measurements of the particle track coordinates in the interaction region. These are used to reconstruct the production and decay vertices of beauty and charm hadrons with a very high accuracy, and play an important role in the full track reconstruction. The ability to distinguish tracks originating in secondary vertices also plays a crucial role in efficient triggering, as described further below.

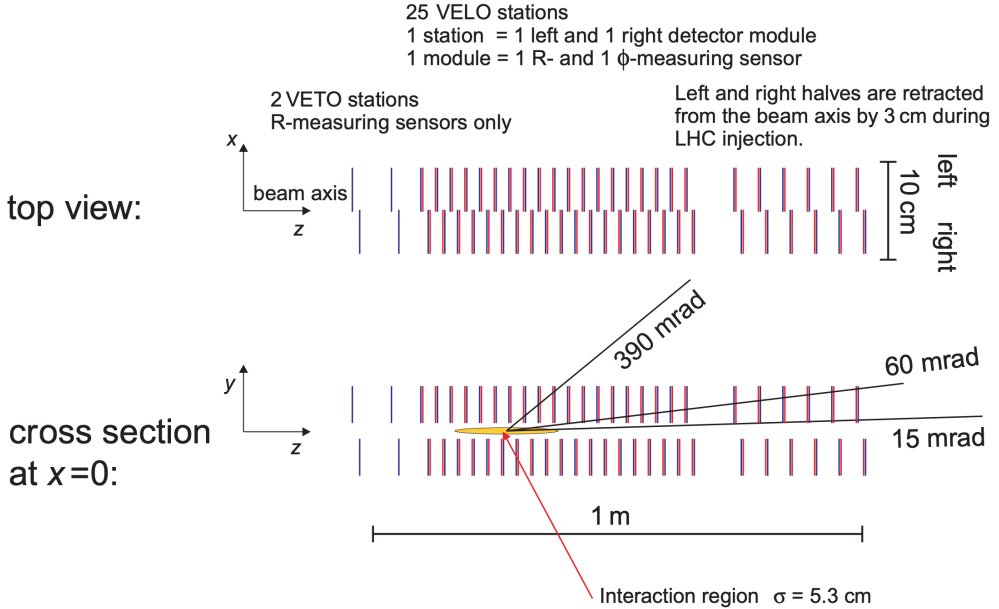


**Figure 3.4:** Overview of the arrangement of VELO stations from the VELO Technical Design Report (TDR) [85]. The actual detector includes 21 stations instead of 25, but the overall design is essentially identical [86].

The detector consists of 21 VELO stations positioned along the beam line as illustrated in Fig. 3.4. Each station consists of two *modules*, mounted on each side of the beam line; each module, in turn, consists of two silicon strip detectors, where the strips are oriented to provide a measurement of  $r$ , the radial distance from the beam line, and  $\phi$ , the azimuthal angle, respectively. This is illustrated in Fig. 3.5. The strip pitch varies between 40 and 100  $\mu\text{m}$  depending on the distance from the beam line. The stations are positioned such that all tracks that are within the acceptance region of the downstream detectors and originate at the interaction point are guaranteed to intersect 3 detector stations. During operation, the modules are located only 8 mm from the beam; this is achieved by mounting them on a moving frame that can be retracted during beam commissioning to avoid radiation damage. The detectors are kept in a vacuum, shielded from the beam vacuum by a 0.3 mm thick *RF foil* made of aluminium that also serves to screen the detector from electric fields induced by the proton beam. The silicon sensors were kept at an operating temperature of about  $-7^\circ\text{C}$ , achieved with a liquid-CO<sub>2</sub> cooling system.

The primary vertex (PV) resolution of the VELO is typically  $\sim 10 \mu\text{m}$  in the  $x$  and  $y$  directions and  $\sim 50 \mu\text{m}$  in the  $z$  direction, improving with the number of tracks originating at the PV, and deteriorating with the overall number of PVs [86]. The typical uncertainty on the decay length of a  $B$  meson is about 230  $\mu\text{m}$ , compared to a typical decay length of  $\mathcal{O}(10)$  mm. The resolution of the *impact parameter*,

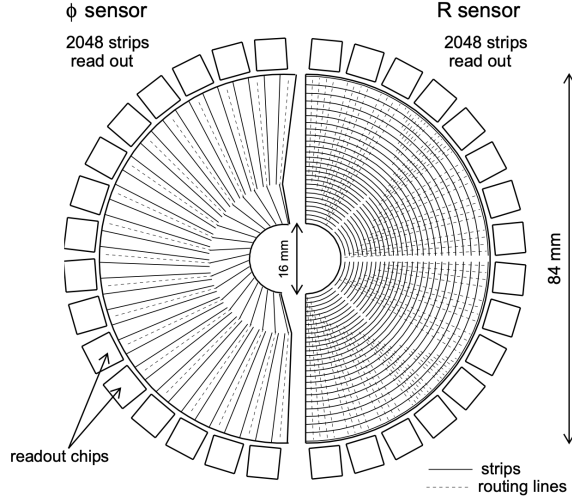


**Figure 3.5:** Illustration of the silicon strip layout in the VELO modules designed to measure (left) the azimuthal angle,  $\phi$ , of a track, and (right) the radial distance from the beam,  $r$ . Reproduced from Ref. [85].

IP, of a track is well-described by the formula  $\sigma_{\text{IP}} = (15 + 29/[p_T/( \text{GeV}/c)]) \mu\text{m}$ . This parameter excellently distinguishes particles produced in secondary decays from those produced in the primary interaction (for which the IP would be zero, were it not for the experimental resolution).

### 3.1.2 Magnet and tracking stations

The LHCb experiment uses a warm (non-superconducting) dipole magnet to measure the momentum of charged particles, by providing a maximum magnetic field strength of approximate 1 T and a total bending power of about 4 T m over the region where  $z \in [2.5, 8] \text{ m}$ . The magnetic field has been measured to a relative precision of about  $4 \times 10^{-4}$  and is uniform in the  $x$  and  $y$  planes to within a percent within the tracking volume [83]. The profile of the magnetic field along the  $z$ -axis is shown in Fig. 3.14 on page 46, where the track types within LHCb are defined. The magnet can provide a magnetic field in either vertical direction; over the span of a year of running the experiment approximately equal amounts of data are collected with the magnet in the "Up" and "Down" configurations; this leads to the cancellation of a number of charge-asymmetry effects, significantly reducing potential systematic uncertainties.

The tracking system consists of the VELO, and four other tracking stations: the Tracker Turicensis (TT) upstream of the magnet, and the tracking stations 1–3 (T1, T2, T3) downstream of the magnet. The downstream tracking stations each consist of an Inner Tracker (IT) based on silicon strips, and an Outer Tracker (OT) that employs drift tubes.

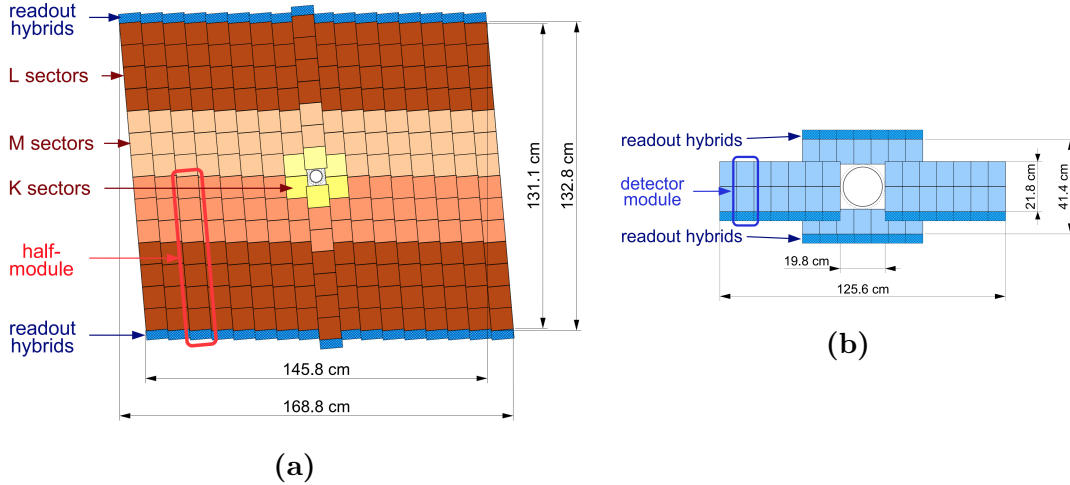


**Figure 3.6:** Overview of (a) a *v*-layer module of the TT and (b) an *x*-layer module of the IT. Reproduced from Ref. [83]

Both the TT and IT are based on silicon strip detectors with a pitch of about 200  $\mu\text{m}$ ; they were developed as a single project and are collectively known as the Silicon Tracker (ST). The TT is a 140 cm wide and 130 cm tall planar tracking station, covering the whole LHCb acceptance. It is shown in Fig. 3.6a. At each of the T1–T3 stations, the IT consist of four modules, arranged around the beam pipe as illustrated in Fig. 3.6b. They do not cover the full LHCb acceptance, only the very-forward region where the number of tracks is largest. Each TT or IT module comprises of four layers of silicon strips, where the central two layers are rotated  $\pm 5^\circ$  with respect to the first and last layer (an *x-u-v-x* geometry). The ST has a spatial resolution for a given track of approximately 50  $\mu\text{m}$ , chosen because the overall momentum resolution is then dominated by multiple-scattering effects for almost all reconstructed tracks.

At the T1–T3 stations, the OT covers the part of the overall acceptance of 300 (250) mrad in the horizontal (vertical) plane that is not covered by the IT. The OT consists of arrays of gas-tight drift tubes with inner diameters of 4.9 mm. The OT is shown illustrated in Fig. 3.7. An Ar/CO<sub>2</sub>/O<sub>2</sub> (70/28.5/1.5) gas mixture is used to fill the tubes that ensures a drift time below 50 ns and a drift coordinate resolution of 200  $\mu\text{m}$ . The use of a drift-chamber detector is necessary, because it was not economically feasible to instrument the whole LHCb acceptance with silicon strip detectors in T1–T3. The condition that the OT occupancy should not be above 10 % in the planned run conditions determined the boundary between the IT and the OT (in practice, the LHCb has been running at twice the original design luminosity so the actual occupancy has been higher).

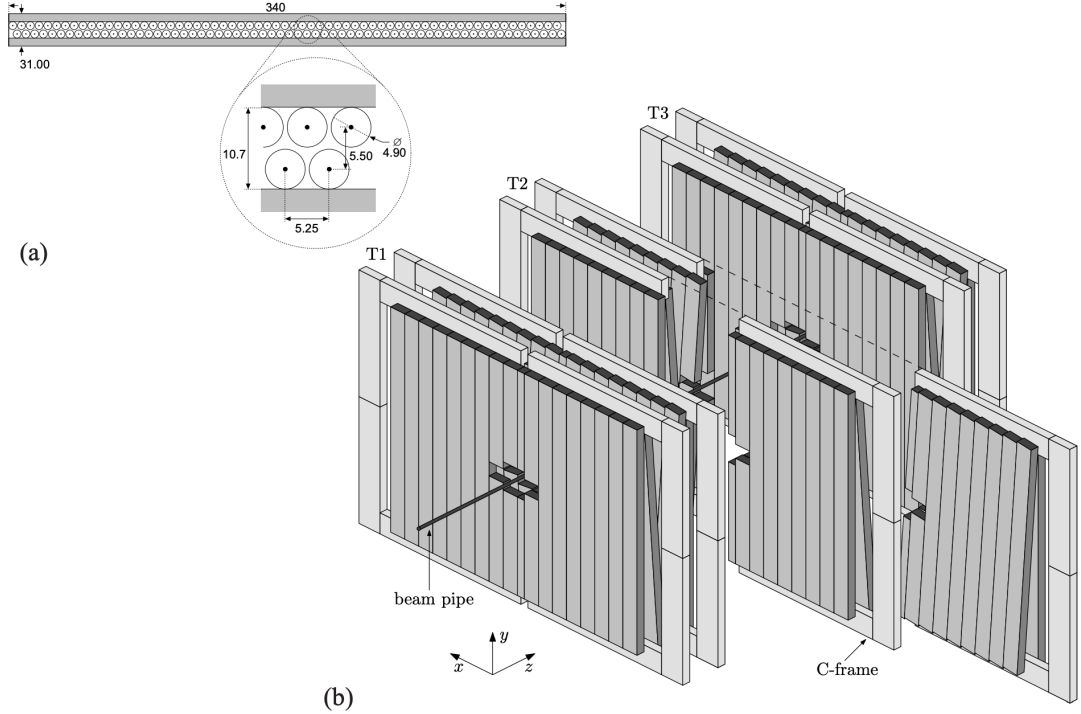


**Figure 3.7:** (a) Cross section of an OT module. (b) Arrangement of the OT modules in tracking stations. Reproduced from Ref. [87].

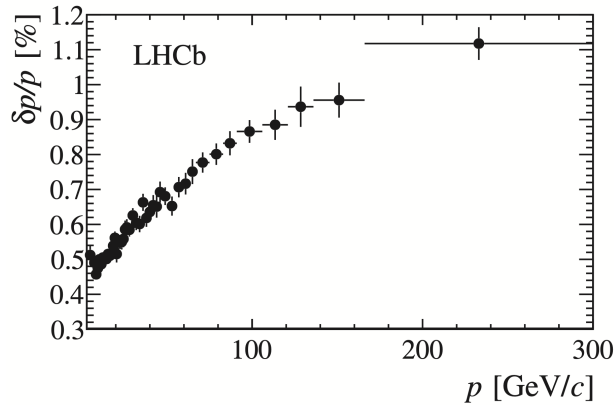


**Figure 3.8:** Relative uncertainty on the momentum of charged tracks (specifically long tracks, cf. the definitions in Section 3.2) in the LHCb detector, determined via the mass resolution obtained in  $J/\psi \rightarrow \mu^+\mu^-$  decays in Run 1 data. Reproduced from Ref. [88]

The overall relative momentum resolution achieved for most charged tracks in LHCb is less than a percent, as illustrated in Fig. 3.8, where it has been determined from a fit to the mass peak in  $J/\psi \rightarrow \mu^+\mu^-$  decays in Run 1 data.

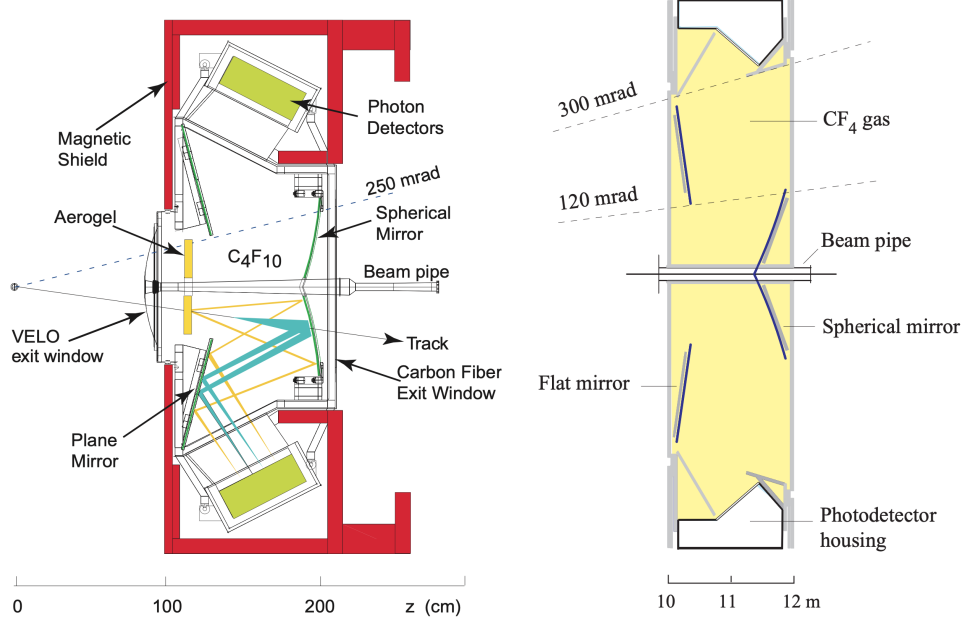


**Figure 3.9:** Overview of (left) the RICH 1 and (right) the RICH 2 detectors. Reproduced from Ref. [83,89].

### 3.1.3 The RICH detectors

Two Ring Imaging CHerenkov detectors (RICH) provide crucial information for particle identification (PID) in LHCb, in particular the ability to separate pions and kaons that is absolutely essential for the measurement presented in the thesis. The RICH 1 detector is located upstream of the magnet, in between the VELO and the TT tracking station. It is designed to provide PID capability for tracks in the momentum range  $p \in [1, 60] \text{ GeV}/c$  using a C<sub>4</sub>F<sub>10</sub> radiator, and covers the full LHCb acceptance. During Run 1 the RICH 1 detector also included an Aerogel radiator designed to provide PID for very low momentum particles; however, it was removed before Run 2 because it did not meet the performance requirements during Run 1 [90,91]. The RICH 2 detector is located downstream of the T1–T3 tracking stations. It is designed to provide PID capabilities for higher momentum tracks in the range  $p \in [15, 100] \text{ GeV}/c$  using a CF<sub>4</sub> radiator. It only covers the very forward region where  $|\theta| < 120 \text{ mrad}$  ( $100 \text{ mrad}$ ) in the horizontal (vertical) directions, as high momentum particles are produced in that region. In both RICH detectors, mirrors are used to reflect the Cherenkov photons to arrays of Hybrid Photon Detectors (HPDs) located outside the LHCb acceptance. The optics are designed such that photons originating from a given track form rings in the HPD arrays, where the radius is determined by the Cherenkov angle  $\theta_c$ . The detectors are illustrated in Fig. 3.9.

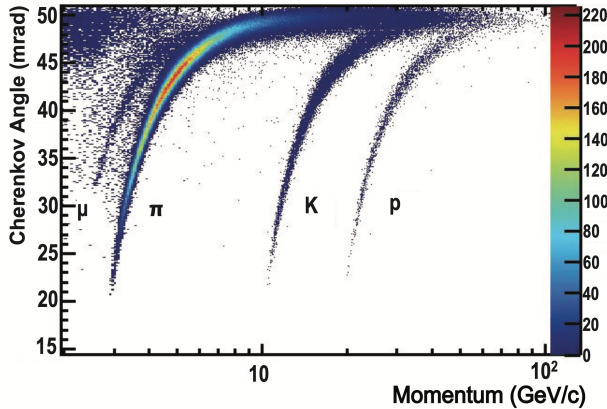


**Figure 3.10:** Cherenkov angle for isolated tracks in the RICH 1 radiator as a function of track momentum. Reproduced from Ref. [90].

The resolution on  $\theta_c$  can be measured by fitting the obtained  $\theta_c$  distribution in high momentum tracks, where the Cherenkov angle is saturated. It is found to be  $1.618 \pm 0.002$  mrad for RICH 1 and  $0.68 \pm 0.02$  mrad for RICH 2 in Run 1 data [90], and was essentially unchanged in Run 2 [91]. Figure 3.10 shows the relation between track momentum and  $\theta_c$  in RICH 1 for *isolated tracks* in Run 1 data; these are tracks where the Cherenkov ring does not overlap with any other Cherenkov rings. The bands for each hadron species are clearly visible, and it can be seen that the RICH detectors also provide some ability to distinguish muons. The definition of the PID variables used in the analysis is discussed in Section 3.2.2, along with the achieved PID performance.

### 3.1.4 Calorimeters

The calorimeter system of the LHCb detector has four components. Ordered from the interaction point, these are the Scintillating Pad Detector (SPD), the Pre-Shower (PS) detector, an Electromagnetic Calorimeter (ECAL), and a Hadron Calorimeter (HCAL). In all four cases, light is produced in organic scintillators and transmitted to Photo Multiplier Tubes (PMTs) via optical fibres [83]. Information from the calorimeters provide identification of electrons, photons, and hadrons, and measurements of their energies and positions, and also plays a crucial role in the triggering, as described below.

The SPD and PS detectors consist of almost identical planes of rectangular scintillator pads, with a 15 mm thick lead absorber located in between. The presence of the SPD before the first absorption layer allows for the separation of photons and electrons in the trigger, because only electrons cause a signal in

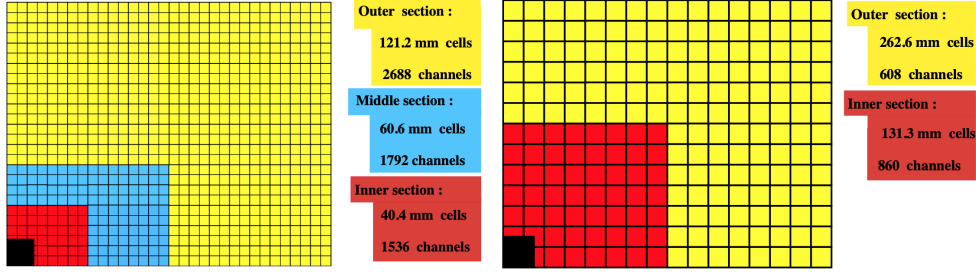


**Figure 3.11:** Illustration of the calorimeter cell size of (left) the ECAL and (right) the HCAL. Reproduced from Ref. [92].

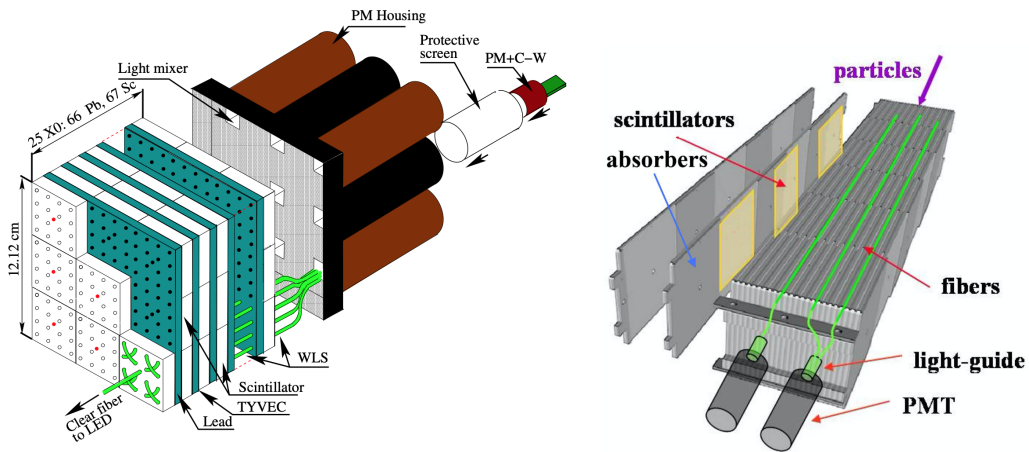


**Figure 3.12:** Illustration of (left) an ECAL and (right) an HCAL module. Reproduced from Refs. [88, 93].

the SPD. The PS allows for the separation of pion and electron tracks, as only the latter interacts significantly with the thin layer of lead. The cell divisions of the detectors closely follow that of the ECAL, shown in Fig. 3.11, to allow for the matching of energy deposits.

The ECAL has a layered "Shashlik" structure, with 66 layers consisting of 2 mm of lead absorber and 4 mm of scintillator; an example of a calorimeter module is shown in Fig. 3.12. Accurate energy measurements require that the full electronic shower is contained in the ECAL, which is achieved since the structure extends for 25 radiation lengths. The scintillators are divided into cells that allow for the determination of the location and shape of energy deposits; the cell dimensions vary as a function of radial distance from the beam pipe as shown in Fig. 3.11, to take into account the varying occupancy. The resolution of the ECAL has been measured to be  $\Delta E/E \simeq (9/\sqrt{E} \oplus 0.8)\%$  ( $E$  in  $\text{GeV}/c^2$ ) [83].

The HCAL is located downstream of the ECAL, designed to measure the energy of hadrons (which leave relatively little energy in the ECAL). It is constructed

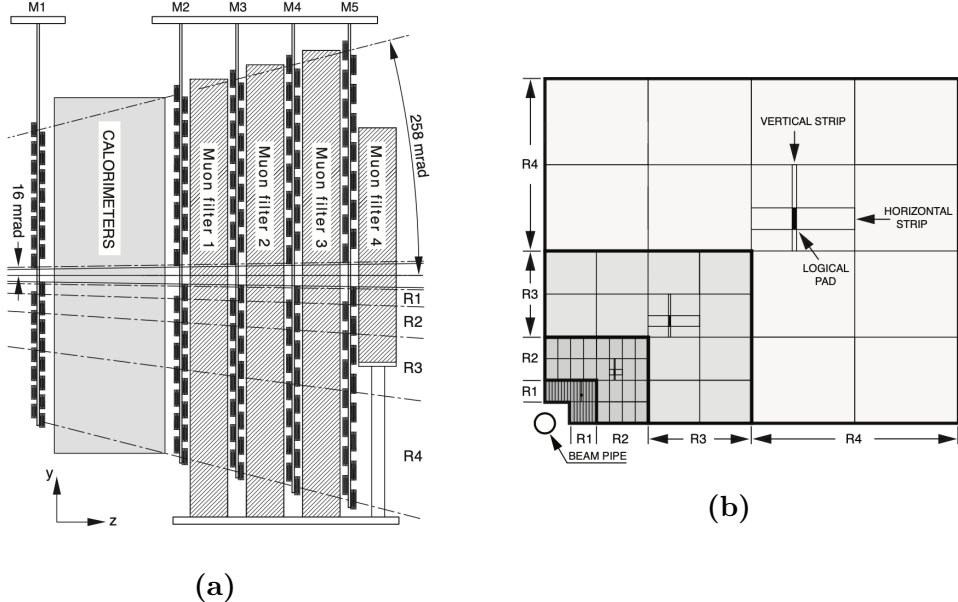


**Figure 3.13:** Illustration of (a) the location of the muon stations along the  $z$ -axis of the experiment and (b) the geometry of the logical pads of the M3 muon station. Reproduced from Ref. [88].

with layers of 1 cm iron absorbers inter-spaced with scintillators, oriented *along* the beam direction, such that a typical track will traverse 16 mm of iron per 4 mm of scintillator [92]. As for the ECAL, the cell size varies as a function of distance to the beam line, as shown in Fig. 3.11. An example of a module is shown in Fig. 3.12. The energy resolution required for efficient triggering is moderate; therefore, the HCAL only has a length of 5.6 interaction lengths and can measure the hadron energies at a resolution of  $\Delta E/E \simeq (69/\sqrt{E} \oplus 9)\%$  ( $E$  in  $\text{GeV}/c^2$ ) [83].

### 3.1.5 Muon detectors

Muon identification and triggering is crucial for a range of high-profile LHCb measurements, such as lepton-universality tests [94, 95] or measurements of  $B_{(s)}^0 \rightarrow \mu^+ \mu^-$  decays [96]. In the thesis, muon identification plays a role in suppressing a number of backgrounds. The LHCb muon system consists of 5 tracking stations, M1–M5, covering the full LHCb acceptance. M1 is located upstream of the ECAL, whereas M2–M5 are located downstream of the HCAL and inter-spaced with 80 cm thick iron absorbers in order to select penetrating muons. This is illustrated in Fig. 3.13a. The detectors are predominantly multiwire proportional chambers (MWPC), organised into logical pads, the dimensions of which define the  $(x, y)$  resolution of the measured spatial points. The exception is the central region of the M1 station, which is a triple gas-electron-multiplier detector, due to the higher

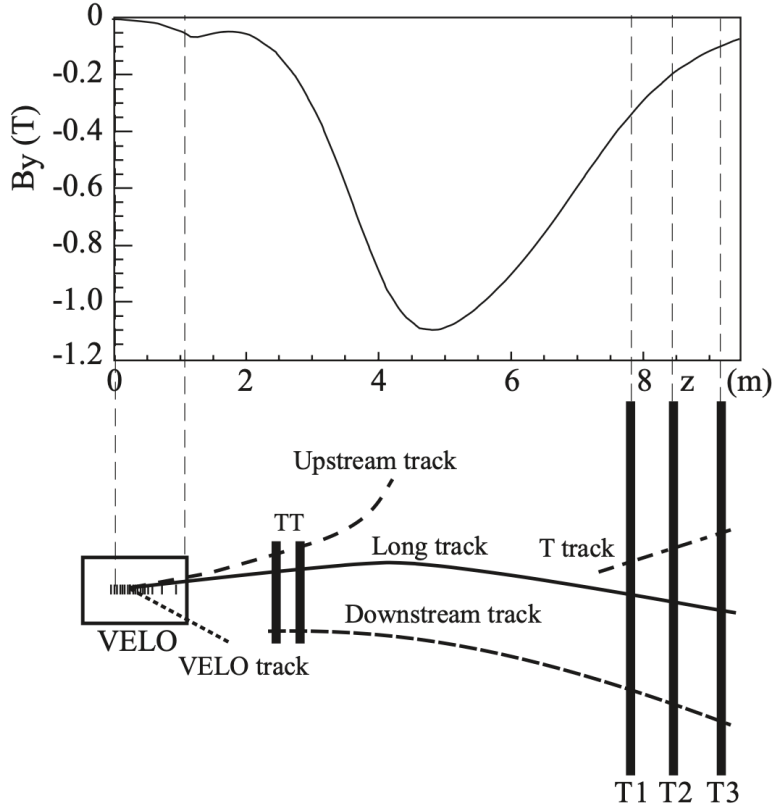


**Figure 3.14:** Definition of track types within the LHCb detector, depending on which set of tracking detectors the track intersects. The profile of the magnetic field is also shown. Reproduced from Ref. [88].

track density in that region [97]. As for the calorimeters, the size of the pads vary as a function of the radial distance from the beam pipe, as illustrated in Fig. 3.13b. The resolution is significantly better in the bending plane ( $x$ ) than in the non-bending plane ( $y$ ). The resolution is also significantly better in the M1–3 stations than in M4 and M5, which are mostly used to identify penetrating tracks. The muon system can independently measure the  $p_T$  of a muon to within 20 %, which allows for efficient triggering.

## 3.2 Reconstruction

This section describes the reconstruction algorithms that fit detector hits in the tracking stations to form track candidates, as well as the algorithms used to identify the types of the particles that formed these tracks.

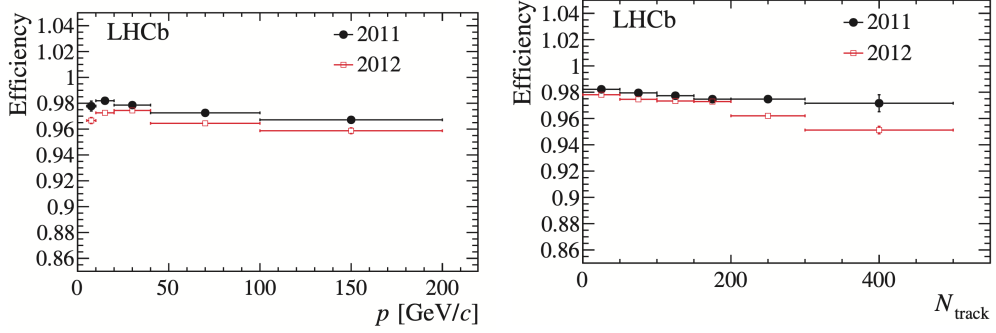


**Figure 3.15:** The long track reconstruction efficiency as a function of (left) track momentum and (right) the number of charged tracks in the event. The lower efficiency in 2012 than 2011 is partially due to the higher event multiplicity, given the higher centre-of-mass energy. The figure is reproduced from Ref. [88].

### 3.2.1 Track reconstruction

The LHCb experiments operates with a number of different particle track types, depending on which subdetectors a track intersects; these are summarised in Fig. 3.14. The two track types that are important for this thesis are *long* tracks, which have hits in the VELO and the TT and T1–T3 tracking stations, and *downstream* tracks that only have hits in the TT and T1–3 tracking stations. The analysis depends on both track types because a number of  $K_S^0$  mesons produced in the signal decay leave the VELO before they decay into the  $\pi^+\pi^-$  final state that is reconstructed; hence these pions necessarily form downstream tracks.

The first step is to form track candidates from hits in the VELO (VELO tracks) and T1–3 stations (T tracks) separately; these tracks are fairly straight since the magnetic field is low in the tracking detectors. Long tracks are formed using two separate search strategies: in one, *forward tracking* [98], VELO tracks are used as seeds and matched with hits in the TT and T1–3 tracking stations by extrapolation. These are combined to form long tracks that are required to pass a set of quality conditions. An alternative approach, *track matching* [99, 100], matches VELO and T tracks by extrapolating both through the bending region, and deciding if they belong together; finally TT hits are added. The union of tracks found via both approaches is saved, where only the track candidate with the best fit quality is kept in the case where a track appears twice. Downstream tracks are formed based on T tracks as seeds, matched with hits in the TT detector in a search region obtained by extrapolation of the seed [101]. Finally, each track is reprocessed using a Kalman filter that takes into account multiple scattering and corrects for energy loss due to ionisation [102, 103].

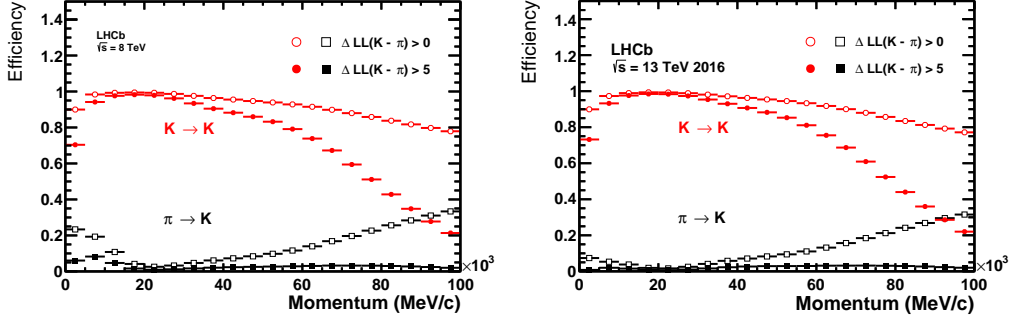


**Figure 3.16:** The probability to correctly identify a kaon/misidentify a pion as a kaon given two different requirements on  $\Delta LL(K - \pi)$ , as a function of track momentum in (left) Run 1 data from 2012 and (right) Run 2 data from 2016. Reproduced from Ref. [105].

Many of the interesting signal decay channels of LHCb have 4–6 charged final state tracks, and therefore it is crucial to have a single-track reconstruction efficiency close to 100 %. The single-track reconstruction efficiency is shown in Fig. 3.15 as a function of track momentum, and as a function of the number of tracks in an *event* (an *event* denotes a  $pp$  collision and all the particles produced therein and in subsequent decays). The efficiencies have been obtained in data, using a tag-and-probe method in  $J/\psi \rightarrow \mu^+ \mu^-$  decays [104]. One muon, the *tag*, is fully reconstructed, while the other, the *probe* is only partially reconstructed, allowing for the  $J/\psi$  invariant mass to be reconstructed with reasonable resolution. If the partially reconstructed probe track is matched to a full long track, the track is classified as efficient. Similar efficiencies have been achieved in Run 2.

### 3.2.2 Particle identification

The information from the RICH detectors, the calorimeters, and the muon system is combined for optimal identification of charged tracks as electrons, muons, pions, kaons, or protons. Photons and neutral pions are identified using the ECAL, but play no role in the thesis and will not be discussed further.

The ability to separate  $B^\pm \rightarrow DK^\pm$  and  $B^\pm \rightarrow D\pi^\pm$  decays is essential to the measurement presented in this thesis. In LHCb, hadron separation is achieved via information from the RICH detectors, using a likelihood method where the observed pattern of hit pixels in the photo detectors is compared to the expected pattern, given all reconstructed tracks in an event under a given set of particle hypotheses. The likelihood is maximised by varying the particle hypotheses for each track being an electron, muon, pion, kaon, or proton [106]. It is necessary to consider all tracks of an event simultaneously because the Cherenkov rings of different tracks overlap.

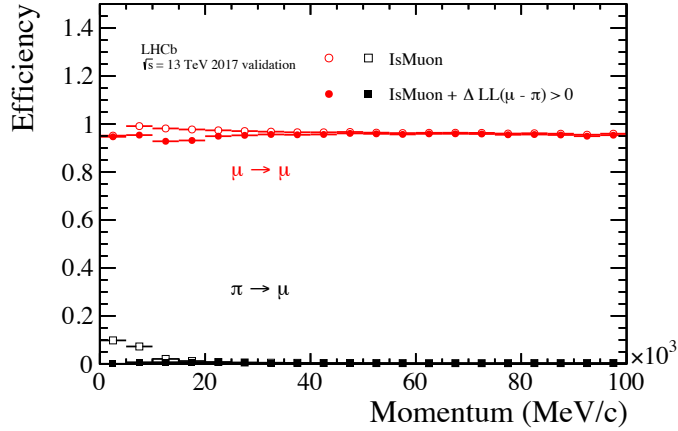


**Figure 3.17:** The probability to correctly identify a muon/misidentify a pion as a muon given requirements on either `isMuon` or  $\Delta LL(\mu - \pi)$ , as a function of track momentum in Run 2 data from 2017. Reproduced from Ref. [105].

For each track, the maximum log likelihood of a particle hypothesis, say that the track is a kaon, relative to the hypothesis that it is a pion

$$\Delta LL_{\text{track}_i}^{\text{RICH}}(K - \pi) = \ln \mathcal{L}_{\max}^{\text{RICH}}(\text{pattern}|\text{track}_i = K) - \ln \mathcal{L}_{\max}^{\text{RICH}}(\text{pattern}|\text{track}_i = \pi), \quad (3.1)$$

is saved to inform PID decisions. In the case of pion-kaon separation, this variable alone is enough to achieve good separation power; in the remainder of the thesis it is denoted `PIDK`. The PID performance for pion-kaon separation has been measured in calibration data, following a procedure described in Section 5.2.1, and is illustrated in Fig. 3.16.

Muons are identified by extrapolating tracks to the muon stations to define fields-of-interest (FOI). A track is considered as a muon candidate when a minimum number of stations (2–4 depending on the track momentum) have hits in the corresponding FOI [107, 108]. This information is encoded in a variable denoted `isMuon` throughout the thesis. Additional information, such as a comparison of the slopes of the track in the main tracker and the muon stations, and the average track-hit distance in the FOI is used to form a  $\Delta LL^{\text{muon}}(\mu - \pi)$  variable analogous to the one defined in Eq. (3.1) for the RICH detectors; again defining as the relative likelihood with respect to the pion hypothesis. This variable can be combined with  $\Delta LL^{\text{RICH}}(\mu - \pi)$  to form a  $\Delta LL(\mu - \pi)$  variable that takes information from both detectors into account, denoted `PIDmu`. The performance of the muon PID variables is shown in Fig. 3.17 as obtained in data. It can be seen that requiring `isMuon=0` rejects muon tracks efficiently at all momenta; this is used in the analysis to veto a number of semi-leptonic backgrounds.

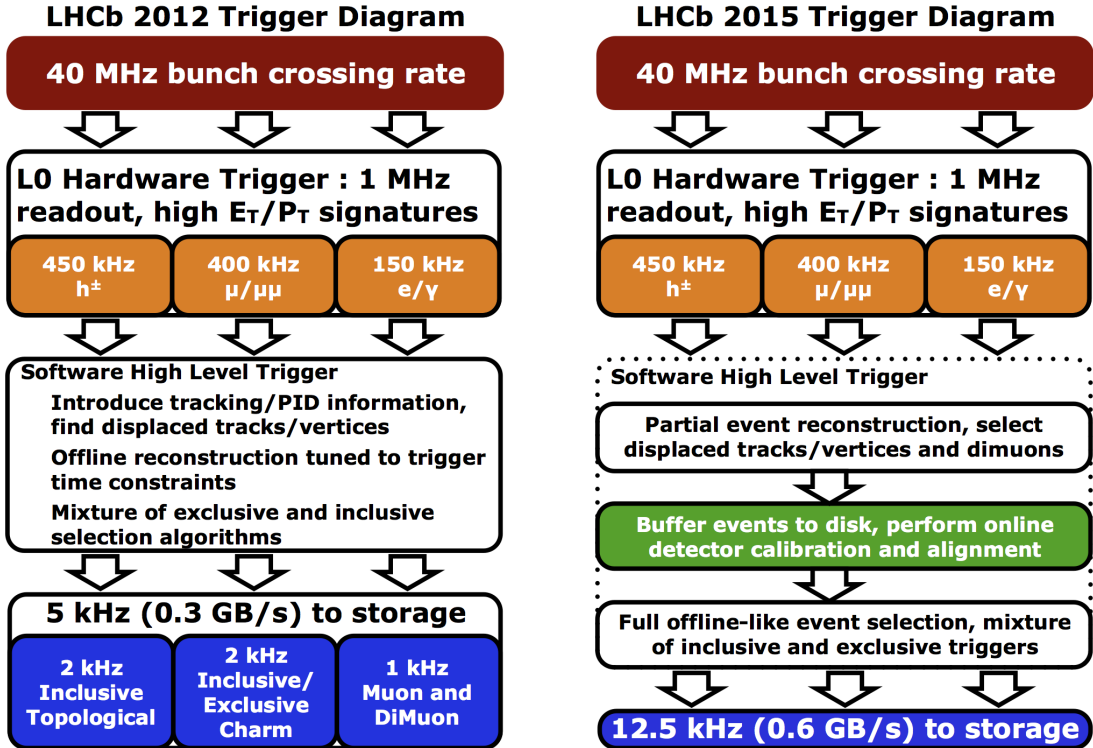


**Figure 3.18:** Illustration of stages and event processing rates in the LHCb trigger during (left) Run 1 and (right) Run 2. Reproduced from Refs. [110, 111].

In similar manner, a potential semi-leptonic background with electrons is also vetoed in the analysis presented in the thesis. In LHCb, electron PID is mainly based on the balance between deposited energy and track momentum in the ECAL [109]. This information is combined with information on photon energy deposits from brehmstrahlung, and energy deposits in the PS and HCAL, as well as information from the RICH and muon detectors, to form yet another  $\Delta LL(e - \pi)$  variable as the likelihood difference between the electron and pion hypotheses, denoted PID $e$ . As an example of the obtainable performance, an average electron selection efficiency of  $(91.9 \pm 1.3)\%$  was achieved in displaced  $J/\psi \rightarrow e^+e^-$  decays in Run 1, with a hadron misidentification rate of  $(5.54 \pm 0.02)\%$  [88].

### 3.3 The LHCb trigger system

The collision rate in the LHC is up to 40 MHz, with a visible inelastic collision rate in LHCb of up to 30 MHz. The LHCb uses a multi-stage trigger to reduce the rate with which events are stored to a manageable level (of eg. 12.5 kHz during Run 2). The first stage consists of a hardware trigger that selects events with high transverse energy in the calorimeters or hits in the muon detectors. This is followed by two

software stages that rely on a reconstruction of tracks in the detector to select events that are likely to include interesting physics. The overall trigger stages were identical in Run 1 and Run 2, however the throughput rate was upgraded significantly between the two data taking periods, as was the quality of the reconstruction in the software trigger stages; in Run 2, the final software trigger decisions are in fact based on an event reconstruction that is fully equivalent to the one performed offline [111]. The stages are illustrated in Fig. 3.18, and described in detail in the following.

A further, offline processing and reconstruction step is applied to all events before they are made available to most LHCb analyses, commonly denoted as the *stripping* step. Although the stripping does not form part of the LHCb trigger, it does constitute an additional, centralised filter on the data, and a description is included in Section 3.3.3.

### 3.3.1 The level-0 hardware trigger

The level-0 (L0) triggers that select physics events are based on the calorimeters and the muon system. The ECAL and HCAL are divided into clusters of  $2 \times 2$  cells, for which the transverse energy is defined as

$$E_T = \sum_{j=1}^4 E_j \sin \theta_j, \quad (3.2)$$

where  $\theta_j$  is the angle of cell  $j$  with respect to the beam axis and the average collision point. The trigger forms a L0Hadron candidate with the highest  $E_T$  found in the HCAL, combined with the ECAL cluster in front of it if such a cluster is present. Photon and electron candidates are formed based on clusters in the ECAL, identified by the presence (lack) of hits in the SPD for an electron (photon). The transverse energies of the candidates are compared to a fixed set of thresholds, and events where at least one candidate is above threshold are retained.

The muon trigger searches for straight line tracks in the muon stations, estimating the associated muon  $p_T$  based on the track direction. An event is retained if either the largest muon  $p_T$  is above a given threshold, or the product of the two highest muon  $p_T$  values is above a different threshold.

High-multiplicity events take a long time to process in the subsequent software stage; therefore it is favourable for the overall retention rate of interesting physics decays to put a maximum limit on the event multiplicity at the L0 stage. This is achieved by requiring the number of hits in the SPD detector to be below a threshold value in most L0 decisions.

### 3.3.2 High-level triggers

The events that pass the L0 trigger are passed to a farm of multiprocessor computing nodes, the Event Filter Farm (EFF), tasked with bringing the rate down from approximately 1 MHz to the  $\mathcal{O}(1 - 10)$  kHz rate that can be saved to disk. The EFF consisted of 900 (1700) nodes during Run 1 (Run 2). The software-based filtering proceeds in two stages: a first filter (HLT1) brings the rate down to approximately 40 (110) kHz based on a limited reconstruction of the event, after which a second stage (HLT2) filters the events further based on a more complete reconstruction. Each step executes a number of different algorithms, each of which can allow an event to be accepted; these are denoted *trigger lines*.

During both runs, the HLT1 performed a partial event reconstruction by building long tracks that satisfy a  $p_T$  requirement using the forward tracking approach described in Section 3.2.1, and determining the location of PVs using VELO tracks. In both runs, the HLT1 included an inclusive trigger that selected a high  $p_T$  track with significant displacement of all PVs (typical of a  $b$  or  $c$  decay). This line is denoted `HLT1TrackAllL0` in Run 1 [110]; for Run 2 the track requirements were reoptimised and the corresponding line is denoted `Hlt1TrackMVA`. Further, an additional inclusive trigger was added that forms a two-prong vertex out of high  $p_T$  tracks inconsistent with originating in a PV, and applies a multivariate classifier to determine if it is signal-like based on a number of track and vertex properties. This line is denoted `Hlt1TwoTrackMVA` [111]. These lines triggered all events included in the analysis of the thesis; other lines exist for selecting events that include muons, calibration data, low-multiplicity events, and a number of exclusive lines, for a total of approximately 20 lines during Run 2 [111].

The rate of events is reduced significantly by HLT1, and therefore the HLT2 decisions can be based on a more complete reconstruction of the event. Indeed, during Run 2 it was based on a complete, fully aligned reconstruction equivalent to the offline reconstruction. During Run 1 the HLT2 reconstruction only included long tracks and did exclude some low momentum tracks; this was a main motivation for the upgrade of the EFF during the shutdown period. The need for full alignment in HLT2 means that it could not be run fully online in Run 2; instead the output events from HLT1 were saved to disk in the EFF, and processed with some delay [111]. The analysis presented in the thesis is based on a number of inclusive "topological" trigger lines, based on combinations of 2, 3, or 4 tracks that satisfy fit quality requirements, have high  $p_T$ , are separated from the PVs, and have a distance-of-closest-approach below 0.2 mm. A multivariate classifier [112] is applied to each formed  $n$ -body object, to determine if the event should be accepted based on

the track momenta, invariant mass, a corrected invariant mass that takes into account missing transverse momentum, distance of closest approach, and the impact parameter and separation with the associated PV. The resulting trigger lines were denoted `Hlt2Topo{2, 3, 4}BodyBBDT` during Run 1 and `Hlt2Topo{2, 3, 4}Body` during Run 2. A large number of other HLT2 lines exist (more than 500 in Run 2), including a significant number of exclusive lines that aim to select specific decays and only save information on the signal decay, not the whole event. This was made possible by the full reconstruction within HLT2 [111], and have allowed for larger signal yields to be collected within the data storage limits.

### 3.3.3 Offline data filtering: the LHCb stripping

Events that are written to disk are processed with the full detector alignment and calibration. In a further, offline processing step denoted the *stripping*, hundreds of different, dedicated reconstructions are performed; decay candidates for various signal decays are built and a number of requirements are made to reject backgrounds from random track combinations. For example, the  $B^\pm \rightarrow D(\rightarrow K_S^0 h^+ h^-) h^\pm$  candidates that are analysed in this thesis are built during the stripping stage, as described further in Section 5.1. The stripping is a centralised computing task, executed on the Worldwide LHC Computing Grid [113], and allows the analysts to process much smaller data sets during their individual analysis. Because the stripping is based on data saved to offline storage it can be repeated; however, the processing of data collected during a year of data taking takes many weeks, so this does not happen often.

## 3.4 Simulation

A centralised LHCb simulation is able to simulate  $pp$  collisions with the proper conditions within LHCb, model subsequent secondary decays and the full detector response, and process the output in the full LHCb reconstruction. In this thesis, simulated decays are used to determine the reconstructed invariant-mass distribution of a number of decay modes, as well as a number of relative selection efficiencies. The  $pp$  collisions are generated using PYTHIA [114] with a configuration specific to LHCb [115]. The time-dependent evolution and decays of unstable particles are described by the EVTGEN [116] package, designed specifically for  $B$  physics. Final-state radiation is generated using PHOTOS [117]. The interaction of the generated particles with the detector, and its response, are implemented using the GEANT4 toolkit [118] as described in Ref. [119].

**Table 3.1:** Overview of the running condition and collected data samples by the LHCb experiment during Run 1 and 2 of the LHC [122]. A brief overview of data taking periods planned for the future is also shown.

| LHC phase | Year | $\sqrt{s}$ / TeV | $\int \mathcal{L} dt / fb^{-1}$ |
|-----------|------|------------------|---------------------------------|
| Run 1     | 2011 | 7                | 1.0                             |
|           | 2012 | 8                | 2.0                             |
| Run 2     | 2015 | 13               | 0.3                             |
|           | 2016 |                  | 1.6                             |
|           | 2017 |                  | 1.7                             |
|           | 2018 |                  | 2.1                             |

The most significant computational cost of the simulation is due to the detector simulation. A single  $pp$  collision produces  $\mathcal{O}(100)$  tracks in the detector, out of which only a handful belong to the signal decay under study. Therefore, significant computational resources can be saved by reusing the detector simulation of non-signal tracks a number of times, while redescaying the signal particle, say a  $B^+$ , each time. This approach is called ReDecay [120], and has been relatively widely adopted within LHCb. ReDecay has been used to produce simulation samples corresponding to the conditions in 2017 and 2018 for this thesis. In some cases, the use of ReDecay necessitates special statistical treatment due the correlated detector occupancies between signal candidates, but for the analysis in this thesis the impact is negligible.

A number of sub-dominant backgrounds are investigated using the fast-simulation package `RapidSim` [121]. This package can decay heavy  $b$  and  $c$  hadrons with kinematic distributions similar to those in LHCb  $pp$  collisions, or with user defined input distributions. The decays are typically evenly distributed over phase space, but can also be handled with `EVTGEN` [116] to take a given resonant structure into account. Furthermore, a smearing of the obtained momenta can be applied that is based on the LHCb resolution.

### 3.5 Data-taking conditions

The LHCb experiment has collected a data set corresponding to  $8.7 fb^{-1}$  during Run 1 and 2 of the LHC. The running conditions for each year are summarised in Table 3.1. The measurement that is the main topic of the thesis is based on the full data set.

The  $B^\pm$  production cross section increased significantly with the higher centre-of-mass energy during Run 2. In the LHCb acceptance, the cross section has been

measured to be approximately  $43\,\mu\text{b}$  at  $\sqrt{s} = 7\,\text{TeV}$ , increasing to about  $87\,\mu\text{b}$  at  $\sqrt{s} = 13\,\text{TeV}$  [123]. In combination with an increased selection efficiency due to improvements to the trigger, this resulted in signal yields per  $\text{fb}^{-1}$  that were about 2.5 times higher in Run 2 than in Run 1 in the measurement described in Chapter 5. Before delving into the details of that analysis, Chapter 4 is dedicated to a phenomenological study of how the measurement is impacted by neutral kaon  $CP$  violation and interaction with the LHCb detector.

# 4

## Neutral kaon $CP$ violation and material interaction in BPGGSZ measurements

The presence of a  $K_S^0$  meson in the  $D \rightarrow K_S^0 h^+ h^-$  final states introduces a small bias in BPGGSZ measurements due to  $CP$ -violation in the neutral kaon sector and asymmetries caused by the interaction between the neutral kaon and detector material. These fundamental physics effects are reviewed in Section 4.1, after which the chapter presents a detailed analysis of the impact on the LHCb measurement that is the subject of the thesis, as well as future  $\gamma$  measurements with the Belle II experiment. Prior to this analysis, the only existing work on the effect on  $\gamma$  measurements suggested a small effect in  $B^\pm \rightarrow D K^\pm$  measurements but potentially *very* significant effects in measurements based on  $B^\pm \rightarrow D \pi^\pm$  decays [38]. However, as described in Section 4.1.1, the analysis in Ref. [38] does not take into account the fundamental aspect of the BPGGSZ method: that it relies on the phase-space distribution of signal decays, not phase-space-integrated asymmetries. Furthermore, the earlier study only considers the  $CP$ -violation effect, not material interaction. Therefore, a more detailed study was necessary before the  $B^\pm \rightarrow D \pi^\pm$  decay mode could reliably be promoted to a signal channel. The full analysis shows the impact on the  $\gamma$  measurement in Chapter 5 to be small, and allows for the assignment of an appropriate systematic uncertainty.

## 4.1 CP violation and material interaction of neutral kaons

A brief review of the general phenomenology of mixing and  $CP$  violation in the neutral kaon system is useful, before analysing the impact on  $\gamma$  measurements. The presentation in this section follows the PDG review of *CP violation in the quark section* [28]. The general theory considers any pair of neutral meson states  $|M^0\rangle$  and  $|\bar{M}^0\rangle$  related by  $CP$  conjugation

$$CP|M^0\rangle = e^{i\phi_M}|\bar{M}^0\rangle \quad CP|\bar{M}^0\rangle = e^{-i\phi_M}|M^0\rangle, \quad (4.1a)$$

where  $\phi_M$  is an arbitrary phase. In this thesis, the convention  $\phi_M = 0$  is chosen, so that

$$CP|M^0\rangle = |\bar{M}^0\rangle \quad CP|\bar{M}^0\rangle = |M^0\rangle. \quad (4.1b)$$

A meson state that starts as a general superposition of  $|M^0\rangle$  and  $|\bar{M}^0\rangle$  states

$$\begin{aligned} \psi_M^0 &\equiv \psi_M(0) = a(0)|M^0\rangle + b(0)|\bar{M}^0\rangle \\ &\equiv \psi_{M^0}^0 + \psi_{\bar{M}^0}^0 \end{aligned} \quad (4.2)$$

will, over time, evolve into a state that consists of a different superposition of  $|M^0\rangle$  and  $|\bar{M}^0\rangle$ , as well as components for all possible states the meson system can decay into

$$\begin{aligned} \psi_M(t) &= a(t)|M^0\rangle + b(t)|\bar{M}^0\rangle + \sum c_i(t)f_i \\ &\equiv \psi_{M^0}(t) + \psi_{\bar{M}^0}(t) + \sum c_i(t)f_i. \end{aligned} \quad (4.3)$$

For time scales that are longer than the typical strong-interaction, the time evolution of the  $M^0-\bar{M}^0$  superposition can be described by a  $2 \times 2$  Hamiltonian

$$\frac{d}{dt} \begin{pmatrix} \psi_{M^0}(t) \\ \psi_{\bar{M}^0}(t) \end{pmatrix} = -i\mathcal{H}_0 \begin{pmatrix} \psi_{M^0}(t) \\ \psi_{\bar{M}^0}(t) \end{pmatrix} \quad (4.4)$$

that is *non-Hermitian* (to allow for decay) but can be parameterised in terms of two Hermitian matrices  $\mathcal{M}$  and  $\Gamma_0$

$$\mathcal{H}_0 = \mathcal{M} - \frac{i}{2}\Gamma_0. \quad (4.5)$$

The quantum states with well-defined (real) masses,  $m_j$ , and (real) decay widths,  $\Gamma_j$ , are the two eigenstates of  $\mathcal{H}_0$  with eigenvalues  $\lambda_j = m_j - \frac{i}{2}\Gamma_j$ . The eigenstates (of course) evolve independently in time, so that

$$\psi_j(t) = e^{-i\lambda_j t}\psi_j^0 = e^{-im_j t - \frac{\Gamma_j}{2}t}\psi_j^0. \quad (4.6)$$

The eigenstates are denoted  $H$  and  $L$  according to the size of  $m_j$ , the real part of the eigenvalues, such that  $m_H > m_L$ . Assuming that  $\mathcal{H}_0$  conserves  $CPT$  the eigenstates have the general form

$$\begin{aligned} |M_H\rangle &\equiv p|M^0\rangle - q|\bar{M}^0\rangle \\ |M_L\rangle &\equiv p|M^0\rangle + q|\bar{M}^0\rangle \end{aligned} \quad (4.7)$$

where  $p$  and  $q$  are complex numbers that satisfy  $|q|^2 + |p|^2 = 1$ . With the convention in Eq. (4.1b) it follows that if  $\mathcal{H}_0$  also conserves  $CP$ , so that  $|M_H\rangle$  and  $|M_L\rangle$  are  $CP$  eigenstates, then  $p = \pm q$ , where the sign depends on which of the heavy and the light meson states is  $CP$  even, and which is  $CP$  odd.

The eigenstates of the Hamiltonian governing the neutral kaon system are almost, but not exactly, equal to the  $CP$  eigenstates

$$|K_1\rangle = \frac{|K^0\rangle + |\bar{K}^0\rangle}{\sqrt{2}} \quad |K_2\rangle = \frac{|K^0\rangle - |\bar{K}^0\rangle}{\sqrt{2}}, \quad (4.8)$$

which are  $CP$  even and odd, respectively. This approximate equality leads to the most prominent feature of the neutral kaon system: the two eigenstates of  $\mathcal{H}_0$  have lifetimes that differ by orders of magnitude. This is best understood by assuming, for a moment, that the states in Eq. (4.8) *do* equal the eigenstates with definite life times. The  $K_1$  state can decay in the  $CP$  even  $\pi^+\pi^-$  and  $\pi^0\pi^0$  modes, and does so almost 100% of the time; these decay modes are not available to the  $K_2$  (in the absence of direct  $CP$  violation) which results in a much lower decay rate and a much longer life time. Therefore, the eigenstates in the kaon system are labelled the *short-lived* kaon,  $K_S^0$ , which is almost  $CP$  even, and the *long-lived* kaon,  $K_L^0$ , which is almost  $CP$  odd. The life times are [28]

$$\tau_{K_S^0} = (8.954 \pm 0.004) \times 10^{-11} \text{s} \quad \tau_{K_L^0} = (5.116 \pm 0.021) \times 10^{-8} \text{s}. \quad (4.9)$$

Experimentally, it is found that the  $K_S^0$  corresponds to the light eigenstate, but that the mass splitting [28]

$$\begin{aligned} \Delta m = m_{K_L^0} - m_{K_S^0} &= (0.5289 \pm 0.0009) \times 10^{10} \hbar s^{-1} \\ &\simeq 3.5 \times 10^{-6} \text{ eV} \end{aligned} \quad (4.10)$$

is tiny compared to the neutral kaon masses of  $m_{K_S^0} = 497.6 \text{ MeV}/c^2$  [28].

However, the discovery of  $K_L^0 \rightarrow \pi\pi$  decays by Kronin and Fitch in 1964 established that the  $K_S^0$  and  $K_L^0$  are *not* exactly equal to the  $CP$  eigenstates in Eq. (4.8), because the  $\mathcal{H}_0$  relevant to the kaon system is  $CP$ -violating. The  $CP$

violation in the kaon sector is conventionally parameterised in terms of the complex parameters  $\epsilon$  and  $\epsilon'$ , in terms of which

$$\frac{A(K_L^0 \rightarrow \pi^+ \pi^-)}{A(K_S^0 \rightarrow \pi^+ \pi^-)} = \epsilon + \epsilon' \quad \frac{A(K_L^0 \rightarrow \pi^0 \pi^0)}{A(K_S^0 \rightarrow \pi^0 \pi^0)} = \epsilon - 2\epsilon'. \quad (4.11)$$

In these expressions  $\epsilon$  denotes the contribution from  $CP$  violation in mixing and  $\epsilon'$  the contribution due to direct  $CP$  violation in the decays. The  $\epsilon$  parameter has been measured to be [28]

$$|\epsilon| = (2.228 \pm 0.011) \times 10^{-3}, \quad \arg \epsilon = (43.52 \pm 0.05)^\circ, \quad (4.12)$$

while the  $\epsilon'$  parameter satisfies [28]

$$\text{Re}(\epsilon'/\epsilon) \simeq \epsilon'/\epsilon \simeq (1.66 \pm 0.23) \times 10^{-3} \quad (4.13)$$

Direct  $CP$  violation is ignored for the remainder of the thesis, because  $\epsilon'$  is measured to be three orders of magnitude smaller than  $\epsilon$ . In terms of the  $CP$  eigenstates of Eq. (4.8), the mass eigenstates  $K_S^0$  and  $K_L^0$  are given by

$$\begin{aligned} |K_S^0\rangle &= \frac{|K_1\rangle + \epsilon|K_2\rangle}{\sqrt{1 + |\epsilon|^2}} &= \frac{(1 + \epsilon)|K^0\rangle + (1 - \epsilon)|\bar{K}^0\rangle}{\sqrt{2(1 + |\epsilon|^2)}} \\ |K_L^0\rangle &= \frac{|K_2\rangle + \epsilon|K_1\rangle}{\sqrt{1 + |\epsilon|^2}} &= \frac{(1 + \epsilon)|K^0\rangle - (1 - \epsilon)|\bar{K}^0\rangle}{\sqrt{2(1 + |\epsilon|^2)}}, \end{aligned} \quad (4.14)$$

corresponding to the definition  $p = (1 + \epsilon)/\sqrt{2(1 + |\epsilon|^2)}$  and  $q = (1 - \epsilon)/\sqrt{2(1 + |\epsilon|^2)}$  in Eq. (4.7).

In an experimental setting, the time evolution of a neutral kaon state is affected by nuclear interactions with the detector. The interaction is governed by the strong force, and therefore sensitive to the *flavour* of the kaon state; the interaction strength is thus different for  $K^0$  and  $\bar{K}^0$  mesons. This difference introduces a non-zero  $K_S^0 \leftrightarrow K_L^0$  transition amplitude for neutral kaons traversing a detector segment. This effect was predicted early in the history of kaon physics [124] and is commonly denoted *kaon regeneration*. The effect can be described by including a material-interaction term in the Hamiltonian that is diagonal in the  $(|K^0\rangle, |\bar{K}^0\rangle)$  basis, so that the equation governing the time evolution is [125, 126]

$$\frac{d}{dt} \begin{pmatrix} \psi_{K^0}(t) \\ \psi_{\bar{K}^0}(t) \end{pmatrix} = -i \left[ \mathcal{H}_0 + \begin{pmatrix} \chi & 0 \\ 0 & \bar{\chi} \end{pmatrix} \right] \begin{pmatrix} \psi_{K^0}(t) \\ \psi_{\bar{K}^0}(t) \end{pmatrix}. \quad (4.15)$$

The complex parameters  $\chi$  and  $\bar{\chi}$  describe the material interaction of the  $K^0$  and  $\bar{K}^0$  flavour eigenstates and are related to their scattering cross section, as

described further in Section 4.3.4. The solution of Eq. (4.15) for the time evolution in the  $K_S^0$  and  $K_L^0$  states is [126]

$$\begin{aligned}\psi_S(t) &= e^{-i\Sigma t} \left( \psi_S^0 \cos \Omega t + \frac{i}{2\Omega} (\Delta\lambda\psi_S^0 - \Delta\chi\psi_L^0) \sin \Omega t \right), \\ \psi_L(t) &= e^{-i\Sigma t} \left( \psi_L^0 \cos \Omega t - \frac{i}{2\Omega} (\Delta\lambda\psi_L^0 + \Delta\chi\psi_S^0) \sin \Omega t \right),\end{aligned}\quad (4.16)$$

in terms of the parameters

$$\begin{aligned}\Delta\chi &= \chi - \bar{\chi}, \\ \Delta\lambda &= \lambda_L - \lambda_S = (m_L - m_S) - \frac{i}{2}(\Gamma_L - \Gamma_S), \\ \Sigma &= \frac{1}{2}(\lambda_S + \lambda_L + \chi + \bar{\chi}), \\ \Omega &= \frac{1}{2}\sqrt{\Delta\lambda^2 + \Delta\chi^2}.\end{aligned}\quad (4.17)$$

In the vacuum limit where  $\chi = \bar{\chi} = 0$ , the expressions in Eq. (4.6) and Eq. (4.16) are equal.

#### 4.1.1 A first look at the impact on $\gamma$ measurements

The effects described above have an impact on measurements of  $CP$  asymmetries in modes with a neutral kaon in the final state. This was analysed for the first time in relation to  $\gamma$  measurements by Grossman and Savastio in 2014 [38]. The authors point out two sources of corrections to be included:

- the fact that  $K_S^0$  is not an exact  $CP$  eigenstate can break potential symmetry relations employed in an analysis, and
- that when the neutral kaon is reconstructed in a  $\pi\pi$  final state there will be contributions from both  $K_S^0$  and  $K_L^0$  decays.

The analysis in this chapter considers yet another effect, not treated by Grossman and Savastio, namely that

- material interaction can emulate the effect of neutral kaon  $CP$  violation, because it couples the almost- $CP$ -even  $K_S^0$  and the almost- $CP$ -odd  $K_L^0$  states.

Due to the presence of  $K_L^0 \rightarrow \pi\pi$  decays, Grossman and Savastio point out that the relevant decay rates to consider in an experimental setting are of the form

$$d\Gamma(t) \propto |\psi_S(t) + \epsilon\psi_L(t)|^2. \quad (4.18)$$

The time dependence of the decay rates considered in Chapter 2 was left out because all terms shared a common time dependence. That is not the case in Eq. (4.18), due to the very different decay rates of the  $K_S^0$  and  $K_L^0$  components of the kaon state. As a consequence, the time-integrated yields have the form

$$N \propto \int dt \eta(t) |\psi_S(t) + \epsilon\psi_L(t)|^2, \quad (4.19)$$

where  $\eta(t)$  is the time acceptance in a given experimental setting. Thus, the acceptance is crucial to model in order to correctly estimate the impact of kaon  $CP$ -violation effects on a given measurement.

Considering BPGBSZ measurements, the main effect of neutral kaon  $CP$  violation is a breakdown of the fundamental Dalitz-plot symmetry that is exploited in the derivation of the bin yield equations. Extending the amplitude definition of Eq. (2.23) to include  $K_L^0$  decays

$$A_{S(L)}^{(\overline{D})}(s_-, s_+) = A((\overline{D}^0 \rightarrow K_{S(L)}^0 \pi^+ \pi^-)), \quad (4.20)$$

the authors point out that  $CP$ -violation in the  $K_S^0$  system means that the relation  $A_S^{(\overline{D})}(s_{-+}) = A_S^D(s_{+-})$  is not exactly true; and in addition, there is now a dependence on  $A_L^D(s_{-+})$  which satisfies a different approximate symmetry, namely  $A_L^{(\overline{D})}(s_{-+}) \simeq -A_L^D(s_{+-})$ . Grossman and Savastio describe these symmetry breaking effects in detail, but do not explicitly derive the corrections to the yield equations of Chapter 2, nor try to quantify the potential bias on  $\gamma$  in a measurement based on the binned yields. Instead, they derive expressions for the bias in a measurement obtained from phase-space integrated  $CP$  asymmetries. This is done for both GLW measurements that use  $D \rightarrow K_S^0 X$  final states and for the  $D \rightarrow K_S^0 h^+ h^-$  final states; however, for their quantitative estimate of  $\Delta\gamma$  the authors make an approximation that corresponds to assuming that the  $D \rightarrow K_S^0 h^+ h^-$  final state is a  $CP$  eigenstate, making the two results identical. The authors find that in this case, assuming a uniform experimental acceptance for all kaon decay times, the asymmetry has the form<sup>1</sup>

$$A = \frac{2r_B \sin \gamma \sin \delta_B + 2\text{Re}[\epsilon]}{1 + r_B^2 - 2r_B \cos \gamma \cos \delta_B}, \quad (4.21)$$

If a measured value of  $A$  is interpreted to obtain  $\gamma$  without taking the  $\epsilon$  term into account, it leads to a bias of

$$\Delta\gamma = -\frac{\text{Re}[\epsilon]}{r_B \cos \gamma \sin \delta_B} + \mathcal{O}(|\epsilon|). \quad (4.22)$$

---

<sup>1</sup>In fact the expression in Eq. (4.21) is missing a term, as will be clear when an analogous expression is derived in detail in Section 4.2.3.

The scaling  $\Delta\gamma \sim \mathcal{O}(r_B/|\epsilon|)$  is the main result of the analysis by Grossman and Savastio. For  $B^\pm \rightarrow DK^\pm$  decays, where  $r_B^{DK^\pm} \simeq 0.1$  this suggests a bias at the percent level, which is negligible compared to current experimental uncertainties. However, in the  $B^\pm \rightarrow D\pi^\pm$  case, where  $r_B^{D\pi^\pm} \simeq 0.005$  [45], their result suggests relative biases that are potentially of  $\mathcal{O}(1)$ .

The conclusions are lacking on two accounts, however. Firstly, as made clear in Section 2.3.5, the  $K_S^0\pi^+\pi^-$  and  $K_S^0K^+K^-$  states are *far from*  $CP$  eigenstates. From the asymmetry expression in that section, it is clear that the bias in a determination of  $\gamma$  based on phase-space asymmetries will in fact scale as

$$\Delta\gamma \sim \mathcal{O}\left(\frac{|\epsilon|}{(2\mathcal{F}_+ - 1)r_B}\right), \quad (4.23)$$

which suggests that Grossman and Savastio severely *underestimated* the potential impact. This is described in detail in Section 4.2.3. More importantly, the analysis of the phase-space integrated asymmetry is in fact *irrelevant* to BPGGSZ measurements as they are currently performed: as described in Section 2.3.5, the information from the global asymmetry is completely discarded. Therefore, it is necessary to analyse the effects of kaon  $CP$ -violation on a full, binned analysis of  $D \rightarrow K_S^0 h^+ h^-$  decays, which is done in detail in the following sections. While the aim is to extend the analysis of Grossman and Savastio, the treatment in the following sections is completely independent of that in Ref. [38]; instead taking inspiration from the discussion of  $D^0 \rightarrow K_S^0\pi^+\pi^-$  and  $D^0 \rightarrow K_L^0\pi^+\pi^-$  decay amplitudes in Ref. [70].

## 4.2 Impact on BPGGSZ measurements of $\gamma$ : principles

The analysis of the impact on BPGGSZ measurements is carried out in two stages. This section treats the leading order effects analytically, and derives the overall order of magnitude of the expected bias in a general setting. Then Section 4.3 presents a detailed numerical study of the expected effect in measurements with the LHCb and Belle II experiments specifically, because these will be crucial to constrain  $\gamma$  during the coming decade [37, 127].

### 4.2.1 Modified symmetry relations

In order to derive the corrections to the asymmetry relation  $A_S^D(s_{-+}) \simeq A_S^{\bar{D}}(s_{+-})$ , it is beneficial to express  $A_{S(L)}^D$  in terms of the amplitudes

$$A_{1/2}^{\bar{D}} = A(\bar{D}^0 \rightarrow K_{1/2}^0\pi^+\pi^-), \quad (4.24)$$

because these amplitudes satisfy the exact symmetries  $A_1^D(s_{+-}) = A_1^{\bar{D}}(s_{+-})$  and  $A_2^D(s_{+-}) = -A_2^{\bar{D}}(s_{+-})$  by definition. This approach is different to that of Grossman and Savastio, but the final results are equivalent. After the decay of a  $D^0$  meson to a neutral kaon, the kaon state is

$$\begin{aligned}\psi^0 &= A_1^D|K_1\rangle + A_2^D|K_2\rangle \\ &= N \left[ (A_1^D - \epsilon A_2^D)|K_S^0\rangle + (A_2^D - \epsilon A_1^D)|K_L^0\rangle \right],\end{aligned}\quad (4.25)$$

with the normalisation constant  $N = \sqrt{1 + |\epsilon|^2}/(1 - \epsilon^2)$ . Thus it can be seen that

$$\begin{aligned}A_S^D(s_{+-}) &= N \left[ (A_1^D(s_{+-}) - \epsilon A_2^D(s_{+-})) \right], \\ A_L^D(s_{+-}) &= N \left[ (A_2^D(s_{+-}) - \epsilon A_1^D(s_{+-})) \right],\end{aligned}\quad (4.26)$$

with an analogous expression for the  $\bar{D}^0$  decay amplitudes. Therefore, the generalised relations between the  $D^0$  and  $\bar{D}^0$  amplitudes are

$$\begin{aligned}A_S^{\bar{D}}(s_{+-}) &= N[A_1^{\bar{D}}(s_{+-}) - \epsilon A_2^{\bar{D}}(s_{+-})] \\ &= N[A_1^D(s_{+-}) + \epsilon A_2^D(s_{+-})] = A_S^D(s_{+-}) + 2N\epsilon A_2^D(s_{+-}), \\ A_L^{\bar{D}}(s_{+-}) &= N[A_2^{\bar{D}}(s_{+-}) - \epsilon A_1^{\bar{D}}(s_{+-})] \\ &= -N[A_2^D(s_{+-}) + \epsilon A_1^D(s_{+-})] = -A_L^D(s_{+-}) - 2N\epsilon A_1^D(s_{+-}).\end{aligned}\quad (4.27)$$

#### 4.2.2 Relationship between the $K_S^0$ and $K_L^0$ amplitudes

The decay amplitude  $A(D^0 \rightarrow K_S^0 \pi^+ \pi^-)$  has been carefully studied, and a number of amplitude models have been published [50, 57–59, 61]. No models have been published for  $D^0 \rightarrow K_L^0 \pi^+ \pi^-$  decays. However, following an approach laid out by the CLEO collaboration [70], the two amplitudes can be related. Again, this is most easily done by relating the  $A_1^D(s_{+-})$  and  $A_2^D(s_{+-})$  amplitudes. In the isobar formalism, the decay amplitude  $A_1^D(s_{+-}) = A(D^0 \rightarrow K_1 \pi^+ \pi^-)$  is expressed as a non-resonant constant amplitude plus a sum of resonances

$$A(D^0 \rightarrow K_1 \pi^+ \pi^-) = k_{\text{NR}} + \sum_{\text{CF}} k_i R^i(s_{K\pi^-}) + \sum_{\text{DCS}} k_j R^j(s_{K\pi^+}) + \sum_{R_{\pi\pi}} k_k R^k(s_{\pi^+\pi^-}).\quad (4.28)$$

The resonances are split into Cabibbo-favoured (CF)  $K^{*-}$  resonances, doubly Cabibbo-suppressed (DCS)  $K^{*+}$  resonances and  $\pi\pi$  resonances.<sup>2</sup> The CF resonances

---

<sup>2</sup>In modern models, the  $\pi\pi$  and  $K\pi$   $S$ -wave components are modelled via the  $K$ -matrix formalism and LASS parametrisations, respectively, instead of sums of individual resonances [50]. This does not alter the arguments below, as the  $R$  functions of Eq. (4.28) can equally well represent such terms.

couple to the  $\bar{K}^0$  component of  $K_1 (\propto K^0 + \bar{K}^0)$ , and therefore the corresponding  $k_i$  in the  $K_2 (\propto K^0 - \bar{K}^0)$  amplitude will have a relative minus sign. The DCS resonances couple to the  $K^0$  component of  $K_1$ , and so the corresponding  $k_j$  in the  $K_2$  amplitude will have a relative plus sign. For the  $h^+h^-$  resonances, there will be a coupling to both the  $K^0$  and  $\bar{K}^0$  components, however the coupling to the  $K^0$  component is expected to be suppressed with a Cabibbo suppression factor  $r_k e^{i\delta_k}$ , where  $r_k \simeq \tan^2 \theta_C \simeq 0.05$  is determined by the Cabibbo angle  $\theta_C$  and  $\delta_k$  can take any value. Therefore, the  $k_k$  for these resonances have a relative  $-(1 - 2r_k e^{i\delta_k})$  factor in the  $K_2$  amplitude. The same effect leads to the differences in decay rates between  $D^0 \rightarrow K_S^0 \pi^0$  and  $D^0 \rightarrow K_L^0 \pi^0$  decays [128, 129]. Thus, given a model of the form in Eq. (4.28), a model for the  $A_2^D(s_{+-}) = A(D^0 \rightarrow K_2 \pi^+ \pi^-)$  amplitude will have the form

$$A(D^0 \rightarrow K_2 \pi^+ \pi^-) = k_{\text{NR}} + \sum_{\text{CF}} (-k_i) R^i(s_{K\pi^-}) + \sum_{\text{DCS}} (+k_j) R^j(s_{K\pi^+}) + \sum_{R_{\pi\pi}} (-(1 - 2r_k e^{i\delta_k}) k_k) R^k(s_{\pi^+\pi^-}). \quad (4.29)$$

An important consequence of these substitution rules is that

$$A_2^D(s_{+-}) = -A_1^D(s_{+-}) + r_A \Delta A(s_{+-}), \quad (4.30)$$

where  $r_A \simeq \tan^2 \theta_C$  and  $\Delta A(s_{+-}) \sim A_1^D(s_{+-})$  are of the same order of magnitude (at least when averaged over the bins used in  $\gamma$  measurements). This relation is sufficient to make the qualitative arguments of this section, while the full set of substitution rules above are used in the quantitative studies of Section 4.3.

### 4.2.3 Modification of the BPFGSZ yield equations

With suitable models to calculate  $A_{S(L)}^{\bar{D}}$  (or  $A_{1/2}^{\bar{D}}$ ) and knowledge of  $\Delta\chi$  for the materials relevant to an experimental setting, the relations derived in the preceding sections can be employed to calculate the expected phase-space bin yields,  $N_i^\pm$ , including the effects of kaon  $CP$  violation and material interaction. The decay rates have additional terms compared to those in Eq. (2.26), because the  $K_L^0$  contribution must be taken into account

$$d\Gamma(t, s_{+-}) \propto |\psi_S(t, s_{+-}) + \epsilon \psi_L(t, s_{+-})|^2, \quad (4.31)$$

where the time-dependence of  $\psi_{S/L}(t, s_{+-})$  is governed by Eq. (4.16), and the phase-space dependence is included in the state component, by defining  $\psi_{S/L}^0$  in terms of

$A_{S(L)}^{\bar{D}}(s_{-+})$ . For example, for the case of a  $B^- \rightarrow DK^-$  decay, the definition is

$$\begin{aligned}\psi_S^{0,B^-}(s_{-+}) &= A_S^D(s_{-+}) + r_B e^{i(\delta_B - \gamma)} A_S^{\bar{D}}(s_{-+}) \\ &= A_1^D(s_{-+}) - \epsilon A_2^D(s_{-+}) + r_B e^{i(\delta_B - \gamma)} (A_1^{\bar{D}}(s_{-+}) - \epsilon A_2^{\bar{D}}(s_{-+})) \\ &= A_1^D(s_{-+}) - \epsilon A_2^D(s_{-+}) + r_B e^{i(\delta_B - \gamma)} (A_1^D(s_{+-}) + \epsilon A_2^D(s_{+-})).\end{aligned}\quad (4.32)$$

It is useful to look at the corrections to the BPGGSZ yield expressions in Eq. (2.28) to lowest order in  $\epsilon$  and  $r_\chi = \frac{1}{2} \frac{\Delta\chi}{\Delta\lambda}$ , the dimensionless parameter governing material interactions. For LHCb and Belle II the average  $|r_\chi| \simeq 10^{-3}$ , as detailed in the Section 4.3. To first order in  $r_\chi$ , the time-dependent kaon states within a material, given in Eq. (4.16), simplify to [126]

$$\begin{aligned}\psi_S(t, s_{+-}) &= e^{-\frac{i}{2}(x+\bar{x})t} e^{-i\lambda_S t} (\psi_S^0(s_{+-}) - r_\chi (1 - e^{-i\Delta\lambda t}) \psi_L^0(s_{+-})), \\ \psi_L(t, s_{+-}) &= e^{-\frac{i}{2}(x+\bar{x})t} e^{-i\lambda_L t} (\psi_L^0(s_{+-}) + r_\chi (1 - e^{+i\Delta\lambda t}) \psi_S^0(s_{+-})).\end{aligned}\quad (4.33)$$

By inserting these expressions into Eq. (4.31) and employing the definition in Eq. (4.32) (and a similar definition for  $B^+$  decays), the binned yields can be calculated by an integration over time and phase space. In the remainder of this section, it is assumed that the experimental time acceptance is  $\eta(t) = 1$  for all times and that  $r_\chi$  is constant at all times; more realistic assumptions are introduced in Section 4.3. In this case, the binned yields are given by the expression

$$\begin{aligned}N_i^- &= h_B^{-'} \left( \hat{K}_{+i} + r_B^2 \hat{K}_{-i} + 2\sqrt{\hat{K}_{+i} \hat{K}_{-i}} (x_- \hat{c}_i + y_- \hat{s}_i) + \mathcal{O}(r\epsilon) \right), \\ N_i^+ &= h_B^{+'} \left( \hat{K}_{-i} + r_B^2 \hat{K}_{+i} + 2\sqrt{\hat{K}_{+i} \hat{K}_{-i}} (x_+ \hat{c}_i - y_+ \hat{s}_i) + \mathcal{O}(r\epsilon) \right),\end{aligned}\quad (4.34)$$

where a number of new parameters have been defined, and where  $\mathcal{O}(r\epsilon)$  denotes terms of  $\mathcal{O}(r_A \epsilon)$ ,  $\mathcal{O}(r_B \epsilon)$ ,  $\mathcal{O}(r_A r_\chi)$ , and  $\mathcal{O}(r_B r_\chi)$ . Since  $r_B \sim r_A \sim 10^{-1}$  (in  $B^\pm \rightarrow DK^\pm$  decays) and  $r_\chi \sim \epsilon \sim 10^{-3}$ , these terms are all of the same order of magnitude.

The new normalisation constants  $h_B^{\pm'} = h_B^\pm (1 + |\epsilon + r_\chi|^2 \frac{\Gamma_S}{\Gamma_L} \mp \Delta h)$  are defined in terms of

$$\Delta h = 2\text{Re}[\epsilon + r_\chi] - 4 \frac{\Gamma_S}{\Gamma_L + \Gamma_S} \frac{\text{Re}[\epsilon + r_\chi] + \mu \text{Im}[\epsilon + r_\chi]}{1 + \mu^2}, \quad \mu = 2 \frac{m_L - m_S}{\Gamma_L + \Gamma_S}. \quad (4.35)$$

The  $\hat{K}_i$  parameters are defined to be

$$\hat{K}_i = \frac{1}{1 + |\epsilon + r_\chi|^2 \frac{\Gamma_S}{\Gamma_L}} \left( K_i^{(1)} + |\epsilon + r_\chi|^2 \frac{\Gamma_S}{\Gamma_L} K_i^{(2)} \right), \quad (4.36)$$

in which the  $K_i^{(1/2)}$  parameters are phase-space integrals, defined as in Eq. (2.30) but for  $A_{1/2}^D$ . To lowest order, the  $\hat{K}_i$  correspond to the fractional  $D^0$  decay yield

in each bin, as obtained in a measurement that averages  $D^0$  and  $\bar{D}^0$  decays, and assumes the  $A_S^{\bar{D}}(s_{-+}) = A_S^D(s_{+-})$  symmetry to be exact:

$$K_i^{\text{meas}} \equiv \frac{N_i^D + N_{-i}^{\bar{D}}}{\sum_j N_j^D + N_{-j}^{\bar{D}}} = \hat{K}_i + \mathcal{O}(r\epsilon). \quad (4.37)$$

Here,  $N_i^D$  ( $N_i^{\bar{D}}$ ) is the expected yield of flavour tagged  $D^0$  ( $\bar{D}^0$ ) mesons into bin  $i$  of the  $D$  decay phase-space.

In similar fashion, the parameters  $(\hat{c}_i, \hat{s}_i)$  have been introduced to denote the *measured* average strong-phases, which are expected to differ from  $(c_i, s_i)$  at  $\mathcal{O}(\epsilon)$ , since neutral kaon  $CP$  violation is not taken into account in the measurements by CLEO and BESIII. Thus, any corrections arising if  $(\hat{c}_i, \hat{s}_i)$  and  $(c_i, s_i)$  are substituted in Eq. (4.34) will appear in the  $\mathcal{O}(r\epsilon)$  terms.

Two observations can be made from the expression in (4.34). The first is that the phase-space *distribution* is only changed at  $\mathcal{O}(r\epsilon)$  compared to the expression in Eq. (2.28), if the measured  $\hat{K}_i$  are used in the experimental analysis.<sup>3</sup> As the  $D^0 - \bar{D}^0$  interference term that provides sensitivity to  $\gamma$  enters at order  $\mathcal{O}(r_B)$ , the impact on  $\gamma$  measurements can be expected to be  $\Delta\gamma/\gamma \sim \mathcal{O}(r\epsilon/r_B)$ . For  $B \rightarrow DK$  analyses, where  $r_B \simeq 0.1$ , this is at the permille level, so the induced  $\Delta\gamma$  bias can be expected to be smaller than  $1^\circ$ . Even in the case of  $B^\pm \rightarrow D\pi^\pm$  decays, this suggests biases that are maximally a few percent. This is the main result of the chapter, because it means that the effect of neutral kaon  $CP$  violation and material interaction is small compared to the precision of the measurement that is the main subject of the thesis.

The second observation relates to potential future measurements of  $\gamma$ , which may also include sensitivity from the total, phase-space-integrated yield asymmetry

$$A_{\text{total}} = \frac{N^- - N^+}{N^- + N^+} = \frac{2(2\mathcal{F}_+ - 1)r_B \sin \delta_B \sin \gamma + \Delta h}{1 + r_B^2 + 2(2\mathcal{F}_+ - 1)r_B \cos \delta_B \cos \gamma} + \mathcal{O}(r\epsilon), \quad (4.38)$$

where the definition of  $\mathcal{F}_+$  from Section 2.3.5 has been employed. In the limit  $r_B \rightarrow 0$  the expression agrees with the result for the analogous asymmetry in  $D^\pm \rightarrow \pi^\pm K_S^0$  decays in Ref. [130], evaluated to  $\mathcal{O}(\epsilon)$  for an infinite and uniform time-acceptance. As hinted at above, the fact that  $\mathcal{F}_+ \simeq 0.5$  means that the asymmetry due to  $\gamma$  being non-zero is not  $\mathcal{O}(r_B)$ , but of approximately the same order of magnitude as the asymmetry due to  $CP$  violation in the neutral kaon sector, governed by  $\Delta h$ . This is illustrated in Fig. 4.1, where the expression in Eq. (4.38) is plotted in the

---

<sup>3</sup>This is equally true whether the  $K_i$  are fitted in the signal channel along with  $x_\pm$  and  $y_\pm$ , as is the case in the measurement presented in the thesis, or if they are obtained in a control channel with flavour tagged  $D$  decays, according to Eq. (4.37).

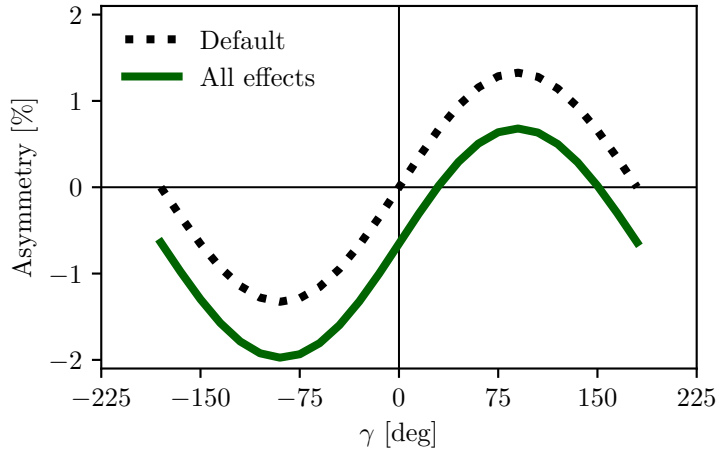


**Figure 4.1:** The asymmetry  $A_{\text{total}}$  as a function of  $\gamma$  calculated to  $O(\epsilon)$  using Eq. (4.38). The calculation is made for (black dotted line) the default case where  $\Delta h = 0$  and (green) including neutral kaon  $CP$ -violation and material interaction with  $r_\chi = \epsilon$ .

default case where  $\Delta h = 0$ , as well as including neutral kaon  $CP$  violation and material interaction effects.<sup>4</sup> The asymmetry changes significantly when including the latter effects. Therefore, measurements based only on the global asymmetry will suffer relative biases of tens of degrees, not a few degrees, if neutral kaon  $CP$  violation and material interaction is not taken into account.

### 4.3 Impact on BPGGSZ measurements of $\gamma$ : LHCb and Belle II measurements

The previous section has established that the bias due to neutral kaon  $CP$  violation and material interaction is at the sub-percent level for measurements based on  $B^\pm \rightarrow DK^\pm$  decays, and just a few percent in  $B^\pm \rightarrow D\pi^\pm$  decays. Thus, the effects only contribute a manageable systematic uncertainty in the measurement that is the subject of the thesis. However, the expected precision on  $\gamma$  measurements will increase significantly in the coming decade, as both the LHCb [37] and Belle II [127] collaborations expect to make BPGGSZ measurements that measure  $\gamma$  with a precision of 1–3°. Therefore a deeper understanding of the expected bias for these specific experiments is important.

This section details a study, where the equations of the previous section are evaluated numerically to all orders in  $\epsilon$ ,  $r_B$ , and  $r_\chi$ , and care is taken to realistically model the experiment-specific conditions. The scope of the original analysis,

---

<sup>4</sup>The calculation uses the amplitude model in Ref. [50] to calculate  $K_i$  and  $c_i$ , and assumes  $r_\chi = \epsilon$ , with  $\epsilon$  taking the value in Eq. (4.12).

published in Ref. [2], was a stand-alone paper that covers both LHCb and Belle II, and which therefore does not rely on full detector simulation. Instead the following approaches are taken to model the necessary input

- the experimental time-acceptance is modelled based on the detector geometry and typical neutral kaon momentum spectrum
- the material interaction is included, using the material budget information available in the technical design reports on each experiment
- both the time-acceptance and material interaction depends on the neutral kaon momentum, for which realistic distributions are estimated using the `RapidSim` simulation package [121].

Each input is described in detail in the following sections. The study has been repeated to assign a systematic uncertainty to the LHCb measurement in Chapter 5, with slight adjustments to match the exact fit setup and with the inputs above extracted from full LHCb simulation. This is described further in Section 4.3.7.

### 4.3.1 Detector geometries

The LHCb geometry and sub detectors are described in details in Chapter 3. In the LHCb measurement discussed in Chapter 5, the  $K_S^0$  mesons are reconstructed in the  $\pi^+\pi^-$  final state and two distinct categories of decay are considered, depending on where in the detector the  $K_S^0$  decay occurs. The categories have very different decay-time acceptance, and therefore two scenarios are considered for LHCb: one in which the decay products of the  $K_S^0$  leave reconstructed tracks in both the silicon vertex detector and downstream tracking detectors (denoted *long-long* or LL), and one in which the decay products of the  $K_S^0$  only leave tracks in the downstream tracking detectors (denoted *down-down* or DD).

The Belle II detector is a general purpose spectrometer, built to collect data from asymmetric  $e^+e^-$  collisions provided by the SuperKEKB accelerator in Japan [131]. A schematic of the detector is shown in Fig. 4.2. The relevant sub detectors for the present study are the tracking detectors: a central silicon vertex detector, comprised of a total of six layers within 140 mm of the beam, and a large volume drift chamber with 56 wire layers, extending to a radius of 1130 mm [127]. A single scenario is considered for Belle II, because essentially all the  $K_S^0$  mesons produced in signal decays in Belle II decay within the tracking volume, with more than 90 % decaying in the vertex detector according to the studies described below. Thus, three scenarios are considered in total: LL LHCb, DD LHCb, and Belle II.

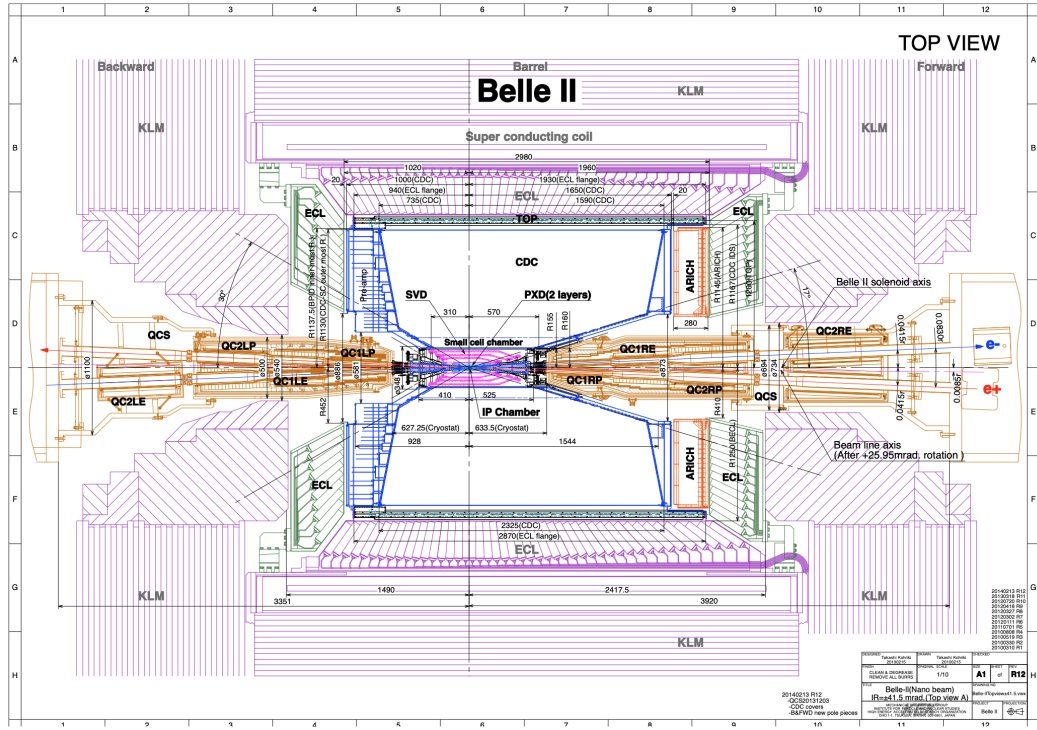


**Figure 4.2:** Schematic of the Belle II detector, reproduced from Ref. [127].

### 4.3.2 Kaon momentum distributions

The neutral kaon momentum distributions are obtained using **RapidSim** [121], a simple tool to generate MC samples. **RapidSim** has an inbuilt capability to generate decays of  $B$  mesons with the kinematic distribution found in LHCb collisions and falling in the LHCb acceptance. However, the distributions need to be reweighted to take the kaon-decay-time acceptance into account. After being reweighted, the **RapidSim** momentum spectra are reasonably close to those found in samples of  $B^\pm \rightarrow D(\rightarrow K_S^0\pi^+\pi^-)K^\pm$  decays from full LHCb simulation, as seen in Fig. 4.3

At Belle II, the signal  $B$  mesons stem from decays of  $\Upsilon(4S)$  mesons produced in asymmetric electron-positron collisions. This leads to substantially different decay kinematics in comparison to those found at LHCb. The momentum distribution in Belle II is estimated by letting **RapidSim** decay  $B$  mesons with a momentum of 1.50 GeV/ $c$  along the  $z$ -axis, corresponding to the  $\gamma\beta = 0.28$  boost of the centre-of-mass system in Belle II when operated at the  $\Upsilon(4S)$  resonance [127]. A perfect  $4\pi$  angular acceptance is assumed. It is not necessary to reweigh the Belle II momentum spectrum to account for the kaon-decay-time acceptance because all produced  $K_S^0$  mesons decay in the tracking volume.

The resulting momentum distributions for the three types of sample are shown in Fig. 4.4.

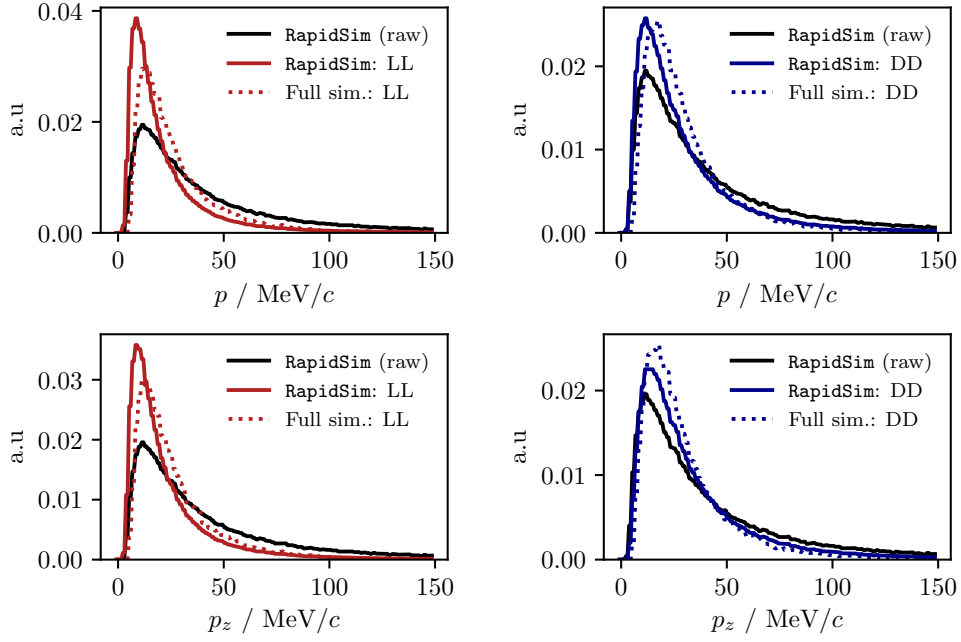


**Figure 4.3:** Momentum spectra for the  $K_S^0$  meson in LHCb, as generated using **RapidSim** (black lines) directly, as well as reweighed to match decay time acceptance in the (red) LL and (blue) DD data categories of LHCb. The LHCb spectra are compared with the spectra in fully simulated signal decays, for both the (dotted red lines) LL and (dotted blue lines) DD data categories.

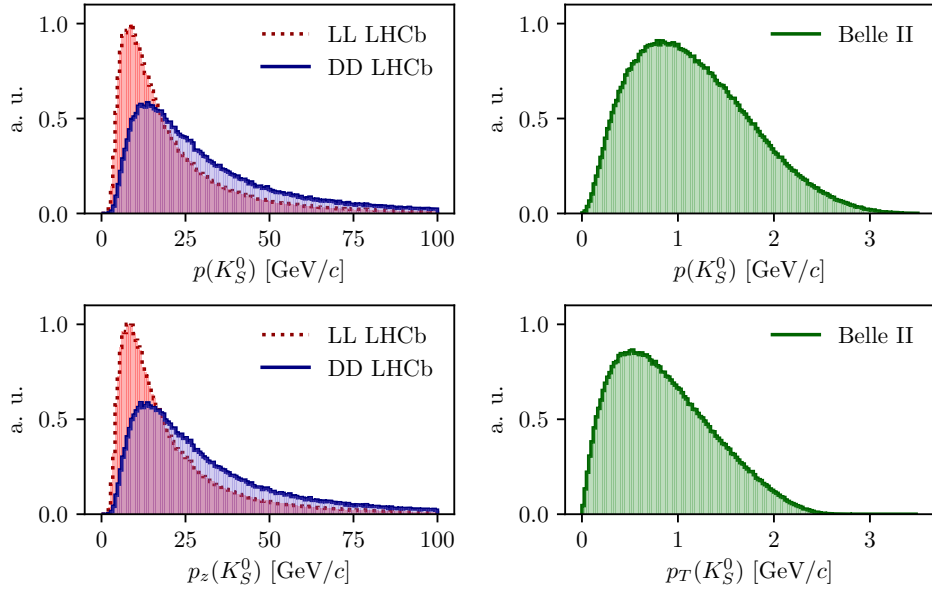


**Figure 4.4:** Momentum distributions for the LHCb (red dotted line) LL and (blue) DD categories, as well as (green) Belle II, obtained using **RapidSim**.

### 4.3.3 Experimental time acceptance

In order to model the experimental time acceptance, the time-dependent decay rates are only integrated over a finite time interval  $(\tau_1, \tau_2)$ . The intervals are defined for each of the three experimental categories, by requiring that a neutral kaon, if produced at  $x = y = z = 0$  with momentum  $p = (p_T, p_z)$ , decays within the relevant part of the corresponding detector. For the LL LHCb category, it is required that the kaon decays before reaching  $z_{max} = 280$  mm, corresponding to a decay where the decay products traverse at least 3 VELO segments (ignoring a number of widely spaced VELO segments placed at a distance of up to  $z = 750$  mm from the interaction point) [132]. For the DD LHCb category a decay at  $z \in [280, 2350]$  mm is required, corresponding to decay between the LL cut-off and the first downstream tracking station [133]. The time acceptance has a significant impact for the LHCb categories, where some 20 % of the kaons escape the tracking stations completely before decaying.

For Belle II, it is assumed that the  $K_S^0$  reconstruction is similar to the Belle  $K_S^0$  reconstruction, which is based on a neural network and reconstructs  $K_S^0$  decays for which the decay product leave tracks in both the drift chamber and silicon vertex detectors, as well as decays that leave tracks in the drift chamber only [134, 135]. Therefore, the  $K_S^0$  decay is required to be within  $r_{max} = 1130$  mm of the beam axis, corresponding to a decay within the outer radius of the drift-chamber. In practice, most of the kaons already decay inside the silicon vertex detector, and requiring a decay before the outer radius of the drift chamber is essentially equivalent to having no time cut-off.

### 4.3.4 Detector material budget

The effect of the material interaction is governed by parameter  $\Delta\chi$  of Eq. (4.17). The parameter varies along a given kaon path, as the kaon intersects detector components made of different materials. In these studies, the calculations are simplified by using a single average material parameter for each experimental scenario. The average material parameters can be estimated for a given experimental scenario by considering the type and length of material traversed by a kaon in the relevant sub-detector(s). The average value is estimated, by exploiting that  $\Delta\chi$  is related to the forward scattering amplitude  $f$  ( $\bar{f}$ ) of  $K^0$  ( $\bar{K}^0$ ) mesons in a given material [125, 126]

$$\Delta\chi = -\frac{2\pi\mathcal{N}}{m_K}(f - \bar{f}) = -\frac{2\pi(N_A\rho/A)}{m_K}(f - \bar{f}), \quad (4.39)$$

where  $\mathcal{N} = N_A \rho / A$  is the scattering centre density of the material,  $m_K$  is the mass of the kaon state,  $A$  and  $\rho$  are the nucleon number and density of the material, and  $N_A$  is Avogadro's number. Measurements made for a range of nuclei [136] show that in the momentum range  $p_K \in [20, 140] \text{ GeV}/c$

$$\left| \frac{f - \bar{f}}{p_K} \right| = 2.23 \frac{A^{0.758}}{p_K^{0.614} (\text{GeV}/c)} \text{ mb}, \quad \arg[f - \bar{f}] = -\frac{\pi}{2} (2 - 0.614), \quad (4.40)$$

where the phase of  $\Delta f$  is determined via a phase-power relation [137]. In the numerical studies presented here, Eq. (4.40) is also used for the low momentum neutral kaons in the Belle II calculations, as a more detailed modelling of the low momentum  $\Delta\chi$  based on Ref. [138] is found to yield very similar results. The scattering centre density  $\mathcal{N}$  is approximated as being constant, equal to the average density along a neutral kaon path due to its intersection with different detector segments. This average is estimated using the simplifying assumption that the total detector material budget is due to silicon. In practice,  $\mathcal{N} = N_A \rho / A$  is calculated using  $A = 28$  and  $\rho = f^{\text{Si}} \rho^{\text{Si}}$ , where  $f^{\text{Si}} < 1$  is the average fraction of a neutral kaon path length that is inside detector material, estimated via the known dimensions of the detector, the average nuclear interaction length seen by a track traversing it cf. the technical design reports [89, 132], and the nuclear interaction length of silicon  $\lambda_I^{\text{Si}} = 465.2 \text{ mm}$  [28]. The average value of  $r_\chi = \frac{1}{2} \frac{\Delta\chi}{\Delta\lambda}$ , which governs the size of the matter regeneration effect, can be calculated for the three considered experimental scenarios and satisfy  $|r_\chi^{\text{LL}}| = 2.7 \times 10^{-3}$ ,  $|r_\chi^{\text{DD}}| = 2.2 \times 10^{-3}$ , and  $|r_\chi^{\text{Belle II}}| = 1.0 \times 10^{-3}$ .

The neutral kaon tracks in LHCb generally pass through somewhere between zero (for a significant amount of the LL tracks) and a hundred (for some DD tracks) distinct detector segments. Therefore it is worth examining the degree to which using a single average  $\Delta\chi$  value, obtained following the procedure outlined above, provides a reasonable description of the average material interaction. This can be done using full LHCb simulation, where the kaon state for a simulated track can be evaluated at all times, by applying Eq. (4.16) iteratively for each detector segment the track traverses, using a  $\Delta\chi$  value appropriate for that segment. This is done in Fig. 4.5 for a simple observable: the yield asymmetry

$$A_{K^0} = \frac{|\psi_{K^0}(t)|^2 - |\psi_{\bar{K}^0}(t)|^2}{|\psi_{K^0}(t)|^2 + |\psi_{\bar{K}^0}(t)|^2}, \quad (4.41)$$

where  $\psi_{K^0}(t)$  ( $\psi_{\bar{K}^0}(t)$ ) is the amplitude for an initial  $K^0$  ( $\bar{K}^0$ ) to decay to two pions at time  $t$ . In this calculation, it is assumed that  $\epsilon = 0$  to isolate the material effect with no asymmetry contribution from the inherent  $CP$ -violation in the neutral kaon sector.

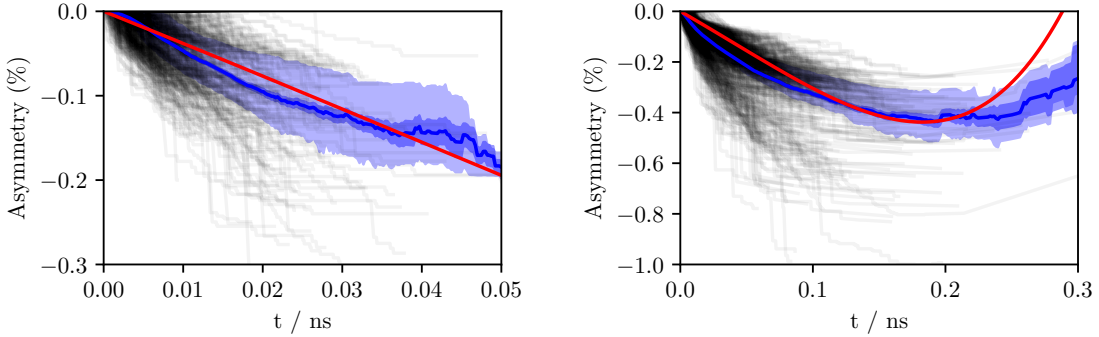


**Figure 4.5:** The asymmetry in Eq. (4.41) as a function of time for  $K_S^0$  tracks in samples of simulated (left) LL and (right) DD decays, using the full LHCb simulation. The light blue area is the central 50 % quantile of all tracks, the dark blue area is the  $1\sigma$  uncertainty band on the mean. The black lines show the result for a subset of individual, randomly sampled tracks. The red lines are calculated using the average  $\Delta\chi$  values that are also used in the calculation of biases in BPFGGSZ measurements.

While the track-by-track asymmetries are found to differ significantly depending on the exact detector segments a track intersects, the average asymmetry is seen to evolve smoothly as a function of decay time, and in reasonable agreement with the asymmetry value that is calculated using the average  $\Delta\chi$  values estimated above.

The LHCb detector is undergoing a significant upgrade prior to the start of the LHC Run 3. However, the material budget and geometry of the relevant sub-detectors will be similar to the sub-detectors used during Run 1 and 2 [139, 140]. Hence the results of this study will be valid for measurements during the upgrade phases of LHCb, even though the detector parameters presented in this section relate to the original LHCb detector.

### 4.3.5 Calculation procedure

The main idea in the bias study is to calculate the BPFGGSZ bin yields including the full effect of neutral kaon  $CP$  violation and material, fit them using the default equations of Chapter 2, and thereby obtain the bias  $\Delta\gamma = \gamma - \gamma^0$  due to the kaon effects not being considered in the parameter extraction. For the purpose of Ref. [2], a simple fit setup of a single  $B^\pm \rightarrow D h^\pm$  mode is investigated, where the  $K_i$  parameters are determined in a control channel with the relevant experimental acceptance. This setup is modified in the study used to assign a systematic uncertainty on the LHCb measurement of Chapter 5, as described in Section 4.3.7 below.

In practice, the amplitude model for  $D^0 \rightarrow K_S^0 \pi^+ \pi^-$  decays in Ref. [50] is taken to represent the  $A_1(s_{+-})$  amplitude. Then  $A_2(s_{+-})$  is obtained as described in Section 4.2.2. In terms of  $A_1$  and  $A_2$ , the amplitudes  $A_{S(L)}^{D^0}(s_{+-})$  can be expressed

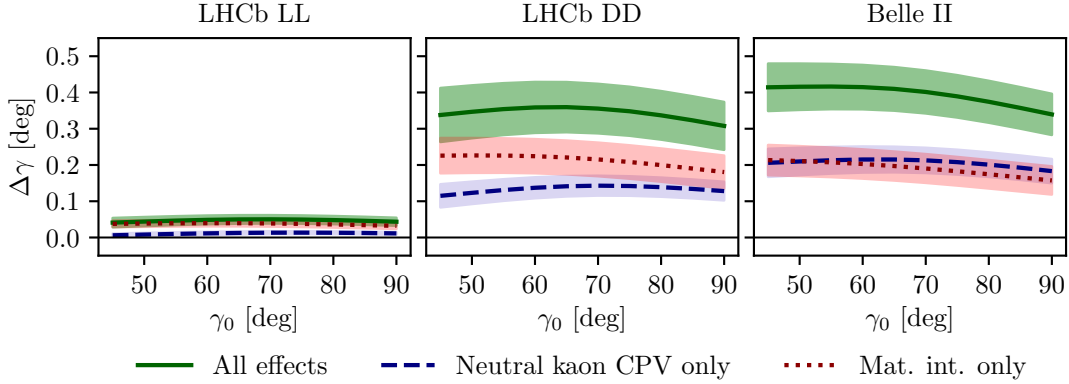


**Figure 4.6:** The bias  $\Delta\gamma$  as a function of input  $\gamma_0$  for (left) the LL LHCb category, (centre) the DD LHCb category, and (right) Belle II. The bias is calculated due to (blue, dashed line) neutral kaon  $CP$  violation alone, (red, dotted line) material interaction alone, and (green line) both effects. The shaded region shows the estimated  $1\sigma$  uncertainty band.

and related via Eqs. (4.26) and (4.27), and the full signal decay amplitudes as a function of phase-space coordinates, time, and the material interaction parameter  $\Delta\chi$  can be calculated for a given set of input parameters  $(\gamma^0, r_B^0, \delta_B^0)$ . The squared decay amplitudes are then integrated over phase space and the kaon decay times to obtain the binned signal yield.

The signal yields depend on the momentum via the time-acceptance parameters  $\tau_1$  and  $\tau_2$ , and because the material interaction parameter  $\Delta\chi$  is momentum dependent. Therefore, the yields are averaged over the  $K_S^0$  momentum distributions of LHCb and Belle II.

The parameters  $x_{\pm}$  and  $y_{\pm}$  are determined by a maximum likelihood fit to the calculated yields, after which the fit result and covariance matrix are interpreted in terms of the physics parameters  $(\gamma, r_B, \delta_B)$  using another maximum likelihood fit [43]. In the fits, the  $K_i$  are obtained using the definition  $K_i = K_i^{\text{meas}} = (N_i^D + N_{-i}^{\bar{D}})/(\sum_j N_j^D + N_{-j}^{\bar{D}})$ , in terms of the expected yields  $N_i^D$  ( $N_i^{\bar{D}}$ ) of a flavour-tagged  $D^0$  ( $\bar{D}^0$ ) decays in bin  $i$  of the  $D$  decay phase space, calculated as described above for  $r_B^0 = 0$ . This corresponds to experimentally measuring the  $K_i$  in a control channel, and takes the effect of neutral kaon  $CP$  violation and material interaction on  $K_i$  measurements into account, as well the experimental time acceptance. The  $(c_i, s_i)$  are calculated using  $A_1(s_{+-})$  and the experimental time acceptance is taken into account in this calculation as well.

### 4.3.6 Results

The obtained bias  $\Delta\gamma$  is shown as a function of input  $\gamma^0$  for the various experimental conditions in Fig. 4.6. The calculations are made using  $(r_B^0, \delta_B^0) = (0.1, 130^\circ)$ , approximately equal to the physics parameters relevant for  $B^\pm \rightarrow DK^\pm$  decays [24, 36]. The bias does not vary significantly with  $\gamma^0$  in the plotted range, which includes the world average value of direct  $\gamma$  measurements as well as the values obtained in full unitarity-triangle fits [24, 33, 36]. For all cases, the bias is found to be below  $0.5^\circ$ , corresponding to relative biases of about half a percent. Thus the biases are of  $\mathcal{O}(re/r_B)$  as expected, given the arguments of Section 4.2.3. The contributions from the individual  $K_S^0$  CPV and material interaction effects are also shown. It is seen that the neutral kaon  $CP$  violation and material interaction effects leads to approximately equal biases in all three cases.

Given the decay-time acceptance and momentum distribution for each experimental category, the mean life time,  $\langle\tau\rangle$ , of the reconstructed kaons can be calculated. In terms of the  $K_S^0$  lifetime  $\tau_{K_S^0} = (0.895 \pm 0.004) \times 10^{-11}$  s [28],  $\langle\tau_{LL}\rangle \simeq 0.1\tau_{K_S^0}$  for the LHCb LL category,  $\langle\tau_{DD}\rangle \simeq 0.8\tau_{K_S^0}$  for the LHCb DD category, and at Belle II  $\langle\tau_{Belle\ II}\rangle \simeq \tau_{K_S^0}$ . The difference in average kaon lifetime is reflected in the observed biases, which are found to be larger in the samples with longer lived kaons. The very small effect in the LL category is to be expected because the  $CP$ -violation effect due to  $K_S^0$  not being  $CP$ -even is approximately cancelled by the  $CP$ -violation effect arising from  $K_S^0 - K_L^0$  interference for kaons with decay times much smaller than  $\tau_{K_S^0}$  [130].

The uncertainty bands in Fig. 4.6 are calculated by repeating the study while varying some of the inputs. The model dependence of the predicted biases is probed by repeating the study using two other amplitude models as input for  $A_1(s_{+-})$  and  $A_2(s_{+-})$ : the model published in Ref. [61] and the model included in EVTGEN [116]. When defining  $A_2(s_{+-})$  in terms of  $A_1(s_{+-})$ , there is an uncertainty due to the unknown  $(r_k, \delta_k)$  parameters used to describe the  $\pi\pi$  resonance terms. This uncertainty is assessed by making the study with several different random realisations of the parameter set. The studies are repeated while varying the time acceptances and material densities with  $\pm 10\%$ . There is an additional uncertainty due to the use of simulation samples generated with `RapidSim` to describe the kaon momentum distribution, in lieu of full detector simulations.

There is also an uncertainty from the use of  $(c_i, s_i)$  as calculated using  $A_1(s_{+-})$ . It is to be expected that the measured values  $(\hat{c}_i, \hat{s}_i)$  from the CLEO collaboration differ by those calculated using  $A_1^D(s_-, s_+)$  by terms of  $\mathcal{O}(\epsilon)$  due to neutral kaon  $CP$  violation, which is not taken into account in the measurement [70]. These

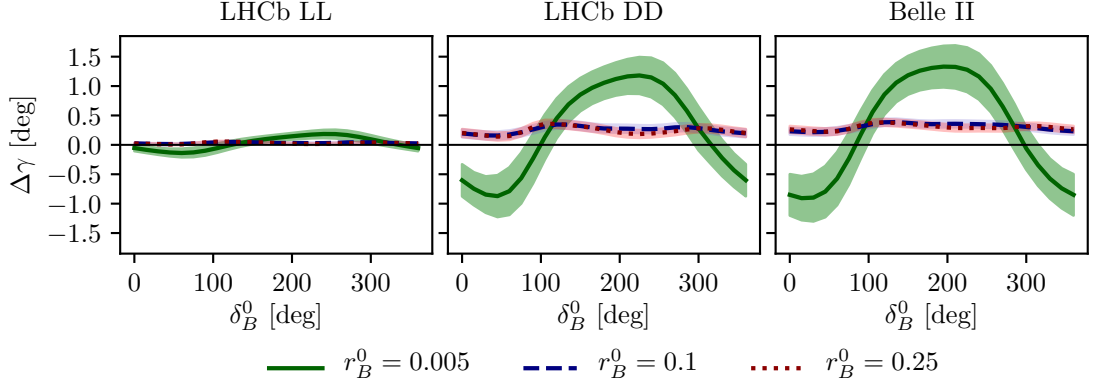


**Figure 4.7:** The bias  $\Delta\gamma$  as a function of input  $\delta_B$  for (left) the LL LHCb category, (centre) the DD LHCb category, and (right) Belle II. The bias is calculated for  $\gamma = 75^\circ$  and (green line)  $r_B = 0.005$ , (blue, dashed line)  $r_B = 0.1$ , and (red, dotted line)  $r_B = 0.25$ . The shaded region shows the estimated  $1\sigma$  uncertainty band.

corrections can be calculated via a procedure analogous to the one used to estimate the corrections on measurements of  $\gamma$  in this paper. However, as these corrections are much smaller than the experimental uncertainties in the measurement, they have not been studied further.

For the purpose of this thesis, it is important to consider the bias in measurements that use  $B^\pm \rightarrow D\pi^\pm$  decays as well, and other  $B$  decay modes can also be used in BPGBSZ measurements, such as  $B^\pm \rightarrow D^*K^\pm$ ,  $B^\pm \rightarrow DK^{*\pm}$ , and  $B^0 \rightarrow DK^{*0}$ . For the purpose of the study presented here, the main difference between the decay channels is that they have different values of  $r_B$  and  $\delta_B$ . Figure 4.7 shows  $\Delta\gamma$  as a function of input  $\delta_B^0$ , for  $\gamma^0 = 75^\circ$  and three different values of  $r_B^0$ . Aside from  $r_B^0 = 0.1$ , the results are shown for  $r_B^0 = 0.005$ , which corresponds to the expectation in  $B^\pm \rightarrow D\pi^\pm$  decays [45] and  $r_B^0 = 0.25$ , which corresponds to  $B^0 \rightarrow DK^{*0}$  decays [44]. The most notable feature is that the biases are significantly larger in the  $B^\pm \rightarrow D\pi^\pm$  case. This is expected: the  $r_B^0$  dependent behaviour is governed by the relative importance of different  $\mathcal{O}(r\epsilon)$  correction terms to the phase-space distribution. There are terms of both  $\mathcal{O}(r_A\epsilon)$  and  $\mathcal{O}(r_B\epsilon)^5$ , which lead to expected biases of size  $\mathcal{O}(r_A\epsilon/r_B)$  and  $\mathcal{O}(r_B\epsilon/r_B) = \mathcal{O}(\epsilon)$ , respectively, cf. the discussion of Section 4.2.3. In the  $B^\pm \rightarrow D\pi^\pm$  case, the  $\mathcal{O}(r_A\epsilon)$  correction terms dominate because  $r_A/r_B \simeq (0.05/0.005) = 10$ . This explains the relatively large bias, as  $|r_A\epsilon/r_B^{D\pi}| \simeq 4\%$ . The bias is seen to be up to  $\pm 1.5^\circ$ , but only about  $+0.2^\circ$  with the expected value of  $\delta_B^{D\pi} \simeq 300^\circ$  [43, 45]. These biases are *much smaller* than the

<sup>5</sup>There are similar terms of  $\mathcal{O}(r_A r_\chi)$  and  $\mathcal{O}(r_B r_\chi)$ , but as  $\epsilon$  and  $r_\chi$  are of the same order of magnitude, these terms can be treated completely analogously to the  $\mathcal{O}(r_A\epsilon)$  and  $\mathcal{O}(r_B\epsilon)$  terms, and have been left out of the discussion for brevity.

precision on  $\gamma$  that is obtainable in a  $B^\pm \rightarrow D\pi^\pm$  analysis with current experimental yields, and do thus not pose a problem. In the  $r_B^0 = 0.1$  and  $r_B^0 = 0.25$  cases the  $\mathcal{O}(r_B\epsilon)$  correction terms dominate, and the biases are of  $O(\epsilon)$ , independent of the  $r_B^0$  value. Therefore both cases have biases of similar size.

Further, it is clear that the biases depend on  $\delta_B^0$  and that the oscillation period of the  $\delta_B$  dependence is different between the  $r_B^0 = 0.005$  case and the  $r_B^0 \in \{0.1, 0.25\}$  cases. It is to be expected that  $\Delta\gamma$  oscillates as a function of  $\delta_B^0$ , because  $\delta_B^0$  enters the yield equations via  $\cos(\delta_B^0 \pm \gamma)$  and  $\sin(\delta_B^0 \pm \gamma)$  terms. As explained above, the  $\mathcal{O}(r_A\epsilon)$  terms dominate the  $B^\pm \rightarrow D\pi^\pm$  bias, and these are independent of  $\delta_B^0$ . The  $\mathcal{O}(r_B\epsilon)$  terms, however, are important for the bias corrections for larger  $r_B$  values, and the terms include factors of  $\cos(\delta_B^0 \pm \gamma)$  and  $\sin(\delta_B^0 \pm \gamma)$ . This explains the different bias dependence on  $\delta_B^0$ .

While the input value of  $\gamma^0 = 75^\circ$  was chosen for these studies, there is minimal variation in the results if another value of  $\gamma^0$  in the range  $[60^\circ, 85^\circ]$  is used.

#### 4.3.7 Coupled $B^\pm \rightarrow DK^\pm$ and $B^\pm \rightarrow D\pi^\pm$ measurements

The studies presented above have been extended on two accounts in order to assign a systematic uncertainty to the LHCb measurement presented in Chapter 5. Firstly, full LHCb simulation has been used to obtain the momentum distributions, as well as to fit a better description of the decay-time acceptance and the reconstruction efficiency profile over the  $D$ -decay phase space. Secondly, the fit setup is modified to correspond to the experimental approach described in Section 2.4 and Chapter 5: the signal yields are calculated for both the  $B^\pm \rightarrow DK^\pm$  and  $B^\pm \rightarrow D\pi^\pm$  channels, and fitted in a combined fit to obtain  $(x_\pm^{DK}, y_\pm^{DK}, x_\xi^{D\pi}, y_\xi^{D\pi})$ , where the  $F_i$  parameters are allowed to float in the fit. The biases obtained for each observable are shown in Fig. 4.8, evaluated using the time-acceptance, momentum distribution, and material budget relevant for the DD category (since the effect in the LL category is much smaller). As will be clear in Chapter 5, these biases are all significantly smaller than the corresponding statistical uncertainties. Thus, the effects of neutral kaon  $CP$  violation and material interactions contribute a manageable systematic uncertainty in current BPGBS measurements, even if the  $B^\pm \rightarrow D\pi^\pm$  channel is promoted to a signal channel.

As the statistical uncertainty becomes comparable with the bias effects described in this chapter, the systematic uncertainty should be assigned by a more accurate study, incorporating the traversed material on a track-by-track basis in full detector simulation. Such a detailed calculations can also be used to apply a bias correction if desired.

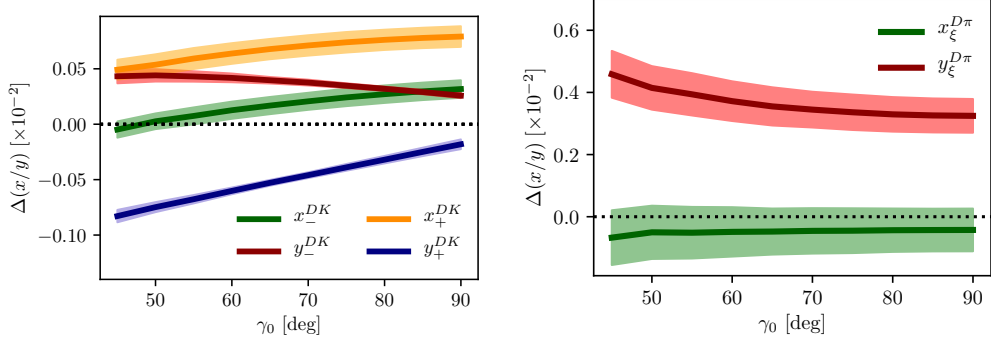


**Figure 4.8:** The bias on (left) the  $B^\pm \rightarrow DK^\pm$  and (right)  $B^\pm \rightarrow D\pi^\pm$   $CP$ -violation observables in the LHCb DD category, evaluated in bias studies with inputs based on full LHCb simulation, calculated as a function of input  $\gamma_0$ . Since the typical size of the  $x_\pm^{DK}$  and  $y_\pm^{DK}$  parameters is  $\sim 0.1$ , the relative biases on the observables are approximately 0.5 %. Thus, the results are similar to the ones shown in Fig. 4.6.

## 4.4 Concluding remarks

The analysis presented in this chapter has shown the expected impact of neutral kaon  $CP$  violation and material interaction on current BPGGSZ measurements to be small compared to the statistical uncertainties; first by simple order-of-magnitude estimates and then by a detailed calculation of the expected effect in LHCb and Belle II.

While the calculations were made for the case of  $D \rightarrow K_S^0 \pi^+ \pi^-$  decays, the BPGGSZ approach can of course also be applied in other  $D$ -decay final states, such as  $D \rightarrow K_S^0 K^+ K^-$  and  $D \rightarrow K_S^0 \pi^+ \pi^- \pi^0$ . The biases on measurements of  $\gamma$  based on the  $D$  decay phase-space distributions should be of similar size in these decay channels. The impact on  $\gamma$  measurements based on the phase-space-integrated yield asymmetry can be expected to be tens of degrees for the  $D \rightarrow K_S^0 K^+ K^-$  channel, where the yield asymmetry is expected to be around 2 %, for the reasons explained in Section 4.2.3. The  $D \rightarrow K_S^0 \pi^+ \pi^- \pi^0$  decay, however, is dominantly  $CP$ -odd [47], and the bias in measurements based on the total asymmetry is therefore expected to be  $\mathcal{O}(\epsilon/r_B)$ , i.e. a few degrees [38]. More precise calculations of the biases would require a repeat of the study included here, with relevant amplitude models and binning schemes in place.

The chapter focuses on the model-independent, binned approach that is the subject of the thesis. However, the underlying mechanism that determines the scale of the bias, namely that the phase-space *distribution* of signal decays is unaffected at  $\mathcal{O}(\epsilon)$  and  $\mathcal{O}(r_\chi)$ , is independent on the exact measurement approach. Therefore it is expected that amplitude-model-based measurements and measurements made

with new unbinned methods such as those in Ref [69] will be similarly biased if kaon  $CP$  violation and regeneration are not accounted for.

# 5

## A BPGBGSZ measurement of $\gamma$ with $B^\pm \rightarrow Dh^\pm$ decays

This chapter describes a model-independent BPGBGSZ measurement of  $\gamma$  with  $B^\pm \rightarrow DK^\pm$  and  $B^\pm \rightarrow D\pi^\pm$  decays where  $D \rightarrow K_S^0\pi^+\pi^-$  and  $D \rightarrow K_S^0K^+K^-$ , commonly denoted  $B^\pm \rightarrow D(\rightarrow K_S^0h^+h^-)h'^\pm$  decays. The measurement is made with the full LHCb data set collected during Run 1 and 2 of the LHC, corresponding to an integrated luminosity of about  $8.7\text{ fb}^{-1}$ . The analysis has been submitted for publication in the Journal of High Energy Physics.

### 5.1 Candidate reconstruction and selection

The  $B^\pm \rightarrow D(\rightarrow K_S^0h^+h^-)h'^\pm$  candidates are constructed during the offline *stripping* stage described in Section 3.3.3. The candidates are defined by first combining tracks to form a  $K_S^0 \rightarrow \pi^+\pi^-$  vertex, then a  $D \rightarrow K_S^0h^+h^-$  vertex, and finally the  $B^\pm \rightarrow Dh'^\pm$  candidate. Each final state track is required to satisfy certain momentum thresholds and track-quality requirements, and to have a minimum impact parameter with respect to all primary interaction vertices. Each decay vertex is required to satisfy a fit-quality threshold and to be separated from the primary vertex. Momentum thresholds are applied to the composite particles and they are required to have reconstructed invariant masses close to their known masses,<sup>1</sup> except that the  $B$  candidate is required to have a reconstructed invariant mass in the interval  $4750\text{--}7000\text{ MeV}/c^2$ . The  $B$  candidate is required to satisfy

---

<sup>1</sup>The exact mass window depends on the particle type and reconstruction category; narrower mass windows are applied at a later stage, as described below.

$\chi_{\text{IP}}^2 < 25$ , where  $\chi_{\text{IP}}^2$  is the difference in  $\chi^2$  value of the primary vertex fit, when the vertex is formed with- and without the  $B$  candidate; this requirement removes  $B$  candidates that correspond to actual particles produced in secondary decays.. As the final part of the stripping stage, a multivariate classifier [112] is applied to the formed  $B$  candidate to reduce the amount of random track combinations, denoted combinatorial background, even further than the aforementioned requirements.

Two data categories are defined, depending upon the tracks used to form the  $K_S^0$  candidate: the LL category where both pions are long tracks, and DD category where both pions are downstream tracks, using the track classifications of Section 3.2.1.

Each of the candidates that pass the stripping stage are re-analysed with the `DecayTreeFitter` (DTF) frame work [141], where a simultaneous fit of the full decay chain is made with a number of constraints applied: the momenta of the composite  $D$  and  $K_S^0$  particles are required to form invariant masses exactly equal to the known particle masses [28], and the momentum of the  $B$  candidate is required to point in the direction defined by the  $B$  decay vertex and the primary vertex. This refit results in improved resolution of the invariant mass of the  $B$  candidate and, very importantly, of the Dalitz coordinates in the  $D$ -decay phase space. It also ensures that all candidates fall in the kinematically allowed region of the  $D$ -decay phase space. Unless otherwise specified, all results in this chapter are based on the refitted track momenta; for reasons explained below, some studies have to be based on parameters that are obtained without the constraints, or with only a subset of them applied.

Following the stripping stage, the further selection of signal candidates is performed in three steps: an initial set of requirements to remove candidates that are very likely to be background, the application of a multivariate analysis algorithm designed to reject combinatorial background decays, and finally a set of particle-identification requirements. The requirements are summarised in Table 5.1, and each step is described in detail in the following sections.

### 5.1.1 Initial requirements

At the hardware trigger level, it is required that a particle associated with the signal decay triggered the hadronic L0 trigger (classifying the event as *Trigger on Signal*, or TOS), or that the L0 decision was caused by a particle that is not associated with the signal decay (*Trigger Independent of Signal*, or TIS). The inclusion of the latter category increases the data sample about 50 %. At the software trigger level, a particle belonging to the signal decay is required to have caused one of each of the inclusive HLT1 and HLT2 lines to accept the events.

**Table 5.1:** Summary of requirements applied to data. The base requirements are applied to all data samples before training or applying the BDT.

| Base requirements  |  |  |
|--|--|--|
| Variable   | Cut  | Comment  |
| Companion momentum, $p$                                    | $< 100 \text{ GeV}/c$                                  |  |
| Companion has RICH   | <i>true</i>  |  |
| $K^\pm$ in $D$ decay: momentum, $p$                        | $< 100 \text{ GeV}/c$                                  | In $D \rightarrow K_S^0 K^+ K^-$   |
| $K^\pm$ in $D$ decay: have RICH                            | <i>true</i>  | In $D \rightarrow K_S^0 K^+ K^-$   |
| DecayTreeFit converged                                     | <i>true</i>  |  |
| $D$ mass   | $m_{D^0} \in m_{D^0}^{PDG} \pm 25 \text{ MeV}/c^2$     | From DTF with constrained $K_S^0$ mass                                   |
| $K_S^0$ mass   | $m_{K_S^0} \in m_{K_S^0}^{PDG} \pm 15 \text{ MeV}/c^2$ | From DTF with constrained $D^0$ mass                                     |
| Background suppressing requirements                        |  |  |
| Variable   | Cut  | Comment  |
| $K_S^0$ flight distance $\chi^2$                           | $> 49$   | for LL only  |
| $\Delta z_{\text{significance}}^{DB}$                      | $> 0.5$  | for all candidates   |
| Particle-identification (PID) requirements                 |  |  |
| Channel  | Cut  | Comment  |
| $B^\pm \rightarrow DK^\pm$                                 | <code>PIDK &gt; 4</code>                               | for companion  |
| $B^\pm \rightarrow D\pi^\pm$                               | <code>PIDK &lt; 4</code>                               | for companion  |
| $B^\pm \rightarrow Dh^\pm$                                 | <code>IsMuon = 0</code>                                | for companion  |
| $B^\pm \rightarrow D(\rightarrow K_S^0 \pi^+ \pi^-) h^\pm$ | <code>isMuon = 0</code>                                | for both charged $D$ decay products                                      |
| $B^\pm \rightarrow D(\rightarrow K_S^0 \pi^+ \pi^-) h^\pm$ | <code>PIDe &lt; 0</code>                               | for charged $D$ decay product with opposite charge to companion particle |
| $B^\pm \rightarrow D(\rightarrow K_S^0 K^+ K^-) h^\pm$     | <code>PIDK &gt; -5 &amp; isMuon = 0</code>             | for charged $D$ decay products   |
| Requirement on Boosted Decision Tree (BDT) output          |  |  |
| Channel  | Cut  | Comment  |
| Run 1, DD  | $> 0.6$  |  |
| Others   | $> 0.8$  |  |

Specifically, the Run 1 events are required to be TOS on the `HLT1TrackAllL0` and `Hlt2Topo{2, 3, 4}BodyBBDT` lines and the Run 2 events are required to be TOS on the `Hlt1{Track, TwoTrack}MVA` and `Hlt2Topo{2, 3, 4}Body` lines. These trigger lines were described in Section 3.3.

Before any processing of the data, a loose preselection is applied to remove obvious background candidates. The reconstructed  $D$  ( $K_S^0$ ) mass is required to be within  $25$  ( $15$ )  $\text{MeV}/c^2$  of the known values [28]. The *companion* particle, the pion or kaon produced in the  $B^\pm \rightarrow Dh^\pm$  decay, is required to have associated RICH information and a momentum less than  $100 \text{ GeV}/c$ ; this ensures good particle-identification performance. Finally, all of the `refits of the full decay chain with kinematic constraints` are required to have converged properly.

Two additional requirements are made at this stage in order to suppress specific backgrounds. In order to suppress decays of the type  $B^\pm \rightarrow K_S^0 h^+ h^- h'^\pm$  with no intermediate  $D$  meson, so called *charmless* decays, it is required that the significance of the  $z$ -separation of the  $D^0$  decay vertex and the  $B^\pm$  decay vertex

is above 0.5. The significance of the  $z$ -separation of the  $D^0$  decay vertex and the  $B^\pm$  decay vertex is defined as

$$\Delta z_{\text{significance}}^{D-B} = \frac{z_{vtx}^D - z_{vtx}^B}{\sqrt{\sigma^2(z_{vtx}^D) + \sigma^2(z_{vtx}^B)}}. \quad (5.1)$$

This source of background described further in section 5.3.1. In order to suppress a background from  $D \rightarrow 4\pi$  and  $D \rightarrow \pi\pi KK$  decays, it is required that the  $K_S^0$  flight distance  $\chi_{\text{FD}}^2$  is greater than 49, where

$$\chi_{\text{FD}}^2 = \left( \frac{\Delta r}{\sigma(\Delta r)} \right)^2, \quad (5.2)$$

and  $\Delta r$  is the measured flight distance of the  $K_S^0$  meson. This background is described in further detail in section 5.3.2.

### 5.1.2 Boosted decision tree

A Gradient Boosted Decision Tree [142] (abbreviated BDT in the following) is applied to classify each candidate on a scale from  $-1$  to  $+1$  as signal-like ( $+1$ ) or combinatorial-background-like ( $-1$ ), based on the values of a number of input parameters for a candidate in question. The BDT is implemented in the TMVA frame work [143]. A number of alternative classification algorithms were considered, including various neural network architectures and BDTs that were trained using alternative boosting schemes. The chosen classifier was found to perform at least as good as any alternative. Furthermore, the approach is well understood from earlier versions of the analysis [3, 68], where has been employed and studied in detail (including careful comparisons of the distribution of input parameters in simulation with those in data samples of signal decays).

A boosted decision tree classifier consists of a number of sequentially trained decision trees, each of which classify events as either signal or background. Each tree bases the decision on an individual subset of variables, out of an overall set of input variables. At each training step, the input events are weighted when training a new tree, so that events that the already-trained trees classify incorrectly are given a higher weight; this is denoted boosting. The term *gradient boosting* denotes a specific weight calculation scheme [142]. The final score is the average over all decision trees.

The full set of input variables is given in Table 5.2. It includes the momenta of particles in the decay; a number of geometric parameters such a absolute and relative vertex positions, and distances of closest approach between tracks;  $\chi_{\text{IP}}^2$  values for a number of particles in the decay chain; the  $\chi^2$  per degree of freedom

**Table 5.2:** Input parameter set used in BDT trained to separate signal and combinatorial background, sorted according to importance in the LL classifier.

| Variable name                              | Importance LL/DD (Rank in DD) | Description   |
|--|-------------------------------|---|
| <code>log(1-Ks_DIRA_BPV)</code>            | 7.2 % / 3.5 % (16)            | $\log \cos \theta_{\text{DIRA}}$ for $K_S^0$                |
| <code>log(Bu_RHO_BPV)</code>               | 5.7 % / 5.5 % (5)             | Radial distance of $B$ vertex to beam line                  |
| <code>log(Bach_PT)</code>                  | 5.2 % / 6.9 % (1)             | $p_T$ of the companion particle                             |
| <code>log(0(1-DO_DIRA_BPV)</code>          | 4.9 % / 5.8 % (4)             | $\log \cos \theta_{\text{DIRA}}$ for $D$                    |
| <code>log(0(1-Bu_DIRA_BPV)</code>          | 4.9 % / 6.4 % (3)             | $\log \cos \theta_{\text{DIRA}}$ for $B^\pm$                |
| <code>log(DO_RHO_BPV)</code>               | 4.8 % / 5.3 % (6)             | Radial distance of $D$ vertex to beam line                  |
| <code>Bu_FTASY_1_5</code>                  | 4.7 % / 4.9 % (7)             | Asymmetry parameters of $B^\pm$                             |
| <code>log(DO_PT)</code>                    | 4.7 % / 6.6 % (2)             | $p_T$ of the $D$ meson                                      |
| <code>log(Bu_constDOOKSPV_CHI2NDDF)</code> | 4.2 % / 4.5 % (9)             | $\chi^2$ /d.o.f of kinematical refit with DecayTreeFitter   |
| <code>log(Bu_FDGH12_QWNPV)</code>          | 3.9 % / 4.1 % (11)            | Flight distance $\chi^2$ of the $B^\pm$                     |
| <code>log(max_Ksh1h2_IPCH12_0WNPV)</code>  | 3.9 % / 3.0 % (20)            | Largest $\chi^2_{\text{IP}}$ of the $K_S^0$ decay products  |
| <code>log(DO_IPCH12_QWNPV)</code>          | 3.8 % / 3.3 % (17)            | $\chi^2_{\text{IP}}$ of the $D$                             |
| <code>log(min_Ksh1h2_IPCH12_0WNPV)</code>  | 3.7 % / 0.9 % (26)            | Smallest $\chi^2_{\text{IP}}$ of the $K_S^0$ decay products |
| <code>log(Bu_P)</code>                     | 3.7 % / 3.9 % (12)            | $p$ of the $B_\pm^0$ meson                                  |
| <code>log(Bu_IPCH12_QWNPV)</code>          | 3.6 % / 4.6 % (8)             | $\chi^2_{\text{IP}}$ of the $B_\pm^0$                       |
| <code>Bu_MAXDOCA</code>                    | 3.6 % / 3.3 % (18)            | "Distance of closest approach" for $B^\pm$ vertex           |
| <code>log(Bach_IPCH12_0WNPV)</code>        | 3.3 % / 4.3 % (10)            | $\chi^2_{\text{IP}}$ of the companion particle              |
| <code>log(Bu_PT)</code>                    | 3.3 % / 3.7 % (14)            | $p_T$ of the $B^\pm$ meson                                  |
| <code>log(max_h1h2_IPCH12_0WNPV)</code>    | 3.1 % / 3.8 % (13)            | Largest $\chi^2_{\text{IP}}$ of the $D$ decay products      |
| <code>log(min_h1h2_IPCH12_0WNPV)</code>    | 3.0 % / 3.4 % (19)            | Smallest $\chi^2_{\text{IP}}$ of the $D$ decay products     |
| <code>log(Ks_VTXCH12D0F)</code>            | 2.9 % / 2.3 % (21)            | $\chi^2$ of vertex fit for $K_S^0$                          |
| <code>DO_MAXDOCA</code>                    | 2.9 % / 1.0 % (25)            | "Distance of closest approach" for $D$ vertex               |
| <code>log(DO_VTXCH12D0F)</code>            | 2.7 % / 1.6 % (24)            | $\chi^2$ of vertex fit for $D$                              |
| <code>log(DO_P)</code>                     | 2.7 % / 1.8 % (22)            | $p$ of the $D$ meson  |
| <code>log(Bach_P)</code>                   | 2.2 % / 3.6 % (15)            | $p$ of the companion particle                               |
| <code>log(Bu_VTXCH12D0F)</code>            | 1.8 % / 1.7 % (23)            | $\chi^2$ of vertex fit for $B^\pm$                          |

of the DTF refit; **DIRA** values, which denote the angle between the fitted particle momenta and the vector spanned by it's production and decay vertices; and finally an isolation variable, defined as

$$A_{p_T} = \frac{p_T(B) - \sum p_T(\text{other})}{p_T(B) + \sum p_T(\text{other})} \quad (5.3)$$

where the sum is over all other tracks in a cone around the  $B$ -candidate. The cone is defined as being within a circle with a radius of 1.5 units around the  $B$  candidate in the  $(\eta, \phi_{azim})$ -plane. This variable is highly efficient in rejecting combinatorial background. Two algorithms are trained, one for the LL category of  $K_S^0$  mesons and one for the DD category, because some input parameters relate to the  $K_S^0$  meson and have very different distributions between the two categories.

The BDTs are trained and tested with input samples representing typical signal and background decay candidates: a signal sample that consists of simulated  $B^\pm \rightarrow D(\rightarrow K_S^0\pi^+\pi^-)\pi^\pm$  decays corresponding to the LHCb running conditions for the years 2012–2018, and a sample of combinatorial background candidates from real data, where the reconstructed invariant mass of the  $B$  meson is larger than 5800 MeV/ $c^2$ . The candidates in both samples were required to have passed the initial requirements described in the preceding section. The input-parameter distributions in the signal and background training samples are shown in Figs. 5.1 and 5.2. The signal and background samples are each split into two before the training stage: one sub sample, the training sample, is used to train the BDT, after which the trained algorithm is applied to the other sub sample, the test sample. The classifier is found to perform well on the test sample, not just the training sample, which ensures that it does not suffer significant overtraining. The BDT output distribution are shown for both test and training samples in Fig. 5.3, where it is clear that the classifier very effectively separates signal and background candidates.

Each candidate in data is classified using the BDT, and candidates that are assigned a score below some threshold value are discarded. The threshold values are chosen in a set of pseudo experiments, such that the expected sensitivity to  $\gamma$  is maximised. This is done by performing preliminary fits to the data set for a range of different BDT threshold values, determining the signal and background yields for each threshold. The fits use the model described in Section 5.4. Then, many pseudo data sets are generated with the obtained yields (and invariant-mass distributions) and the full fit and interpretation procedure is applied to each data set, as described in Sections 5.4–5.7. Thus, the expected uncertainty on  $\gamma$  is obtained for the signal and background yields corresponding to a range of threshold

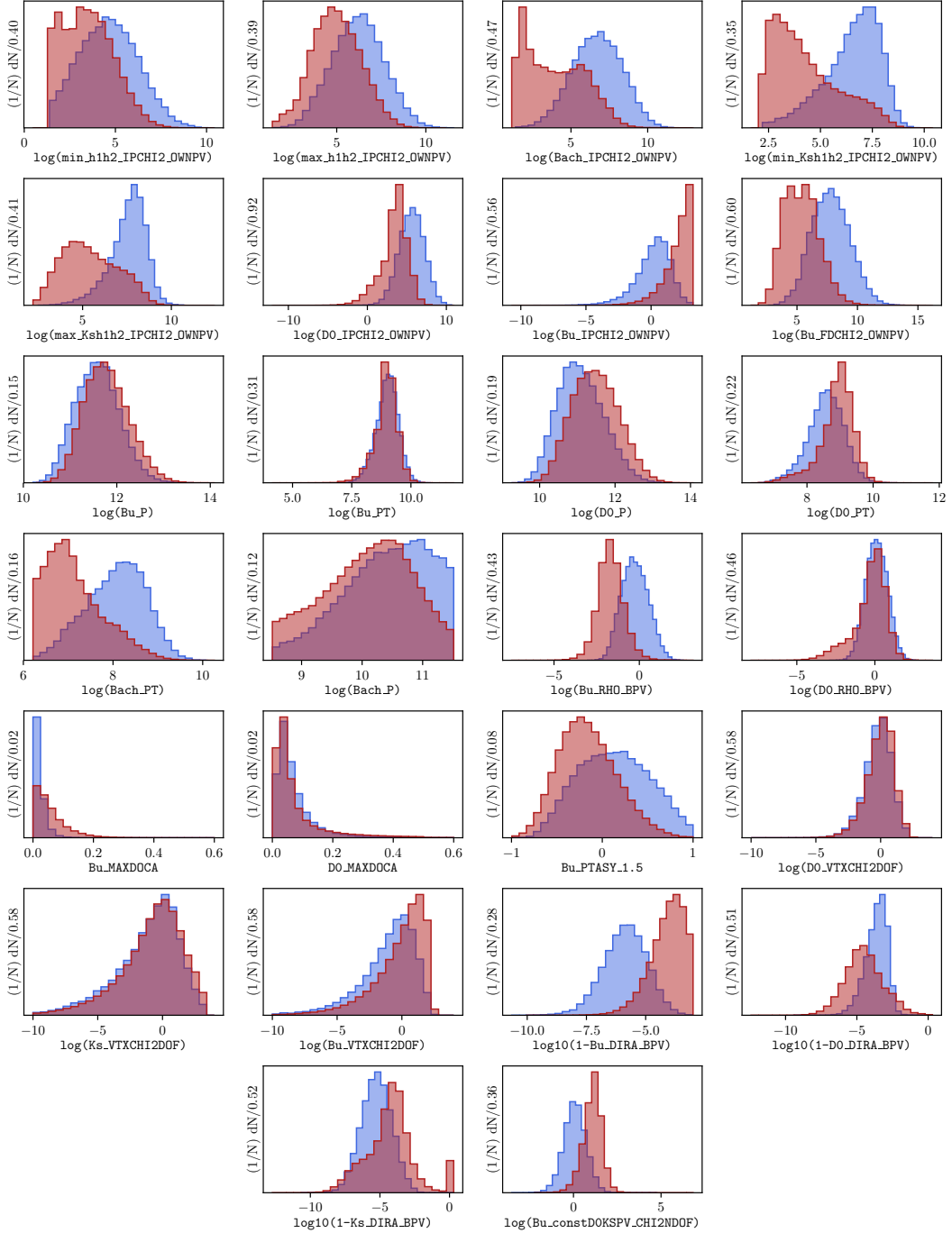


**Figure 5.1:** Distribution of input parameters in the LL training samples of (blue) signal decays from simulation and (red) background decays from the upper  $B$  sideband. The variable names are defined in Table 5.2.

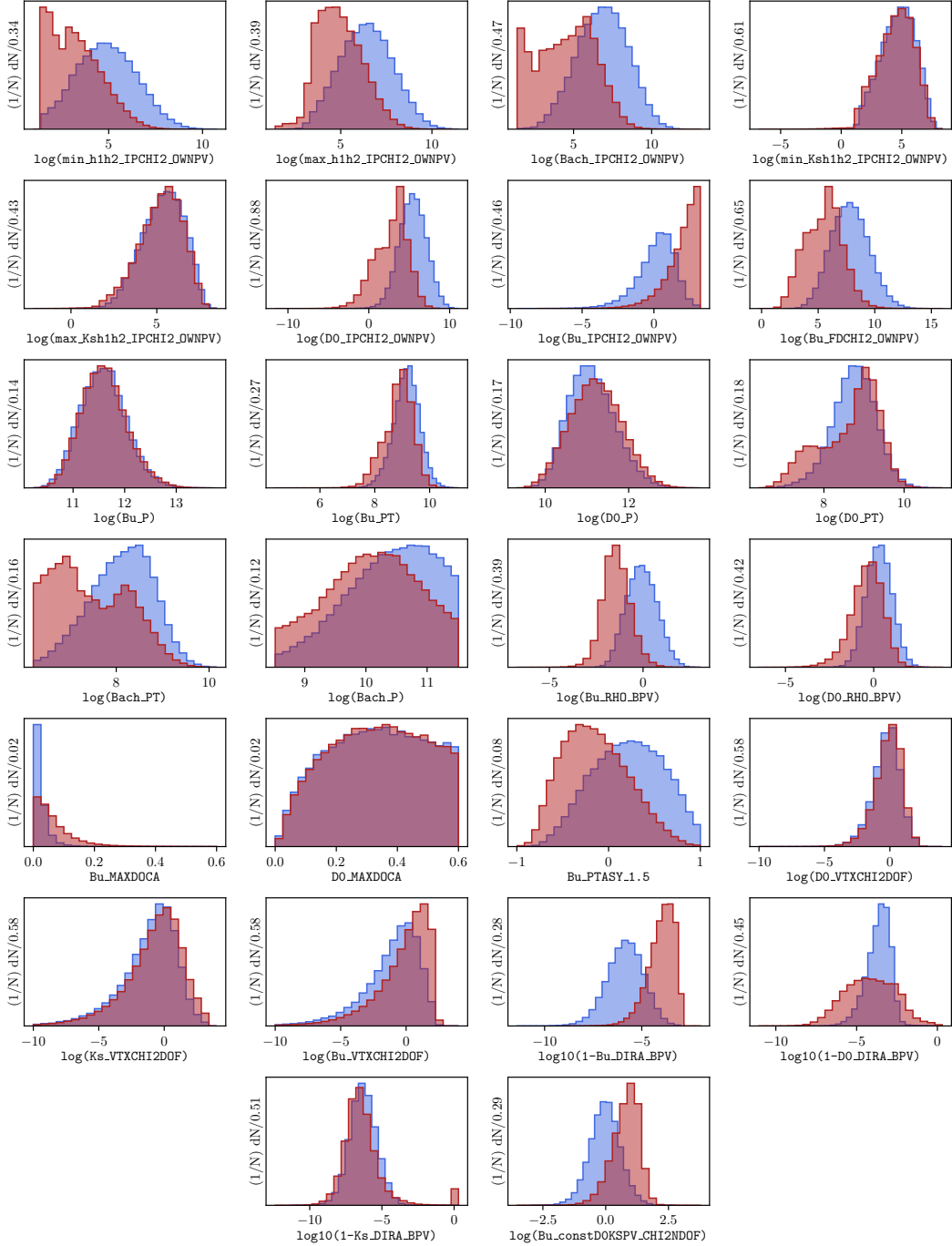


**Figure 5.2:** Distribution of input parameters in the DD training samples of (blue) signal decays from simulation and (red) background decays from the upper  $B$  sideband. The variable names are defined in Table 5.2.

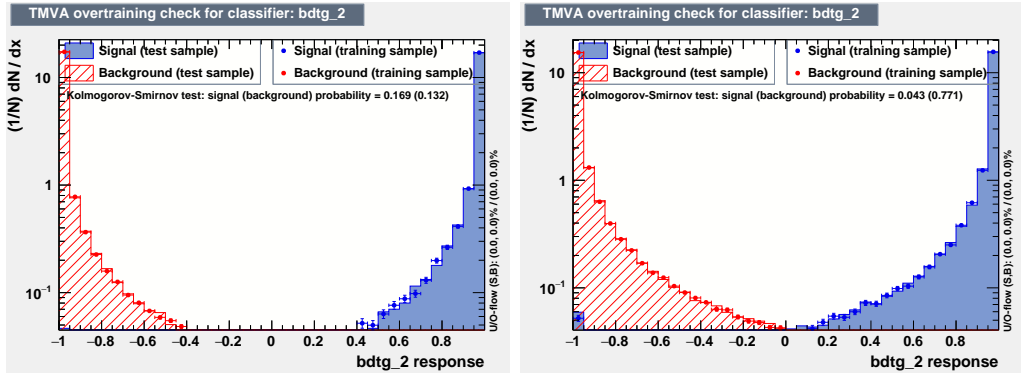


**Figure 5.3:** Distribution of BDT variable on test and training samples for (left) the LL and (right) the DD category, with logarithmic  $y$ -scale.

values. The procedure is applied independently for the LL and DD categories, as well as for the Run 1 and Run 2 data sets, because some parameter distributions differ slightly between the two runs. The optimal threshold values are found to be 0.8 in all situations, except for DD candidates in Run 1 where it is 0.6. This is illustrated in Fig. 5.4 where the results of the threshold scans are shown. The same classifier is applied to both  $B^\pm \rightarrow D\pi^\pm$  and  $B^\pm \rightarrow DK^\pm$  candidates, and both  $D$  final state categories. While the classifiers were trained using samples of  $B^\pm \rightarrow D(\rightarrow K_S^0\pi^+\pi^-)\pi^\pm$  simulation and data, the decays are similar enough that no significant improvement in performance was obtained when considering a more elaborate setup. Across all categories, the requirement on the BDT output is found to remove approximately 98 % of the combinatorial background, while being approximately 93 % efficient on signal.

### 5.1.3 Particle-identification requirements

A PID requirement is made to separate  $B^\pm \rightarrow DK^\pm$  and  $B^\pm \rightarrow D\pi^\pm$  candidates in the data sample, by requiring that the PIDK of the companion particle satisfies  $\text{PIDK} < 4$  for  $B^\pm \rightarrow D\pi^\pm$  candidates and  $\text{PIDK} > 4$  for  $B^\pm \rightarrow DK^\pm$  candidates. This ensures that any given candidate is selected into only one of these samples. The PIDK variable was defined in Section 3.1.3, as were the other PID variables entering the list below.

Further to the requirement on the companion, PID requirements are made to suppress semi-leptonic backgrounds as well as decays where a final state particle decays in flight, and a loose PID requirement is made in the  $D \rightarrow K_S^0 K^+ K^-$  channels where it leads to a higher signal purity:

- the companion particle is required to satisfy `isMuon = 0`.

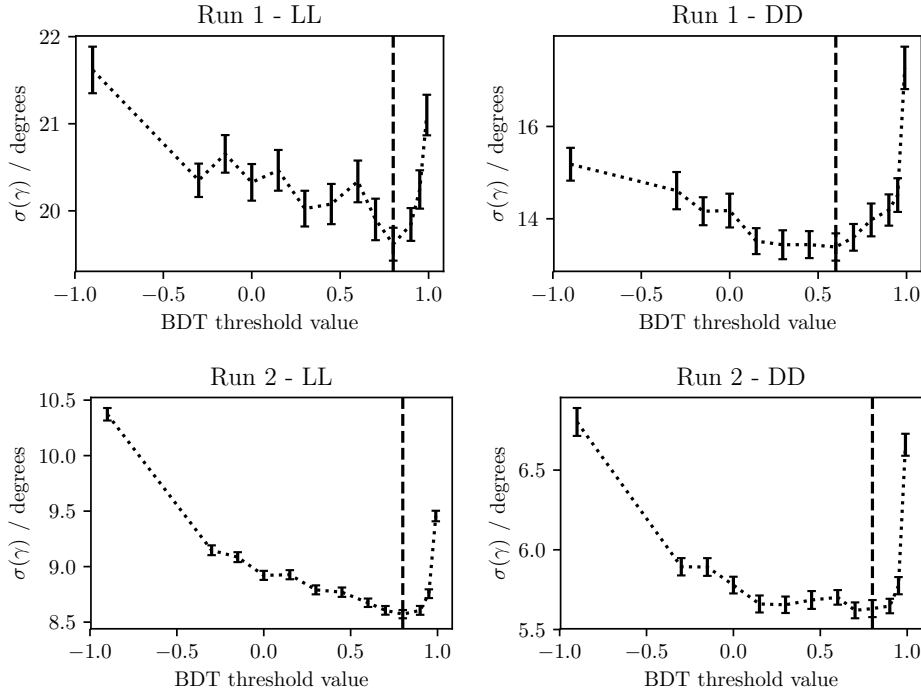


**Figure 5.4:** The mean uncertainty on  $\gamma$  in pseudo experiments, performed with the signal and background yields corresponding to a given BDT requirement, using (top) the Run 1 and (bottom) Run 2 datasets, using only candidates in (left) the LL category and (right) the DD category. The dashed line shows the threshold value employed to discard background-like candidates in the selection.

- For the  $B \rightarrow D(\rightarrow K_S^0 \pi^+ \pi^-)h^\pm$  samples it is required that the charged pion track from the  $D$  decay with opposite charge to the companion satisfies  $\text{PIDe} < 0 \& \text{isMuon} = 0$ , and for the other charged pion that  $\text{isMuon} = 0$ . A very loose requirement of  $\text{PIDK} < 20$  is applied to both pions from the  $D$ -decay in the stripping stage.
- For the  $B \rightarrow D(\rightarrow K_S^0 K^+ K^-)h^\pm$  samples it is required that the charged kaon tracks from the  $D$  decay have RICH information, a momentum less than 100  $\text{GeV}/c$  and  $\text{PIDK} > -5 \& \text{isMuon} = 0$ .

These backgrounds are described in Section 5.3.3.

#### 5.1.4 Final requirements

For a small fraction of candidates in the final sample, it is the case that two or more candidates originate in the same  $pp$  collision. In order to make sure that all candidates are completely independent, a single, arbitrary candidate from each  $pp$  collision is kept for these collisions, and the other candidates discarded.

**Table 5.3:** Final candidate yield in each data category after the full selection has been applied, including removing candidates outside the region  $m_B \in [5080, 5800] \text{ MeV}/c^2$ .

| $B$ Decay                    | $D$ final state   | $K_S^0$ type | Run 1 | Run 2  | Total  |
|------------------------------|-------------------|--------------|-------|--------|--------|
| $B^\pm \rightarrow DK^\pm$   | $K_S^0\pi^+\pi^-$ | LL           | 2275  | 10525  | 12800  |
|                              |                   | DD           | 5097  | 23508  | 28605  |
|                              | $K_S^0K^+K^-$     | LL           | 383   | 1610   | 1993   |
|                              |                   | DD           | 772   | 3397   | 4169   |
| $B^\pm \rightarrow D\pi^\pm$ | $K_S^0\pi^+\pi^-$ | LL           | 18209 | 90509  | 108718 |
|                              |                   | DD           | 40167 | 205807 | 245974 |
|                              | $K_S^0K^+K^-$     | LL           | 2879  | 13757  | 16636  |
|                              |                   | DD           | 6033  | 29790  | 35823  |

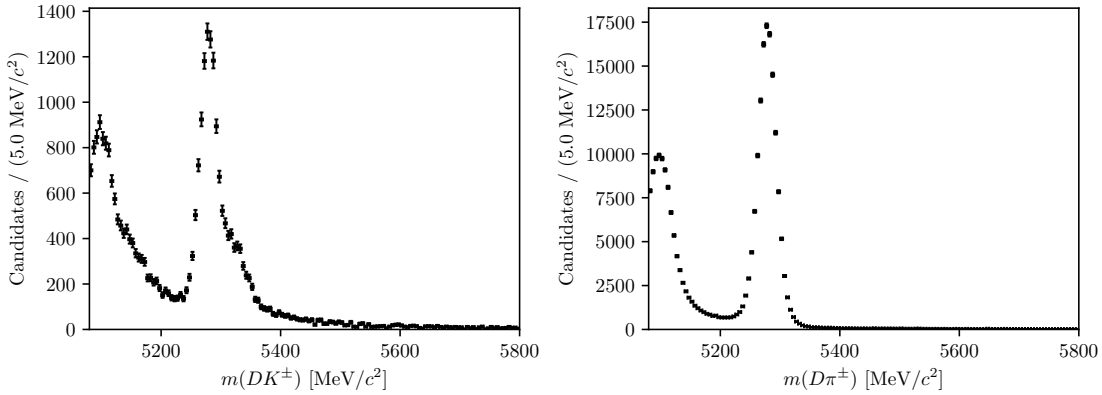


**Figure 5.5:** The spectrum of  $m_B$  in the (left)  $B^\pm \rightarrow DK^\pm$  and (right)  $B^\pm \rightarrow D\pi^\pm$  samples where  $D \rightarrow K_S^0\pi^+\pi^-$  and the  $K_S^0$  meson is reconstructed in the DD category, after the full selection has been applied. The spectra in other data categories look similar; they can be seen in Figs. 5.33 and 5.34 along with projections of the fit model described in Section 5.4 superimposed.

This requirements results in the removal of less than 0.7% of candidates in each data category.

Furthermore, the  $D$  mass value used to define the binning schemes described in Ref. [70] differs slightly from the value used in the refit of each signal decay chain with kinematic constraints applied. Therefore, a few of the decays are reconstructed with Dalitz coordinates outside the allowed kinematic region. This problem concerns less than 0.5% (1%) of candidates in the  $D \rightarrow K_S^0\pi^+\pi^-$  ( $D \rightarrow K_S^0K^+K^-$ ) channel and they are simply discarded. The  $B^\pm \rightarrow DK^\pm$  and  $B^\pm \rightarrow D\pi^\pm$  channels are equally affected, and therefore the effect is inherently taken into account in the analysis, similarly to other phase-space-dependent acceptance effects.

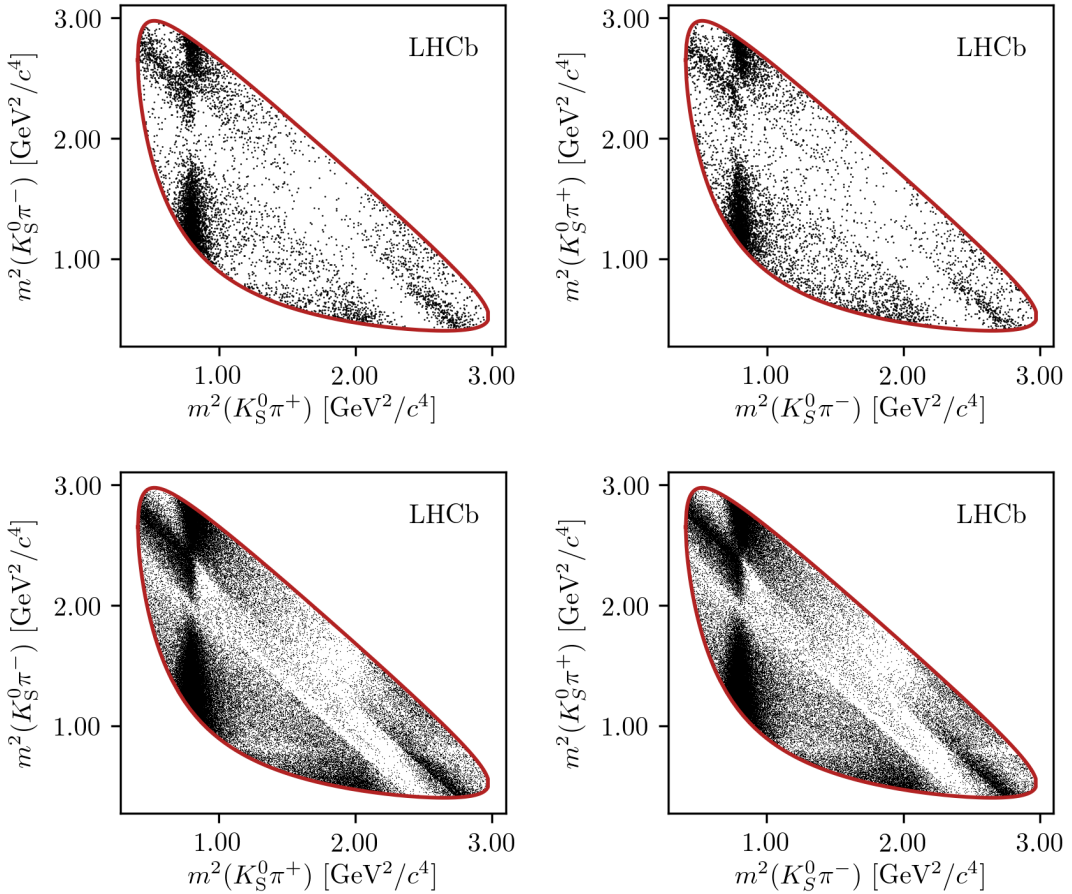


**Figure 5.6:** Dalitz plots of (left)  $B^+ \rightarrow Dh^+$  and (right)  $B^- \rightarrow Dh^-$  candidates in the signal region, in the (top)  $B^\pm \rightarrow DK^\pm$  and (bottom)  $B^\pm \rightarrow D\pi^\pm$  channels where  $D \rightarrow K_S^0\pi^+\pi^-$ . The LL and DD categories have been combined.

### 5.1.5 Selected candidates

In total, about 47,000  $B^\pm \rightarrow DK^\pm$  candidates and 400,000  $B^\pm \rightarrow D\pi^\pm$  candidates are selected, as summarised in Table 5.3. An example of the  $B$  mass distribution in one of the data categories is shown in Fig. 5.5. It is clear that a significant number of these candidates are background decays, including a visible shoulder on the signal peak in the sample of  $B^\pm \rightarrow DK^\pm$  candidates, due to misidentified  $B^\pm \rightarrow D\pi^\pm$  decays.

The Dalitz plots for candidates in the signal region where  $m_B \in [5249, 5309] \text{ MeV}/c^2$  are shown in Fig. 5.6 and 5.7. Due to the large yields in the full Run 1 and 2 LHCb data set, the asymmetries between the  $B^+$  and  $B^-$  distributions are visible to the eye in the  $B^\pm \rightarrow DK^\pm$  plots.

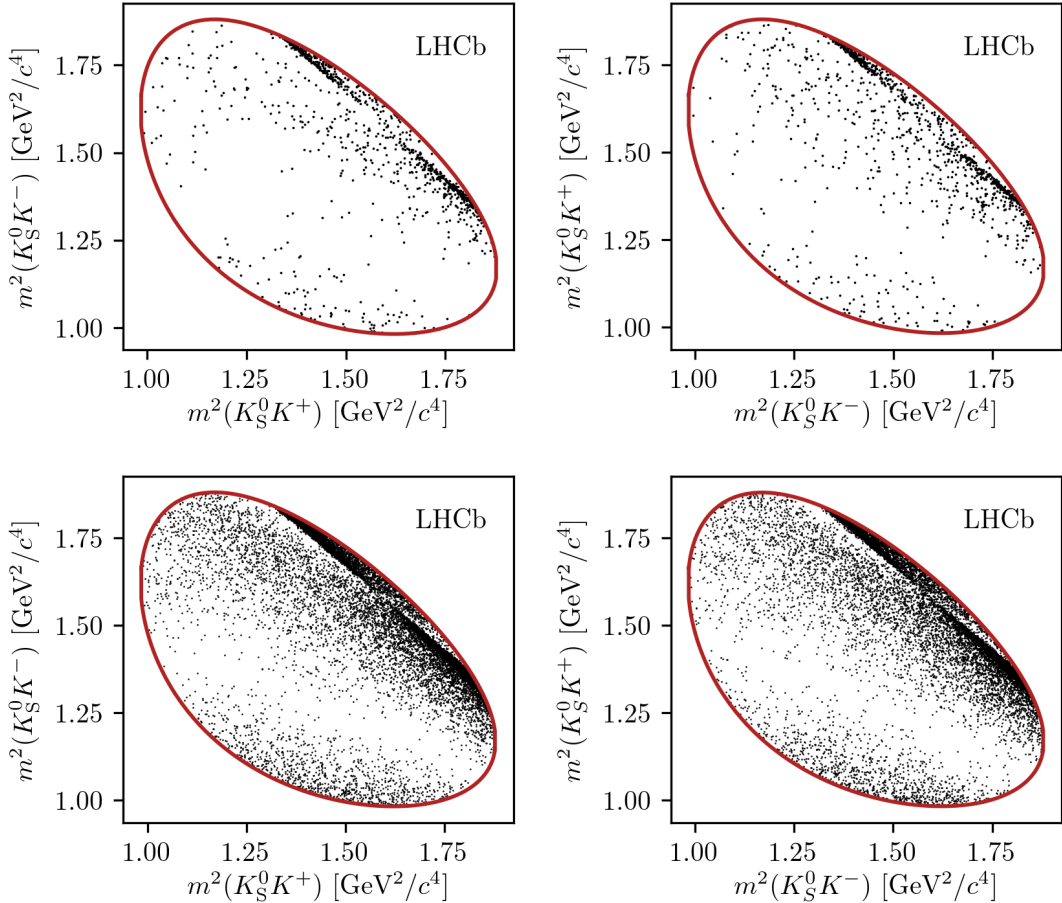


**Figure 5.7:** Dalitz plots of (left)  $B^+ \rightarrow Dh^+$  and (right)  $B^- \rightarrow Dh^-$  candidates in the signal region, in the (top)  $B^\pm \rightarrow DK^\pm$  and (bottom)  $B^\pm \rightarrow D\pi^\pm$  channels where  $D \rightarrow K_S^0 K^+ K^-$ . The LL and DD categories have been combined.

## 5.2 Signal selection efficiencies

The efficiency of each step of the selection on signal decays can be investigated using simulated decays. In the  $B^\pm \rightarrow D\pi^\pm$  channel, only decays that were placed in the "test" sample when training the BDT are used, in order to avoid overestimating the efficiency.

In general, the total selection efficiency up until the PID requirements, including the offline stage and the effect of the geometrical LHCb acceptance, is about 1 permille, slightly higher for  $B^\pm \rightarrow DK^\pm$  than  $B^\pm \rightarrow D\pi^\pm$  decays, slightly higher for  $D \rightarrow K_S^0 K^+ K^-$  than  $D \rightarrow K_S^0 \pi^+ \pi^-$  decays, and somewhat higher in the Run 2 than in Run 1 due to improvements in the trigger. The PID requirements are investigated separately in Section 5.2.1 below, using samples of calibration data. The overall selection efficiency does not impact the measurement at all, because the observables of interest are sensitive *only* to the distribution of decays over the

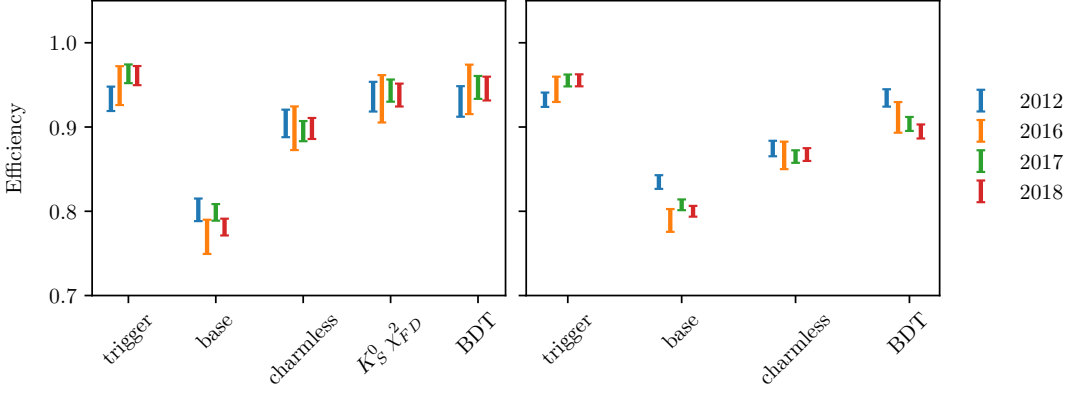


**Figure 5.8:** The efficiency of each selection step in samples of simulated  $B^\pm \rightarrow D(\rightarrow K_S^0 \pi^+ \pi^-) \pi^\pm$  signal decays in the (left) LL and (right) DD categories. The selection steps are applied on top of each other, from left to right on the horizontal axis, and the shown efficiency of each step is for candidates that have passed all preceding requirements. Further, all candidates were required to have been successfully reconstructed and to have passed the stripping stage; thus the efficiency of these stages of the selection are not included in the plotted efficiencies.. The samples are split by year.

Dalitz plot (except, of course, in the sense that a higher signal efficiency is desirable because it leads to larger signal yields). Likewise, it makes no difference that the overall selection efficiencies differ slightly between  $B^\pm \rightarrow DK^\pm$  and  $B^\pm \rightarrow D\pi^\pm$  decays, as long as the efficiency profile over the Dalitz plot is identical between the two decay channels. This is confirmed separately in Section 5.2.2 below.

The efficiencies of each individual selection step are shown in Fig. 5.8, obtained using simulated  $B^\pm \rightarrow D\pi^\pm$  decays. The main reason that some signal decays do not survive the base requirements is the removal of candidates for which  $p_{\text{companion}} > 100 \text{ GeV}/c$ , done to ensure that the PID performance for the companion is good. For the removed decays, only about 60 % of  $B^\pm \rightarrow DK^\pm$  decays survive the subsequent  $\text{PID}K > 4$  requirement and the cross-feed from misidentified  $B^\pm \rightarrow D\pi^\pm$  decays is 50 % larger than in the current selection. Thus, loosening this requirement leads to little statistical gain, while leading to larger systematic effects from the crossfeed background.

An equivalent plot for the combinatorial background is shown in Fig. 5.9, using  $B^\pm \rightarrow D(\rightarrow K_S^0 \pi^+ \pi^-) \pi^\pm$  candidates in data with a reconstructed  $B$  mass above  $5600 \text{ MeV}/c^2$ ; it can be seen that the BDT is very efficient at rejecting combinatorial background, but that the base requirements and the requirement on the  $K_S^0$  flight distance also remove a decent amount of background.

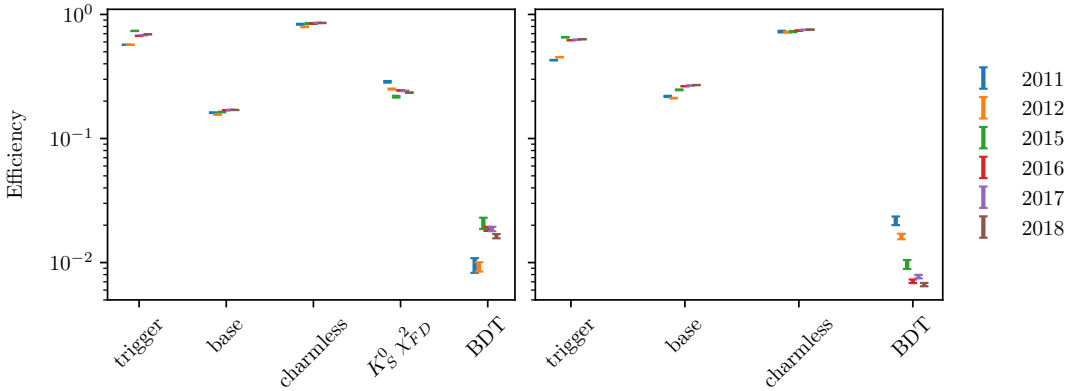


**Figure 5.9:** The efficiency of each selection step in samples of  $B^\pm \rightarrow D(\rightarrow K_s^0 \pi^+ \pi^-) \pi^\pm$  candidates in data where the reconstructed  $B$  mass is above  $5600 \text{ MeV}/c^2$ , meaning the candidates stem from combinatorial background. The efficiency is shown for candidates in the (left) LL and (right) DD categories. The selection steps are applied on top of each other, from left to right on the horizontal axis, and the shown efficiency of each step is for candidates that have passed all preceding requirements. Since the plotted efficiencies are from candidates in real data, all candidates were required to have been successfully reconstructed and to have passed the stripping stage; thus the efficiency of these stages of the selection are not included in the plotted efficiencies. The samples are split by year. Notice the logarithmic scale on the vertical axis.

### 5.2.1 Efficiency of the PID requirements

The efficiencies of the PID requirements on the companion enter the yield parameterisations of the mass fits in Section 5.4 and 5.5 and must therefore be known. They are determined using samples of calibration data selected without relying on PID variables, as implemented in the `PIDCalib` frame work [144]. Reasonably pure samples of pion and kaon tracks are obtained from  $D^0 \rightarrow K^- \pi^+$  decays, where the  $D$  meson originates in a  $D^{*+} \rightarrow D^0 \pi^+$  decay and can therefore be flavour tagged. The remaining background is subtracted via the `sPlot` [145] procedure (described in some detail in Section 5.4.2), based on a two-dimensional fit of the  $m(K^- \pi^+)$  and  $m(D^0 \pi^+) - m(D^0)$  distributions. The obtained weights are employed to calculate the average efficiency of the requirement on PIDK for a number of bins in the momentum and pseudorapidity of the calibration tracks, and the number of charged tracks in the detector, thus constructing a three-dimensional efficiency lookup table. The procedure is carried out for each PID requirement, companion species, data-taking year, track charge, and magnet polarity. Based on these tables, expected PID efficiencies for the  $B^\pm \rightarrow D\pi^\pm$  and  $B^\pm \rightarrow DK^\pm$  signal decays are calculated that take the kinematical distribution and detector occupancy in the BPGGSZ data samples into account, by using the high-purity sample of  $B^\pm \rightarrow D\pi^\pm$  candidates in the signal region as a reference. The dominating uncertainty on the efficiencies

**Table 5.4:** PID efficiencies obtained with the `PIDCalib` tool. The uncertainty incorporates statistical uncertainty due to the size of the reference sample, the systematic uncertainty due to the choice of binning scheme in `PIDCalib`, and a systematic uncertainty due to the `sWeight` calculation in `PIDCalib` of 0.1 %.

| Efficiency   | Particle | $D$ final state                   | $\varepsilon_{\text{PID}}$ (%) |                  |
|--------------|----------|-----------------------------------|--------------------------------|------------------|
|              |          |                                   | LL                             | DD               |
| Run I and II |          |                                   |                                |                  |
| Correct ID   | Kaon     | $D \rightarrow K_S^0 \pi^+ \pi^-$ | $86.74 \pm 0.13$               | $86.90 \pm 0.22$ |
|              |          | $D \rightarrow K_S^0 K^+ K^-$     | $86.22 \pm 0.26$               | $86.56 \pm 0.30$ |
|              | Pion     | $D \rightarrow K_S^0 \pi^+ \pi^-$ | $97.11 \pm 0.11$               | $97.17 \pm 0.13$ |
|              |          | $D \rightarrow K_S^0 K^+ K^-$     | $97.07 \pm 0.11$               | $97.16 \pm 0.14$ |

is statistical in nature, due to the finite size of the reference sample. In addition, systematic uncertainties are included due to the fit procedure used by `PIDCalib`, estimated at 0.1 % [144], and due to the choice of binning scheme, estimated by repeating the procedure using a number of alternative binning schemes. The final estimates of the correct-ID efficiencies,  $\varepsilon_{\text{PID}}$ , are shown in Table 5.4, including all sources of uncertainty. Note that the probability to misidentify a decay satisfies  $\varepsilon_{\text{mis-ID}} = 1 - \varepsilon_{\text{PID}}$  by construction, due to the the definition of the `PIDK` variable (given in Section 3.2.2) and the chosen PID requirement.

### 5.2.2 Efficiency profile over the Dalitz plot

The analysis strategy depends on sharing the  $F_i$  parameters between the  $B \rightarrow D\pi$  and  $B \rightarrow DK$  channels. This is reasonable, since the phase-space dependence of the reconstruction efficiency is expected to be very similar between the two decays, given the similar kinematics; an assumption that is verified using samples of simulated decays. The full selection is applied to the samples. The  $B \rightarrow D\pi$  sample of LL (DD) candidates includes about 63,000 (146,000) simulated decays, and the  $B \rightarrow DK$  samples include 60,000 (142,000) simulated decays. For the  $B \rightarrow D\pi$  mode, this is approximately equal to the number of decays in the full Run 1+2 data sample, and for  $B \rightarrow DK$  this is a factor of about 12 larger than the data sample. The decays were simulated with an equal decay probability across the  $D$ -decay phase space, so that any non-uniform distribution of reconstructed decays is completely determined by a phase-space dependent reconstruction and selection efficiency. Therefore the assumption that the phase-space dependence is identical between the  $B \rightarrow D\pi$  and  $B \rightarrow DK$  channels is verified by investigating whether the Dalitz coordinates are distributed differently between the samples of simulated  $B \rightarrow D\pi$  and  $B \rightarrow DK$  decays.

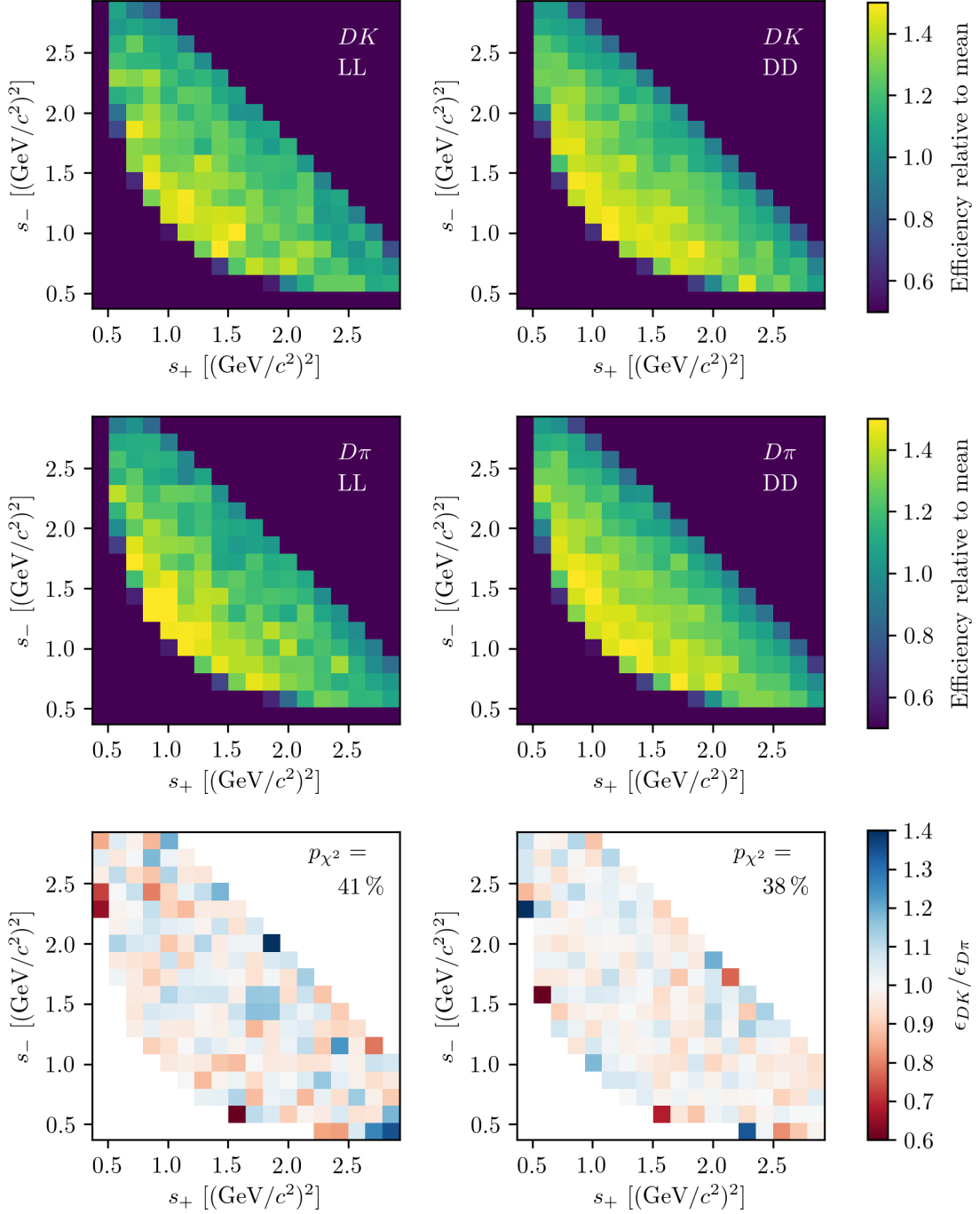


**Figure 5.10:** The acceptance profile in simulated samples of (top row)  $B \rightarrow DK$  decays and (centre row)  $B \rightarrow D\pi$  decays where  $D \rightarrow K_S^0\pi^+\pi^-$ , as well as (bottom row) the ratio between the two histograms. The plots are shown for candidates in the (left) LL and (right) DD categories. The  $p$  values are the results of  $\chi^2$  compatibility tests between the two histograms.

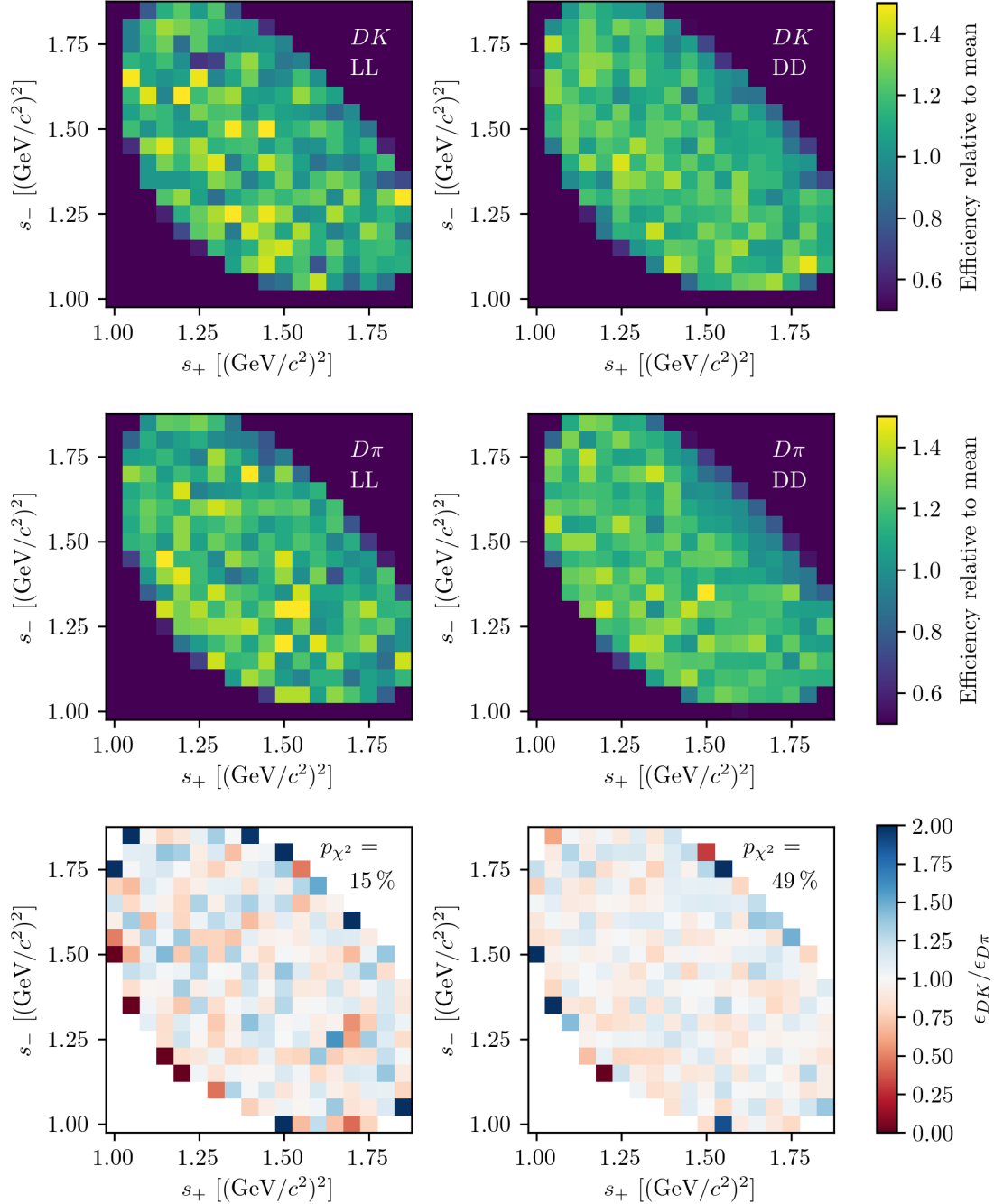


**Figure 5.11:** The acceptance profile in simulated samples of (top row)  $B \rightarrow DK$  decays and (centre row)  $B \rightarrow D\pi$  decays where  $D \rightarrow K_S^0 K^+ K^-$ , as well as (bottom row) the ratio between the two histograms. The plots are shown for candidates in the (left) LL and (right) DD categories. The  $p$  values are the results of  $\chi^2$  compatibility tests between the two histograms.

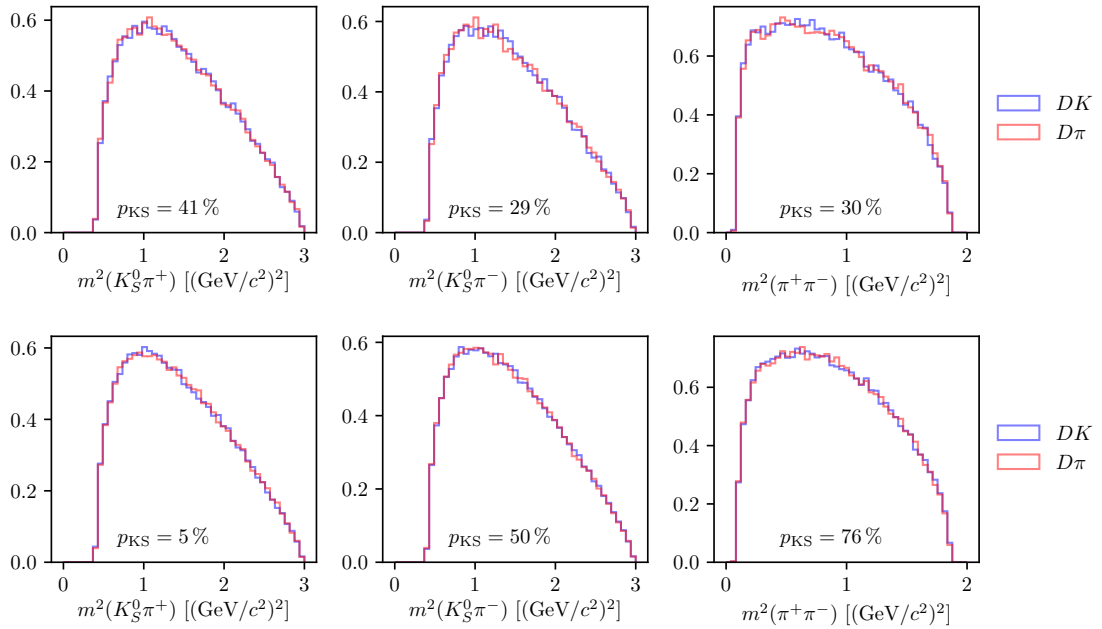


**Figure 5.12:** One-dimensional distributions of  $m^2(K_S^0\pi^+)$ ,  $m^2(K_S^0\pi^-)$ , and  $m^2(\pi^+\pi^-)$  in simulated (blue)  $B^\pm \rightarrow DK^\pm$  and (red)  $B^\pm \rightarrow D\pi^\pm$  decays where  $D \rightarrow K_S^0\pi^+\pi^-$  in the (top) LL and (bottom) DD categories. The  $p$  values are the results of Kolmogorov-Smirnov compatibility tests between the distributions.

This is investigated with two statistical tests. The first is a  $\chi^2$  comparison of two-dimensional histograms of the distribution of  $m^2(K_S^0 h^+)$  and  $m^2(K_S^0 h^-)$  in the different  $B \rightarrow D\pi$  and  $B \rightarrow DK$  channels. These histograms, and the ratio between them, are shown in Figs. 5.10 and 5.11, along with the  $p$ -values from the  $\chi^2$  tests. It can be seen that, in all cases, the probability of obtaining the two histograms assuming that they share the same underlying distribution has a reasonable value, and that there is no clear trend in the ratio plots. The second test is a Kolmogorov-Smirnov test [146] of the compatibility of the one-dimensional distributions of  $m^2(K_S^0 h^+)$ ,  $m^2(K_S^0 h^-)$ , and  $m^2(h^+h^-)$ . These distributions, and the corresponding  $p$ -values, are shown in Fig. 5.12 and 5.13. Again, all the  $p$  values are reasonable. Therefore, it is concluded that there are no statistically significant differences between the phase-space dependence of the reconstruction and selection efficiency between the  $B \rightarrow D\pi$  and  $B \rightarrow DK$  channels, given the present sample sizes. Because the simulation samples have approximately the same amount of decays as data (or significantly more, in the  $B \rightarrow DK$  case), any potential differences will be negligible with data yields. Thus, sharing the  $F_i$  parameters between the  $B \rightarrow D\pi$  and  $B \rightarrow DK$  channels is viable, and no efficiency correction is necessary.

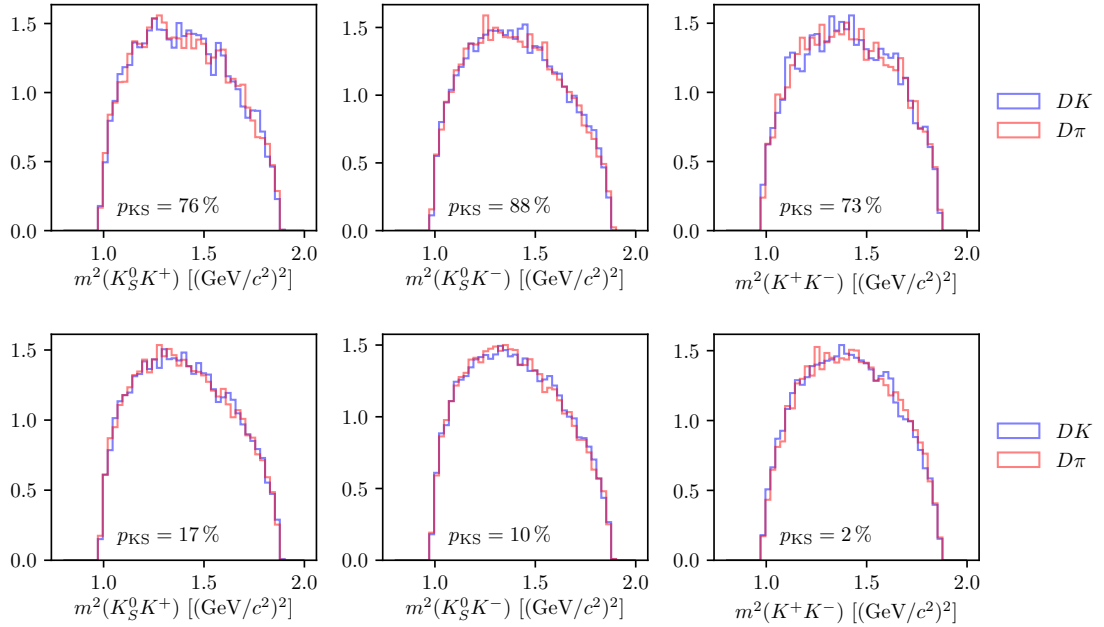


**Figure 5.13:** One-dimensional distributions of  $m^2(K_S^0 K^+)$ ,  $m^2(K_S^0 K^-)$ , and  $m^2(K^+ K^-)$  in simulated (blue)  $B^\pm \rightarrow DK^\pm$  and (red)  $B^\pm \rightarrow D\pi^\pm$  decays where  $D \rightarrow K_S^0 K^+ K^-$  in the (top) LL and (bottom) DD categories. The  $p$  values are the results of Kolmogorov-Smirnov compatibility tests between the distributions.

### 5.3 Background studies

A wide range of backgrounds can potentially pollute the sample of signal candidates. The backgrounds group into three categories depending on how they are treated in the analysis:

- backgrounds that can be effectively removed in the selection,
- backgrounds that are only present at a level where the impact on the measurement result is small, and which do therefore not have to be modelled, and
- backgrounds that are present at a level where they have to be modelled in the fit to data, and cannot effectively be rejected further in the selection.

The latter category comprises of combinatorial background, which remains present at a non-negligible level after the application of the BDT described in Section 5.1.2; contributions from a number of partly reconstructed  $B \rightarrow Dh^\pm X$  decays, where  $X$  denotes a pion or photon that is not included in the reconstructed decay, and which can only be separated from signal decays by their  $m(Dh)$  distribution; and

finally  $B^\pm \rightarrow D\pi^\pm$  decays that are categorised as  $B^\pm \rightarrow DK^\pm$  decays in the particle-identification step and vice-versa. These background sources are described in detail in Section 5.4. This section focuses on backgrounds that led to specific requirements in the selection or proved to be small enough to not merit special treatment.

### 5.3.1 Charmless decays

There is potentially a so-called *charmless* background present in data, consisting of  $B^\pm \rightarrow K_S^0 h^+ h^- h'^\pm$  decays. These have the same final state as the signal decay, but no intermediate  $D$  meson. Because all final state particles are reconstructed, this background peaks in the  $B$  mass spectrum. This background is suppressed by requiring the reconstructed  $B$  and  $D$  decay vertices to be separated in the  $z$  direction; specifically by requiring that  $\Delta z_{\text{significance}}^{D-B} > 0.5$ , where  $\Delta z_{\text{significance}}^{D-B}$  was defined in Eq. (5.1). The remaining background level can be investigated by investigating the  $D$  mass sidebands.

However, the use of the `DecayTreeFitter`  $\chi^2_{\text{DTF}}$  as an input variable in the BDT *removes* essentially all of the  $D$  (and  $K_S^0$ ) sideband, due to the mass constraints in the decay chain fit. Therefore separate BDT's are trained for LL and DD candidates without the  $\chi^2_{\text{DTF}}$  as an input variable, and used when selecting candidates for the background studies presented in this section, and the following. In a similar manner, all mass window requirements are made on the *default* reconstructed masses, obtained with no use of `DecayTreeFitter`. The overlap of the two sets of selected candidates in the signal  $B$ -mass window is above 95 %.

The reconstructed  $B$  mass spectrum is shown for  $B^\pm \rightarrow D\pi^\pm$  candidates in the  $D$  sidebands in Fig. 5.14, both before and after making a requirement on  $\Delta z_{\text{significance}}^{D-B}$ . The check is based on the upper  $D$  sideband for  $D \rightarrow K_S^0 \pi^+ \pi^-$  decays and the lower  $D$  sideband for  $D \rightarrow K_S^0 K^+ K^-$  decays to avoid contamination from real  $B^\pm \rightarrow Dh^\pm$  decays with subsequent  $D \rightarrow K_S^0 K^\pm \pi^\mp$  decays, or crossfeed between the two signal  $D$ -decay modes. A peak is clearly visible, the size of which is reduced by the requirement. This peak is partly due to a contribution from  $B^\pm \rightarrow K_S^0 \pi^+ \pi^- \pi^\pm$  decays ( $B^\pm \rightarrow K_S^0 K^+ K^- \pi^\pm$  decays) in the  $D \rightarrow K_S^0 \pi^+ \pi^-$  ( $D \rightarrow K_S^0 K^+ K^-$ ) channel, and partly due to real signal decays that leak into the  $D$  sidebands. The number of real signal decays can be calculated from the yield obtained in the fit of Section 5.4, and the reconstructed  $m_D$  distribution in simulated signal decays. Subtracting this contribution, it is estimated that approximately 450 (200) charmless decays are present in the  $K_S^0 \pi^+ \pi^-$  ( $K_S^0 K^+ K^-$ ) data samples. In similar fashion, Fig. 5.15 shows the  $m_B$  spectra for  $B^\pm \rightarrow DK^\pm$  candidates in the  $D$  sidebands. In these plots, the peaks are at  $m_B$  values that are lower (higher) than the  $B$  mass in the  $K_S^0 \pi^+ \pi^-$

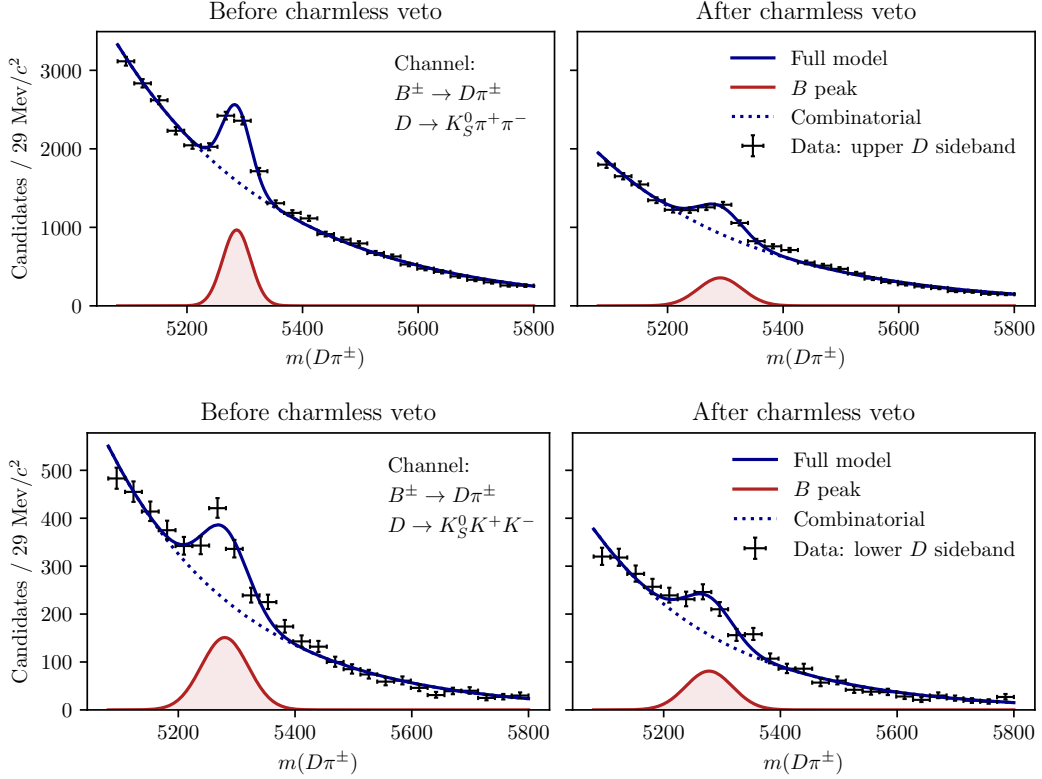


**Figure 5.14:** The  $B$  mass distribution of (top)  $B^\pm \rightarrow D(\rightarrow K_S^0 \pi^+ \pi^-)\pi^\pm$  and (bottom)  $B^\pm \rightarrow D(\rightarrow K_S^0 K^+ K^-)\pi^\pm$  candidates reconstructed in both the LL and DD categories, residing in the upper  $D$  mass sideband  $m_D \in [1910, 1960] \text{ MeV}/c^2$  for  $D \rightarrow K_S^0 \pi^+ \pi^-$  and in the lower sideband  $m_D \in [1910, 1960] \text{ MeV}/c^2$  for  $D \rightarrow K_S^0 K^+ K^-$ , with (left) no requirement on  $\Delta z_{\text{significance}}^{BD}$  and (right) after a requirement of  $\Delta z_{\text{significance}}^{BD} > 0.5$ .

( $K_S^0 K^+ K^-$ ) categories, because they stem from real  $B^\pm \rightarrow K_S^0 K^+ K^- \pi^\pm$  decays where a kaon is mis-reconstructed as a pion or a pion is misreconstructed as a kaon, respectively. The total contribution of charmless decays in the  $B^\pm \rightarrow DK^\pm$  data samples is estimated to be about 200 decays. As described further in Section 5.6.11, the presence of a charmless background at these levels has a negligible impact on the measurement results. It is not favourable to tighten the requirement further due to the associated loss in the selection efficiency of signal decays.

### 5.3.2 Background from four-body $D$ decays

A similar potential background is from real  $B^\pm \rightarrow Dh^\pm$  decays where the  $D$  meson decays directly to the  $\pi^+ \pi^- h^+ h^-$  final state, without an intermediate  $K_S^0$  meson. This background can be investigated by looking for a peak in the  $B$  mass spectrum for candidates in the  $K_S^0$  sideband, as illustrated in Fig. 5.16. The figure shows the spectrum in the final data sample, illustrating the significant

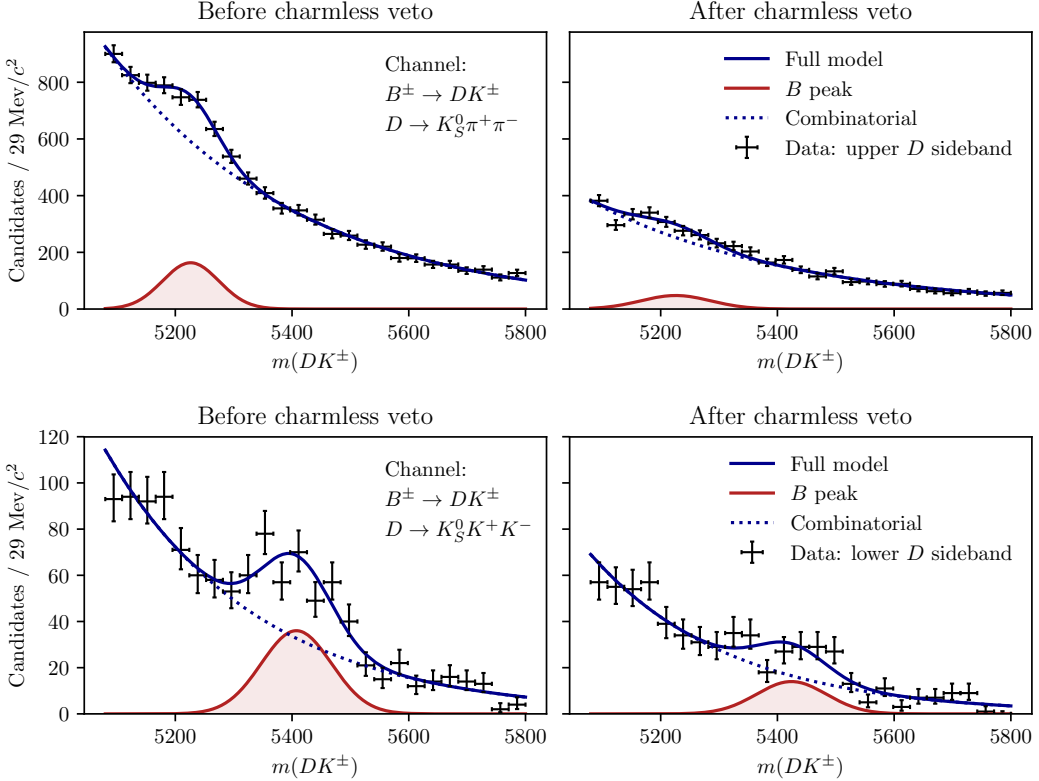


**Figure 5.15:** The  $B$  mass distribution of (top)  $B^\pm \rightarrow D(\rightarrow K_S^0 \pi^+ \pi^-)K^\pm$  and (bottom)  $B^\pm \rightarrow D(\rightarrow K_S^0 K^+ K^-)K^\pm$  candidates reconstructed in both the LL and DD categories, residing in the upper  $D$  mass sideband  $m_D \in [1910, 1960] \text{ MeV}/c^2$  for  $D \rightarrow K_S^0 \pi^+ \pi^-$  and in the lower sideband  $m_D \in [1910, 1960] \text{ MeV}/c^2$  for  $D \rightarrow K_S^0 K^+ K^-$ , with (left) no requirement on  $\Delta z_{\text{BD}}^{\text{significance}}$  and (right) after a requirement of  $\Delta z_{\text{significance}}^{\text{BD}} > 0.5$ .

effect of making the requirement on the  $K_S^0$  flight distance that was discussed in Section 5.1.1. The BDT that does *not* rely on the DTF  $\chi_{\text{DTF}}^2$  has been used to suppress combinatorial background. The remaining peak after requiring  $\chi_{\text{FD}}^2 > 49$  is completely accounted for by real signal decays that leak into the  $K_S^0$  sideband. The requirement is made for candidates in the LL category only; if the pions stemming from a  $K_S^0$  candidate are reconstructed as downstream tracks it implies that the  $K_S^0$  has travelled from the interaction region.

### 5.3.3 Semi-leptonic backgrounds

The data sample has a minor background from  $B \rightarrow D\mu\nu_\mu X$  decays, visible in the  $B$  mass spectrum when the companion is required to satisfy `isMuon=1`. This is shown in Fig. 5.17 for both the  $B^\pm \rightarrow DK^\pm$  and  $B^\pm \rightarrow D\pi^\pm$  channels where  $D \rightarrow K_S^0 \pi^+ \pi^-$ . The  $B$  mass spectra for simulated  $B^\pm \rightarrow D\mu^\pm \nu_\mu$  decays reconstructed in each category are also shown, from simulation samples produced via

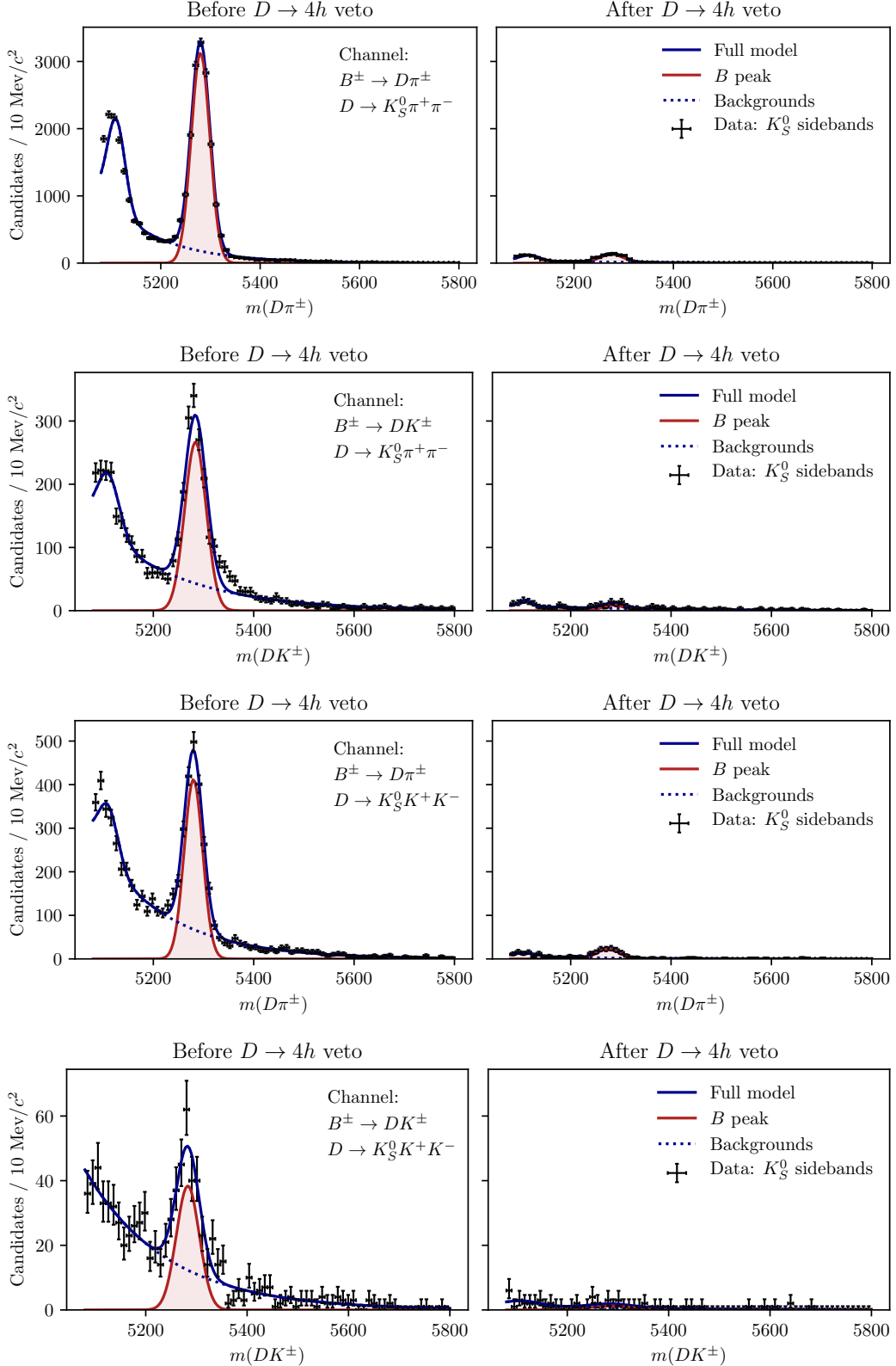


**Figure 5.16:** The  $B$  mass spectrum in the  $K_S^0$  sideband where  $m_{K_S^0} \in [467, 482] \text{ MeV}/c^2$  or  $m_{K_S^0} \in [512, 527] \text{ MeV}/c^2$  (left) without a requirement on the  $K_S^0$  flight distance significance, and (right) after the requirement implemented in the analysis.

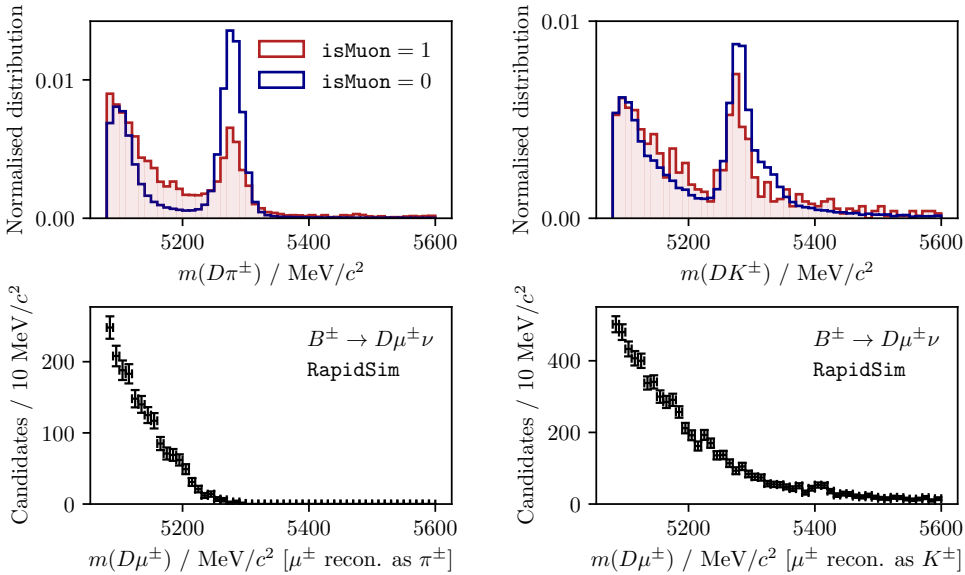


**Figure 5.17:** (Top) The  $m_B$  spectra in data split by the value of `isMuon` for the companion particle, in (left) the  $D\pi^\pm$  and (right) the  $DK^\pm$  samples where  $D \rightarrow K_S^0\pi^+\pi^-$ . The two histograms are normalised independently, so that the distributions can be compared. The fractions of candidates in data (with  $m_B \in [5080, 5800] \text{ MeV}/c^2$ ) where the companion satisfies `isMuon=1` are 1.6 % and 1.8 % for the  $D\pi^\pm$  and  $DK^\pm$  channels respectively. (Bottom) the `RapidSim` mass spectra for  $B^\pm \rightarrow D^0\mu^\pm\nu_\mu$  decays reconstructed in the (left)  $D\pi^\pm$  and (right)  $DK^\pm$  categories.

`RapidSim`. The background is very efficiently vetoed by requiring `isMuon=0` on the companion. This requirement removes approximately 85 % of the background decays, as estimated using the `PIDCalib` calibration samples and the  $(p, p_T)$  distribution for the muon in the `RapidSim` samples. The fraction of signal candidates for which the companion satisfies `isMuon=1` in simulated signal samples is  $\leq 0.9\%$  so the impact on the signal yield is small.

The analogous  $B \rightarrow D\nu_e X$  background is investigated by inspecting the  $B$  mass spectra after making requirements on `PIDe` for the companion candidate, but a presence of the semi-leptonic background in data is not visible and no electron veto is applied to the companion.

### Background from semi-leptonic D decays

There is a potential background from real  $B^\pm \rightarrow Dh^\pm$  decays where the  $D$  meson decays semi-leptonically:  $D^0 \rightarrow K_S^0\pi^-\ell^+\nu_\ell$ . This background is particularly dangerous because it peaks at the  $B$  mass, when the  $D$ -mass requirement is applied and it is reconstructed in the  $D \rightarrow K_S^0\pi^+\pi^-$  category. This is illustrated in

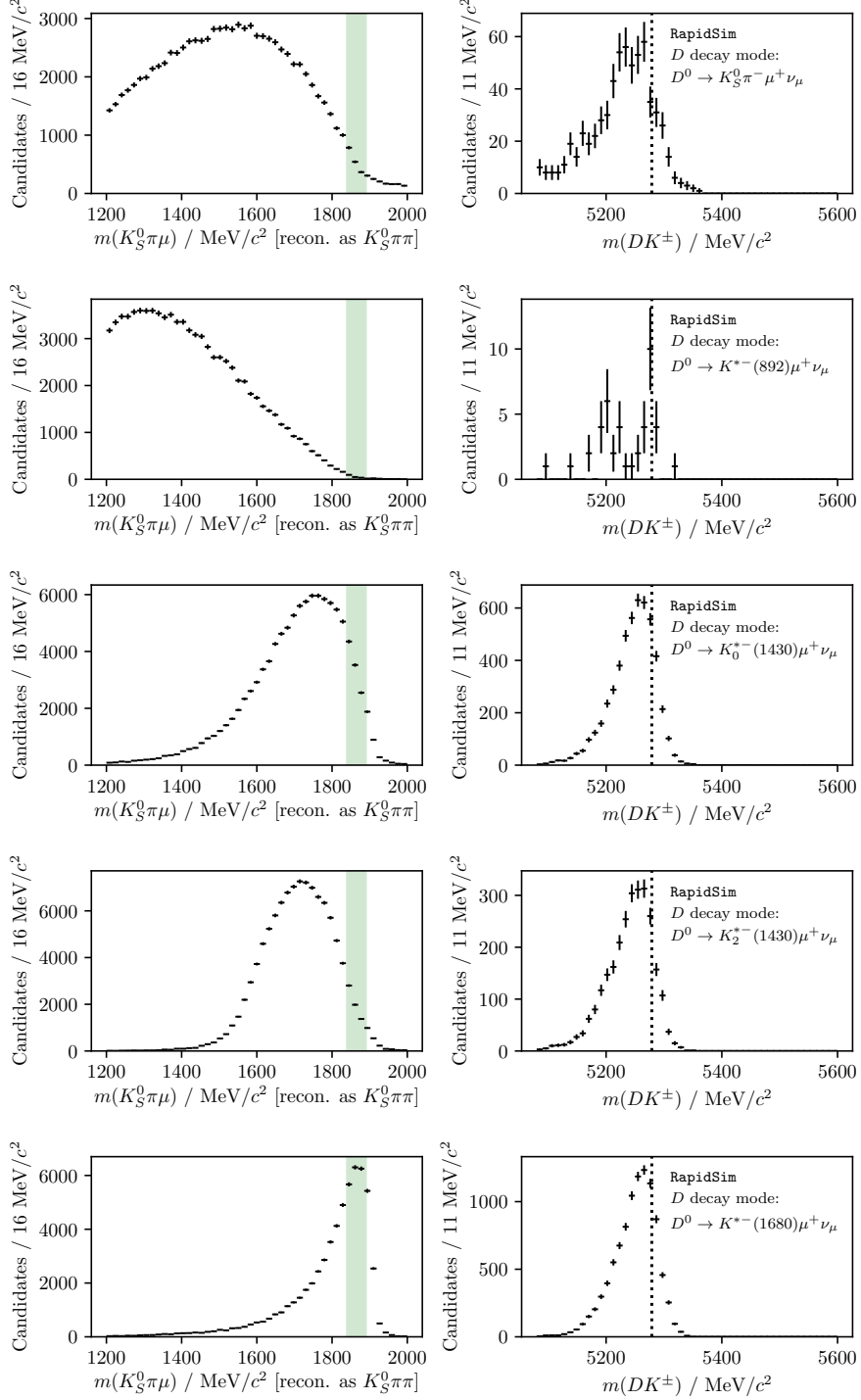


**Figure 5.18:** The reconstructed (left)  $m(K_S^0 \pi^+ \pi^-)$  and (right)  $m(DK^\pm)$  distributions in **RapidSim** samples of  $B^\pm \rightarrow DK^\pm$  decays where  $D^0 \rightarrow K_S^0 \pi^- \mu^+ \nu_\mu$ . The top plot is for decays that were uniformly distributed over phase space, and the following plots show the distribution where the  $K_S^0 \pi^-$  originate in the resonances  $K^{*-}(892)$ ,  $K_0^{*-}(1430)$ ,  $K_2^{*-}(1430)$ , and  $K^{*-}(1680)$ . The shapes for the  $D^0 \rightarrow K_S^0 \pi^- e^+ \nu_e$  case are almost identical.

Fig. 5.18 using **RapidSim** samples of  $B^\pm \rightarrow D(\rightarrow K^{*-}(\rightarrow K_S^0\pi^-)\ell^+\nu_\ell)h^\pm$  decays for  $K^* \in \{K^*(892), K_0^*(1430), K_2^*(1430), K^*(1680)\}$ . The correct spin of each resonance is taken into account in generation, by handling the decay via **EVTGEN**. The expected background yields relative to signal can be estimated by applying the  $B$  and  $D$  mass cuts to decays in the **RapidSim** samples, and using the relative branching ratios. Only the  $D^0 \rightarrow K^{*-}(892)\ell\nu_\ell$  branching fractions have been measured [28], but there is no reason to expect that higher  $K^*$  resonances should not contribute. To estimate their potential contribution, the branching ratios are approximated by

$$\text{BR}[D^0 \rightarrow K^{*-}(X)(\rightarrow K_S^0\pi^-)\ell\nu_\ell] \simeq \frac{\text{BR}[D^0 \rightarrow K^{*-}(X)(\rightarrow K_S^0\pi^-)\pi^+]}{\text{BR}[D^0 \rightarrow K^{*-}(892)(\rightarrow K_S^0\pi^-)\pi^+]} \text{BR}[D^0 \rightarrow K^{*-}(892)(\rightarrow K_S^0\pi^-)\ell\nu_\ell]$$

because all the relevant  $D^0 \rightarrow K^{*-}(\rightarrow K_S^0\pi^-)\pi^+$  branching fractions are known [28]. The efficiencies and branching ratios relative to the signal channel are given in Table 5.5. It is clear that the higher  $K^*$  resonances are important: the smaller branching ratios are compensated for by a higher selection efficiency, due to the smaller phase-space of the missed neutrino. The total background yield is 1.1% of the signal yield in both the  $B^\pm \rightarrow D\pi^\pm$  and  $B^\pm \rightarrow DK^\pm$  channels. However, there will be an additional contribution in the  $B^\pm \rightarrow DK^\pm$  channel from real  $B^\pm \rightarrow D\pi^\pm$  decays with semi-leptonic  $D$  decays and a mis-identification of the companion. This background also peaks, and the yield is approximately 0.4% of the  $B^\pm \rightarrow DK^\pm$  signal yield.

The potential impact from the presence of the background is estimated by

1. calculating the expected  $B^\pm \rightarrow D\pi^\pm$  and  $B^\pm \rightarrow DK^\pm$  signal yields in each bin for physics parameters similar to the world average values
2. then calculating the background bin yields in each bin, using the relative branching fractions and efficiencies described above and taking the bin-distribution from the **RapidSim** samples. The **RapidSim** samples are produced using the **ISGW2** model in **EVTGEN** [116], yielding the Dalitz distributions in Fig. 5.19.
3. adding the signal and background yields, and fitting the new  $B^\pm \rightarrow D\pi^\pm$  and  $B^\pm \rightarrow DK^\pm$  yields back with the default signal-yield expressions (including a fit of the  $F_i$  parameters)

**Table 5.5:** The selection efficiencies of  $B^\pm \rightarrow DK^\pm$  decays where  $D^0 \rightarrow K_S^0\pi^-\ell^+\nu_\ell$  when reconstructed in the  $D \rightarrow K_S^0\pi^+\pi^-$  mode in **RapidSim** relative to the signal selection efficiencies, for a number of decay modes: uniformly distributed over phase space (PHSP), as well as resonant production where the  $K_S^0\pi^-$  pair originates in one of several  $K^*$  resonances. The relative branching ratios are also shown, calculated as explained in the main text, as well as the predicted relative yields.

| Mode  | $\epsilon_{bkg}/\epsilon_{signal}$ (%) | $\Gamma_{bkg}/\Gamma_{signal}$ (%) | $N_{bkg}/N_{signal}$ (%) |
|---|--|------------------------------------|--------------------------|
| $D \rightarrow K_S^0\pi^-\mu^+\nu_\mu$ (PHSP)             | $0.92 \pm 0.05$                        | $18.3 \pm 14.8$                    | $0.17 \pm 0.14$          |
| $D \rightarrow (K_S^0\pi^-)_{K^{*-}(892)}\mu^+\nu_\mu$    | $0.06 \pm 0.01$                        | $22.3 \pm 3.2$                     | $0.013 \pm 0.003$        |
| $D \rightarrow (K_S^0\pi^-)_{K_0^{*-}(1430)}\mu^+\nu_\mu$ | $7.3 \pm 0.1$                          | $3.7 \pm 0.8$                      | $0.27 \pm 0.06$          |
| $D \rightarrow (K_S^0\pi^-)_{K_2^{*-}(1430)}\mu^+\nu_\mu$ | $3.7 \pm 0.1$                          | $0.5 \pm 0.3$                      | $0.02 \pm 0.01$          |
| $D \rightarrow (K_S^0\pi^-)_{K^{*-}(1680)}\mu^+\nu_\mu$   | $24.4 \pm 0.3$                         | $0.6 \pm 0.5$                      | $0.15 \pm 0.12$          |
| $D \rightarrow K_S^0\pi^-e^+\nu_e$ (PHSP)                 | $0.53 \pm 0.02$                        | $20.8 \pm 16.3$                    | $0.11 \pm 0.09$          |
| $D \rightarrow (K_S^0\pi^-)_{K^{*-}(892)}e^+\nu_e$        | $0.15 \pm 0.02$                        | $25.6 \pm 2.5$                     | $0.04 \pm 0.01$          |
| $D \rightarrow (K_S^0\pi^-)_{K_0^{*-}(1430)}e^+\nu_e$     | $6.3 \pm 0.1$                          | $4.2 \pm 0.8$                      | $0.26 \pm 0.05$          |
| $D \rightarrow (K_S^0\pi^-)_{K_2^{*-}(1430)}e^+\nu_e$     | $4.12 \pm 0.08$                        | $0.5 \pm 0.3$                      | $0.02 \pm 0.01$          |
| $D \rightarrow (K_S^0\pi^-)_{K^{*-}(1680)}e^+\nu_e$       | $10.0 \pm 0.2$                         | $0.7 \pm 0.5$                      | $0.07 \pm 0.05$          |
| Total   | -                                      | -                                  | $1.1 \pm 0.4$            |

The obtained biases are shown in Fig. 5.20, where they are calculated a number of times, each time varying the efficiencies within statistical uncertainties and the relevant branching fractions within the measurement uncertainties. The systematic uncertainty due to the unknown branching fractions and the use of **RapidSim** in lieu of full simulation is not included, but is of course significant. Nevertheless it is clear that the potential biases are significant compared to the size of the systematic uncertainties of the analysis presented in Section 5.6. Therefore the backgrounds are vetoed by requiring `isMuon=0` and `PIDe < 0` on the pions from the  $D$ -decay with opposite charge to the companion in the  $D \rightarrow K_S^0\pi^+\pi^-$  channel. This requirement removes 88 % of the muonic background and 99 % of the electron background, according to PID efficiencies obtained via the `PIDCalib` package, using the  $(p, p_T)$  distribution for the muon/electron in the **RapidSim** samples. The survival rate for signal decays in full simulation is 94 %, so the impact on the obtainable precision is only about 3 %. A systematic uncertainty is assigned to account for the potential remaining background.

In the  $D \rightarrow K_S^0K^+K^-$  channel an analogous study shows the relative yields to be similar. The selection efficiencies are higher, as are the relative branching ratios due to the lower  $D \rightarrow K_S^0K^+K^-$  branching fraction, but in this mode the `PIDK > -5` requirement placed on the pion and lepton removes approximately

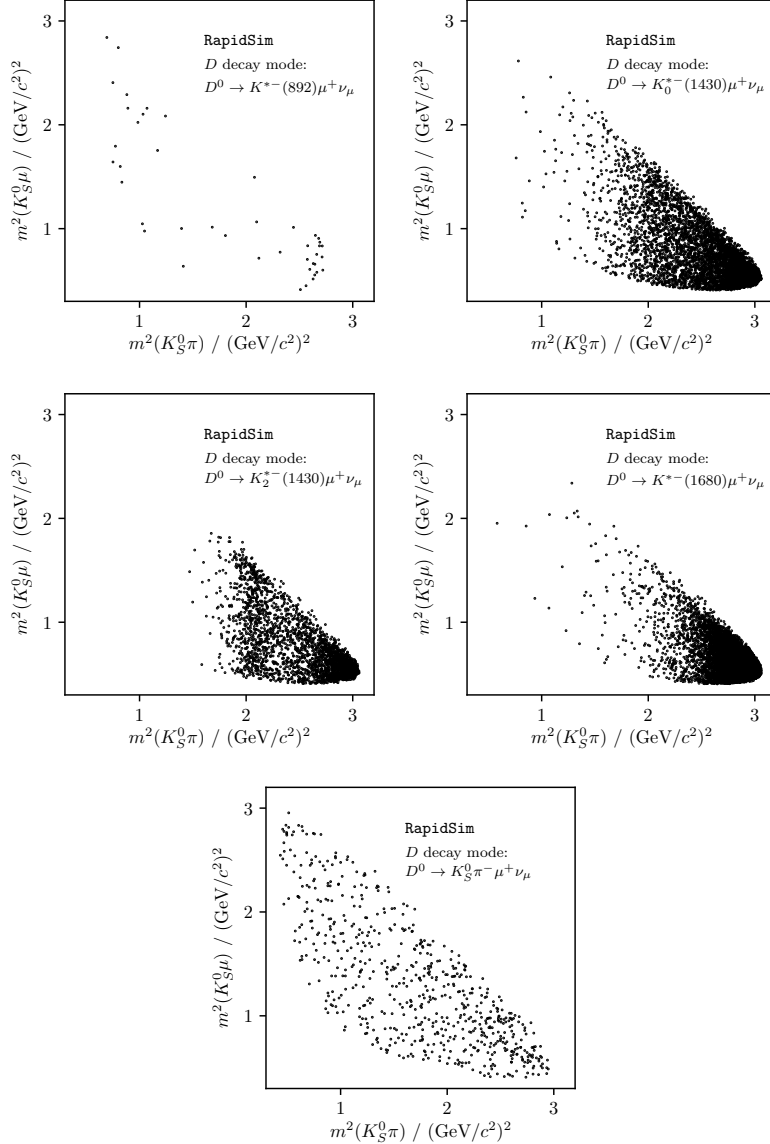


**Figure 5.19:** Dalitz plots for  $D \rightarrow K_S^0\pi\mu\nu_\mu$  decays in **RapidSim**, where the  $K_S^0\pi^-$  originate in the resonances  $K^{*-}(892)$ ,  $K_0^{*-}(1430)$ ,  $K_2^{*-}(1430)$ , and  $K^{*-}(1680)$ , as well as for a uniform distribution over phase space.

90 % of the background, leaving the relative rate similar to in  $D \rightarrow K_S^0\pi^+\pi^-$ . However, importantly, *the background is not peaking*, as shown in Fig. 5.21. The presence of a percent-level, *non-peaking* background in the  $D \rightarrow K_S^0K^+K^-$  channel is safe to ignore and thus no veto is applied to remove semileptonic  $D$  decays in the  $D \rightarrow K_S^0K^+K^-$  channel.

The muon-veto for the semi-leptonic background does remove some signal decays, where an original pion or kaon results in hits in the muon detectors. A significant contribution is from particles that decay in flight. The track quality

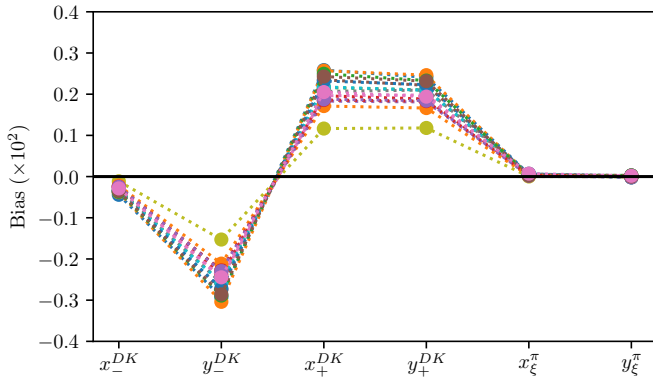


**Figure 5.20:** Estimated biases on the measured observables due to the presence of  $D \rightarrow K_S^0 \pi^\pm \ell \nu_\ell$  backgrounds, calculated while varying efficiencies and branching ratios within uncertainties.

of these decays is worse than for nominal decays, which affects the resolution on the reconstructed Dalitz coordinates. In simulated signal decays the standard deviation of  $\Delta m_\pm^2 = m_{reco}^2(K_S^0 \pi^\pm) - m_{TRUE}^2(K_S^0 \pi^\pm)$  is 50 % larger for decays where one of the  $D$ -decay products has `isMuon=1` than in decays where this is not the case. This can lead to systematic biases on the observables, as described further in Section 5.6.7. The overall effect is small, as evidenced by the systematic uncertainty described in that section; nevertheless this fact motivates removing decay-in-flight decays of the  $D$ -decay products. Therefore it is also required that `isMuon=0` for the  $D$ -decay pion with the same charge as the companion in the  $D \rightarrow K_S^0 \pi^+ \pi^-$  channels, and on the  $D$ -decay kaons in the  $D \rightarrow K_S^0 K^+ K^-$  channels. This veto removes about 2 % of signal candidates in simulation that survive the lepton vetoes described in the previous sections.

### 5.3.4 Cross-feed from other $D \rightarrow K_S^0 h^+ h^-$ decays

Misidentification of a  $D$  decay product can lead to background from cross-feed between the  $B^\pm \rightarrow D(\rightarrow K_S^0 \pi^+ \pi^-)h^\pm$  and  $B^\pm \rightarrow D(\rightarrow K_S^0 K^+ K^-)h^\pm$  signal channels, or cross-feed from  $B^\pm \rightarrow D(\rightarrow K_S^0 K\pi)h^\pm$  decays into either of the signal channels. However, this background is very highly suppressed by the employed requirement on the  $D$  mass. This is illustrated in Fig. 5.22, where the  $D$  mass distribution in samples of simulated  $B^\pm \rightarrow D(\rightarrow K_S^0 K\pi)K^\pm$  decays are shown, when reconstructed as  $D \rightarrow K_S^0 \pi^+ \pi^-$  and  $D \rightarrow K_S^0 K^+ K^-$  decays. Essentially no decays that fall in the selected  $D$  mass window survive the full selection. Therefore this background is not considered further. Neither is the background due to cross-feed between  $B^\pm \rightarrow D(\rightarrow K_S^0 \pi^+ \pi^-)h^\pm$  and  $B^\pm \rightarrow D(\rightarrow K_S^0 K^+ K^-)h^\pm$ , since it involves two

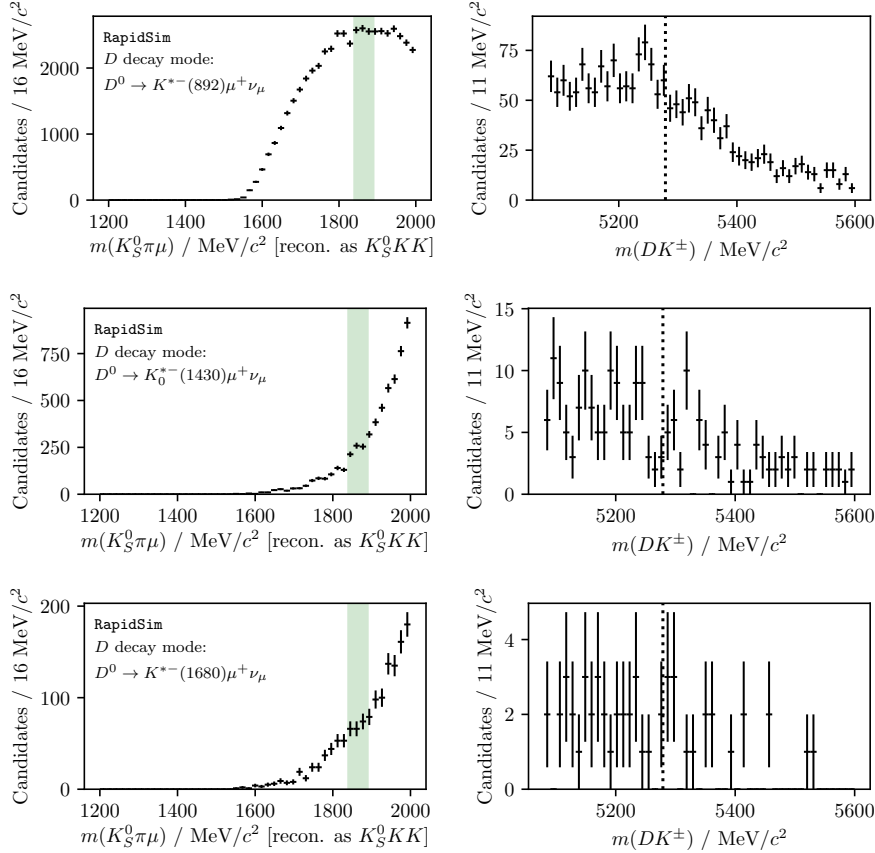


**Figure 5.21:** The reconstructed (left)  $m(K_S^0 K^+ K^-)$  and (right)  $m(DK^\pm)$  distributions in **RapidSim** samples of  $B^\pm \rightarrow DK^\pm$  decays where  $D^0 \rightarrow K_S^0 \pi^- \mu^+ \nu_\mu$ , where the  $K_S^0 \pi^-$  originate in (top to bottom) the resonances  $K^{*-}(892)$ ,  $K_0^{*-}(1430)$ , and  $K^{*-}(1680)$ . The shapes for the  $D^0 \rightarrow K_S^0 \pi^- e^+ \nu_e$  case are almost identical.

misidentified particles, and therefore will result in reconstructed  $D$  masses even further away from the selected mass window. A very loose PID requirement on the charged  $D$  decay products is nonetheless included in the  $D \rightarrow K_S^0 K^+ K^-$  channel, because it helps reduce the level of combinatorial background.

### 5.3.5 Swapped-track backgrounds

A possible peaking background stems from real  $B \rightarrow DhX$  decays with the same final state tracks as in the signal case, but where some tracks are misassigned in the reconstruction. Examples are  $B^+ \rightarrow (K_S^0 h^+ h')_D h^+$  decays where the companion and the  $D$ -decay product with the same charge are swapped, or  $B^\pm \rightarrow (K^- \pi^+)_D K_S^0 h^\pm$  decays, where the  $K_S^0$  is assigned to the  $D$  decay and the real companion is swapped with the  $D$ -decay product of the same charge. The signature of this background type is a peak at the  $D$  mass, when the invariant mass corresponding to the companion track and some subset of the  $D$ -decay tracks

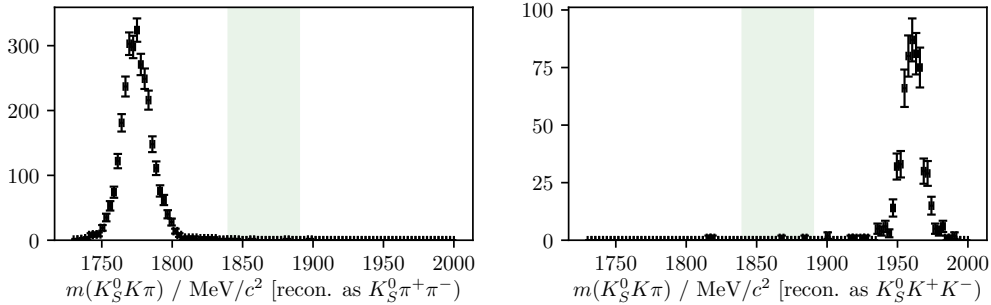


**Figure 5.22:** Simulated samples of  $B^\pm \rightarrow D(\rightarrow K_S^0 K \pi) \pi^\pm$  decays reconstructed in the (left)  $D \rightarrow K_S^0 \pi^+ \pi^-$  and (right)  $D \rightarrow K_S^0 K^+ K^-$  channels, combining the LL and DD categories. The  $D$ -mass region included in the selection of signal decays is illustrated with the green band. The plots in the  $B^\pm \rightarrow DK^\pm$  channels look almost identical.

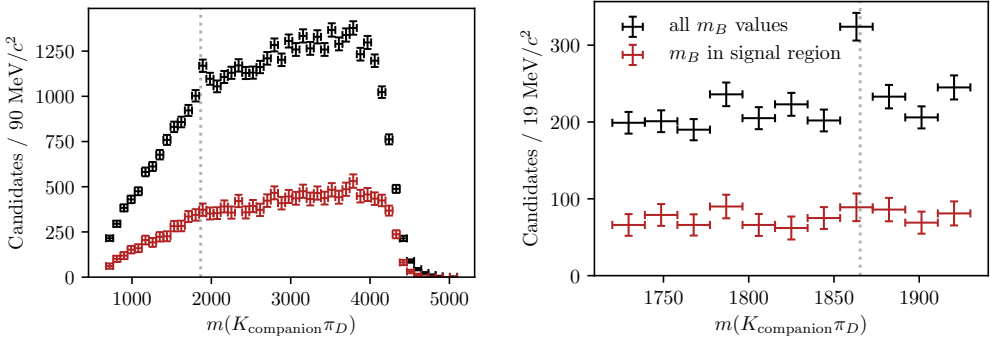


**Figure 5.23:** Invariant mass spectrum of the  $m^2(K^\pm \pi^\mp)$  combination in the  $B^\pm \rightarrow (K_S^0 \pi^+ \pi^-) K^\pm$  data sample for (black) all candidates and (red) candidates for which  $m_B \in m_B^{PDG} \pm 30 \text{ MeV}/c^2$ . The LL and DD categories are combined. The only difference between the left and right plots is the  $m(K\pi)$  mass range on the horizontal axis. The dotted line indicated the known  $D$  mass [28].

is formed. The presence of the background has been investigated by forming all such combinations, for all data categories, after the full selection has been applied. Only in a single channel is a peak visible: the  $B^\pm \rightarrow (K_S^0 \pi^+ \pi^-) K^\pm$  channel, where  $m(K^\pm \pi^\pm)$  has a peak, as shown in Fig. 5.23. Thus, a background is present from the favoured two-body  $D$  decay  $B^\pm \rightarrow (K^\pm \pi^\mp)_D K_S^0 \pi^\pm$ , where the  $K^\mp$  is reconstructed as the companion, and the  $K_S^0$  meson and both pions are assigned to the  $D$  decay.

It is not favourable to veto this background, because a requirement on the invariant mass of a track combination that includes the companion track would impact the Dalitz-plot acceptance differently in the  $DK^\pm$  and  $D\pi^\pm$  channels. Thus it would break a fundamental underlying feature of the measurement: the identical selection efficiency profile between these modes. However, the yield excess in the  $m(K^\pm_{\text{companion}} \pi^\mp_D)$  range around  $m_D$ , attributed to the background, corresponds

to only about 0.5 % of the signal yield. A background at this level does not lead to a limiting systematic uncertainty on the measurement, as described in Section 5.6.9.

## 5.4 Signal and background mass shapes

The measurement employs *extended maximum-likelihood fits* [147] to the  $m(Dh^\pm)$  distribution of signal candidates to determine the observables of interest. The analysis implements a two-step fit procedure: first the data samples are analysed without separating the candidates by  $B$  charge or Dalitz bin, in order to determine appropriate parametrisations of the  $m(Dh^\pm)$  distribution of the signal and relevant background components. The parameterisations are then kept fixed in a subsequent fit of the observables of interest, where the candidates are split by  $B$  charge and Dalitz bin. This section describes the first step, whereas the latter fit is the subject of Section 5.5.

In both steps, the candidates are split in 8 categories depending on whether the companion is categorised as a kaon or pion, whether the  $K_S^0$  meson is in the LL or DD category, and by whether the  $D$  meson is reconstructed in the  $K_S^0\pi^+\pi^-$  or  $K_S^0K^+K^-$  final state. In the remainder of this text, these categories are indexed with the letter  $c$ . For each category,  $c$ , the expected number of observed decays at a given  $B$  mass,  $F^c(m)$ , is given by the sum of a signal contribution and a number of background distributions

$$F^c(m|\theta) = N_s^c(\theta)f_s^c(m|\theta) + \sum_b N_b^c(\theta)f_b^c(m|\theta), \quad (5.4)$$

where  $\theta$  denotes a set of parameters that describe the mass shapes and expected yields, in which some parameters are shared between categories. The distributions  $f_{s/b}^c$  are normalised to integrate to unity, and the expected signal (background) yields are denoted  $N_s^c$  ( $N_b^c$ ). A total, normalised distribution can then be defined

$$f^c(m|\theta) = \frac{1}{N_{\text{tot}}^c(\theta)}F^c(m|\theta), \quad N_{\text{tot}}^c(\theta) = N_s^c(\theta) + \sum_b N_b^c(\theta). \quad (5.5)$$

Given a set of  $N_{\text{observed}}^c$  measured  $B$  masses,  $\{m_i^c\}$ , in a given category, the extended log-likelihood function is defined

$$\ln \mathcal{L}_c(\theta|\{m_i^c\}) \equiv \sum_i \ln f^c(m_i^c|\theta) + \ln \text{Poisson}(N_{\text{tot}}^c(\theta), N_{\text{observed}}^c) \quad (5.6)$$

In a simultaneous fit the total, negative log-likelihood is  $-\ln \mathcal{L} = -\sum_c \mathcal{L}_c$ , and this function can be minimised to find the maximum-likelihood estimates of the

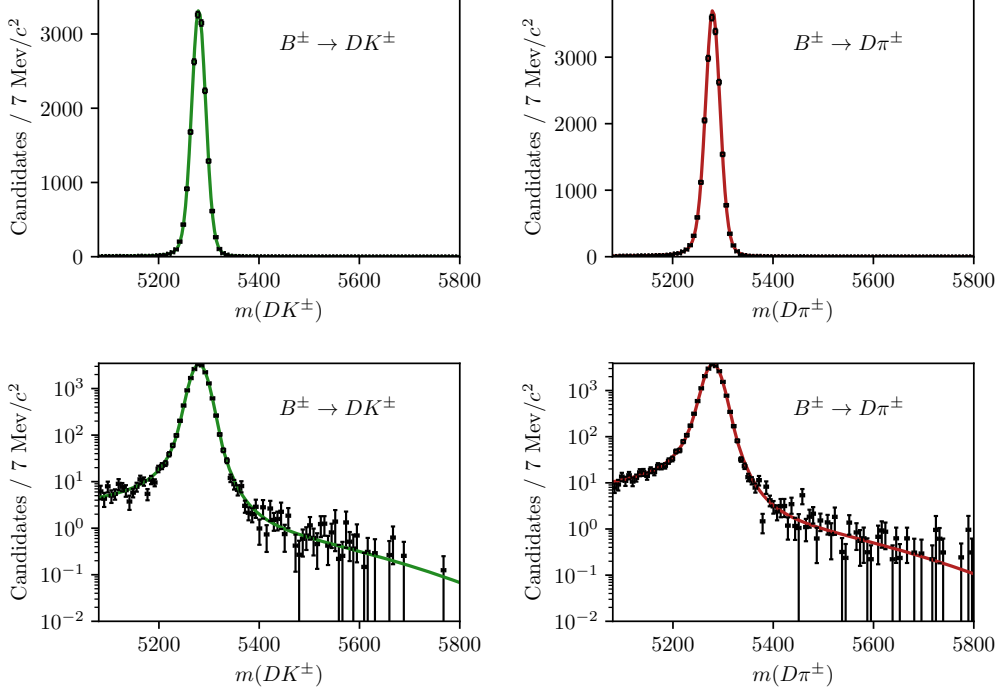


**Figure 5.24:** Fit projection of the signal shape to simulated  $B^\pm \rightarrow D(\rightarrow K_0^0\pi^+\pi^-)h^\pm$  samples reconstructed in the LL category. (Left) shows  $DK$  shapes, and (right) shows  $D\pi$  shapes. The shapes are shown with both linear and logarithmic  $y$ -axis scales.

parameters in  $\theta$ , as well as their confidence regions and correlation coefficients. This is handled with the `RooFit` package [148].

Apart from signal decays, the fit includes components that describe combinatorial background, backgrounds from decays where a companion pion is misidentified as a kaon or vice versa, and partially reconstructed backgrounds. Each of these components are described in detail in the following, before the results of the first-stage fit are presented in Section 5.4.5.

### 5.4.1 Signal decays

The signal component is modelled with a sum of a Gaussian density function,  $f_G(m|m_B, \sigma)$ , and a modified Gaussian distribution with the parameterisation

$$f_C(m|m_B, \sigma, \alpha_L, \alpha_R, \beta) \propto \begin{cases} \exp\left[\frac{-\Delta m^2(1+\beta\Delta m^2)}{2\sigma^2+\alpha_L\Delta m^2}\right], & \Delta m = m - m_B < 0 \\ \exp\left[\frac{-\Delta m^2(1+\beta\Delta m^2)}{2\sigma^2+\alpha_R\Delta m^2}\right], & \Delta m = m - m_B > 0, \end{cases} \quad (5.7)$$

which is Gaussian when  $\Delta m^2 \ll \sigma^2/\alpha_{L/R}$  or  $\Delta m^2 \gg \beta^{-1}$  (with widths of  $\sigma$  and  $\sqrt{\alpha_{L/R}/\beta}$  respectively), with an exponential-like transition that is able to model the effect of the experimental resolution of LHCb very well, and which

can also model the asymmetric, radiative tail of the signal peak. For the case  $\beta = 0$  the shape is denoted the *Cruijff* shape; however, in this case it tends to a uniform distribution for large  $\Delta m^2$  values, and cannot model the tails of the signal distribution. Thus, the full density function is

$$f_s(m|m_B, \sigma, \alpha_L, \alpha_R, \beta) = k_C f_C(m|m_B, \sigma, \alpha_L, \alpha_R, \beta) + (1 - k_C) f_G(m|m_B, \sigma). \quad (5.8)$$

The tail parameters  $(\alpha_{L/R}, \beta)$  and the constant  $k_C$  are determined in fits to simulated signal decays that have passed the full selection. The parameters are shared between the  $K_S^0 \pi^+ \pi^-$  and  $K_S^0 K^+ K^-$  channels, but otherwise independent in the fit categories. An example of a fit to simulated  $B^\pm \rightarrow D(\rightarrow K_S^0 \pi^+ \pi^-) h^\pm$  decays is given in Fig. 5.24. The location of the signal peak,  $m_B$ , and the resolution parameters,  $\sigma$ , are determined in the fit to actual data. Separate resolution parameters are determined in the LL and DD categories, because the LL category has a better resolution on the  $K_S^0$  momentum, and therefore a narrower peak in reconstructed  $B$  mass. Likewise, separate resolution parameters are used for  $B^\pm \rightarrow D\pi^\pm$  and  $B^\pm \rightarrow DK^\pm$  decays, because the smaller  $Q$  value in the latter case leads to smaller momenta of the decay products, and a correspondingly better resolution.

The signal yields are determined independently in each  $B^\pm \rightarrow D\pi^\pm$  category. The yields in the  $B^\pm \rightarrow DK^\pm$  categories are then parameterised in terms of a single yield-ratio  $\mathcal{R}_{K/\pi}$ , and  $\epsilon^c$ , the corresponding selection efficiency for a given category. They are defined

$$N_{DK^\pm}^c = \mathcal{R}_{K/\pi} \times N_{D\pi^\pm}^c \times \frac{\epsilon_{DK^\pm}^c}{\epsilon_{D\pi^\pm}^c}. \quad (5.9)$$

The selection efficiency is obtained in simulation, except for the PID efficiencies which are obtained in calibration data as described in Section 5.1.3. The parameter  $\mathcal{R}_{K/\pi}$  is shared between all categories, and corresponds to the branching ratio between  $B^\pm \rightarrow DK^\pm$  and  $B^\pm \rightarrow D\pi^\pm$  decays. Therefore, it can be compared to the known branching ratio [28], which serves as an important cross check of the determination of relative efficiencies.

### 5.4.2 Cross-feed between $B^\pm \rightarrow Dh^\pm$ channels

There is a cross-feed between the  $B^\pm \rightarrow D\pi^\pm$  and  $B^\pm \rightarrow DK^\pm$  channels, where real  $B^\pm \rightarrow D\pi^\pm$  decays are reconstructed as  $B^\pm \rightarrow DK^\pm$  decays, or where  $B^\pm \rightarrow DK^\pm$  decays are reconstructed as  $B^\pm \rightarrow D\pi^\pm$  decays. Due to relative branching fractions the former contribution is by far the most important, but both are modelled.

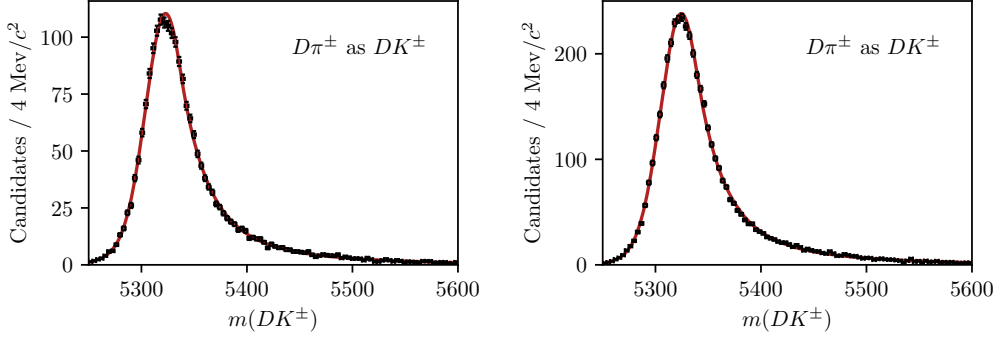


**Figure 5.25:** Fitted shape of the  $B^\pm$  invariant mass spectrum for  $B^\pm \rightarrow D\pi^\pm$  decays misidentified as  $B^\pm \rightarrow DK^\pm$  decays for (left) LL and (right) DD candidates in the  $D \rightarrow K_S^0 \pi^+ \pi^-$  mode.

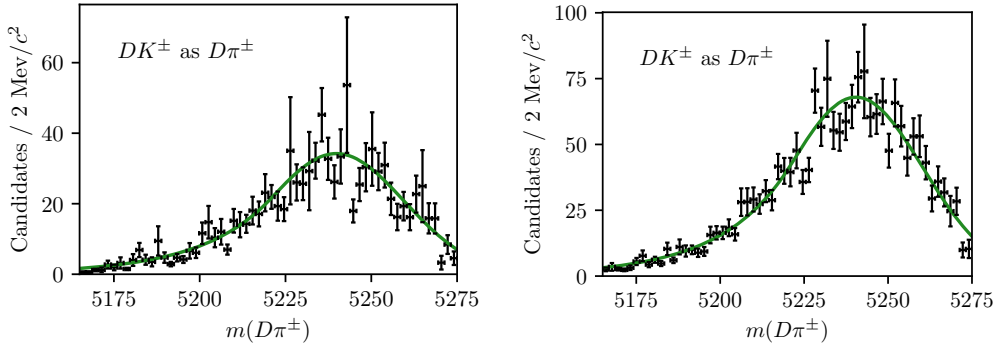


**Figure 5.26:** Fitted shape of the  $B^\pm$  invariant mass spectrum for  $B^\pm \rightarrow DK^\pm$  decays misidentified as  $B^\pm \rightarrow D\pi^\pm$  decays for (left) LL and (right) DD candidates in the  $D \rightarrow K_S^0 \pi^+ \pi^-$  mode.

The cross-feed shapes are obtained in a data-driven manner, described below, using the so-called *sPlot* method [145],

The cross-feed shapes are obtained in a data-driven manner and fixed in the fit to data. Separate shapes are determined for each category, using the following steps:

- The procedure is based on the reasonably pure  $B^\pm \rightarrow D\pi^\pm$  sample obtained when the full selection is applied. A simple mass fit is performed to the invariant mass spectrum and the *sPlot* method [145] is used to obtain the *sWeights*,  $w_s$ , for the signal component. The mass fit uses the same components for signal, low mass shape, and combinatorial background as described in this section.
- A set of weights are defined, based on the candidate-by-candidate PID efficiencies obtained as described in Section 5.1.3:

- The extracted PID efficiencies of the  $\text{PIDK} < 4$  cut  $\epsilon_{D\pi \rightarrow D\pi}(p, \eta, n_{\text{tracks}})$  are used to reverse-weight the  $B^\pm \rightarrow D\pi^\pm$  sample, in order to obtain the companion kinematic distributions before the  $\text{PIDK} < 4$  cut is applied.
- The extracted PID efficiencies of the  $\text{PIDK} > 4$  cut  $\epsilon_{D\pi \rightarrow DK}(p, \eta, n_{\text{tracks}})$  are used to obtain the companion kinematic distribution of the  $B^\pm \rightarrow D\pi^\pm$  candidates mis-identified as  $B^\pm \rightarrow DK^\pm$ .
- The raw distribution of the invariant mass of  $B^\pm$  particles with a misidentified companion,  $m_B^{\text{mis-ID}}$ , is produced by also doing the **DecayTreeFitter** kinematic refit while swapping the companion mass hypothesis of each  $B^\pm \rightarrow D\pi^\pm$  candidate to a kaon hypothesis.
- Each candidate is reweighted by the overall weight  $w = w_s^{\text{cand.}} / \epsilon_{D\pi \rightarrow D\pi}^{\text{cand.}} \cdot \epsilon_{D\pi \rightarrow DK}^{\text{cand.}}$ , and the reweighed  $m_B^{\text{mis-ID}}$  distribution is fitted to obtain the cross-feed mass distribution function.

The distributions are modelled with a sum of two Crystal Ball density functions, each defined by the parameterisation [149]

$$f_{\text{CB}}(m, \mu, \sigma, \alpha, n) \propto \begin{cases} \exp \left[ -\frac{1}{2} \left( \frac{m-\mu}{\sigma} \right)^2 \right] & \text{if } (m-\mu)/\sigma > -\alpha \\ A \left( B - \frac{m-\mu}{\sigma} \right)^{-n} & \text{otherwise,} \end{cases} \quad (5.10)$$

where  $\alpha > 0$ , and

$$A = \left( \frac{n}{\alpha} \right)^n \exp[-\alpha^2/2], \quad B = \frac{n}{\alpha} - \alpha. \quad (5.11)$$

The obtained  $m_B^{\text{mis-ID}}$  spectrum and obtained mass shape is given in Fig. 5.25 for the  $D \rightarrow K_S^0 \pi^+ \pi^-$  category; the  $D \rightarrow K_S^0 K^+ K^-$  shapes are very similar. An analogous procedure is used to obtain the mass distribution of  $B^\pm \rightarrow DK^\pm$  decays reconstructed in the  $B^\pm \rightarrow D\pi^\pm$  category. In the first stage where sPlots are extracted by a fit to the  $B^\pm \rightarrow DK^\pm$  mass spectrum, the  $D\pi$ -cross-feed shape determined as described above is included. An example of one of the resulting shapes is given in Fig. 5.26. The shapes obtained in this manner perform better in the fit to real data than those obtained using simulated decays, because the precision of the momentum determination is slightly overestimated in simulation.

The yield of cross-feed from  $B^\pm \rightarrow D\pi^\pm$  decays in a given  $B^\pm \rightarrow DK^\pm$  category is parameterised in terms of the yield of correctly identified  $B^\pm \rightarrow D\pi^\pm$  decays and the mis-identification probability extracted from calibration samples as described

in Section 5.1.3. Denoting the rate at which a pion is reconstructed as a kaon by  $\epsilon_{\pi \rightarrow K}^c$  in a given category,  $c$ , the yield is

$$N_{\pi \rightarrow K}^c = N_{D\pi^\pm}^c \frac{\epsilon_{\pi \rightarrow K}^c}{1 - \epsilon_{\pi \rightarrow K}^c}, \quad (5.12)$$

with an analogous definition of the yield of the cross-feed component from  $B^\pm \rightarrow DK^\pm$  decays in the  $B^\pm \rightarrow D\pi^\pm$  spectrum.

### 5.4.3 Partially reconstructed backgrounds

A number of background candidates stem from partly reconstructed  $B$  decays of the type  $B \rightarrow DhX$ , where  $X$  denotes a photon or a pion that is not reconstructed. It is not possible to reject these decays in the selection, due to the similarity to signal decays. The missing momentum results in reconstructed  $B$  masses below the actual  $B$  mass, and therefore the backgrounds are also denoted *lowmass* backgrounds. These mass distributions are modelled with analytic shapes, derived based on two principles. Firstly, the kinematic endpoints of the distributions are fully defined by the particle masses in the decay. Secondly, the angular distribution of the missing particle has a one-to-one relation to the missing momentum, and therefore to the reconstructed  $B$  mass. Depending on the spin-parity of the particles and resonances involved in the decay, two different mass distributions arise.

In  $B$  decays where the missing particle is a scalar that is produced in the decay of a vector resonance (eg.  $B^\pm \rightarrow D^{*0}(\rightarrow D^0\pi^0)\pi^\pm$  decays where the  $\pi^0$  is not reconstructed), the  $m(D^0\pi^\pm)$  distribution has a double-peak structure. The  $D^{*0}$  helicity angle  $\theta$  is defined as the angle between the  $\pi^0$  momentum vector in the  $D^{*0}$  rest frame and the  $D^{*0}$  boost vector in the  $B$  rest frame. The helicity of the  $D^{*0}$  meson means that the  $\pi^0$  will travel predominantly in the direction where  $\theta = 0$  or  $\theta = \pi$ . When  $\theta = 0$  the fraction of momentum carried by the missing  $\pi^0$  is lower, leading to a higher reconstructed  $m(D^0\pi^\pm)$ . When  $\theta = \pi$  the converse occurs. The resulting  $B$  mass distribution is a parabola  $f_{\text{HORNS}}^0(m)$  peaking near both kinematic endpoints  $a$  and  $b$

$$f_{\text{HORNS}}^0(m) = \begin{cases} (m - \frac{a+b}{2})^2, & \text{if } a < m < b \\ 0, & \text{otherwise.} \end{cases} \quad (5.13)$$

Due to the double-peaking structure, and the fact that it was developed by Paolo Gandini for the two-body ADS/GLW analyses [150], this shape is denoted a *HORNsdini* shape when convolved with a resolution function as described below.

The second relevant decay situation is where the missing particle is a vector, again produced via the intermediate decay of a vector resonance (eg.  $B^\pm \rightarrow D^{*0}(\rightarrow$

$D^0\gamma)\pi^\pm$  decays where the photon is not reconstructed). In this case, the spin-parity of the photon ( $1^-$ ) means that it will decay preferentially in the  $\theta = \frac{\pi}{2}$  or  $\theta = \frac{3\pi}{2}$  directions, and so a double-peak structure is not seen. In this case the parabolic distribution  $f_{\text{HILL}}^0(m)$  with kinematic endpoints  $a, b$  has negative curvature and can be described by

$$f_{\text{HILL}}^0(m) = \begin{cases} -(m-a)(m-b), & \text{if } a < m < b \\ 0, & \text{otherwise.} \end{cases} \quad (5.14)$$

This shape is denoted a *HILLdini* shape when convolved with a resolution function. A convolution is applied to take into account the non-perfect resolution in the momentum determination. The resolution function is chosen to be a sum of two Gaussians. For a single Gaussian shape  $f_G(x|\mu, \sigma)$  with mean  $\mu$  and width  $\sigma$ , the double Gaussian is expressed as

$$f_{DG}(x) = f_G(x|\mu, \sigma) + k_G f_G(x|\mu, R_\sigma \sigma). \quad (5.15)$$

where  $\sigma$  is the width of the first Gaussian,  $k_G$  is the relative fractions between the two Gaussians, and  $R_\sigma$  is their relative widths. Further, selection effects can distort the horns shape such that one of the peaks is higher than the other. This is taken into account by introducing a linear polynomial with slope parameter  $\xi$ . As  $\xi \rightarrow 0$ , the left hand peak decreases in size relative to the right hand peak. The resulting *HORNsdini* and *HILLdini* distributions are therefore

$$f_{\text{HORNs/HILL}}(m) = \int_a^b dx f_{\text{HORNs/HILL}}^0(x) f_{DG}(m|x, \sigma, k_G, R_\sigma) \left( \frac{1-\xi}{b-a}x + \frac{b\xi - a}{b-a} \right). \quad (5.16)$$

Examples of the shapes are given in Fig. 5.27. These shapes are used to fit all partially reconstructed backgrounds, as described in the following section.

### Determination of the partially reconstructed background distributions

In both the  $B^\pm \rightarrow DK^\pm$  and  $B^\pm \rightarrow D\pi^\pm$  categories, components are included to describe contributions from the partially reconstructed decays

- $B^\pm \rightarrow (D^{*0} \rightarrow D^0[\pi^0])h^\pm$ , described using a *HORNsdini* distribution,
- $B^\pm \rightarrow (D^{*0} \rightarrow D^0[\gamma])h^\pm$ , described using a *HILLdini* distribution
- $B^0 \rightarrow (D^{*\pm} \rightarrow D^0[\pi^\pm])h^\mp$ , described using a *HORNsdini* distribution,
- $B^{\pm(0)} \rightarrow D^0 h^\pm [\pi^{0(\mp)}]$ , described using a *HORNsdini* distribution,

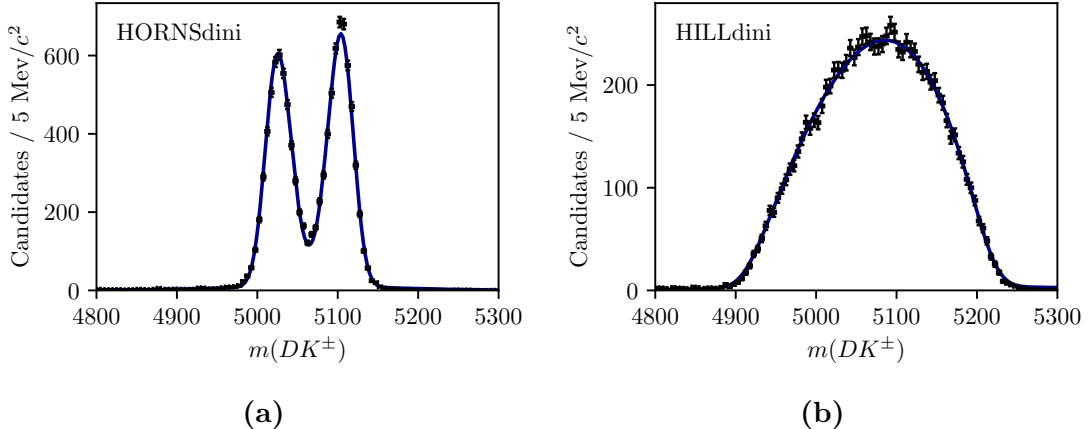


**Figure 5.27:** Examples of (a) the *HORN**smini* distribution fit to simulated  $B \rightarrow (D^* \rightarrow D^0[\pi])h^\pm$  decays, and (b) the *HILL**smini* distribution fit to simulated  $B^\pm \rightarrow (D^{*0} \rightarrow D^0[\gamma])h^\pm$  decays. The fits in this figure are made to illustrate the features of each shape, but do not enter the actual fit to data.

where the particle in square brackets is not reconstructed. The mass distributions of all the  $B \rightarrow D^* h^\pm$  contributions are obtained from fits to samples of full LHCb simulation. Examples of these fits are shown in Fig. 5.28. All shape parameters are kept fixed in the fit to data, except for the parameter  $\sigma$  of the resolution function in Eq. (5.15) which is allowed to obtain the value preferred by data.

The mass distribution of  $B^\pm \rightarrow D^0 h^\pm [\pi^0]$  and  $B^0 \rightarrow D^0 h^\pm [\pi^\mp]$  decays reconstructed in the  $B^\pm \rightarrow D\pi^\pm$  categories is obtained from full LHCb simulation samples of  $B^\pm \rightarrow D^0 \rho^\pm$  and  $B^0 \rightarrow D^0 \rho^0$  decays. The shapes were compared to those predicted by an amplitude model for  $B^0 \rightarrow D^0 \pi^\pm \pi^\mp$  decays developed by LHCb [151], but found to be very similar for the  $m(D\pi^\pm)$  range relevant to this analysis. The obtained shapes are shown in Fig. 5.29.

The mass distribution of  $B^\pm \rightarrow D^0 K^\pm [\pi^0]$  and  $B^0 \rightarrow D^0 K^+ [\pi^-]$  decays reconstructed in the  $B^\pm \rightarrow DK^\pm$  categories, on the other hand, is obtained from a sample of signal decays, generated via a an amplitude model for  $B^0 \rightarrow D^0 K^+ \pi^-$  decays developed by LHCb [152] and smeared to take the LHCb resolution into account. This follows an approach developed in the context of a GLW analysis based on partially reconstructed decays made within LHCb [153]. The obtained shape is shown in Fig. 5.30.

The background yields of these backgrounds are parameterised in terms of one total yield parameter, accounting for all partially reconstructed  $B^\pm$  and  $B^0$  decays, and a number of parameters that describe the relative rates of the different contributions. In the  $B^\pm \rightarrow D\pi^\pm$  channels, the relative rates of the  $B^\pm \rightarrow (D^{*0} \rightarrow D^0[\pi^0])h^\pm$  and  $B^0 \rightarrow (D^{*\pm} \rightarrow D^0[\pi^\pm])h^\mp$  backgrounds are fixed

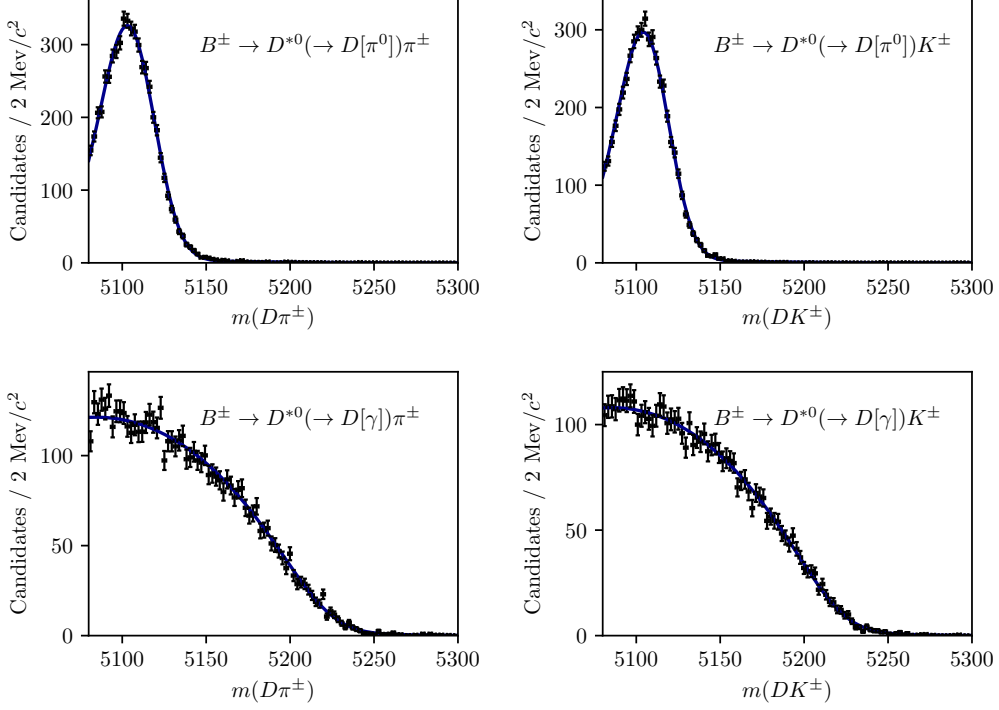


**Figure 5.28:** Fit projection of the fit to (top) simulated  $B^+ \rightarrow D^{*0}(\rightarrow D^0[\pi^0])h^\pm$  decays and (bottom) simulated  $B^+ \rightarrow D^{*0}(\rightarrow D^0[\gamma])h^\pm$  decays, all reconstructed in the DD category. Both the (left)  $DK$  and (right)  $D\pi$  shapes are shown.

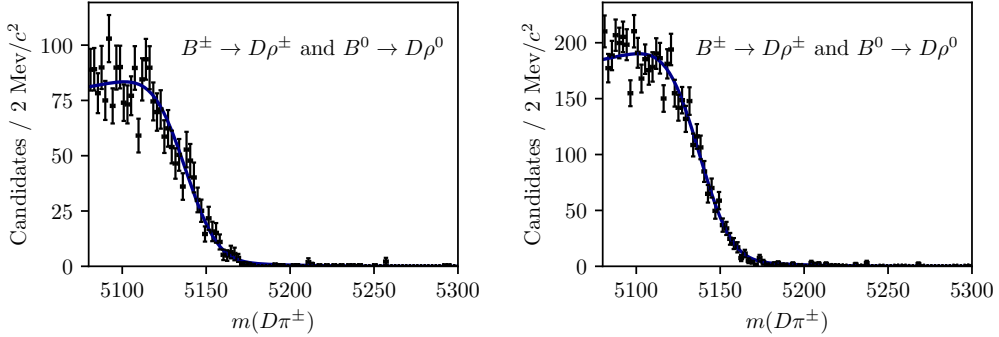


**Figure 5.29:** Projections of the fit to simulated  $B^\pm \rightarrow D\rho^\pm$  and  $B^0 \rightarrow D\rho^0$  samples reconstructed as  $B^\pm \rightarrow D\pi^\pm$  decays for the (left) LL and (right) DD categories.

from the known branching fractions, and relative selection efficiencies in simulation. These backgrounds have almost identical mass distributions and it is not possible to determine the ratio in the fit to data. The relative yield of  $B^\pm \rightarrow D^*(\rightarrow D^0[\gamma])\pi^\pm$  decays compared to the  $B \rightarrow D^*(\rightarrow D^0[\pi])\pi^\pm$  mode is denoted  $f_{D^*\gamma}^{D\pi}$  and is floated in the fit to data, as is the relative yield of  $B \rightarrow D^0\pi^\pm[\pi]$  decays compared to the  $B \rightarrow D^*\pi$  modes, denoted  $f_{D\pi\pi}^{D\pi}$ . In the  $B^\pm \rightarrow DK^\pm$  channels, all the relative background rates are fixed via known branching fractions and relative selection

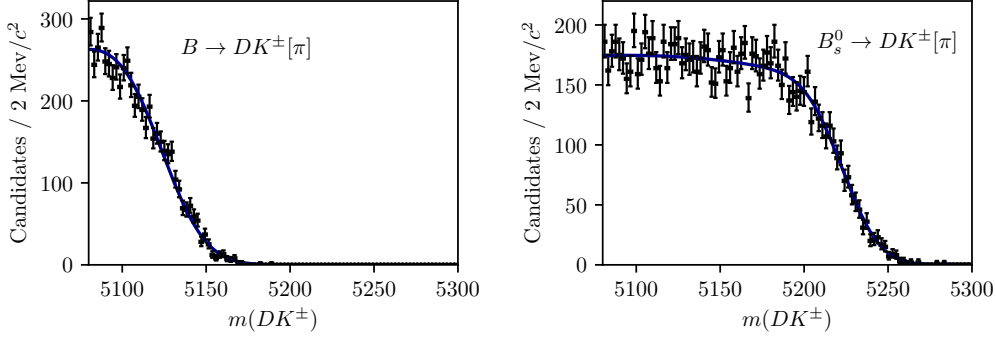


**Figure 5.30:** Fit projection for the fit used to obtain a shape for the partly reconstructed background from (left)  $B \rightarrow DK\pi$  decays and (right)  $B_s^0 \rightarrow DK^+\pi^-$  decays where a pion is not reconstructed.

efficiencies; this is necessary to obtain a stable fit, due to the lower yields.

In the  $B^\pm \rightarrow DK^\pm$  categories, an additional partially reconstructed background is considered from  $B_s^0 \rightarrow \bar{D}^0[\pi^+]K^-$  (and conjugate) decays. The mass shape is obtained from simulated decays, generated using an amplitude model published by LHCb [154] and smeared to account for the experimental resolution. The simulated decays are fit with a HORSdini PDF; the obtained shape is shown in Fig. 5.30. The yield of this background component is fixed relative to the signal yields in the corresponding  $B^\pm \rightarrow D\pi^\pm$  category, taking the relative efficiencies, branching ratios and hadronisation factors into account [28, 155].

In the  $B^\pm \rightarrow DK^\pm$  channels there is a contribution from partially reconstructed  $B \rightarrow D^*\pi^\pm X$  decays where the companion pion is misidentified as a kaon. The reverse contribution is negligible due to the relative branching fractions, and the fact that the  $K \rightarrow \pi$  misidentification shifts most of these background decays below the mass range of the fit. These are modelled using analytic, empirical mass distributions (essentially sums of a number of regular *HORN*/*HILLdini* distributions), with parameters that are determined in fits to simulated  $B \rightarrow D^*\pi^\pm$  and  $B \rightarrow D\rho$  decays where the pion is reconstructed with the kaon mass hypothesis. The shapes are fixed in the fit to data.

### Partially reconstructed backgrounds that are not modelled

It was considered whether a background from  $\Lambda_b^0 \rightarrow D^0 p \pi^-$  decays where a pion is not reconstructed, and the proton is misidentified as the companion, can be expected to contribute significantly. This background has been investigated using full LHCb simulation samples for the  $D$  final state  $K_S^0 \pi^+ \pi^-$ . Taking into account the selection

efficiencies, branching fractions, and hadronisation fraction of this background, the expected relative yield of the  $\Lambda_b^0$  background compared to signal of 0.03 % in the  $B^\pm \rightarrow D\pi^\pm$  channel, which is completely negligible. In the  $B^\pm \rightarrow DK^\pm$  channel the yield relative to signal is about 1.2 %, for total of about 200 decays. However, most of these lie at  $B$  masses smaller than the signal peak, and their impact is small. Therefore it is not necessary to model the background in the nominal fit; a systematic uncertainty is assigned that accounts for the small potential impact.

In the analogous case of  $\Lambda_b^0 \rightarrow D^0 p K^-$  decays, the missing energy of the non-reconstructed kaon results in a reconstructed  $B$  mass below the fit range.

It has also been investigated whether a background from  $\Lambda_b^0 \rightarrow \Lambda_c^+ \pi^-$  or  $\Lambda_b^0 \rightarrow \Lambda_c^+ K^-$  decays can be expected, where  $\Lambda_c^+ \rightarrow p K_S^0 \pi^+ \pi^-$ , a pion is missed, and the proton is misidentified as a pion or kaon from the  $D$  decay. In practice, the background is sufficiently suppressed from the applied  $D$  mass requirement to have no significant impact, and is therefore not modelled. A systematic uncertainty is assigned that accounts for any potential impact on the measurement due to this choice.

#### 5.4.4 Combinatorial background

The combinatorial background is modelled with an exponentially falling density function, where both the yield and exponential slope are determined independently for each category. This shape is found to model the combinatorial background well in all categories, most evident in the high- $m_B$  regions where this background dominates.

#### 5.4.5 Fit results

The fit range is chosen to be  $m_B \in [5080, 5800] \text{ MeV}/c^2$ . The low end of this interval includes the higher mass peak of the double-peak structure in the partially reconstructed background, which helps the fit constrain the relative contributions of backgrounds in the lowmass region. A number of additional backgrounds exist at even lower  $m_B$  values, thus extending the fit range to lower masses would necessitates an extended model, but not benefit the description of the signal region. The high end of the interval includes enough combinatorial background to allow the fit to determine the exponential slope parameter accurately.

A large number of pseudo experiments are carried out to verify that the fit procedure is self-consistent, in which simulated data sets are generated according to the expected  $B$  mass distributions, and then fit. None of the parameters obtained in the fit exhibit a mean bias different from zero. For most parameters

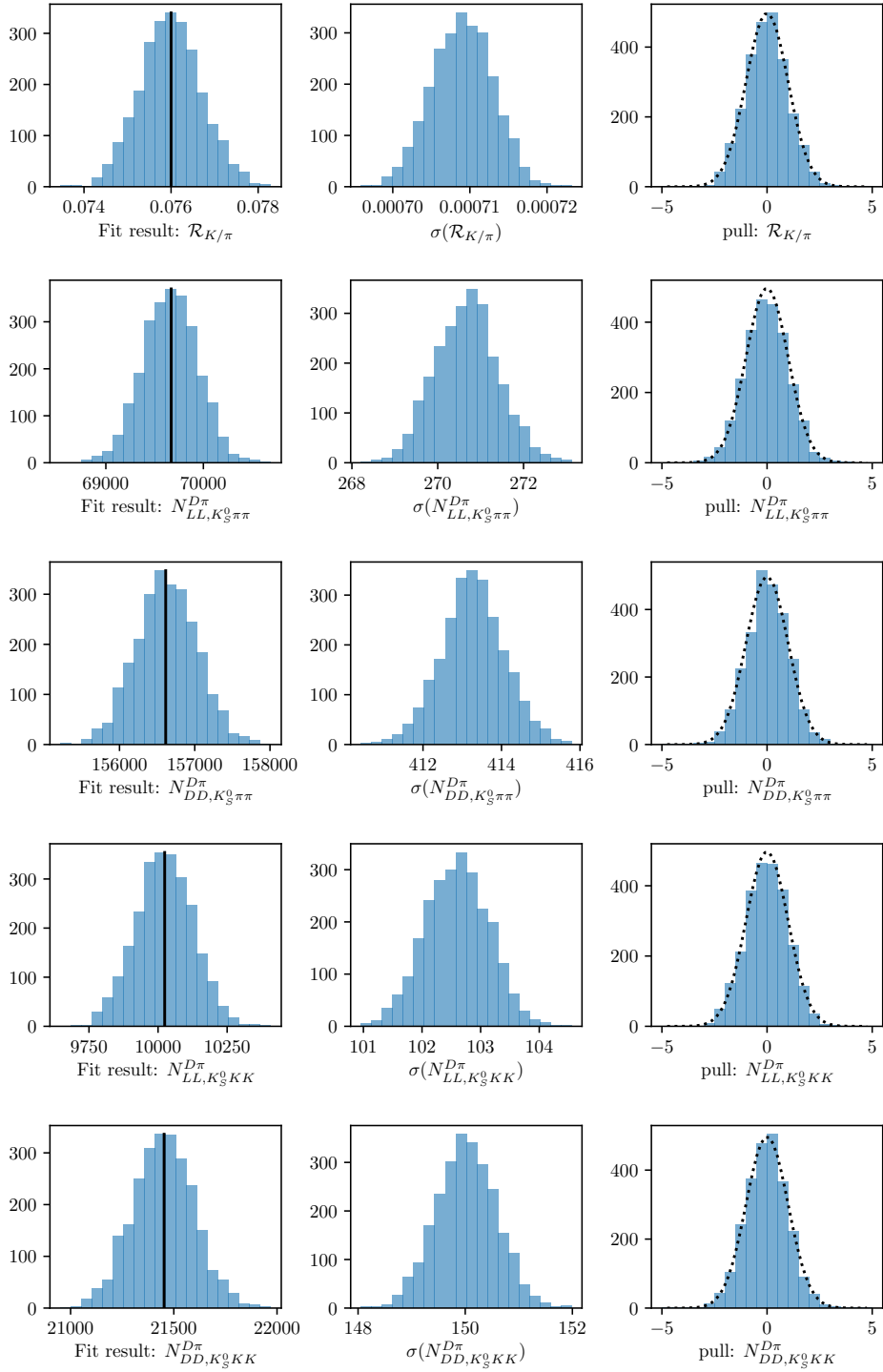


**Figure 5.31:** The (left) fitted value, (centre) estimated statistical uncertainty, and (right) pull plots for the signal yield parameters, as obtained in a number of pseudo experiments. The black line on the left shows the value used to generate the pseudo data sets; the dotted line on the right shows a Gaussian distribution with mean equal to zero and a standard deviation equal to unity.

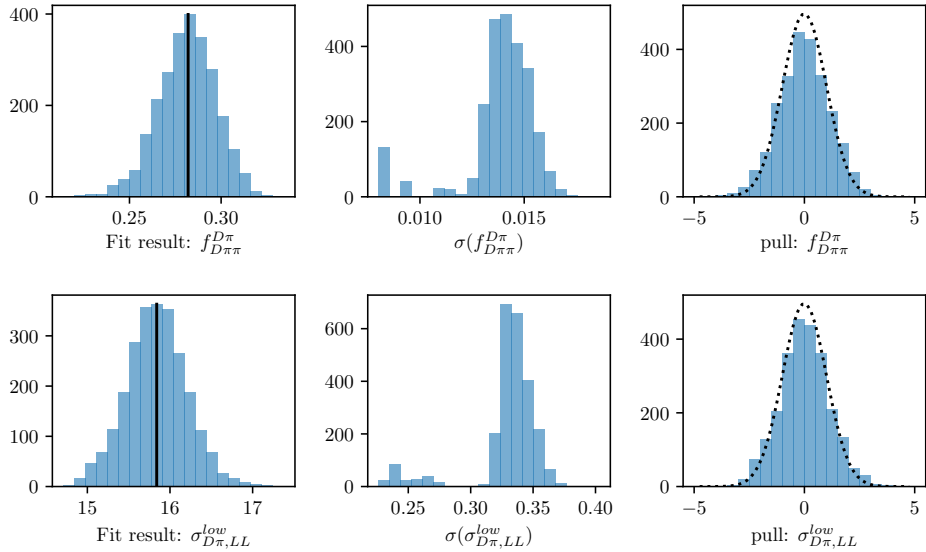


**Figure 5.32:** The (left) fitted value, (centre) estimated statistical uncertainty, and (right) pulls obtained in a number of pseudo experiments for two examples of parameters relating to the partially reconstructed backgrounds, where the uncertainties are slightly underestimated on average. The standard deviation of the pull distributions is approximately 1.15 in both cases.

the uncertainties are well estimated. This is the case for the signal yields, and the  $DK^\pm - D\pi^\pm$  yield ratio  $\mathcal{R}_{K/\pi}$ , as evidenced by the pull plots in Fig. 5.31. The fit underestimates the uncertainty by 10-20 % for some of the parameters related to the partly reconstructed backgrounds, as shown in Fig. 5.32, but this is taken into account when the uncertainties are propagated to the observables in the second-stage fit, as described in Section 5.6.3.

The projections of the fit to data are shown in Figs. 5.33 and 5.34, for the  $D \rightarrow K_S^0 \pi^+ \pi^-$  and  $D \rightarrow K_S^0 K^+ K^-$  data sets, respectively. The obtained yields for each fit component are given in Table 5.6. The total yield of  $B^\pm \rightarrow D\pi^\pm$  decays is approximately 230,000 across all channels. The obtained value of the yield ratio is  $\mathcal{R}_{K/\pi} = (7.7 \pm 0.1) \%$ , corresponding to a total  $B^\pm \rightarrow DK^\pm$  yield of 16,500, of which about 14,300 pass the PID requirement and are reconstructed in the  $B^\pm \rightarrow DK^\pm$  category. This value of  $\mathcal{R}_{K/\pi}$  is in excellent agreement with expectation from the known branching fractions [28], which predict  $\mathcal{R}_{K/\pi}^{\text{PDG}} = (7.8 \pm 0.3) \%$ .<sup>2</sup> The shape parameters determined in the fit to data are summarised in Table 5.7.

<sup>2</sup>The quoted measurement result for  $\mathcal{R}_{K/\pi}$  does not include any systematic uncertainties, which explains why the branching ratio seems to be determined with a much better precision than the current world average uncertainty.

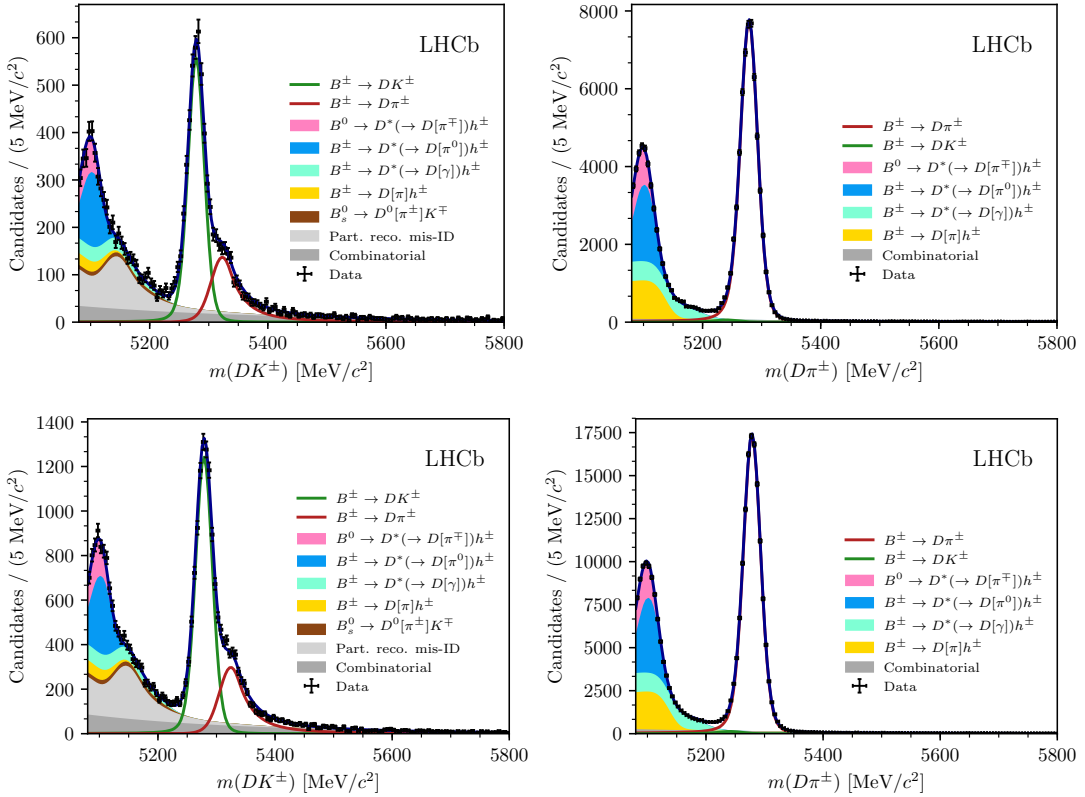


**Figure 5.33:** The invariant mass distribution for the (left)  $B^\pm \rightarrow DK^\pm$  channel and (right)  $B^\pm \rightarrow D\pi^\pm$  channel, where  $D \rightarrow K_S^0\pi^+\pi^-$  and the  $K_S^0$  is in the (top) LL and (bottom) the DD categories. The particle within square brackets in the legend denotes the particle that has not been reconstructed.

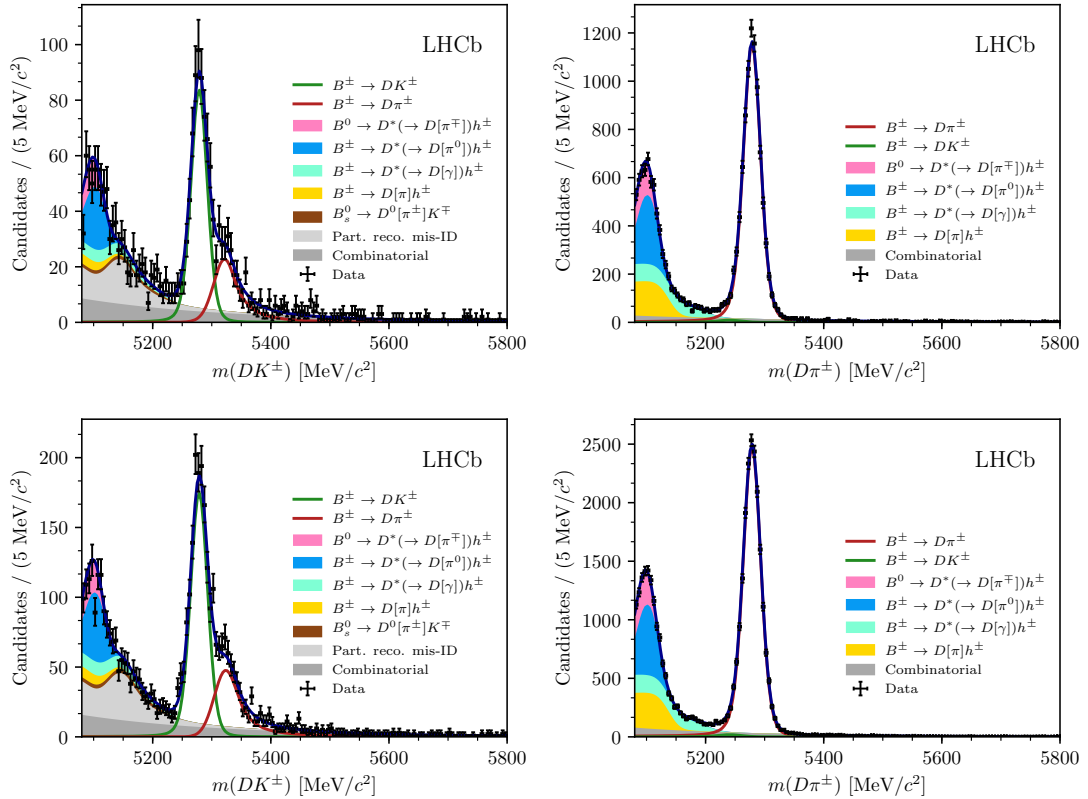


**Figure 5.34:** The invariant mass distribution for the (left)  $B^\pm \rightarrow DK^\pm$  channel and (right)  $B^\pm \rightarrow D\pi^\pm$  channel, where  $D \rightarrow K_S^0 K^+ K^-$  and the  $K_S^0$  is in the (top) LL and (bottom) the DD categories. The particle within square brackets in the legend denotes the particle that has not been reconstructed.

**Table 5.6:** Fitted total candidate yields. The quoted signal yields are for the number of candidates that survive the respective PID cut, whereas the  $DK^\pm$ - $D\pi^\pm$  ratio is corrected for PID and selection efficiencies so that it corresponds to the branching ratio.

| Component   | LL               | DD                |
|---|------------------|-------------------|
| Signal  |                  |                   |
| $B^\pm \rightarrow D(\rightarrow K_S^0\pi^+\pi^-)\pi^\pm$ | $61,573 \pm 254$ | $139,080 \pm 389$ |
| $B^\pm \rightarrow D(\rightarrow K_S^0K^+K^-)\pi^\pm$     | $9,160 \pm 98$   | $19,910 \pm 144$  |
| $R_{K/\pi} = n(DK)/n(D\pi)$ (%)                           |                  | $7.72 \pm 0.08$   |
| Combinatorial background                                  |                  |                   |
| $B^\pm \rightarrow D(\rightarrow K_S^0\pi^+\pi^-)\pi^\pm$ | $3,479 \pm 198$  | $9,928 \pm 376$   |
| $B^\pm \rightarrow D(\rightarrow K_S^0K^+K^-)\pi^\pm$     | $1,103 \pm 94$   | $2,545 \pm 155$   |
| $B^\pm \rightarrow D(\rightarrow K_S^0\pi^+\pi^-)K^\pm$   | $1,826 \pm 107$  | $3,987 \pm 177$   |
| $B^\pm \rightarrow D(\rightarrow K_S^0K^+K^-)K^\pm$       | $380 \pm 39$     | $655 \pm 58$      |
| Partially reconstructed background                        |                  |                   |
| $B^\pm \rightarrow D(\rightarrow K_S^0\pi^+\pi^-)\pi^\pm$ | $43,004 \pm 242$ | $95,452 \pm 403$  |
| $B^\pm \rightarrow D(\rightarrow K_S^0K^+K^-)\pi^\pm$     | $6,247 \pm 99$   | $13,241 \pm 157$  |
| $R_{K/\pi}^{low} = n_{low}(DK)/n_{low}(D\pi)$ (%)         |                  | $6.65 \pm 0.12$   |

**Table 5.7:** Fitted parameter values.

|   | LL  | DD                 |
|---|---|--------------------|
| $\sigma_{D\pi}$ (MeV/ $c^2$ )                             | $14.27 \pm 0.05$                          | $14.58 \pm 0.04$   |
| $\sigma_{DK}$ (MeV/ $c^2$ )                               | $13.61 \pm 0.24$                          | $14.19 \pm 0.17$   |
| $\mu$ (MeV/ $c^2$ )                                       |   | $5278.60 \pm 0.04$ |
| Combinatorial Slopes                                      |   |                    |
| Decay mode  | Slope ( $10 \times 10^{-3} GeV^{-1}c^2$ ) |                    |
| $B^\pm \rightarrow D(\rightarrow K_S^0\pi^+\pi^-)\pi^\pm$ | $-3.1 \pm 0.2$                            | $-4.0 \pm 0.1$     |
| $B^\pm \rightarrow D(\rightarrow K_S^0K^+K^-)\pi^\pm$     | $-4.1 \pm 0.4$                            | $-5.5 \pm 0.3$     |
| $B^\pm \rightarrow D(\rightarrow K_S^0\pi^+\pi^-)K^\pm$   | $-3.2 \pm 0.2$                            | $-3.9 \pm 0.2$     |
| $B^\pm \rightarrow D(\rightarrow K_S^0K^+K^-)K^\pm$       | $-4.2 \pm 0.4$                            | $-4.3 \pm 0.4$     |
| Part. Reco.   |   |                    |
| $\sigma_{D\pi}^{low}$ (MeV/ $c^2$ )                       | $13.73 \pm 0.33$                          | $13.78 \pm 0.28$   |
| $f_{D\pi\pi}^{D\pi}$                                      |   | $0.268 \pm 0.013$  |
| $f_{D^*\gamma}^{D\pi}$                                    |   | $0.317 \pm 0.005$  |

## 5.5 Measurement of the CP-violation observables

The section describes the second fit stage, in which the *CP*-violation observables of interest are determined. Compared to the first fit stage, the candidates are further split by *B* charge, and by the assigned Dalitz bin number, making for a total of 160 subcategories.<sup>3</sup> Another extended maximum-likelihood fit is carried out, in which shape parameters of all signal and background components are fixed to those determined in the first fit stage, and all floating parameters relate to the signal and background yields. The signal yields are expressed in terms of the observables of interest,  $(x_\pm^{DK}, y_\pm^{DK}, x_\xi^{D\pi}, y_\xi^{D\pi})$ , allowing the fit to determine their optimal values. The details of the fit setup are summarised in the following section, along with a number of studies that lead to the specific setup being chosen. The results are presented in Section 5.5.2, and a wide range of consistency checks are described in Section 5.5.3.

### 5.5.1 Fit setup

The basic principle of the measurement is that the signal yields in each bin (in a given category) are defined using the equations of Chapter 2, in order to allow for the determination of the *CP*-violation observables. In practice, a set of variables are defined

$$\begin{aligned} Y_{c,i}^- &= F_{c,-i} + [(x_-^c)^2 + (y_-^c)^2]F_{c,-i} + 2\sqrt{F_{c,i}F_{c,-i}}(c_i^cx_-^c + s_i^cy_-^c), \\ Y_{c,i}^+ &= F_{c,i} + [(x_+^c)^2 + (y_+^c)^2]F_{c,i} + 2\sqrt{F_{c,i}F_{c,-i}}(c_i^cx_+^c - s_i^cy_+^c), \end{aligned} \quad (5.17)$$

for each data category,  $c$ , in terms of which the bin yields that enter the likelihood are given by

$$N_{c,i}^\pm = \frac{Y_{c,i}^\pm}{\sum_j Y_{c,j}^\pm} \times N_{c,\text{total}}^\pm. \quad (5.18)$$

This parameterisation is essentially identical to the expressions in Section 2.4, slightly modified so that the phase-space-integrated yields of  $B^+$  and  $B^-$  decays in a given category are determined directly, in lieu of the normalisation constants  $h^\pm$  of that section. As discussed briefly in Section 2.4, there are choices to be made in terms of how the  $x$  and  $y$  are parameterised in the  $B^\pm \rightarrow D\pi^\pm$  channel, and how the  $F_i$  parameters are determined. A series of feasibility studies were carried out to determine the optimal setup; these are presented in the following section, before the final fit setup is described in detail.

---

<sup>3</sup>In the thesis, the word *category* is used for the 8-way split of data by companion species,  $K_S^0$  track type, and *D*-decay mode, indexed with a  $c$ ; the word *bin* denotes the 16 (4) regions of the  $D \rightarrow K_S^0\pi^+\pi^-$  ( $D \rightarrow K_S^0K^+K^-$ ) Dalitz plots, indexed with an  $i$ ; the simultaneous grouping by *category*, *bin*, and *B* charge is denoted a *subcategory*, of which there are  $4 \times 2 \times (16 + 4) = 160$ .

## Feasibility of alternative fit setups

The motivation for promoting the  $B^\pm \rightarrow D\pi^\pm$  channel to a signal channel is two-fold: one aim is to extract the information on  $\gamma$  from the  $B^\pm \rightarrow D\pi^\pm$  data, even if the precision gain is limited, and another is to be able to determine the  $F_i$  parameters directly from the  $B^\pm \rightarrow Dh^\pm$  channels, to avoid the need for a control channel and a simulation-reliant efficiency correction. Two different sets of observables can be defined to describe the  $CP$ -violation effects in the  $B^\pm \rightarrow D\pi^\pm$  channel:

- One option, defined the 8-parameters setup below, is to define an independent set of four Cartesian observables for the  $B^\pm \rightarrow D\pi^\pm$  mode,  $(x_-^{D\pi}, y_-^{D\pi}, x_+^{D\pi}, y_+^{D\pi})$ , which are analogous to the four  $B^\pm \rightarrow DK^\pm$  observables. They are thus defined

$$x_\pm^{D\pi} = r_B^{D\pi} \cos(\delta_B^{D\pi} \pm \gamma), \quad y_\pm^{D\pi} = r_B^{D\pi} \sin(\delta_B^{D\pi} \pm \gamma). \quad (5.19)$$

- Another option, proposed in Refs. [79, 80], is to introduce the parameter

$$\xi^{D\pi} = \left( \frac{r_B^{D\pi}}{r_B^{DK}} \right) \exp[i(\delta_B^{D\pi} - \delta_B^{DK})] \quad (5.20a)$$

and then determine the observables

$$x_\xi^{D\pi} = \text{Re}[\xi^{D\pi}] \quad y_\xi^{D\pi} = \text{Im}[\xi^{D\pi}]. \quad (5.20b)$$

This is denoted the 6-parameters setup below. In terms of  $x_\xi^{D\pi}$  and  $y_\xi^{D\pi}$ , the usual Cartesian  $x_\pm$  and  $y_\pm$  are given by

$$x_\pm^{D\pi} = x_\xi^{D\pi} x_\pm^{DK} - y_\xi^{D\pi} y_\pm^{DK}, \quad y_\pm^{D\pi} = x_\xi^{D\pi} y_\pm^{DK} + y_\xi^{D\pi} x_\pm^{DK}. \quad (5.21)$$

The former parameterisation has the benefit that information on  $\gamma$  from the  $B^\pm \rightarrow DK^\pm$  and  $B^\pm \rightarrow D\pi^\pm$  channels is encoded in separate sets of observables, whereas the latter parameterisation encodes information on  $CP$  violation from both channel in the  $(x_\pm^{DK}, y_\pm^{DK})$  parameters. In combinations of many measurements, it is a useful cross check to be able to compare constraints obtained from individual decay modes; a good example is the LHCb combination from 2016 [43] where both  $B^\pm \rightarrow DK^\pm$  and  $B^\pm \rightarrow Dh^\pm$  combinations are made and compared in detail. This is only possible with the former parameterisation. On the other hand, the latter parameterisation avoids the introduction of two non-physical degrees of freedom, which, as seen below, leads to better statistical behaviour.

In order to inform the choice of parameterisation, a series of pseudo experiments has been carried out to compare the obtainable precision on  $\gamma$  (these studies

were performed, and discussed within LHCb, prior to the publication of Ref. [80]; thus, the results presented here constitute independent work, even if there is some overlap in scope and conclusions with that reference). Many simulated data sets were generated, constituting of a number signal yields approximately equal to the expected yields in the full Run 1 and 2 LHCb data set: approximately 15,000  $B^\pm \rightarrow DK^\pm$  decays and 210,000  $B^\pm \rightarrow D\pi^\pm$  decays.<sup>4</sup> The signal decays were distributed between Dalitz bins according to  $(\gamma, r_B^{DK}, \delta_B^{DK}) = (75^\circ, 0.1, 130^\circ)$  in the  $B^\pm \rightarrow DK^\pm$  mode, which is to the world average values of direct  $\gamma$  measurements at the time. In the  $B^\pm \rightarrow D\pi^\pm$  mode, the behaviour is investigated for different sets of input values; of most importance is the case  $(r_B^{D\pi}, \delta_B^{D\pi}) = (0.005, 300^\circ)$ , because it corresponds to the solution in the LHCb combination [43] that is in agreement with the theoretical expectation  $r_B^{D\pi} \simeq 0.005$  [45]. The behaviour at larger  $r_B^{D\pi}$  values is also investigated. For each generated data set

1. the observables are measured in a fit to the data set, using both the 6-parameter and 8-parameter setups
2. the obtained observables are then fitted to obtain the underlying physics parameters  $(\gamma, r_B^{DK}, \delta_B^{DK}, r_B^{D\pi}, \delta_B^{D\pi})$  using a maximum-likelihood fit, essentially following the procedure outlined in Section 5.7.1.

In the 8-parameter setup it is possible to determine  $\gamma$  using the results in either the  $B^\pm \rightarrow DK^\pm$  or  $B^\pm \rightarrow D\pi^\pm$  channels separately, or consider the combined results; in the 6-parameter setup only the latter option is available. The studies are performed in two modes: with the  $F_i$  floating in the fit, emulating a realistic fit to data, as well as with the  $F_i$  fixed to the input values used in data generation. The latter studies emulate a setup where the  $F_i$  parameters are determined in an ultra-high statistics control channel, and perfect efficiency corrections are applied. In all cases, a single set of  $F_i$  parameters is shared between the  $B^\pm \rightarrow DK^\pm$  and  $B^\pm \rightarrow D\pi^\pm$  modes.

The 6-parameter setup shows significantly better statistical performance than the 8-parameter setup in the realistic case where the  $F_i$  parameters are determined in the fit and  $r_B^{D\pi} \sim 0.005$ .<sup>5</sup> The fits that employ the 6-parameter setup behave well in this case, whereas the additional degrees of freedom in the 8-parameter fit leads to essentially all parameters being 100% (anti-)correlated, and a significant number of fits not converging. For the fits that do converge, the uncertainties

---

<sup>4</sup>No backgrounds were included in these studies, and thus the quoted uncertainties on  $\gamma$  are better than what is obtainable in the final measurement; a similar study including realistic backgrounds is presented for the final setup below.

<sup>5</sup>For larger, non-physical values of  $r_B^{D\pi} > 0.03$  both fit setups behave well.

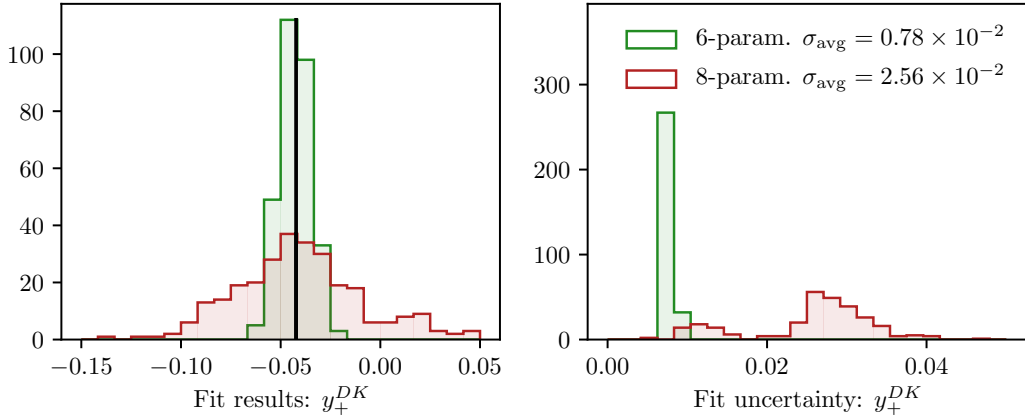


**Figure 5.35:** The distribution of (left) fit values and (right) statistical uncertainty estimate for  $y_+^{DK}$  in a series of pseudo experiments, for both the (green) 6-parameter and (red) 8-parameter setups.

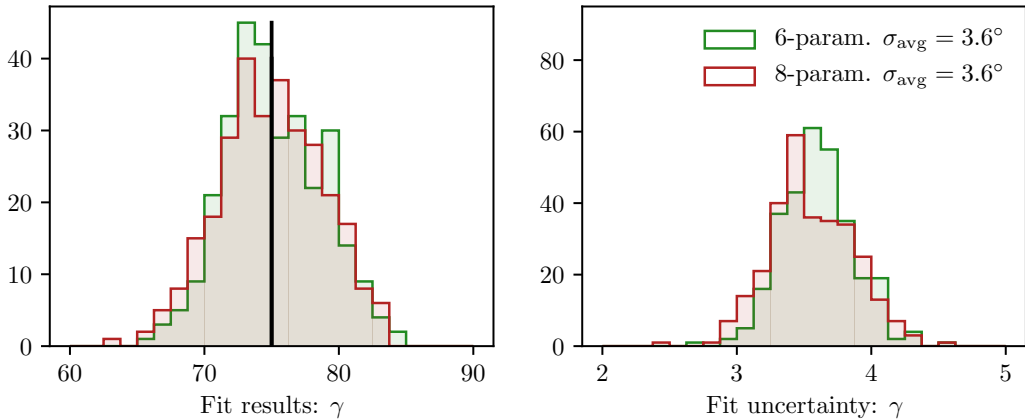


**Figure 5.36:** The distribution of (left) fit values and (right) statistical uncertainty estimate for  $\gamma$  in a series of pseudo experiments, for both the (green) 6-parameter and (red) 8-parameter setups.

on the observables are significantly larger due to the large correlations, as shown exemplified with the case of  $y_+^{DK}$  in Fig. 5.35. This essentially determines the choice of parameterisation: it is possible to reliably model  $CP$  violation in the  $B^\pm \rightarrow D\pi^\pm$  channel and simultaneously determine the  $F_i$  parameters by using the 6-parameter setup, but not by using the 8-parameter setup.

Interestingly, when the constraints on  $\gamma$  are compared, both setups lead to similar precision; in spite of the large uncertainties on the individual observables in the 8-parameter setups, the constraints on  $\gamma$  are tight. This is illustrated in Fig. 5.36. Nevertheless, it remains true that the 8-parameter setup is ruled out due to the statistical behaviour in the determination of the observables.

Furthermore, both the 6- and 8-parameter setups lead to fits that behave well in the studies where the  $F_i$  parameters are kept fixed, and the resulting uncertainties on the Cartesian observables and  $\gamma$  are essentially identical. Thus, the 6-parameter setup does not inherently lead to a gain in precision over the 8-parameter setup; the strength of the parameterisation is that it allows for a reliable, simultaneous determination of the  $F_i$  parameters and the observables of interest. This conclusion differs somewhat from the one drawn in Ref. [80].

The fixed- $F_i$  studies allow for an assessment of the gain in precision on  $\gamma$  due to the inclusion of the  $B^\pm \rightarrow D\pi^\pm$  mode, by comparing the precision obtained in the simultaneous fits with that obtained from the  $B^\pm \rightarrow DK^\pm$  channel alone. In the realistic case where  $r_B^{D\pi} = 0.005$ , the gain in precision is about  $0.1^\circ$ . The reason for the small impact, in spite of the yield being approximately 14 times larger in the  $B^\pm \rightarrow D\pi^\pm$  channel than in the  $B^\pm \rightarrow DK^\pm$  channel, is that  $r_B$  is 20 times smaller, and the  $CP$  asymmetries are proportional to  $r_B$ . Thus, the main improvement to the analysis from including  $B^\pm \rightarrow D\pi^\pm$  as a signal channel comes from the ability to determine the  $F_i$  parameters without adding a large systematic uncertainty.<sup>6</sup>

Finally, it is worth considering whether any precision can be gained by including further information on the  $F_i$  parameters from a control channel, even if the fit is well behaved without external information. The potential yield in the  $\bar{B}^0 \rightarrow D^{*+}(\rightarrow D^0\pi^+)\mu^-\bar{\nu}_\mu X$  control channel is approximately three times larger than in the  $B^\pm \rightarrow D\pi^\pm$  channel, and it does therefore offer a better statistical handle on the  $F_i$  values (at the significant cost of having to worry about efficiency corrections). This question can be answered by comparing the obtained precision on  $\gamma$  in the fits where  $F_i$  parameters were floating, to the precision in the case where they were kept fixed. Such a comparison is shown for the 6-parameter setup in Fig. 5.37 for the realistic scenario where  $r_B^{D\pi} = 0.005$ . The difference in the average  $\sigma(\gamma)$  is *less than*  $0.05^\circ$ , which is of course completely negligible. Therefore, no gain in precision can be obtained by including the control channel in the analysis, and it is not considered further.

---

<sup>6</sup>If this comparison is made using the parameter set  $(r_B^{D\pi}, \delta_B^{D\pi}) = (0.03, 330^\circ)$ , which corresponds to the alternative, non-physical solution in the LHCb combination [43], the gain in precision from the  $B^\pm \rightarrow D\pi^\pm$  channel is  $1.3^\circ$  instead, resulting in a final uncertainty of about  $2.3^\circ$ . This fact made the statistical interpretation of the  $B^\pm \rightarrow Dh^\pm$  combination in Ref. [43] non-trivial.

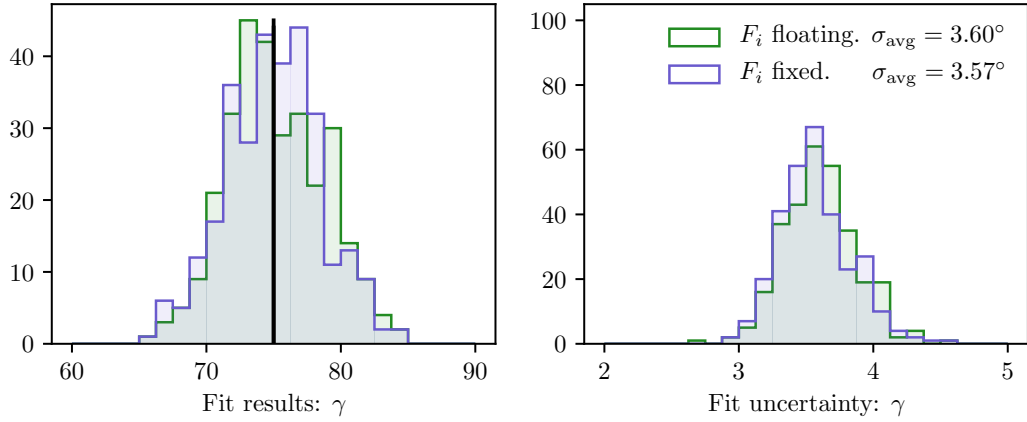


**Figure 5.37:** The distribution of (left) central values and (right) statistical uncertainty estimate for  $\gamma$  in a series of pseudo experiments that use the 6-parameter setup, where (green) the  $F_i$  parameters are determined in the fit and (blue) where they are kept fixed at their input values.

### Final choice of observables and the determination of the $F_i$ parameters

In the chosen setup, a single set of four parameters,  $(x_-^{DK}, y_-^{DK}, x_+^{DK}, y_+^{DK})$ , are shared between *all*  $B^\pm \rightarrow DK^\pm$  categories; they enter the expressions of Eq. (5.17) directly, and are thus determined in the fit. In the  $B^\pm \rightarrow D\pi^\pm$  categories, the yield are also expressed via Eq. (5.17), but the four parameters  $(x_-^{D\pi}, y_-^{D\pi}, x_+^{D\pi}, y_+^{D\pi})$  are parameterised in terms of  $(x_\pm^{DK}, y_\pm^{DK})$  and the additional two observables  $(x_\xi^{D\pi}, y_\xi^{D\pi})$  cf. Eq. (5.21). The  $F_i$  parameters are determined in the fit, being shared between the  $B^\pm \rightarrow DK^\pm$  and  $B^\pm \rightarrow D\pi^\pm$  channels. However, separate parameter sets are determined for the LL and DD categories because the acceptance profile over the Dalitz plot differs between them.

The  $F_i$  parameters are subject to the constraint that  $\sum_{i=-N}^N F_i^c = 1$ , for each category,  $c$ . Therefore, it is beneficial to introduce a reparameterisation in the likelihood function, where the  $F_i$  parameters are expressed in terms of a set of recursive fractions

$$\mathcal{R}_i = \begin{cases} F_i & , \quad i = -N \\ F_i / (\sum_{j \geq i} F_j) & , \quad -N < i < +N \end{cases} , \quad (5.22)$$

for which the constraint is much simpler, namely that each individual  $\mathcal{R}_i$  parameter lies in the interval  $[0, 1]$ . This parameterisation leads to well behaved fits, where the  $\mathcal{R}_i$  parameters do not suffer from significant correlations.

## Strong-phase inputs

The strong-phase parameters ( $c_i, s_i$ ) are fixed in the fit to data. In the  $D \rightarrow K_S^0 \pi^+ \pi^-$  channels, the combined CLEO [70] and BESIII [71] results are used, as reported in Ref. [71]. The  $D \rightarrow K_S^0 K^+ K^-$  categories also use combined CLEO [71] and BESIII results [72], which are reported in Ref. [72]. The experimental uncertainty on these measurements is propagated to the measured  $CP$ -violation observables as part of the systematic uncertainties in Section 5.6.1.

## Treatment of backgrounds

The yield of combinatorial background decays is determined independently in each subcategory. A single, overall yield of partially reconstructed background from  $B^\pm$  and  $B^0$  decays is determined in each of the 160 subcategories; the relative contribution from each individual background is fixed from the results of the first-stage fit, corrected for the different fit region (a systematic uncertainty is assigned due to this choice). In the  $B^\pm \rightarrow DK^\pm$  channels, the bin yields of the partially reconstructed background from  $B_s^0 \rightarrow \bar{D}^0[\pi^+]K^-$  decays are expressed via the  $F_i$ , exploiting that a positive companion particle is always produced along with a  $\bar{D}^0$  meson (and vice versa). The overall yield is fixed from the results of the first stage fit. Finally, the yield of the  $D\pi^\pm \leftrightarrow DK^\pm$  cross-feed components in each bin are determined via the obtained yield of correctly identified decays in the corresponding bin, and the known PID efficiencies. This is true for both fully and partially reconstructed decays, although only a  $D\pi^\pm \rightarrow DK^\pm$  component is included in the latter case.

## The choice of fit range

The fit range is decreased to  $m_B \in [5150, 5800] \text{ MeV}/c^2$ . The information from candidates with lower reconstructed  $B$  masses was useful in determining the relative rates and free mass shape parameters of the partially reconstructed background components in the first-stage fit; however, with these fixed in the second-stage fit, this is no longer the case. Furthermore, the setup assumes that the shape of the partially reconstructed background is identical across the Dalitz bins. This assumption is not perfectly true, but the impact is minimal when the lower limit of the fit range is taken to be  $5150 \text{ MeV}/c^2$ , as described further in Section 5.6.3.

**Table 5.8:** Mean biases and pulls for the observables of interest in the final, binned fit, obtained in a large number of pseudo experiments.

| Parameter      | Mean bias ( $\times 10^{-2}$ ) | Mean pull        | Pull width      |
|----------------|--------------------------------|------------------|-----------------|
| $x_-^{DK}$     | $-0.018 \pm 0.022$             | $-0.01 \pm 0.02$ | $1.01 \pm 0.02$ |
| $y_-^{DK}$     | $-0.014 \pm 0.026$             | $-0.00 \pm 0.02$ | $0.99 \pm 0.02$ |
| $x_+^{DK}$     | $-0.018 \pm 0.022$             | $-0.01 \pm 0.02$ | $1.00 \pm 0.02$ |
| $y_+^{DK}$     | $-0.016 \pm 0.028$             | $0.01 \pm 0.02$  | $1.00 \pm 0.02$ |
| $x_\xi^{D\pi}$ | $0.029 \pm 0.052$              | $0.06 \pm 0.02$  | $1.00 \pm 0.02$ |
| $y_\xi^{D\pi}$ | $0.000 \pm 0.060$              | $0.01 \pm 0.02$  | $1.00 \pm 0.02$ |

### Self-consistency check

In order to establish the fit stability and investigate a potential bias, a series of pseudo experiments are run, in which data sets are generated using the model, and then fitted back. The total yields are taken from the first-stage fit. The signal yields are distributed between Dalitz bins using input physics parameters that approximately equal the values obtained in Section 5.5.2 from the results of the fit to data. The  $F_i$  parameters are taken from a fit to data. The partly reconstructed background is distributed as " $D^0$ -like", i.e. in the  $B^\pm$  channels  $N_i^\pm \propto F_{\mp i}$ , except for the  $B_s^0$  background, which is " $\bar{D}^0$ -like" ( $N_i^\pm \propto F_{\pm i}$ ). The combinatorial background includes real  $D$  mesons paired with a random companion, as well as fake  $D$  mesons that are themselves made up of random tracks. The former is distributed as 50/50  $D^0$ -like and  $\bar{D}^0$ -like in generation, whereas the latter is assumed to be evenly distributed over the Dalitz plot (i.e. the bin yield is proportional to the bin area).

A set of 2000 pseudo experiments has been run, out of which 98.8 % converged properly. The pull plots for the observables of interest are shown in Figs. 5.38 and 5.39; the mean biases and pulls are summarised in Table 5.8. No biases are statistically significant, and the uncertainties are seen to be well estimated.

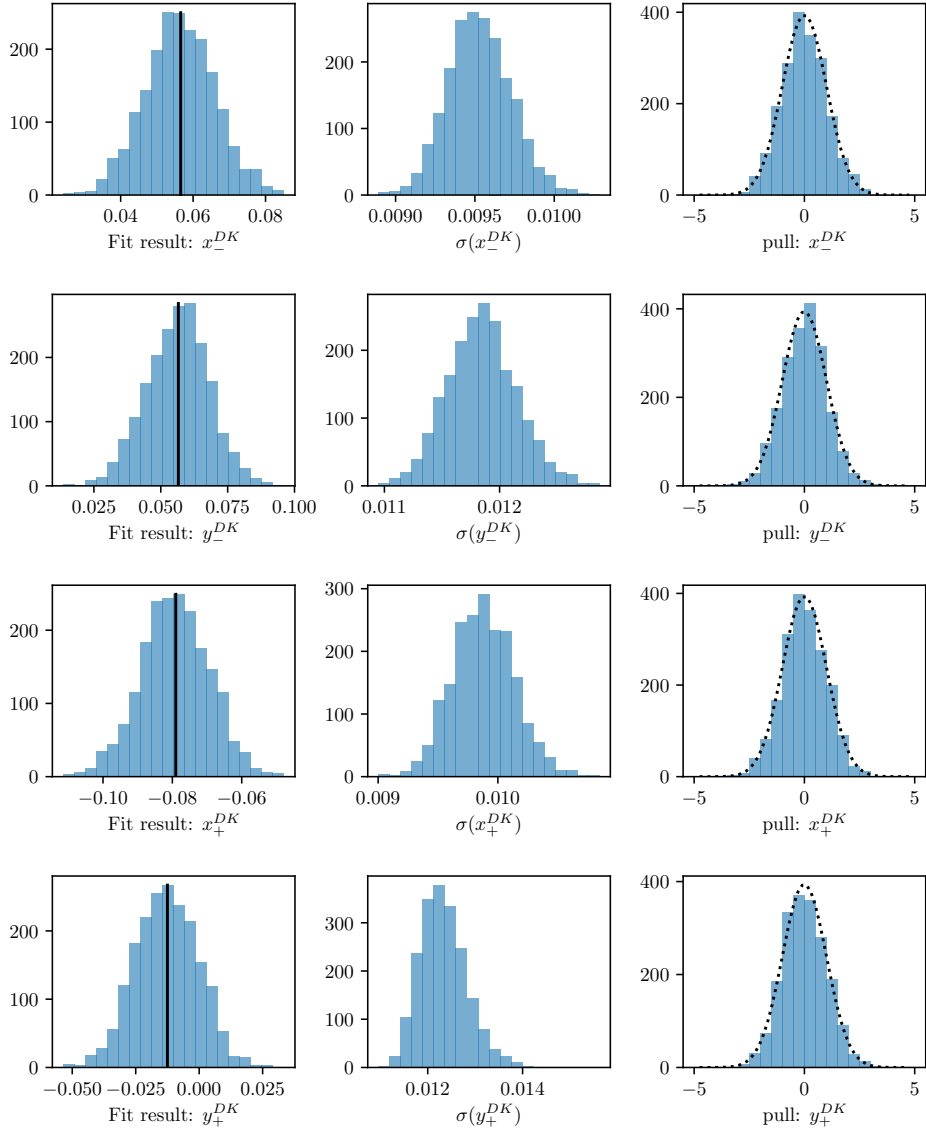


**Figure 5.38:** The (left) fitted value, (centre) estimated statistical uncertainty, and (right) pulls for the  $B^\pm \rightarrow DK^\pm$  observables, as obtained in a number of pseudo experiments. The black line on the left shows the value used to generate the pseudo data sets; the dotted line on the right shows a Gaussian distribution with mean equal to zero and a standard deviation equal to unity.

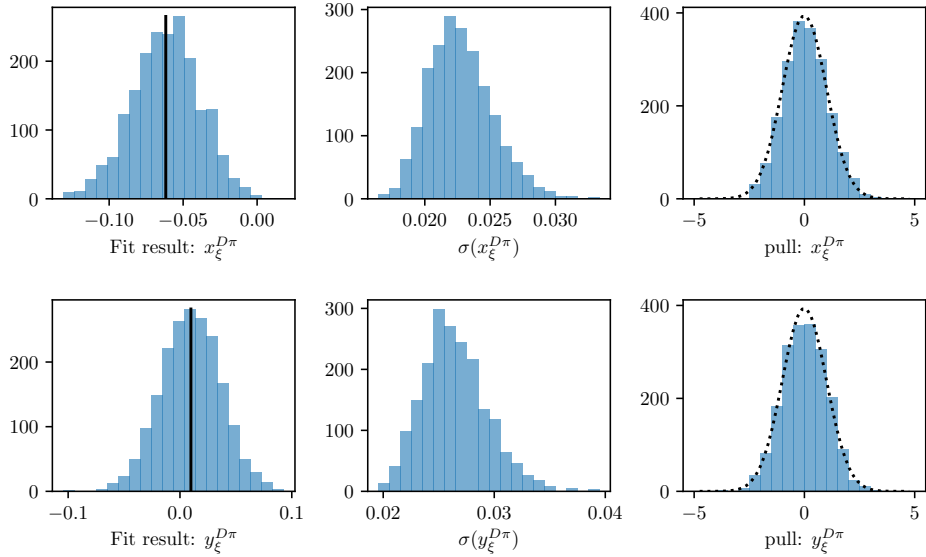


**Figure 5.39:** The (left) fitted value, (centre) estimated statistical uncertainty, and (right) pulls for the  $B^\pm \rightarrow D\pi^\pm$  observables, as obtained in a number of pseudo experiments. The black line on the left shows the value used to generate the pseudo data sets; the dotted line on the right shows a Gaussian distribution with mean equal to zero and a standard deviation equal to unity.

### 5.5.2 Main results

The values and statistical uncertainties of observables obtained in the fit are

$$\begin{aligned} x_-^{DK} &= (-5.68 \pm 0.96) \times 10^{-2}, & y_-^{DK} &= (-6.55 \pm 1.14) \times 10^{-2}, \\ x_+^{DK} &= (-9.30 \pm 0.98) \times 10^{-2}, & y_+^{DK} &= (-1.25 \pm 1.23) \times 10^{-2}, \\ x_\xi^{D\pi} &= (-5.47 \pm 1.99) \times 10^{-2}, & y_\xi^{D\pi} &= (0.71 \pm 2.33) \times 10^{-2}. \end{aligned} \quad (5.23)$$

The statistical correlation matrix for the observables is given in Table 5.9. None of the correlations are larger than 15 % and the values of both uncertainties and correlation coefficients are similar to those obtained in the feasibility studies. The two-dimensional log-likelihood profile for the observables is shown in Fig. 5.40, based on a full likelihood scan, where the fit is repeated with the observables fixed to a range of values around the optimal solution. It can be seen in the figure that the likelihood profile obtained in the scan is very well modelled by the Gaussian approximation, based on the Hessian matrix at maximum likelihood. Thus, the statistical uncertainties quoted in Eq. (5.23) are likely to be accurate. The signature of  $CP$  violation is that  $(x_+^{DK}, y_+^{DK}) \neq (x_-^{DK}, y_-^{DK})$ , very clearly the case for the measurement results. Finally, the figure illustrates how the opening angle between the two points defined by  $(x_+^{DK}, y_+^{DK})$  and  $(x_-^{DK}, y_-^{DK})$  is equal to  $2\gamma$ .

**Table 5.9:** Statistical uncertainties and correlation matrix for the fit to data.

| Uncertainty ( $\times 10^{-2}$ ) |            |            |            |            |                |                |
|----------------------------------|------------|------------|------------|------------|----------------|----------------|
|                                  | $x_-^{DK}$ | $y_-^{DK}$ | $x_+^{DK}$ | $y_+^{DK}$ | $x_\xi^{D\pi}$ | $y_\xi^{D\pi}$ |
| $\sigma$                         | 0.96       | 1.14       | 0.96       | 1.20       | 1.99           | 2.34           |

| Correlations      |            |            |            |            |                |                |
|-------------------|------------|------------|------------|------------|----------------|----------------|
|                   | $x_-^{DK}$ | $y_-^{DK}$ | $x_+^{DK}$ | $y_+^{DK}$ | $x_\xi^{D\pi}$ | $y_\xi^{D\pi}$ |
| $x_-^{DK\pm}$     | 1.000      | -0.125     | -0.013     | 0.019      | 0.028          | -0.165         |
| $y_-^{DK\pm}$     |            | 1.000      | -0.011     | -0.009     | 0.105          | 0.030          |
| $x_+^{DK\pm}$     |            |            | 1.000      | 0.088      | -0.099         | 0.038          |
| $y_+^{DK\pm}$     |            |            |            | 1.000      | -0.076         | -0.141         |
| $x_\xi^{D\pi\pm}$ |            |            |            |            | 1.000          | 0.146          |
| $y_\xi^{D\pi\pm}$ |            |            |            |            |                | 1.000          |

The full set of fit projections in all 160 subcategories is included in Appendix A. While the  $CP$  asymmetry of the phase-space integrated yield is small, this is not the case for all individual bin-pairs. This is shown in Fig. 5.41 where, as an example, the fit projections for the  $B^+ \rightarrow DK^+$  decays in bin +2 and the  $B^- \rightarrow DK^-$  decays in bin -2 of the  $D \rightarrow K_S^0 \pi^+ \pi^-$  Dalitz plot are compared. The presence of  $CP$  violation is clearly visible.

The obtained  $F_i$  parameter values are shown in Table 5.10. These parameters can be useful in other BPGBS measurements made within the LHCb collaboration: it is expected that the systematic uncertainty due to differences between the Dalitz-plot acceptance profile in  $B^\pm \rightarrow Dh^\pm$  decays and, say,  $B \rightarrow D^*K$  or  $B \rightarrow DK^*$  decays is smaller than the systematic arising from extracting the efficiency profile from simulated decays. Therefore, the central values and uncertainties will be made public [1], including a set of systematic uncertainties discussed in Section 5.6.12.<sup>7</sup>

---

<sup>7</sup>In practice, it is the obtained  $\mathcal{R}_i$  values that are made public, related to the  $F_i$  parameters via Eq. (5.22).

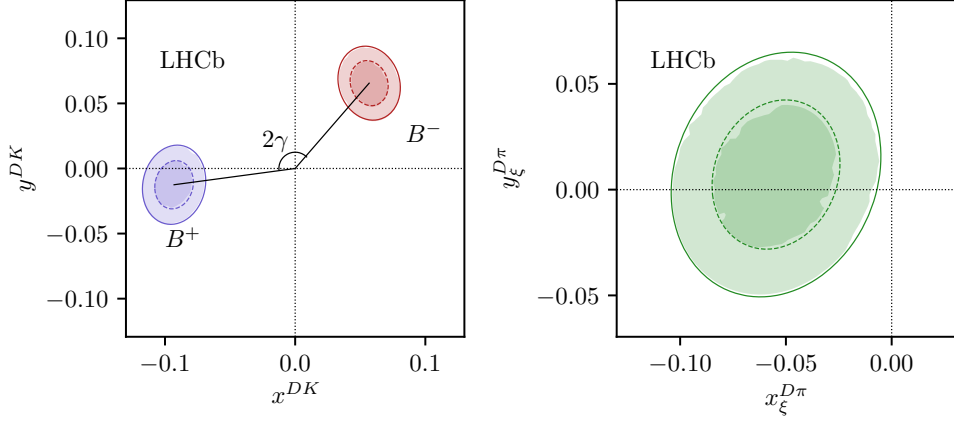


**Figure 5.40:** The 68 % and 95 % confidence regions for the fitted observables. The lines show the regions estimated from the covariance matrix returned by the default fit. The shaded areas are obtained in a likelihood scan, where the binned fit is run many times with all observables held at fixed values, scanning pairs of observables over the relevant ranges. The scan is made separately for the three pairs  $(x_-^{DK}, y_-^{DK})$ ,  $(x_+^{DK}, y_+^{DK})$ , and  $(x_\xi^{D\pi}, y_\xi^{D\pi})$ , holding the four other parameters fixed at their default-fit central values during a given scan (the scans were also made where *all* parameters, except the two for which the likelihood scan is made, are allowed to float, corresponding to a true likelihood marginalisation. The resulting plots are essentially identical, except that the likelihood contours suffer slightly more from numerical noise). Then the minimum log-likelihood is related to a  $\chi^2$  via  $\mathcal{L}_{\min} = \frac{1}{2}\chi^2$  (discarding an irrelevant constant), and the confidence region limits placed at  $\chi^2 = 2.30$  and  $\chi^2 = 6.18$ , yielding the relevant percentiles for a  $\chi^2$  distribution with 2 degrees of freedom.

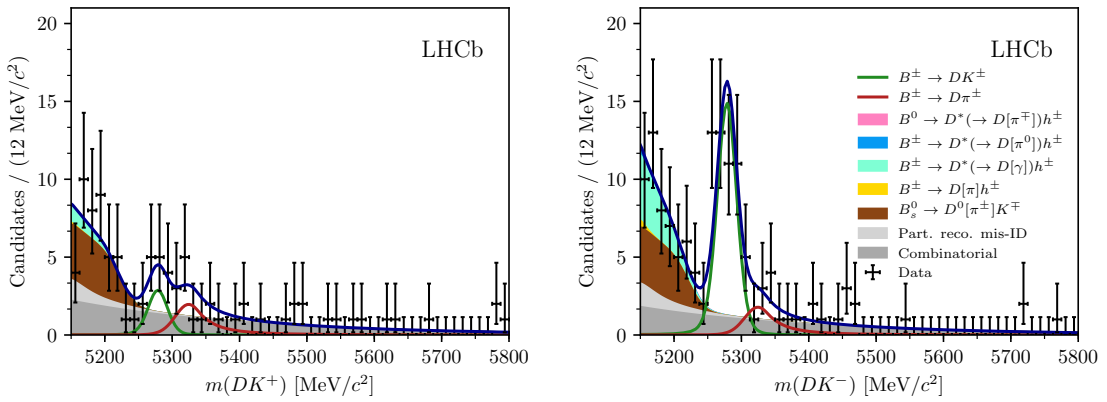


**Figure 5.41:** The invariant mass distribution for the (left)  $B^+ \rightarrow DK^+$  candidates in bin -2 and (right) the  $B^- \rightarrow DK^-$  candidates in bin +2, where  $D \rightarrow K_S^0 \pi^+ \pi^-$  and the  $K_S^0$  is reconstructed in the DD category.

**Table 5.10:** The fitted  $F_i$  values including statistical uncertainties. The associated systematic uncertainties are negligible, as discussed in Section 5.6.12.

| $F_i$ values: $D \rightarrow K_S^0 \pi^+ \pi^-$ |                   |                   |
|---|-------------------|-------------------|
| bin   | LL                | DD                |
| -8  | $0.024 \pm 0.001$ | $0.024 \pm 0.000$ |
| -7  | $0.127 \pm 0.001$ | $0.133 \pm 0.001$ |
| -6  | $0.062 \pm 0.001$ | $0.056 \pm 0.001$ |
| -5  | $0.046 \pm 0.001$ | $0.042 \pm 0.001$ |
| -4  | $0.095 \pm 0.001$ | $0.095 \pm 0.001$ |
| -3  | $0.160 \pm 0.001$ | $0.160 \pm 0.001$ |
| -2  | $0.153 \pm 0.001$ | $0.153 \pm 0.001$ |
| -1  | $0.095 \pm 0.001$ | $0.097 \pm 0.001$ |
| 1   | $0.022 \pm 0.001$ | $0.020 \pm 0.000$ |
| 2   | $0.005 \pm 0.000$ | $0.005 \pm 0.000$ |
| 3   | $0.004 \pm 0.000$ | $0.004 \pm 0.000$ |
| 4   | $0.055 \pm 0.001$ | $0.056 \pm 0.001$ |
| 5   | $0.027 \pm 0.001$ | $0.022 \pm 0.000$ |
| 6   | $0.004 \pm 0.000$ | $0.003 \pm 0.000$ |
| 7   | $0.055 \pm 0.001$ | $0.057 \pm 0.001$ |
| 8   | $0.067 \pm 0.001$ | $0.072 \pm 0.001$ |

| $F_i$ values: $D \rightarrow K_S^0 K^+ K^-$ |                   |                   |
|---|-------------------|-------------------|
| bin   | LL                | DD                |
| -2  | $0.207 \pm 0.004$ | $0.202 \pm 0.003$ |
| -1  | $0.222 \pm 0.004$ | $0.230 \pm 0.003$ |
| 1   | $0.290 \pm 0.005$ | $0.296 \pm 0.003$ |
| 2   | $0.281 \pm 0.005$ | $0.271 \pm 0.003$ |

### 5.5.3 Cross checks

A series of cross checks are performed to verify that the fit to data is behaving as expected.

#### Comparison to results of earlier analyses

It is confirmed that the results obtained in fits of the Run 1 or 2015+16 data sets in isolation are compatible with the results obtained in the original LHCb analyses of those data sets [3, 68]. In order to do so, the whole analysis procedure is carried out using only the relevant subset of data, and the strong-phase inputs from the CLEO collaboration are used in the fit. Two effects need to be taken into account when comparing the central values.

Firstly, the overlap between the data samples is not 100 % due to changes in the candidate selection. The overlap between the new selection and the data set of the original analysis of Run 1 data is about 70 %, whereas is it about 90 % for the 2015+16 data set. In order to determine the expected difference between the observables fitted from data sets with significant overlap, a large number of simulated data sets were generated in sets of two, where 70 (90) % of decays were shared between the data sets. Both data sets were fitted and the difference between the obtained central values for each observable tabulated; the standard deviation of these distributions are used to calculate the pulls between the old analysis results and the new fits to data. This check does not take into account that the semi-leptonic PID cuts were introduced to remove a potential peaking background, which may have had a small systematic effect on the earlier measurement results. Thus the expected differences are likely to be slightly underestimated and the check is conservative.

Furthermore, the  $F_i$  parameters were determined in a semi-leptonic control channel in the earlier analyses. Therefore, the expected difference obtained above is adjusted by adding the  $F_i$ -related systematic uncertainty of the original analysis in quadrature, when comparing the old results to those in new fits to the Run 1 and 15+16 data sets. No further corrections have been made to the expected differences, which effectively assumes all other systematic uncertainties to be 100 % correlated. Also for this reason can the check be considered conservative. As can be seen in Tables 5.11 and 5.12, neither the Run 1 and 2015+16 comparisons show unreasonable differences in central values.

**Table 5.11:** Comparison between the results on the Run 1 analysis [68] and the central values obtained when fitting the Run 1 dataset with the selection and fit setup described in the thesis. The pull is calculated using the  $1\sigma$  expected difference, which takes the sample overlap and the systematic uncertainty on the  $F_i$  parameters in the previous analysis into account, but assumes all other systematic uncertainties to be perfectly correlated. The new fits are performed using the CLEO strong-phase inputs.

| Observable             | Run 1 result [68] | New Fit<br>(central value $\times 10^{-2}$ ) | Pull  |
|------------------------|-------------------|--|-------|
| $x_-^{DK}$             | 2.50              | 4.04   | 0.85  |
| $y_-^{DK}$             | 7.50              | 9.14   | 1.02  |
| $x_+^{DK}$             | -7.70             | -9.40  | -0.91 |
| $y_+^{DK}$             | -2.20             | 0.80   | 1.77  |
| <i>p</i> -value: 0.057 |                   |  |       |

**Table 5.12:** Comparison between the results on the 2015+16 analysis [3] and the central values obtained when fitting the 2015+16 dataset with the selection and fit setup described in the thesis. The pull is calculated using the  $1\sigma$  expected difference, which takes the sample overlap and the systematic uncertainty on the  $F_i$  parameters in the previous analysis into account, but assumes all other systematic uncertainties to be perfectly correlated. The new fits are performed using the CLEO strong-phase inputs.

| Observable             | 15+16 result [3] | New Fit<br>(central value $\times 10^{-2}$ ) | Pull  |
|------------------------|------------------|--|-------|
| $x_-^{DK}$             | 9.00             | 8.36   | -0.50 |
| $y_-^{DK}$             | 2.10             | 1.16   | -0.62 |
| $x_+^{DK}$             | -7.70            | -8.58  | -0.56 |
| $y_+^{DK}$             | -1.00            | -2.82  | -1.39 |
| <i>p</i> -value: 0.239 |                  |  |       |

### Directly fitting the signal yields

As a cross-check, the fit is run in an alternative mode, in which the signal yields of each bin are independent parameters. The obtained yields are compared to those predicted from the results of the default fit in Fig. 5.42. The yields are shown for each "effective bin", where effective bin  $i$  is defined as bin  $+i$  for  $B^+$  decays and bin  $-i$  for  $B^-$  decays; in the  $CP$  symmetric case, these bins are expected to have equal yields (modulo production and detection asymmetries). The agreement between the two fit set-ups is seen to be excellent. The normalised yield asymmetries, defined as

$$A^i \equiv \frac{N_{-i}^- - N_i^+}{N_{-i}^- + N_i^+} \quad (5.24)$$

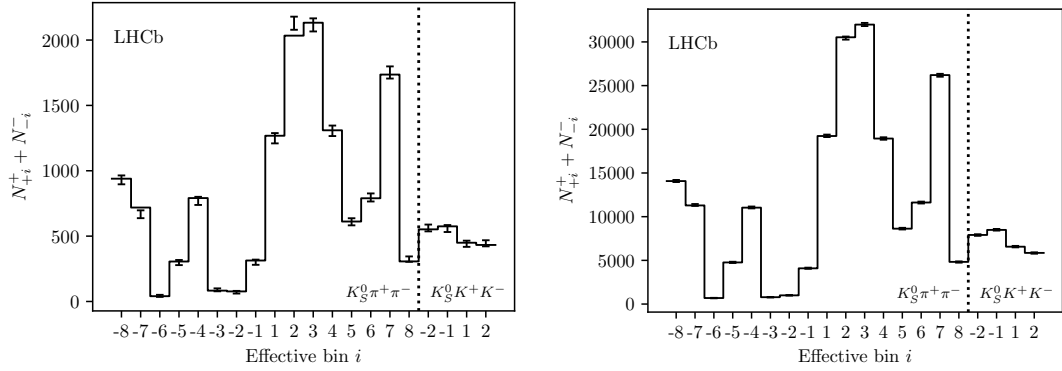


**Figure 5.42:** Comparison of (lines) the predicted yield given the determined  $CP$  observables and (error bars) the yield obtained in fits to data where each yield is an independent parameter. The yields are shown for (left)  $B^\pm \rightarrow DK^\pm$  decays and (right)  $B^\pm \rightarrow D\pi^\pm$  decays. The LL and DD categories have been combined, as has the  $B^+$  and  $B^-$  yields for each effective Dalitz bin, defined as bin  $+i$  for  $B^+$  decays and bin  $-i$  for  $B^-$  decays.

are shown in Fig. 5.43 for all decay channels. Again, the agreement between the nominal fit and the alternative fit with independent yields is found to be excellent for both  $B^\pm \rightarrow Dh^\pm$  decays. It is also clear how, in the case of  $B^\pm \rightarrow DK^\pm$  decays, the asymmetry is significantly different from zero for a number of bin pairs. A fit that does not allow for  $CP$  violation is also carried out, the results of which are also shown in the figure. The reason that the yield asymmetry is not zero in this fit, is that the overall yield of  $B^+$  and  $B^-$  decays are allowed to differ in this fit; only the phase-space distribution of the decays is enforced to be  $CP$ -symmetric. The observed asymmetry is due to a combination of production and detection asymmetries,  $CP$ -violation and material interaction of the  $K_S^0$  meson, and  $CP$  violation in the  $B^\pm \rightarrow Dh^\pm$  decays, but no attempt is made to disentangle the effects.

### Fitting subsets of the data separately

A cross check is carried out by determining the  $CP$  observables using a number of independent sub samples of the data set separately. This is done for the following following data splits

- Fig. 5.44a shows the same plots, comparing the fits to the data set split by  $K_S^0$  track type.
- Fig. 5.44b shows the same plots, comparing the fits to the data set split by whether the  $D$  meson decays to the  $K_S^0\pi^+\pi^-$  or  $K_S^0K^+K^-$  final state.

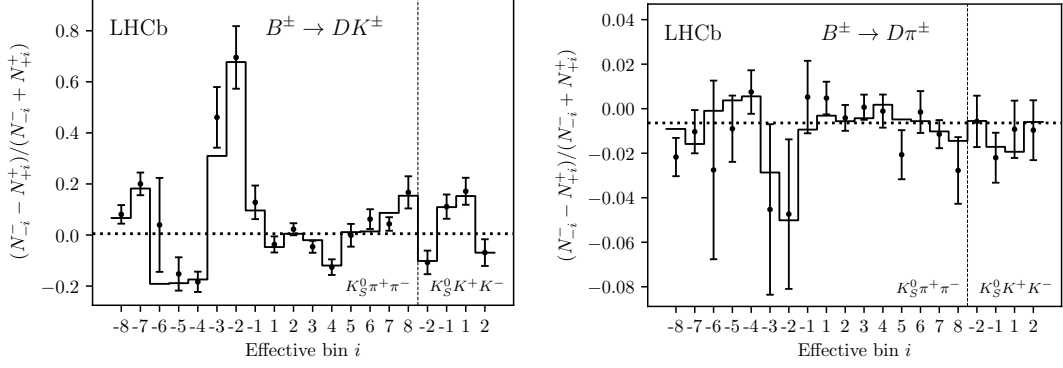


**Figure 5.43:** The bin-by-bin asymmetries  $(N_{-i}^- - N_{+i}^+)/N_{-i}^- + N_{+i}^+$  for each Dalitz-plot bin number for (left)  $B^\pm \rightarrow DK^\pm$  decays and (right)  $B^\pm \rightarrow D\pi^\pm$  decays. The prediction from the central values of the  $CP$ -violation observables is shown with a solid line and the asymmetries obtained in fits with independent bin yields are shown with the error bars. The predicted asymmetries in a fit that does not allow for  $CP$  violation are shown with a dotted line.

- Fig. 5.45a shows the two dimensional log likelihood contours for the observables for fits to the Run 1, 2015+16, 2017 and 2018 datasets separately
- Fig. 5.45b shows the same plots, comparing the fits to the data set split by whether the candidate event was triggered by one of the signal particles at the hardware level (TOS), or by another particle in the underlying event (TIS).
- Fig. 5.45c shows the same plots, comparing the fits to the data set split the magnet polarity during data taking.

All figures show the Gaussian likelihood contours corresponding to the statistical uncertainties. There is good agreement between the results in all cases, given that in each cases the sub datasets are independent and therefore the statistical errors are uncorrelated.

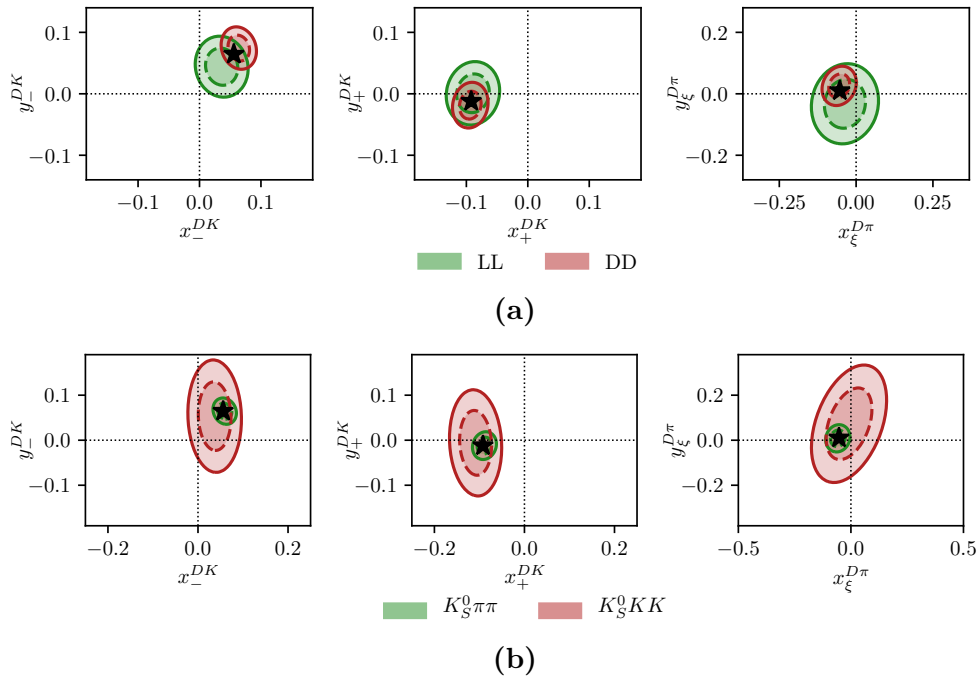


**Figure 5.44:** Comparison of the 68 % and 95 % confidence regions for (left)  $(x_-^{DK}, y_-^{DK})$ , (centre)  $(x_+^{DK}, y_+^{DK})$ , and (right)  $(x_\xi^{D\pi}, y_\xi^{D\pi})$  obtained from fits to sub sets of the data set. The uncertainties are statistical only. The central values of the default fit are shown with a black star. The dataset is split by (a) LL and DD  $K_S^0$  types and (b)  $D$  decay mode.

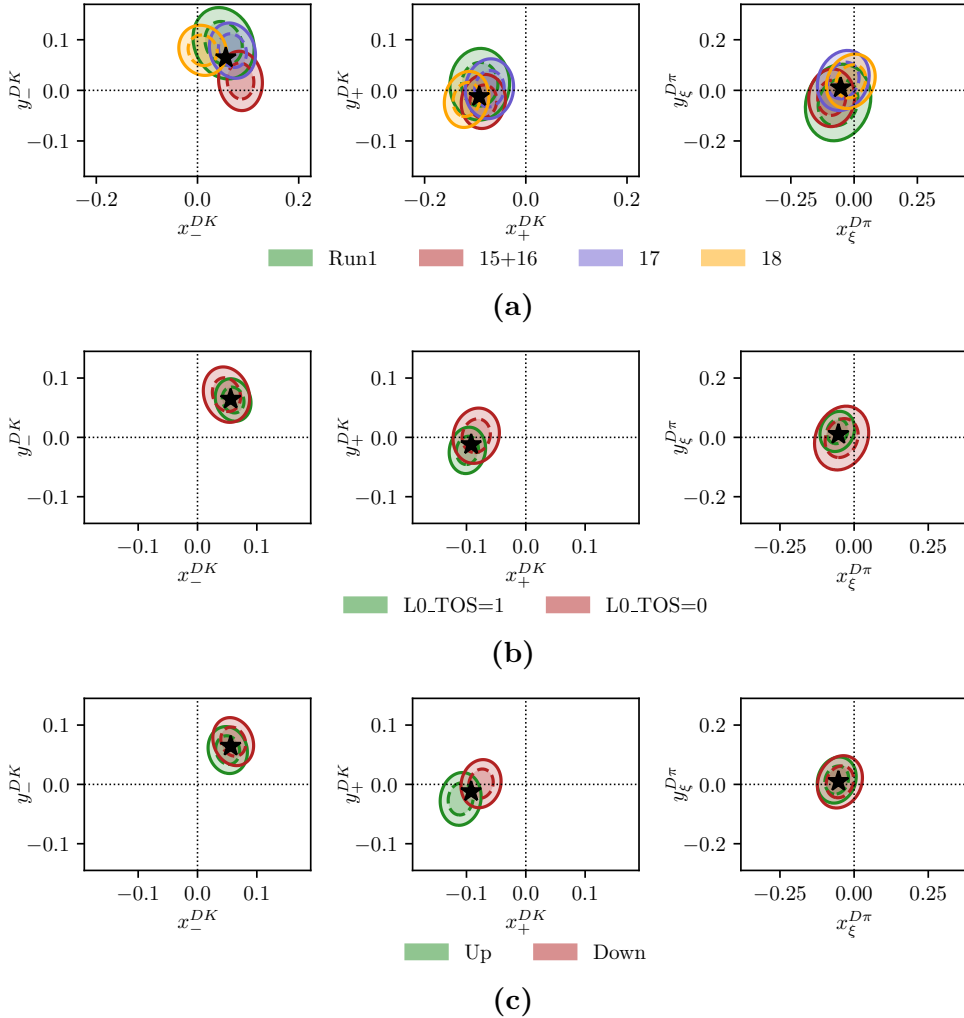


**Figure 5.45:** Comparison of the 68 % and 95 % confidence regions for (left)  $(x_-^{DK}, y_-^{DK})$ , (centre)  $(x_+^{DK}, y_+^{DK})$ , and (right)  $(x_\xi^{D\pi}, y_\xi^{D\pi})$  obtained from fits to sub sets of the data set. The uncertainties are statistical only. The central values of the default fit are shown with a black star. The dataset is split by (a) data taking year, (b) trigger category, and (c) magnet polarity.

### Constraints from a subset of bins

An alternative way to subdivide the data is to examine the constraints from a subset of bins individually; this forms as a cross check because the observables favoured by each sub set should be compatible, and also serves as a useful illustration of the features of the BPFGGSZ method. Likelihood contours for  $(x_\pm^{DK}, y_\pm^{DK})$  are shown in Fig. 5.46, obtained using the binned yields in the  $D \rightarrow K_S^0 \pi^+ \pi^-$  bins, determined in the fits of individual bin yields described in Section 5.5.3. The bins are split by whether they are ADS-like, GLW-like, or Odd-even according to the classification in Section 2.3.5. It is clear that the likelihood regions show a reasonable overlap, and also how it is the GLW bins that constrain the  $x_\pm$  parameter, while the Odd-even and ADS-like bins provide the ability to constrain the  $y_\pm$  parameters.

### Significantly reducing the $B^\pm \rightarrow D\pi^\pm$ to $B^\pm \rightarrow DK^\pm$ cross feed

One of the dominant backgrounds in the signal region of the  $B^\pm \rightarrow DK^\pm$  channel is from partly reconstructed  $B \rightarrow D\pi X$  decays where the companion pion is misidentified as a kaon. The background mode is well described by the included shape component, and included in all relevant systematic studies. Nevertheless, an additional cross check is carried out to ensure that it is not having a significant effect on the fit: the analysis is repeated with PID requirement of  $\text{PID}_K > 12$  required to place a candidate in the  $B^\pm \rightarrow DK^\pm$  category, instead of  $\text{PID}_K > 4$ . With this requirement 99.7 % of  $B^\pm \rightarrow D\pi^\pm$  decays are correctly identified, making the cross-feed component in the  $B^\pm \rightarrow DK^\pm$  channels significantly smaller than in the default fit. This is clearly visible in Fig. 5.47, where the fit projections for the global fit of the  $D \rightarrow K_S^0 \pi^+ \pi^-$  modes are shown. In return, the probability of correctly identifying a kaon companion drops to about 68–69 %, resulting in a smaller effective signal yield.

The measurement results are compared in Table 5.13, where the differences in central value are seen to be reasonably small. It is not trivial to determine whether the difference is statistically significant or not: the same candidates are analysed in both cases, the difference being that a number of candidates that are placed in the  $B^\pm \rightarrow DK^\pm$  category in the nominal fit are placed in the  $B^\pm \rightarrow D\pi^\pm$  category in the alternative fit. The uncertainty will not be 100 % correlated because signal events that move from the  $DK$  to  $D\pi$  category are placed in a region with high background; however, this is somewhat compensated for by candidates that remain in the  $DK$  category gaining statistical power due to the increased purity. An estimate of the expected statistical fluctuation can be determined by taking the difference of the statistical uncertainties in quadrature. Using this estimate, the observed shifts are found to be consistent with statistical fluctuation, and thus there is no sign of the background from  $D\pi^\pm \rightarrow DK^\pm$  cross-feed causing issues.

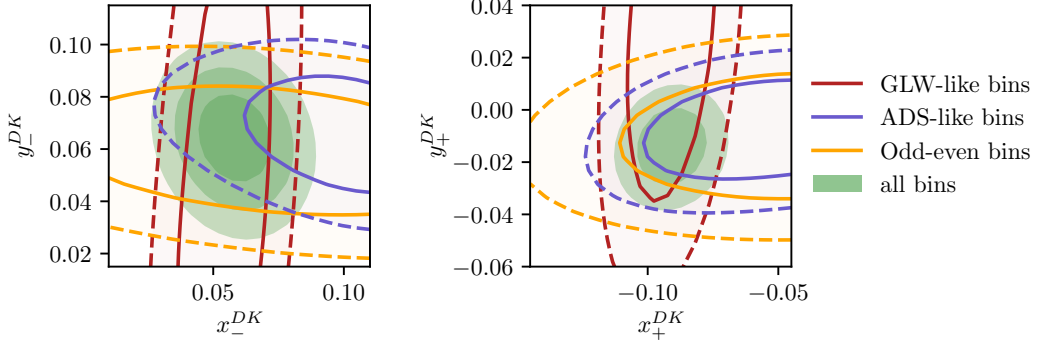


**Figure 5.46:** Constraints on the  $B^\pm \rightarrow DK^\pm$  observables from the signal yields of different subsets the  $D \rightarrow K_S^0 \pi^+ \pi^-$  Dalitz bins, using the bin categorisation developed in Section 2.3.5.

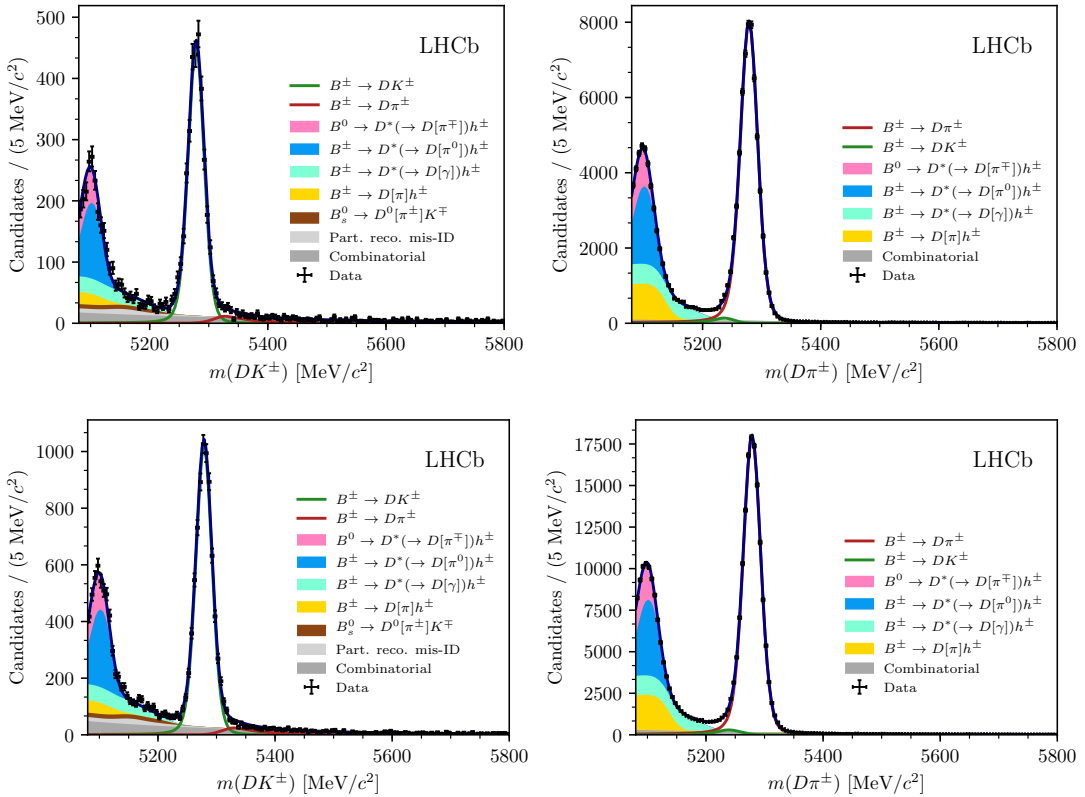


**Figure 5.47:** Fit projections for fits to the  $D \rightarrow K_S^0 \pi^+ \pi^-$  candidates with a companion PIDK requirement at 12 instead of 4 used to split into (left)  $B^\pm \rightarrow DK^\pm$  and (right)  $B^\pm \rightarrow D\pi^\pm$  candidates, for the (top) LL and (bottom) DD categories.

**Table 5.13:** Results of running the measurement with the default PIDK requirement at 4 used to separate  $B^\pm \rightarrow DK^\pm$  and  $B^\pm \rightarrow D\pi^\pm$  candidates, as well as with an alternative PIDK requirement at 12, resulting in much lower cross-feed from misidentified  $B^\pm \rightarrow D\pi^\pm$  decays. We also show the pulls, defined as  $\Delta x / \sqrt{|\sigma_{PIDK>12}^2 - \sigma_{PIDK>4}^2|}$  as described in the main text body. The comparison was made before the BESIII measurement of the  $D \rightarrow K_S^0 K^+ K^-$  strong-phase inputs became available; therefore the fits use the CLEO-only results [70] for this mode, which explains why the results quoted for  $PIDK > 4$  differ slightly from the nominal fit results.

| Parameter      | $PIDK > 4$       | $PIDK > 12$      | $\sigma = \sqrt{\sigma_{PIDK>12}^2 - \sigma_{PIDK>4}^2}$ | Pull |
|----------------|------------------|------------------|--|------|
| $x_-^{DK}$     | $5.59 \pm 0.96$  | $5.82 \pm 1.01$  | 0.30   | 0.77 |
| $y_-^{DK}$     | $6.45 \pm 1.14$  | $6.86 \pm 1.19$  | 0.36   | 1.13 |
| $x_+^{DK}$     | $-9.21 \pm 0.96$ | $-8.94 \pm 1.01$ | 0.30   | 0.93 |
| $y_+^{DK}$     | $-1.21 \pm 1.20$ | $-0.94 \pm 1.26$ | 0.37   | 0.71 |
| $x_\xi^{D\pi}$ | $-5.30 \pm 1.99$ | $-5.13 \pm 2.02$ | 0.32   | 0.52 |
| $y_\xi^{D\pi}$ | $1.03 \pm 2.34$  | $1.71 \pm 2.33$  | 0.28   | 2.40 |

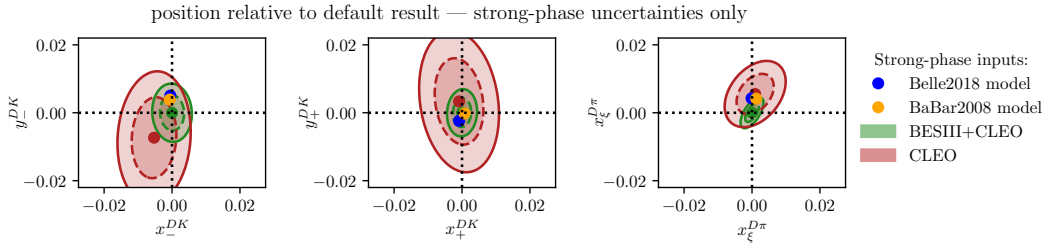


**Figure 5.48:** Fit results for (left)  $(x_-^{DK}, y_-^{DK})$ , (centre)  $(x_+^{DK}, y_+^{DK})$ , and (right)  $(x_\xi^{D\pi}, y_\xi^{D\pi})$  depending on strong-phase inputs, shown relative to the default fit results. The included results are based on (green) the BESIII-CLEO combination, which is the default, (red) the CLEO-only results, (blue dot) the 2018 Belle model [50] and (orange dot) the 2008 BaBar model [58]. For the measurements, only strong-phase related uncertainties are included in the plotted confidence regions.

### Compare results obtained with different strong-phase inputs

It is interesting to compare the results obtained with different strong-phase inputs. This is done in Fig. 5.48, where the default fit results are compared to those obtained if the  $CP$  fit is done with the CLEO-only inputs [70], and with the model predictions from the 2018 Belle model [50] and the 2008 BaBar model [58]. For the measurements, only the strong-phase-related uncertainties are included in the plot, since the statistical uncertainties are correlated. All results are found to agree well.

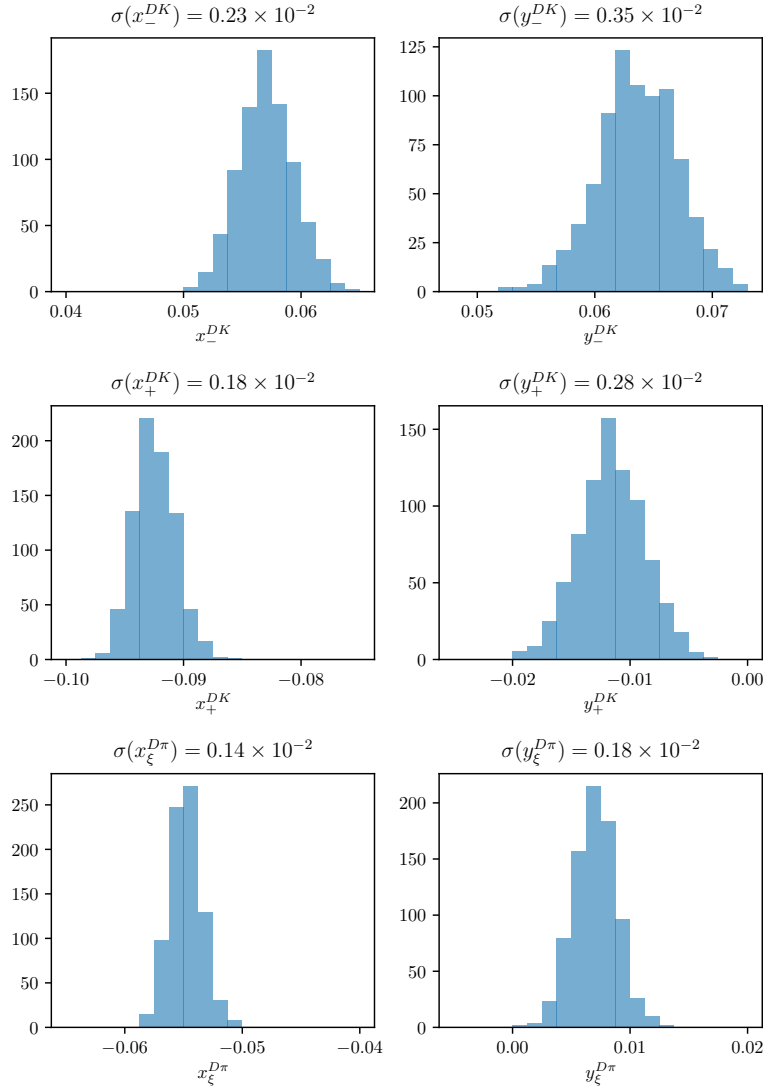


**Figure 5.49:** Distribution of the central values for the obtained observables when the input  $c_i$  and  $s_i$  from the BESIII+CLEO combination are varied according to their uncertainties and correlations in the fit to data.

## 5.6 Systematic uncertainties

The following sections cover the suite of systematic uncertainties on the measurement that has been considered. All uncertainties are summarised in Section 5.6.12.

### 5.6.1 Strong phase uncertainties

The observables  $x_\pm^{DK}$ ,  $y_\pm^{DK}$ ,  $x_\xi^{D\pi}$  and  $y_\xi^{D\pi}$  are extracted using the central values of  $c_i$  and  $s_i$  from the BESIII–CLEO combinations [70–72]. The measurement uncertainty on these inputs is propagated to the observables by performing a large set of fits to data that use alternative values of  $c_i$  and  $s_i$ . The new  $c_i$  and  $s_i$  values are

**Table 5.14:** Systematic uncertainties and correlation matrix due to strong-phase inputs.

| Uncertainty ( $\times 10^{-2}$ ) |            |            |            |            |                |                |
|----------------------------------|------------|------------|------------|------------|----------------|----------------|
|                                  | $x_-^{DK}$ | $y_-^{DK}$ | $x_+^{DK}$ | $y_+^{DK}$ | $x_\xi^{D\pi}$ | $y_\xi^{D\pi}$ |
| $\sigma$                         | 0.23       | 0.35       | 0.18       | 0.28       | 0.14           | 0.18           |

| Correlations      |            |            |            |            |                |                |
|-------------------|------------|------------|------------|------------|----------------|----------------|
|                   | $x_-^{DK}$ | $y_-^{DK}$ | $x_+^{DK}$ | $y_+^{DK}$ | $x_\xi^{D\pi}$ | $y_\xi^{D\pi}$ |
| $x_-^{DK\pm}$     | 1.000      | -0.047     | -0.490     | 0.322      | 0.189          | 0.144          |
| $y_-^{DK\pm}$     |            | 1.000      | 0.059      | -0.237     | -0.116         | -0.117         |
| $x_+^{DK\pm}$     |            |            | 1.000      | 0.061      | 0.004          | -0.139         |
| $y_+^{DK\pm}$     |            |            |            | 1.000      | 0.127          | -0.199         |
| $x_\xi^{D\pi\pm}$ |            |            |            |            | 1.000          | 0.638          |
| $y_\xi^{D\pi\pm}$ |            |            |            |            |                | 1.000          |

obtained by smearing the central values by their measured statistical and systematic uncertainties while taking into account their correlations. The use of different  $c_i$  and  $s_i$  values changes the extracted  $x_\pm^{DK}$ ,  $y_\pm^{DK}$ ,  $x_\xi^{D\pi}$  and  $y_\xi^{D\pi}$  values. The standard deviation of the distributions of central values extracted from 1000 data fits are assigned as a systematic uncertainty. The distributions are shown in Fig. 5.49 and the assigned uncertainties are summarised in Table 5.14. The correlation matrix related to the strong-phase uncertainty can be obtained from the correlations observed between observables in the fits, and is also given in the table.

The set of  $(c_i, s_i)$  that was employed in this analysis will be used in a series of future BPFGGSZ measurements, both with additional  $B$  decay modes within the LHCb collaboration and by the Belle II collaboration. This introduces some correlation between the measurement results. In order to allow for an estimate of the degree of correlation by future analysts, the 1000 sampled  $(c_i, s_i)$  values and the corresponding fit results for  $(x_\pm^{DK}, y_\pm^{DK}, x_\xi^{D\pi}, y_\xi^{D\pi})$  will be made public as supplementary material to Ref. [1].

### 5.6.2 Efficiency-profile-related systematic uncertainties

The non-trivial efficiency profile over the Dalitz plot,  $\eta(s_-, s_+)$ , can have a range of effects, considered in the sections below.

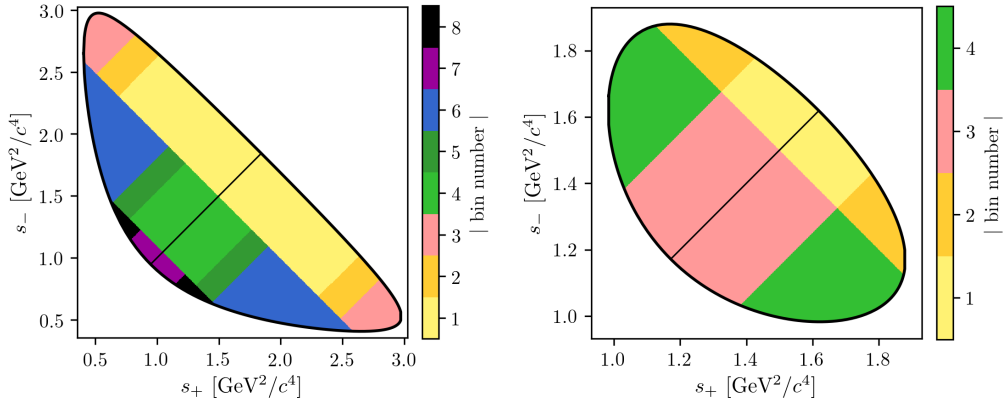


**Figure 5.50:** The rectangular binning schemes used to group candidates in (left) the  $D \rightarrow K_S^0 \pi^+ \pi^-$  and (right) the  $D \rightarrow K_S^0 K^+ K^-$  categories in a number of systematic uncertainty studies.

#### The assumption that $\eta^{DK}(s_-, s_+) = \eta^{D\pi}(s_-, s_+)$

The assumption that the acceptance profile over the  $D$ -decay Dalitz plot is identical between  $B^\pm \rightarrow DK^\pm$  and  $B^\pm \rightarrow D\pi^\pm$  decays was examined in detail in Section 5.2.2. It was found that with signal yields similar to those in the data set, no statistically significant difference between the efficiency profiles  $\eta^{DK}(s_-, s_+)$  and  $\eta^{D\pi}(s_-, s_+)$  was discernible, and no additional uncertainty due to this assumption is assigned.

#### The assumption that $\eta(s_-, s_+) = \eta(s_+, s_-)$

The measurement is sensitive to effects that break the assumption  $\eta(s_-, s_+) = \eta(s_+, s_-)$ . Such a breakdown would mean that opposite points on the Dalitz plot have different efficiencies and can only arise through a charge detection asymmetry (e.g that it is more likely to detect a  $K^+$  in the detector rather than a  $K^-$ ).<sup>8</sup>

The potential size of such an asymmetry can be studied in simulation where the  $D$  decay has a uniform distribution over the allowed phase space; in such simulated samples, it would manifest itself as an observation of different fractional yields of  $B^-$  decays in bin  $i$  and  $B^+$  decays in bin  $-i$ . This effect has been looked for using the large samples of  $B^\pm \rightarrow D\pi^\pm$  decays that were generated for the analysis of 2015 and 2016 data. The study is performed using the rectangular binning schemes shown in Fig. 5.50, because this scheme is most sensitive to effects that vary smoothly over phase space. The comparison plots are shown in Fig. 5.51, where it can be seen that the  $p$  values for the hypothesis that there is no asymmetry all take on reasonable values. Hence no further systematic uncertainty is considered.

<sup>8</sup>Note that the measurement is insensitive to any asymmetry in the reconstruction of the companion track.

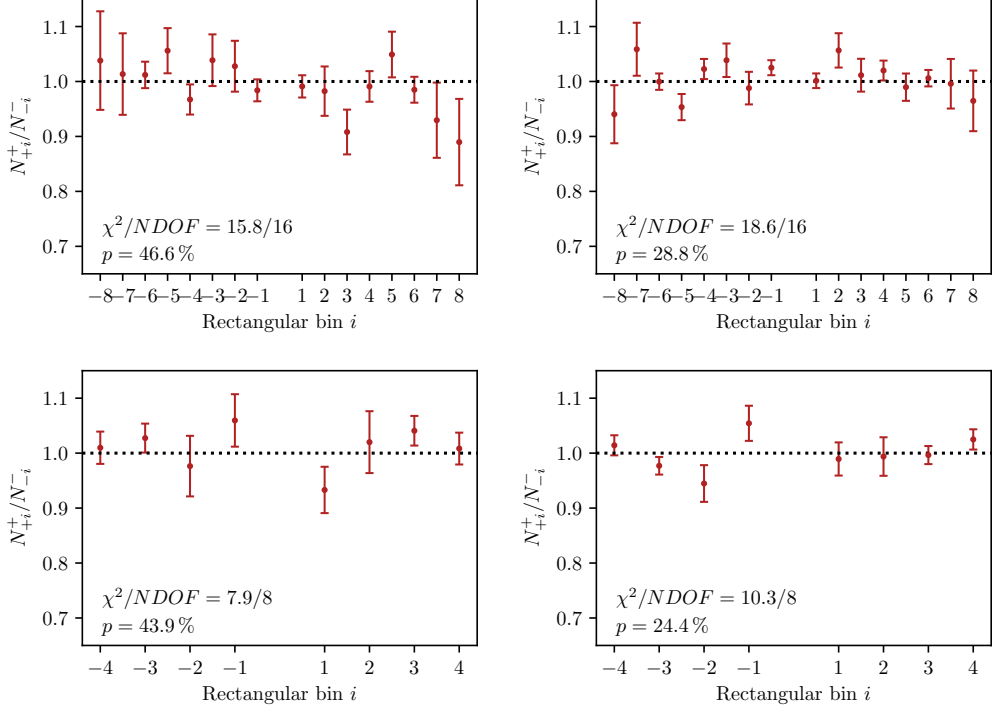


**Figure 5.51:** Comparison of the ratio of  $B^+$  decays reconstructed in bin  $+i$  to  $B^-$  decays reconstructed in bin  $-i$  for simulated  $B^\pm \rightarrow D\pi^\pm$  decays where (top)  $D \rightarrow K_S^0 \pi^+ \pi^-$  and (bottom)  $D \rightarrow K_S^0 K^+ K^-$ , also split into (left) the LL and (right) the DD categories, using the rectangular binning schemes in Fig. 5.50. Calculated  $p$  values for the hypothesis that the ratio is flat are also shown, all of them being at least 20 %.

### Effect of the phase-space efficiency profile on $c_i$ and $s_i$

As discussed in Section 2.4 there is a small bias, because the  $c_i$  and  $s_i$  values that are used correspond to the definition

$$c_i = \frac{\int_i ds^2 |A_S^D(s_{-+})| |A_S^D(s_{+-})| \cos[\Delta\delta_D(s_{-+})]}{\sqrt{\int_i ds^2 |A_S^D(s_{-+})|^2} \sqrt{\int_i ds^2 |A_S^D(s_{+-})|^2}}, \quad (\text{and equivalent for } s_i,) \quad (5.25)$$

whereas the non-flat efficiency profile in LHCb,  $\eta(s_-, s_+) \equiv \eta(s_{-+})$ , means that the appropriate  $c_i$  and  $s_i$  entering the exact yield expressions are actually given by

$$c_i^{\text{eff}} = \frac{\int_i ds^2 \eta(s_{-+}) |A_S^D(s_{-+})| |A_S^D(s_{+-})| \cos[\Delta\delta_D(s_{-+})]}{\sqrt{\int_i ds^2 \eta(s_{-+}) |A_S^D(s_{-+})|^2} \sqrt{\int_i ds^2 \eta(s_{-+}) |A_S^D(s_{+-})|^2}}, \quad (\text{and equivalent for } s_i^{\text{eff}}.) \quad (5.26)$$

The shifts  $\Delta c_i = c_i^{\text{eff}} - c_i$ ,  $\Delta s_i = s_i^{\text{eff}} - s_i$  can be estimated using the efficiency profile in simulation and the latest amplitude models: the 2018 Belle model [50] for  $D \rightarrow K_S^0 \pi^+ \pi^-$  and the 2010 BaBar model [59] for  $D \rightarrow K_S^0 K^+ K^-$ . The strong-phase parameters are first calculated assuming a uniform reconstruction efficiency

**Table 5.15:** The  $c_i$  and  $s_i$  values for  $D \rightarrow K_S^0 \pi^+ \pi^-$  decays calculated via the 2018 Belle model [50] in two cases: assuming a uniform reconstruction efficiency over phase space, denoted  $(c/s)_i^{\text{model}}$ , and including the LHCb efficiency profile as obtained in simulation, averaged for LL and DD, denoted  $(c/s)_i^{\text{eff}}$ . The change due to including the efficiency is also tabulated.

| Bin | $c_i^{\text{model}}$ | $c_i^{\text{eff}}$ | $\Delta c_i$ | $s_i^{\text{model}}$ | $s_i^{\text{eff}}$ | $\Delta s_i$ |
|-----|----------------------|--------------------|--------------|----------------------|--------------------|--------------|
| 1   | -0.027               | -0.007             | 0.019        | 0.812                | 0.794              | -0.018       |
| 2   | 0.837                | 0.859              | 0.022        | 0.164                | 0.152              | -0.012       |
| 3   | 0.163                | 0.163              | -0.000       | 0.872                | 0.880              | 0.008        |
| 4   | -0.914               | -0.915             | -0.001       | 0.076                | 0.082              | 0.006        |
| 5   | -0.149               | -0.170             | -0.021       | -0.856               | -0.854             | 0.002        |
| 6   | 0.373                | 0.362              | -0.011       | -0.782               | -0.805             | -0.023       |
| 7   | 0.863                | 0.862              | -0.000       | -0.203               | -0.202             | 0.002        |
| 8   | 0.860                | 0.862              | 0.002        | 0.330                | 0.336              | 0.006        |

**Table 5.16:** The  $c_i$  and  $s_i$  values for  $D \rightarrow K_S^0 K^+ K^-$  decays calculated via the 2010 BaBar model [59] in two cases: assuming a uniform reconstruction efficiency over phase space, denoted  $(c/s)_i^{\text{model}}$ , and including the LHCb efficiency profile as obtained in simulation, averaged for LL and DD, denoted  $(c/s)_i^{\text{eff}}$ . The change due to including the efficiency is also tabulated.

| Bin | $c_i^{\text{model}}$ | $c_i^{\text{eff}}$ | $\Delta c_i$ | $s_i^{\text{model}}$ | $s_i^{\text{eff}}$ | $\Delta s_i$ |
|-----|----------------------|--------------------|--------------|----------------------|--------------------|--------------|
| 1   | 0.738                | 0.735              | -0.002       | 0.266                | 0.263              | -0.003       |
| 2   | -0.697               | -0.744             | -0.046       | 0.332                | 0.329              | -0.003       |

over phase space according to Eq. (5.25), obtaining a set of values  $\{c_i^{\text{model}}, s_i^{\text{model}}\}$ . Then, an alternative set is calculated,  $\{c_i^{\text{eff}}, s_i^{\text{eff}}\}$ , using the same model, and the reconstruction efficiency profile found in full LHCb simulation. The LHCb reconstruction efficiency at a given point in phase-space is taken to be proportional to the yield in simulation, as the simulated decays were generated with a uniform distribution over phase space. The efficiency is averaged over the LL and DD categories in the calculation, according to the relative signal yields in these categories. The results, as well as their differences, are tabulated in Tables 5.15 and 5.16.

A systematic uncertainty due to employing the measured  $c_i$  and  $s_i$  directly in the fit is assigned by generating a large number of simulated data sets where the signal yields are calculated using  $(c_i^{\text{eff}}, s_i^{\text{eff}})$ , and then fitting the data sets using  $(c_i^{\text{model}}, s_i^{\text{model}})$ . The mean bias of each observable in these fits is assigned as the systematic uncertainty, and is determined to be  $0.1 \times 10^{-2}$  or less for all observables. The smallness of the effect is the reason no effort is made to correct the  $c_i$  and  $s_i$  values in the nominal measurement.

### 5.6.3 Mass shapes

A number of uncertainties relate to the mass distributions that enter the fit model. Each is described in detail the sections below.

#### Determination of shape parameters

The statistical uncertainties on the shape parameters that are obtained in fits to simulated decays and in the first stage fit to data need to be propagated to the uncertainty on the obtained parameters. This is done via a bootstrapping procedure [156], repeating these steps many times:

- Each of the data sets used to determine parameters of the signal, crossfeed, and lowmass shapes that are fixed in the first-stage fit to data of Section 5.4 are re-sampled with replacement, drawing a number of events equal to the original data-set size. These are from simulation for signal and lowmass shapes, and real data for the crossfeed shapes. All of the shapes are fit again, on the re-sampled data sets.
- The real dataset is re-sampled with replacement, drawing a number of events equal to the original data-set size. Then, the first-stage fit of Section 5.4 is repeated with the shapes obtained as described above, obtaining values for the remaining shape parameters.
- Finally, the *CP* fit is repeated using the shape parameters determined in the preceding steps, but *without* re-sampling the dataset (to avoid a statistical spread in the obtained central values that is independent of the shape parameters).

The uncertainty on each observable is taken to be the standard deviation of the set of central values obtained as described above. This procedure propagates the statistical uncertainty on the fixed parameters to the observables, in a way that takes correlations into account, and which does not rely on the uncertainty estimates in the preliminary fits being accurate. The uncertainties are less than  $0.1 \times 10^{-2}$  for all  $DK^\pm$  observables and less than  $0.2 \times 10^{-2}$  for all  $D\pi^\pm$  observables.

A potential bias arises due the use of the sPlot method when obtaining the mass distribution of decays where a  $\pi \leftrightarrow K$  misidentification has taken place. This is because the  $m_{\text{swap}}(Dh^\pm)$  mass that is calculated while assuming a swapped companion hypothesis and the nominal  $m_{\text{default}}(Dh^\pm)$  mass are correlated (it is always the case that  $m_{\text{swap}} > m_{\text{default}}$  for a  $\pi \rightarrow K$  misidentification, for example).

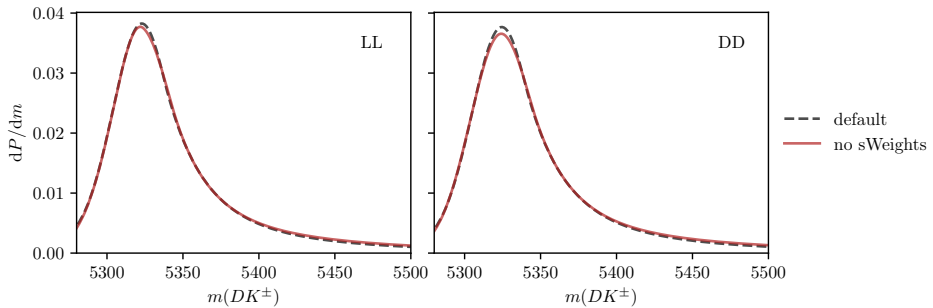


**Figure 5.52:** Comparison of the default and no-sWeights alternative shape for the  $D\pi \rightarrow DK$  cross-feed component in the (left) LL and (right) DD categories where  $D \rightarrow K_S^0 \pi^+ \pi^-$ . The binned fit obtains essentially the same central values for the  $CP$ -violation observables, independently of which shape is used.

Thus, the assumptions of the sPlot method are not satisfied [145]. The correlation coefficient in the signal region is about 20 % for simulated signal decays. In order to assess the potential impact, an alternative mass distribution for  $(B^\pm \rightarrow D\pi^\pm) \rightarrow (B^\pm \rightarrow DK^\pm)$  cross-feed is derived that does not rely on sWeights. Instead of fitting  $B^\pm \rightarrow D\pi^\pm$  sample in the whole fit range and assigning sWeights before recalculating the  $B$  mass under the kaon companion hypothesis, the shape is obtained using  $B^\pm \rightarrow D\pi^\pm$  candidates in the signal region. This is possible because the  $B^\pm \rightarrow D\pi^\pm$  sample is very pure. The shapes are compared in Fig. 5.52 and are seen to be almost identical. Thus the sWeights do successfully subtract the contribution of combinatorial and partially reconstructed backgrounds in the default setup. The impact on the obtained  $CP$ -violation observables of using one or the other shape in the fits is negligible, and no further systematic uncertainty is assigned due to this effect.

### Using the same mass shapes in all Dalitz bins

The mass shapes obtained the first-stage fit where all Dalitz bins are combined, are used in each individual bin of the subsequent binned fit. However, there could be some variation in the shape over the  $D$ -decay phase space, due to correlations between the phase-space coordinates and particle kinematics. The potential effect is investigated in pseudo experiments, where simulated data sets are generated with alternative signal, cross-feed, and combinatorial-background shapes that are allowed to differ between bins, and fitted with the default shapes. The partially reconstructed background is treated in a separate study, because further physics effects contribute to bin-by-bin variation, as described in the following section.

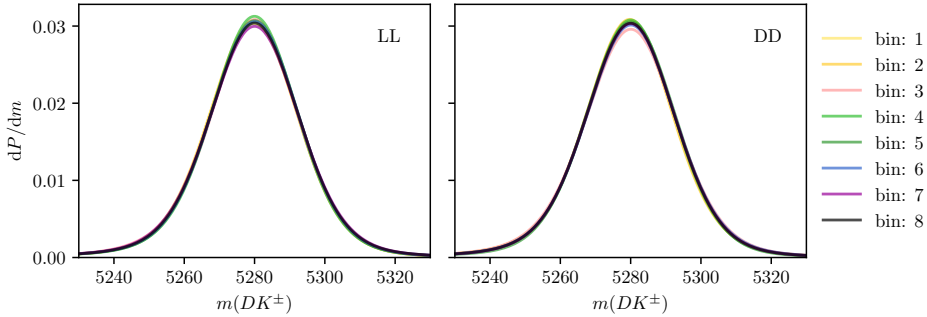


**Figure 5.53:** Signal shapes obtained in fits simulated  $B^\pm \rightarrow D\pi^\pm$  decays for individual Dalitz bins in the optimal binning scheme, for (left) LL and (right) DD candidates in the  $B^\pm \rightarrow D(\rightarrow K_S^0\pi^+\pi^-)\pi^\pm$  category.

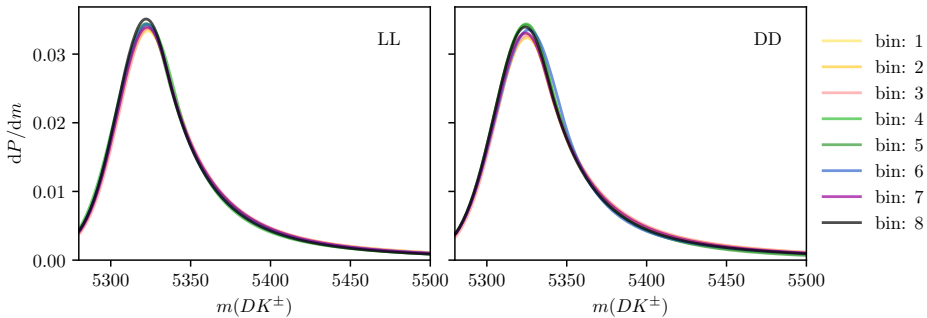


**Figure 5.54:** Mass shapes for  $D\pi \rightarrow DK$  cross feed obtained for individual Dalitz bins in the optimal binning scheme, for (left) LL and (right) DD candidates in the  $D \rightarrow K_S^0\pi^+\pi^-$  category.

The alternative signal and cross-feed mass shapes are fitted independently in each bin, following identical procedures to those outlined in Sections 5.4.1 and 5.4.2. Examples of the obtained shapes are compared in Figs. 5.53 and 5.54.

The shape of the combinatorial background can also vary over the  $D$  decay phase-space; for example, the relative amount of fake  $D$  candidates versus real  $D$  decays paired with a random companion certainly depends on the real  $D$ -decay amplitude for a given phase-space region. The effect is investigated in the high  $B$ -mass sideband  $m_B \in [5600, 6500] \text{ MeV}/c^2$ , in which the  $m(Dh^\pm)$  distribution is fitted with a single exponential distribution, in bins of the Dalitz plot. The fits combine  $B^+$  and  $B^-$  candidates and merge bins  $+i$  and  $-i$ , and are carried out for both the *optimal* binning scheme of Fig. 2.7 (on page 24) and a *rectangular* binning scheme, shown in Fig. 5.50, which better captures continuous trends over the Dalitz plot. The study is done for  $D \rightarrow K_S^0\pi^+\pi^-$  only due to available statistics. The DD category of  $B^\pm \rightarrow D\pi^\pm$  decays has the largest yield and shows the largest variation, and the fitted slopes for this channel are shown in Fig. 5.55. Two effects are visible:

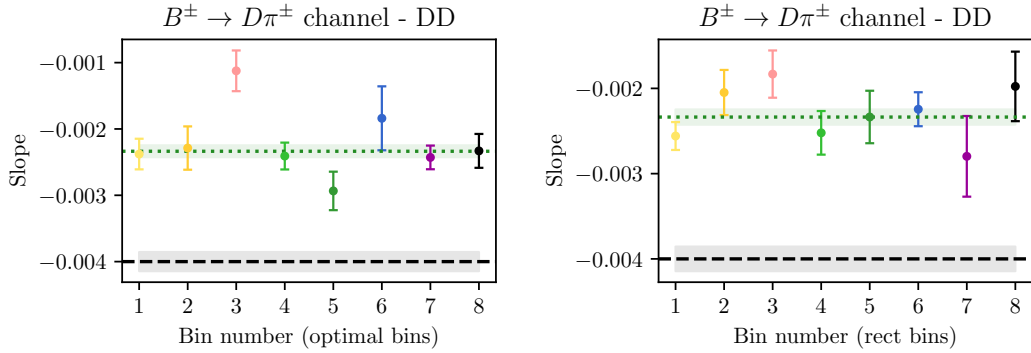


**Figure 5.55:** Plot of (dots) combinatorial slope in the high  $B$  mass background for each bin in the (left) the optimal binning scheme and (right) the rectangular binning scheme, for the DD  $B^\pm \rightarrow D(\rightarrow K_S^0 \pi^+ \pi^-) \pi^\pm$  category. The slope when all bins are combined (green, dashed line) is also shown, and compared with (black dashed line) the slope in the default fit region.

1) there is some variation in the slope as a function of the Dalitz bin, especially visible for the rectangular scheme, and 2) the exponential slope is larger in general in the high  $B$ -mass sideband than in the signal region. The latter effect does not pose a problem, since the employed exponential is found to provide an excellent fit in the default fit region. It does however need to be taken into account when deriving alternative, bin-dependent combinatorial slopes relevant for the default fit region. In order to do so, the alternative slope for bin  $i$  is defined

$$\alpha_{\text{default-range}}^i = \frac{\alpha_{\text{high-}m_B}^i}{\alpha_{\text{high-}m_B}^{\text{all-}DP}} \times \alpha_{\text{default-range}}^{\text{all-}DP}, \quad (5.27)$$

and used when generating the combinatorial-background component of the simulated data sets for the study.

The average bias obtained for each observable in the ensemble of pseudo-experiments is assigned as a systematic uncertainty, found to be about  $0.1 \times 10^{-2}$  for each observable.

### Ignoring physics effects in the lowmass background

In the  $CP$  fit, the same relative fractions of partly reconstructed  $B^\pm$  and  $B^0$  backgrounds are used in each bin, as determined in the first-stage fit described in Section 5.4 (whereas the partly reconstructed  $B_s^0 \rightarrow \bar{D}^0[\pi^+]K^-$  background is treated separately). However the distribution over the Dalitz plot depends on whether the partly reconstructed decays occur via an intermediate  $D^0$  meson, a  $\bar{D}^0$  meson, or an admixture of both. Consider a decay reconstructed as  $B^- \rightarrow DK^-$  but which is actually a partially-reconstructed background. There are then four types of background that should be considered:

- Decays in which the  $D$ -meson in the true decay is a  $D^0$ -meson. An example of this is  $B^- \rightarrow D^{*0}(D^0\pi^0)\pi^-$  for which the  $\pi^0$  from the  $D^{*0}$  decay is missed and the  $\pi^-$  is misidentified as the companion  $K^-$ . These are denoted ‘ $D^0$ -like’.<sup>9</sup>
- Decays in which the  $D$ -meson in the true decay is a  $\bar{D}^0$ -meson. An example of this is  $B_s^0 \rightarrow \bar{D}^0\pi^+K^-$  for which the  $\pi^+$  is missed and the  $K^-$  is reconstructed as the companion  $K^-$ . These are denoted ‘ $\bar{D}^0$ -like’.
- Decays in which the  $D$  meson in the true decay can be either flavour, and both  $D$  flavours contribute to the decay amplitude. An example of this is  $B^- \rightarrow D^*K^-$  for which the total decay amplitude into a  $D$  final state has contributions from both  $D^{*0}$  (decaying to  $D^0$ ) and  $\bar{D}^{*0}$  (decaying to  $\bar{D}^0$ ). The relative amplitude magnitude and phase between the two possible  $B$  decays are denoted  $r_B^{D^*}$  and  $\delta_B^{D^*}$  respectively. These are denoted ‘ $r_B$ -like’.
- Decays that can be reconstructed as both  $D^0$ - and  $\bar{D}^0$ -like but where there is no quantum-mechanical interference. An example is  $\bar{B}^0 \rightarrow D^0\pi^+\pi^-$  decays where either the  $\pi^+$  or  $\pi^-$  can be reconstructed as the companion particle.<sup>10</sup> These are denoted 50/50  $D^0$ -like and  $\bar{D}^0$ -like.

For  $B^+ \rightarrow DK^+$  decays everything is  $CP$  conjugated. The Dalitz-plot distribution for each of these cases is:

- $D^0$  decays (‘ $D^0$ -like’)

$$\begin{aligned} N_{\pm i}(B^-) &\propto F_{\pm i} \\ N_{\pm i}(B^+) &\propto F_{\mp i} \end{aligned} \tag{5.28}$$

- $\bar{D}^0$  decays (‘ $\bar{D}^0$ -like’):

$$\begin{aligned} N_{\pm i}(B^-) &\propto F_{\mp i} \\ N_{\pm i}(B^+) &\propto F_{\pm i} \end{aligned} \tag{5.29}$$

- Decays with a quantum-mechanical admixture of  $D^0$  and  $\bar{D}^0$  (‘ $r_B$ -like’):

$$\begin{aligned} N_{\pm i}(B^-) &\propto F_{\pm i} + (r_B^*)^2 F_{\mp i} + 2\sqrt{F_{+i}F_{-i}}[x_{-}^*c_{\pm i} + y_{-}^*s_{\pm i}] \\ N_{\pm i}(B^+) &\propto F_{\mp i} + (r_B^*)^2 F_{\pm i} + 2\sqrt{F_{+i}F_{-i}}[x_{+}^*c_{\pm i} - y_{+}^*s_{\pm i}] \end{aligned} \tag{5.30}$$

where  $(x_{\pm}^*, y_{\pm}^*)$  are defined analogously to the standard  $B^\pm \rightarrow DK^\pm$  case.

---

<sup>9</sup>The naming convention is defined in terms of the  $D$  present in candidates reconstructed as  $B^-$  decays. For the charge conjugate case this decay would of course happen via a  $\bar{D}^0$ , but is still denoted  $D^0$ -like.

<sup>10</sup>This mode is likely to show a small amount of  $CP$  violation, similar to  $B^\pm \rightarrow D\pi^\pm$  decays. However, it is a very good approximation that a true  $D^0$  will be reconstructed with a positive or negative companion with equal probability.

- 50/50  $D^0$ -like and  $\bar{D}^0$ -like:

$$\begin{aligned} N_{\pm i}(B^-) &\propto F_{\pm i} + F_{\mp i} \\ N_{\pm i}(B^+) &\propto F_{\pm i} + F_{\mp i} \end{aligned} \quad (5.31)$$

The use of a single background shape across all bins may therefore introduce biases because such a shape has no sensitivity to the bin-to-bin variations that will arise if an admixture of these backgrounds is present.

In the  $D\pi$  channel, the dominant backgrounds are all  $D^0$ -like ( $\bar{B}^0 \rightarrow D^{*-}\pi^0$ ,  $B^- \rightarrow D^0\rho^-$ ,  $B^- \rightarrow D^{*0}\pi^-$ ). There is a small contribution from  $\bar{B}^0 \rightarrow D^0\rho(\rightarrow \pi^+\pi^-)$  decays where either the  $\pi^+$  or  $\pi^-$  from the  $\rho^0$  decay can be assigned as the companion, and thus this background is 50/50  $D^0$ -like and  $\bar{D}^0$ -like (assuming negligible  $CP$  violation). The background only corresponds to about 0.5 % of the total partially reconstructed background and thus the impact is small. Nevertheless it is considered in the study described below.

In the  $DK$  channel all categories of background appear. In the mass region of the  $CP$  fit approximately 75.5% of backgrounds are  $D^0$ -like ( $\bar{B}^0 \rightarrow D^{*-}K^-$ , mis-identified  $B^- \rightarrow D^{*0}\pi^-$ , and mis-identified  $B^- \rightarrow D^0\rho^-$ ), 7.5 % are  $\bar{D}^0$ -like ( $B_s^0 \rightarrow \bar{D}^0\pi^+K^-$ ), 1% is 50/50  $D^0$ - $\bar{D}^0$ -like (mis-identified  $B^0 \rightarrow D\rho^0$ ; assuming negligible  $CP$  violation), and 16% are  $r_B$ -like ( $B^- \rightarrow D^*K^-$ ,  $B^0 \rightarrow DK^{*0}$ , and  $B^- \rightarrow DK^{*-}$ ).

In order to estimate the bias due to ignoring this effect, a large number of simulated data sets are generated using the default low mass shapes and total yields from the first-stage fit in Section 5.4, but distributing each of them individually over the Dalitz-bins according to Eqs. (5.28)-(5.30). When calculating the distribution of  $B^+ \rightarrow D^{*0}K^+$  decays over the Dalitz plot, the values [44]

$$r_B^{D^*} = 0.191 \quad \delta_B^{D^*} = 331.6^\circ \quad (5.32)$$

are used. When calculating the distribution of  $B^+ \rightarrow D^0K^{*+}$  decays over the Dalitz plot the values [44]

$$r_B^{K^*} = 0.092 \quad \delta_B^{K^*} = 40^\circ. \quad (5.33)$$

are used. The data sets are then fit with the default set up, and the observed mean bias assigned as the corresponding uncertainty. The corresponding uncertainties were found to be about  $0.1 \times 10^{-2}$  for all uncertainties. The variation in the shapes is rather small in the mass range included in the fit, which explains the small impact.

If the  $B_s^0$  background is *not* treated separately in the default fit, but instead included in a single lowmass background shape along with the  $B^0$  and  $B^\pm$  contributions, the systematic uncertainty is an order of magnitude larger when evaluated as described above, and would be a dominating systematic. This motivates the separate treatment of the  $B_s^0$  background.

### 5.6.4 $CP$ violation and material interaction of the $K_S^0$

A systematic uncertainty due to  $CP$ -violation effects and material interaction of the  $K_S^0$  is assigned using the results obtained in Section 4.3.7. In that section, the expected bias on each of the observables in a combined  $B^\pm \rightarrow Dh^\pm$  measurement was evaluated for the detector geometry and particle kinematics of the LHCb experiment. The calculation was made for  $(r_B^{DK/D\pi}, \delta_B^{DK/D\pi})$  values close to the world averages, and a number of  $\gamma$  values; the results were summarised in Fig. 4.8. The systematic uncertainty is taken to be the largest absolute bias observed for each parameter in the study. The largest uncertainty (on  $y_\xi^{D\pi}$  where it is  $0.46 \times 10^{-2}$ ) is still an order of magnitude smaller than the statistical uncertainty.

### 5.6.5 Impact of $D$ mixing

The effect of  $D$ -mixing is not accounted for in the measurement, which leads to a small bias. Earlier studies have shown this to lead to a sub-degree bias on measurements of  $\gamma$  in  $B^\pm \rightarrow DK^\pm$  decays, in the case where the  $F_i$  parameters are determined experimentally under the same experimental conditions as the  $\gamma$  measurement [157]. A number of pseudo experiments are carried out to verify that this is also the case for the combined  $DK^\pm-D\pi^\pm$  setup employed in the thesis. They are performed following the same procedure described in Section 5.6.4 for the case of neutral-kaon  $CP$  violation. The yields are calculated while taking  $D$  mixing into account, using the mixing parameter values  $x = (0.39^{+0.11}_{-0.12})\%$  and  $y = (0.65^{+0.06}_{-0.07})\%$  [28], and then fitted back assuming no  $D$  mixing. The biases are found to be small, as expected, all of them smaller than  $0.05 \times 10^{-2}$ . The largest relative biases are on the  $B^\pm \rightarrow D\pi^\pm$  parameters, but even for those the relative effect is less than 2 %. In agreement with Ref. [157], it is found that the biases increase by an order of magnitude if the  $F_i$  parameters are fixed to the expected values with no  $D$ -mixing, instead of being determined as part of the fit.

### 5.6.6 PID efficiencies

The uncertainty related to PID efficiencies is assessed by repeating the full two-stage fit procedure a number of times, each time varying the PID efficiencies within the uncertainties. The used uncertainty includes both a statistical and systematic component, as described in detail in Section 5.1.3. The standard deviations of the central values obtained for each observable are assigned as the systematic uncertainty. The uncertainties come out below  $0.1 \times 10^{-2}$  for all observables.

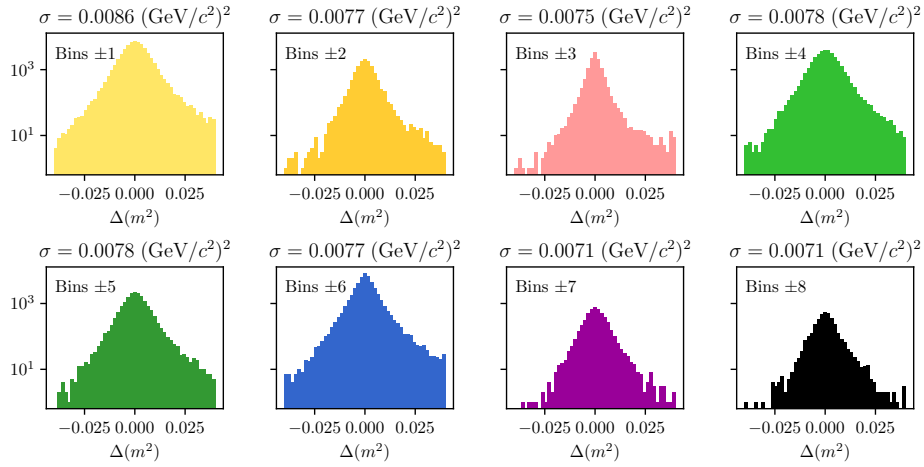


**Figure 5.56:** Distribution of the biases  $\Delta(m^2) = m_{\text{true}}^2 - m_{\text{reconstructed}}^2$  in simulation for  $m^2(K_S^0\pi^+)$  in bins of the rectangular binning scheme of Fig. 5.50.

### 5.6.7 Dalitz-coordinate resolution

There is a small systematic uncertainty related to Dalitz-plot-bin migration, where the non-perfect resolution on the momentum measurement means that a candidate is assigned to a different bin than it truly belongs to. This leads to non-negligible net migration between bins that share a border in a region of phase space where the amplitude varies rapidly. Since the  $F_i$  parameters are measured in the data set, all leading order effects of migration are inherently taken into account. The measurement is only sensitive to differences in migration between the  $DK^\pm$  and  $D\pi^\pm$  channels and the effect is small.

The systematic uncertainty due to this effect is assigned using pseudo experiments. The study is made for the  $D \rightarrow K_S^0\pi^+\pi^-$  mode only, which is sufficient since it completely dominates the overall sensitivity.

1. Signal  $B^\pm \rightarrow DK^\pm$  and  $B^\pm \rightarrow D\pi^\pm$  decays are generated continuously over phase space, according to the expected distribution obtained with the latest amplitude model from the Belle collaboration [50], assuming values of  $\gamma$  and  $(r_B^{DK/D\pi}, \delta_B^{DK/D\pi})$  close to the current world averages.
2. The Dalitz coordinates of each candidate are then smeared using the experiment resolution obtained in simulation. This is described further below.
3. Finally, the generated candidates are binned and fit using the default setup.

The resolution is obtained via simulation, by comparing the reconstructed phase-space coordinates with those calculated from the true momenta in samples of

simulated  $D \rightarrow K_S^0 \pi^+ \pi^-$  decays. As can be seen in Fig. 5.56, the resolution is found to vary over phase space and the distribution of shifts has significant exponential tails. In order to take both effects into account, the smearing is done by shifting each generated decay with a coordinate shift found in full LHCb simulation, for a random simulated decay that took place at approximately the same place in the Dalitz plot. The shift is multiplied with 120 % to take into account that the resolution is generally better in simulation than data. If the shift results in Dalitz coordinates outside the kinematically allowed region, a different shift is applied randomly instead.

The average bias seen in the pseudo experiments is assigned as the systematic uncertainty. The uncertainties come out at about  $(0.1 - 0.2) \times 10^{-2}$  for all parameters. It is found that the bias is towards a smaller value of  $r_B^{DK}$  for all four  $DK^\pm$  parameters; this is to be expected, as bin migration washes out the asymmetries in different areas of the Dalitz plot.

### 5.6.8 The fixed yield fractions

A number of relative yields are fixed from efficiencies in simulation and branching fractions. In the  $DK^\pm$  modes, this is the case for all the relative yields of the partially reconstructed backgrounds, including partially reconstructed  $B \rightarrow D\pi[X]$  decays where the pion is misidentified as a kaon, and the yield of the  $B_s^0 \rightarrow DK\pi$  background relative to the  $B \rightarrow D\pi$  yield. In the  $B^\pm \rightarrow D\pi^\pm$  channel, the only fixed yield ratio is that of the partially reconstructed  $B^\pm \rightarrow D^{*0}(\rightarrow D\pi^0)\pi^\pm$  and  $B^0 \rightarrow D^{*\mp}(\rightarrow D\pi^\mp)\pi^\pm$  modes. The uncertainty on the observables due to uncertainties on these fixed fractions is assessed by repeating the two-stage fit procedure many times, each time shifting the yield ratios randomly within their uncertainties. The uncertainty on each observable is taken to be the standard deviation of the set of central values obtained in these fits. These are all smaller than  $0.1 \times 10^{-2}$ .

### 5.6.9 Systematic uncertainty due to backgrounds that are not modelled in fit

There are a number of backgrounds that are expected to be present at a small level, but which are not modelled in the fits to data because their impact on the fit results is minimal. Instead, a systematic uncertainty is assigned. Each contribution is described in the following sections and the related systematic uncertainties are summarised in Table 5.17.

**Table 5.17:** Summary of systematic uncertainties due to backgrounds that are potentially present with a small yield, but not included in the mass fit.

| All uncertainties are quoted with implicit: $\times 10^{-2}$ |                    |                    |                    |                    |                        |                        |
|--|--------------------|--------------------|--------------------|--------------------|------------------------|------------------------|
| Mode   | $\sigma(x_-^{DK})$ | $\sigma(y_-^{DK})$ | $\sigma(x_+^{DK})$ | $\sigma(y_+^{DK})$ | $\sigma(x_\xi^{D\pi})$ | $\sigma(y_\xi^{D\pi})$ |
| $\Lambda_b^0$ backgrounds                                    | 0.04               | 0.05               | 0.04               | 0.06               | 0.08                   | 0.13                   |
| $B \rightarrow D\mu\nu X$                                    | 0.04               | 0.07               | 0.04               | 0.05               | 0.10                   | 0.11                   |
| $B^\pm \rightarrow D(\rightarrow K_S^0\pi\mu\nu)h^\pm$       | 0.00               | 0.03               | 0.02               | 0.02               | 0.00                   | 0.00                   |
| Swapped tracks   | 0.10               | 0.13               | 0.12               | 0.08               | 0.00                   | 0.01                   |
| Total  | 0.11               | 0.16               | 0.13               | 0.12               | 0.08                   | 0.13                   |

## Background from $\Lambda_b$ decays

This section considers the possible impact of the two potential backgrounds from  $\Lambda_b^0$  decays described in Section 5.4.3:  $\Lambda_b^0 \rightarrow D^0 p\pi^-$  decays where the pion is not included in the candidate reconstruction and the proton assigned as the companion, and  $\Lambda_b^0 \rightarrow \Lambda_c^+(\rightarrow pK_S^0\pi^+\pi^-)\pi^-$  decays where a pion in the  $\Lambda_c^+$  decay is not reconstructed and the proton reconstructed as one of the  $D$  decay products. The impact of not including these in the default fit is assessed by generating simulated data sets where the backgrounds are included in the generation step, which are then fitted back with default model. The former background is distributed over the Dalitz plot as  $\bar{D}^0$ -like, cf. the terminology of Section 5.6.3, since a positive companion is produced along with a  $D^0$  meson (assuming no  $CP$  violation). The latter is also distributed as  $\bar{D}^0$ -like in the study; the exact distribution is unknown, but a  $\bar{D}^0$ -like background is likely to have the largest effect and thus this is a conservative choice. The total yields are taken relative to the signal yields, using the yield ratios discussed in Section 5.4.3. The  $m(Dh^\pm)$  distributions are obtained using simulated samples, produced with `RapidSim`. The mean biases come out to be less than  $0.1 \times 10^{-2}$  for each  $CP$ -violation observable, which is assigned as a systematic uncertainty.

## Semi-leptonic backgrounds

The impact of remnant  $B \rightarrow D\mu\nu_\mu$  decays after requiring `isMuon=0` on the companion is assessed in pseudo experiments. Data sets are generated where the background is added in the generation step at a rate corresponding to the expectation after the veto, which are then fit with the default model. The background yield relative to signal and the mass shape are obtained from a sample of fully simulated decays for conditions corresponding to the run conditions in 2012. The obtained mean bias in the fits is assigned as the systematic uncertainty: it is below  $0.1 \times 10^{-2}$  for all parameters.

The systematic uncertainty relating to the presence of  $D^0 \rightarrow K_S^0\pi^-\mu^+\nu_\mu$  is estimated by repeating the bias studies of Section 5.3.3, but scaling the background yields to 10% to take into account the lepton veto on the  $D$  decay products. All biases are less than  $0.05 \times 10^{-2}$  in this case.

### Swapped tracks

There is a peaking background present from  $B^\pm \rightarrow D(\rightarrow K^\mp\pi^\pm)K_S^0\pi^\pm$  decays where the kaon is reconstructed as the companion and the  $K_S^0$  is assigned to the  $D$  decay. The yield of this background is determined to be 0.5% of the signal yield in the  $B^\pm \rightarrow DK^\pm$  channel in Section 5.3.5. The potential impact from the presence of the background is estimated by

1. Calculating the expected  $B^\pm \rightarrow D\pi^\pm$  and  $B^\pm \rightarrow DK^\pm$  signal yields in each bin for physics parameters similar to the world average values.
2. Then calculating the background bin yields in each  $B^\pm \rightarrow DK^\pm$  bin, using a total yield equal to 0.5% of the signal yield, and the bin distribution from simulated samples of  $B^\pm \rightarrow D(\rightarrow K^\mp\pi^\pm)K_S^0\pi^\pm$  decays, produced via **RapidSim**. The study is carried out for multiple simulated samples, including decays where the  $K_S^0\pi$  pair in the  $B$  decay originate in different  $K^*$  resonances (generated with EvtGen and the proper resonance-spin models), as well as  $B$  decays that are evenly distributed over the allowed phase space.
3. For each sample, the signal and background yields are added, and the new  $B^\pm \rightarrow D\pi^\pm$  and  $B^\pm \rightarrow DK^\pm$  yields are fit with the default signal-yield expressions (including a fit of the  $F_i$  parameters).

For each parameter, the most significant bias seen across the different **RapidSim** samples is taken as the related systematic uncertainty. The uncertainty is below  $0.15 \times 10^{-2}$  for all parameters.

### 5.6.10 Bias correction

In the default sensitivity study, the bias was found to be compatible with zero. However, the size of a potential bias can vary depending on the input parameters. The size of the bias has been investigated with alternate input values of  $(\gamma, r_B^{DK}, \delta_B^{DK}, r_B^{D\pi}, \delta_B^{D\pi})$ , obtaining the results in Table 5.18. A systematic uncertainty due to a potential, small bias is calculated as the difference between the maximum and minimum bias for a given parameter. The uncertainty assigned in this way is very small in general, and less than  $0.1 \times 10^{-2}$  for all parameters.

**Table 5.18:** Biases observed with alternative input parameters and the systematic uncertainty assigned for the bias correction. All numbers are quoted with an implicit  $\times 10^{-2}$ .

| Input ( $\gamma, r_B^{DK}, \delta_B^{DK}, r_B^{D\pi}, \delta_B^{D\pi}$ ) | $x_-^{DK}$ | $y_-^{DK}$ | $x_+^{DK}$ | $y_+^{DK}$ | $x_\xi^{D\pi}$ | $y_\xi^{D\pi}$ |
|--|------------|------------|------------|------------|----------------|----------------|
| (72, 0.080, 117, 0.005, 288)   | -0.02      | -0.01      | -0.02      | -0.02      | 0.03           | 0.00           |
| (75, 0.100, 130, 0.005, 300)   | -0.03      | -0.04      | -0.00      | 0.02       | 0.01           | -0.03          |
| (82, 0.112, 144, 0.005, 330)   | 0.00       | -0.01      | 0.00       | 0.03       | -0.03          | 0.02           |
| (71, 0.099, 129, 0.005, 300)   | -0.02      | -0.04      | -0.00      | -0.00      | 0.05           | -0.00          |
| Syst. uncertainty  | 0.04       | 0.03       | 0.02       | 0.04       | 0.09           | 0.05           |

### 5.6.11 Charmless backgrounds

As discussed in Section 5.3.1, a small number of charmless background decays survive the  $D$  flight distance requirement. In this section the systematic uncertainty related to those is assessed in a series of pseudo experiments. Simulated data sets are generated where a charmless background component is included, using the yields and shapes obtained in the studies of Section 5.3.1. The Dalitz-bin distribution is obtained by repeating the fits of that section for each bin individually. These data sets are subsequently fit using the default model, which does not include a charmless component. No statistically significant bias is observed.

The study described above does not allow for charge-asymmetries in the charmless backgrounds, in terms of overall yields or phase-space distributions. These asymmetries are likely to be present, due to large local  $CP$ -violation in regions of phase space in  $B^\pm$  decays to hadrons [158,159]. The yields in the data-driven studies of Section 5.3.1 are not large enough to assess asymmetries, let alone asymmetric bin distributions with any degree of statistical precision. Instead, an extreme-case scenario is investigated, where *all* the charmless background is added to either the  $B^+$  or  $B^-$  data sample in generation. In both cases, no statistically significant biases are observed, and it is concluded that the impact of charmless background is negligible.

### 5.6.12 Summary of systematic uncertainties

The complete set of included systematic uncertainties is summarised in Table 5.19. It can be seen that the measurement is statistically limited. The correlation matrix pertaining to the LHCb related systematics is given in Table 5.20. For studies where the systematic uncertainty is obtained by repeating fits to data multiple times while varying some input, the correlation matrix is obtained from the correlations of the central values. For studies that are based on generating a large number of

**Table 5.19:** Overview of all sources of uncertainty on the measurement. Due to the number of pseudo experiments used to determine the systematic uncertainties, the *uncertainty on the quoted systematic uncertainties* is approximately  $0.05 \times 10^{-2}$ . In many cases that is of approximately the same size as the uncertainties themselves, but much smaller than the dominating, statistical uncertainty.

| All uncertainties are quoted with implicit: $\times 10^{-2}$ |                    |                    |                    |                    |                        |                        |
|--|--------------------|--------------------|--------------------|--------------------|------------------------|------------------------|
| Source   | $\sigma(x_-^{DK})$ | $\sigma(y_-^{DK})$ | $\sigma(x_+^{DK})$ | $\sigma(y_+^{DK})$ | $\sigma(x_\xi^{D\pi})$ | $\sigma(y_\xi^{D\pi})$ |
| Statistical  | 0.96               | 1.14               | 0.96               | 1.20               | 1.99                   | 2.34                   |
| Strong-phase inputs  | 0.23               | 0.35               | 0.18               | 0.28               | 0.14                   | 0.18                   |
| Efficiency correction of $(c_i, s_i)$                        | 0.11               | 0.05               | 0.05               | 0.10               | 0.08                   | 0.09                   |
| Mass-shape parameters  | 0.05               | 0.08               | 0.03               | 0.08               | 0.16                   | 0.17                   |
| Mass-shape bin dependence                                    | 0.05               | 0.07               | 0.04               | 0.08               | 0.07                   | 0.09                   |
| Lowmass physics effects                                      | 0.04               | 0.10               | 0.15               | 0.05               | 0.10                   | 0.09                   |
| $CP$ violation of $K_S^0$                                    | 0.03               | 0.04               | 0.08               | 0.08               | 0.09                   | 0.46                   |
| $D$ mixing   | 0.04               | 0.01               | 0.00               | 0.02               | 0.02                   | 0.01                   |
| PID efficiencies   | 0.03               | 0.03               | 0.01               | 0.05               | 0.02                   | 0.02                   |
| Fixed yield ratios   | 0.05               | 0.06               | 0.03               | 0.06               | 0.02                   | 0.02                   |
| Dalitz-bin migration   | 0.04               | 0.08               | 0.08               | 0.11               | 0.18                   | 0.10                   |
| Bias correction  | 0.04               | 0.03               | 0.02               | 0.04               | 0.09                   | 0.05                   |
| Small backgrounds  | 0.11               | 0.16               | 0.13               | 0.12               | 0.08                   | 0.13                   |
| Total LHCb systematic  | 0.20               | 0.25               | 0.24               | 0.26               | 0.32                   | 0.54                   |
| Total systematic   | 0.31               | 0.43               | 0.30               | 0.38               | 0.35                   | 0.57                   |

**Table 5.20:** Total LHCb-related systematic uncertainties and their correlation matrix.

| Uncertainty ( $\times 10^{-2}$ ) |            |            |            |            |                |                |
|----------------------------------|------------|------------|------------|------------|----------------|----------------|
|                                  | $x_-^{DK}$ | $y_-^{DK}$ | $x_+^{DK}$ | $y_+^{DK}$ | $x_\xi^{D\pi}$ | $y_\xi^{D\pi}$ |
| $\sigma$                         | 0.20       | 0.25       | 0.24       | 0.26       | 0.32           | 0.54           |
| Correlations                     |            |            |            |            |                |                |
|                                  | $x_-^{DK}$ | $y_-^{DK}$ | $x_+^{DK}$ | $y_+^{DK}$ | $x_\xi^{D\pi}$ | $y_\xi^{D\pi}$ |
| $x_-^{DK\pm}$                    | 1.000      | 0.864      | 0.734      | 0.897      | 0.349          | 0.318          |
| $y_-^{DK\pm}$                    |            | 1.000      | 0.874      | 0.903      | 0.408          | 0.362          |
| $x_+^{DK\pm}$                    |            |            | 1.000      | 0.771      | 0.563          | 0.447          |
| $y_+^{DK\pm}$                    |            |            |            | 1.000      | 0.507          | 0.451          |
| $x_\xi^{D\pi\pm}$                |            |            |            |            | 1.000          | 0.484          |
| $y_\xi^{D\pi\pm}$                |            |            |            |            |                | 1.000          |

simulated data sets and determining the average bias, the correlation of a systematic on two observables is taken to be +100 % if the biases are in the same direction, and -100 % if they are in opposite directions. The total systematic correlation matrix, including both LHCb-related systematics and that of the strong-phase inputs, is given in Table 5.21.

The studies described in this section also allow for an estimate of the systematic

**Table 5.21:** Total systematic uncertainties and their correlation matrix, including contributions due to strong-phase inputs as well as LHCb-related uncertainties.

| Uncertainty ( $\times 10^{-2}$ ) |            |            |            |            |                |                |
|----------------------------------|------------|------------|------------|------------|----------------|----------------|
|                                  | $x_-^{DK}$ | $y_-^{DK}$ | $x_+^{DK}$ | $y_+^{DK}$ | $x_\xi^{D\pi}$ | $y_\xi^{D\pi}$ |
| $\sigma$                         | 0.31       | 0.43       | 0.30       | 0.38       | 0.35           | 0.57           |

| Correlations      |            |            |            |            |                |                |
|-------------------|------------|------------|------------|------------|----------------|----------------|
|                   | $x_-^{DK}$ | $y_-^{DK}$ | $x_+^{DK}$ | $y_+^{DK}$ | $x_\xi^{D\pi}$ | $y_\xi^{D\pi}$ |
| $x_-^{DK\pm}$     | 1.000      | 0.301      | 0.156      | 0.576      | 0.265          | 0.231          |
| $y_-^{DK\pm}$     |            | 1.000      | 0.437      | 0.218      | 0.183          | 0.170          |
| $x_+^{DK\pm}$     |            |            | 1.000      | 0.445      | 0.414          | 0.310          |
| $y_+^{DK\pm}$     |            |            |            | 1.000      | 0.353          | 0.243          |
| $x_\xi^{D\pi\pm}$ |            |            |            |            | 1.000          | 0.502          |
| $y_\xi^{D\pi\pm}$ |            |            |            |            |                | 1.000          |

uncertainties on the  $\mathcal{R}_i$  parameters of Eq. (5.22) or, equivalently the  $F_i$  parameters, in a completely analogous manner to how the uncertainty on the  $CP$ -violation observables was assigned. In all cases, however, the systematic uncertainty found to be much smaller than the statistical uncertainties that were given in Table 5.10. The central values, statistical, and systematic uncertainties of the  $\mathcal{R}_i$  parameters will be made public in Ref. [1] because they can be employed in future LHCb measurements, as discussed in Section 5.5.2.

## 5.7 Obtained constraints on $\gamma$

The measured values of  $(x_\pm^{DK}, y_\pm^{DK}, x_\xi^{D\pi}, y_\xi^{D\pi})$  can be used to put constraints on the possible values of the CKM angle  $\gamma$  and the hadronic nuisance parameters  $r_B^{DK}$ ,  $\delta_B^{DK}$ ,  $r_B^{D\pi}$ , and  $\delta_B^{D\pi}$ . This is handled using the `gammacombo` package, which is also used to combine all measurements of  $\gamma$  made by the LHCb collaboration [43, 160].

### 5.7.1 Statistical approach

The optimal central values are determined in a maximum likelihood fit. The set of all observables for which a measurement has been made is denoted  $A$ , and the set of underlying physics parameters is denoted  $\theta$ . The physics parameters of course determine the probability density function of measurement results of  $A$ ,  $f(A|\theta)$ . Given a specific set of measurement results,  $A_{\text{obs}}$ , a likelihood function is defined

$$\mathcal{L}(\theta|A_{\text{obs}}) = f(A_{\text{obs}}|\theta) \quad (5.34)$$

and the estimate of  $\theta$  is the set of parameters that maximize the likelihood

$$\hat{\theta} = \arg \max_{\theta} \mathcal{L}(\theta | A_{\text{obs}}). \quad (5.35)$$

In practice, a  $\chi^2$  function is defined

$$\chi^2(\theta | A_{\text{obs}}) = -2 \ln \mathcal{L}(\theta | A_{\text{obs}}) \quad (5.36)$$

and minimized instead. In the specific case where the likelihood profile is Gaussian, it can be described by the simple expression

$$\chi^2(\theta | A_{\text{obs}}) = (A_{\text{obs}} - A(\theta))^T \Sigma_{A_{\text{obs}}}^{-1} (A_{\text{obs}} - A(\theta)) + c, \quad (5.37)$$

where  $\Sigma_{A_{\text{obs}}}$  is the *measured* covariance matrix for the observables (used as an estimate of the true, underlying covariance matrix),  $A(\theta)$  denotes the value of the observables expressed in terms of the underlying physics parameters, and  $c$  is a constant that is independent of  $\theta$ . In the specific case considered here

$$\begin{aligned} A &= (x_-^{DK}, y_-^{DK}, x_+^{DK}, y_+^{DK}, x_\xi^{D\pi}, y_\xi^{D\pi}) \\ \theta &= (\gamma, r_B^{DK}, \delta_B^{DK}, r_B^{D\pi}, \delta_B^{D\pi}). \end{aligned} \quad (5.38)$$

The likelihood scan presented in Section 5.5.2 proved that the Gaussian expression in Eq. (5.37) provides an excellent description of the likelihood profile of the measurement, when  $\Sigma_{A_{\text{obs}}}$  is taken to be the covariance matrix obtained in that section. Thus, the  $\chi^2$  function defined in Eq. (5.37) is minimised to determine the best estimate of  $\gamma$ .

Two different methods are employed to construct confidence regions for the observables of interest, known within the `gammacombo` framework as the PROB and PLUGIN methods. Both methods aim to construct confidence regions for some subset,  $\phi$ , of the full parameter set  $\theta$ . The remaining parameters, dubbed nuisance parameters below, are denoted  $\eta = \theta \setminus \phi$ . In practice,  $\phi$  most often denotes a single parameter, and of special interest is of course the case where  $\phi = \gamma$ . Both methods aim to solve the problem that due to the number of parameters in  $\theta$  (five in the case considered here, but up to 40 in the latest LHCb combination [44]), it is not feasible to derive the confidence regions from a full-fledged Neumann construction [161]. Under assumptions discussed below, the methods achieve reasonable coverage nonetheless, i.e. had the measurement been repeated many times, the confidence region is expected to cover the true parameter(s) with a probability at least at large as the quoted confidence level (CL), independently of the true parameter value. The presentation follows the `gammacombo` manual [160].

The **PROB** method is a simple profile-likelihood method. The minimum value of the  $\chi^2$  function is denoted  $\chi_{\min}^2 \equiv \chi^2(\hat{\theta}|A_{\text{obs}})$ . To evaluate the CL for a specific value (set of values) of  $\phi_0$ , the  $\chi^2$  function is again minimised, this time under the constraint that  $\phi = \phi_0$ , resulting in a new minimum  $\hat{\theta}' = (\phi_0, \hat{\eta}')$ . In the approximation that all likelihoods are exactly Gaussian, the variable

$$\Delta\chi^2(\phi_0|A_{\text{obs}}) = \chi^2(\hat{\theta}'|A_{\text{obs}}) - \chi_{\min}^2 \quad (5.39)$$

follows a  $\chi^2$  distribution with  $n$  degrees of freedom, where  $n$  is the number of parameters in  $\phi$  [28]. This can be used to evaluate CL at that point as

$$CL(\phi_0|A_{\text{obs}}) = F_n(\Delta\chi^2(\phi_0|A_{\text{obs}})) \quad (5.40)$$

where  $F_n$  is the cumulative distribution function of a  $\chi^2$  distribution with  $n$  degrees of freedom. The method takes its colloquial name from the fact that this function is named **Prob** in the **ROOT** package. Confidence regions can be defined by scanning the values of  $\phi_0$  over a region of interest. These confidence regions assume that the estimates  $\hat{\theta}$  follow a Gaussian distribution centred on the true values, which is the case for maximum likelihood estimates in asymptotically large samples [162]; in other cases they may not have good coverage properties. Given the Gaussian shape obtained in the likelihood scan of Section 5.5.2 the confidence regions are likely to be well behaved in the case considered here.

However, for the purpose of comparing to the combination of several LHCb measurements in Section 5.5.3 below, the **PLUGIN** method is necessary. The method is described in Ref. [163], based on the hybrid resampling method presented in Ref. [164]. It foregoes the assumption that  $\Delta\chi^2$  follows a  $\chi^2$  distribution and instead estimates the distribution in a bootstrapping scheme. The procedure is as follows: the values of  $\hat{\theta}$ ,  $\hat{\theta}'$ , and  $\Delta\chi^2(\phi_0|A_{\text{obs}})$  are determined as described above; then the following steps are carried out a number,  $N_{\text{toys}}$ , of times

1. Generate a "toy" result,  $A_{\text{toy}}^i$ , following the distribution  $f(A|\hat{\theta}')$
2. Determine  $\Delta\chi^2(\phi_0|A_{\text{toy}}^i)$  by minimising the  $\chi^2$  function for the results  $A_{\text{toy}}^i$  twice, once where all parameters in  $\theta$  are free, and once where  $\phi = \phi_0$  is enforced

Then the CL is defined by

$$CL(\phi_0) = 1 - \frac{N(\Delta\chi^2(\phi_0|A_{\text{obs}}) < \Delta\chi^2(\phi_0|A_{\text{toy}}^i))}{N_{\text{toys}}} \quad (5.41)$$

While the coverage properties are not proven, evidence is presented in terms of asymptotic results and simulation studies in Refs. [163,164]. The coverage properties have also been investigated in relation to LHCb combinations, and the intervals were found to perform well in most cases [43].

### 5.7.2 Interpretation results

The central values and confidence regions obtained for the physics parameters are

$$\begin{aligned}\gamma &= (68.7^{+5.2}_{-5.1})^\circ, \\ r_B^{DK} &= 0.0904^{+0.0077}_{-0.0075}, \\ \delta_B^{DK} &= (118.3^{+5.5}_{-5.6})^\circ, \\ r_B^{D\pi} &= 0.0050^{+0.0017}_{-0.0017}, \\ \delta_B^{D\pi} &= (291^{+24}_{-26})^\circ,\end{aligned}\tag{5.42}$$

where the quoted uncertainties are obtained via the **PLUGIN** method. A second solution exists where  $\gamma' = \gamma + 180^\circ$  and  $\delta'_B = \delta_B + 180^\circ$ ; as is conventional, the solution where  $\gamma \in [0^\circ, 180^\circ]$  is reported. The one-dimensional CL plots are shown in Fig. 5.57. It is clear that the **PROB** and **PLUGIN** confidence regions agree well; this is expected given the Gaussian likelihood. A series of two-dimensional confidence regions are shown in Fig. 5.58, where it can be seen that the observables define a single solution for  $\gamma$  as expected. It is worth noticing that the uncertainty of this measurement alone is on par with the current world average, due to the increased data sample, and the significant reduction of systematic uncertainties due to the new measurement strategy and updated strong-phase inputs from BESIII. The result for  $\gamma$  is in agreement with the expected value given other CKM measurements,  $\gamma = (65.66^{+0.90}_{-2.65})^\circ$  [33].

The contribution to the uncertainty on  $\gamma$  from each of the statistical, strong-phase-related, and LHCb-related uncertainties in isolation can be estimated by repeating the interpretation while only including subsets of the uncertainties on the input parameters. Such studies have been performed using the **PROB** method. Running with statistical uncertainties only yields an uncertainty on  $\gamma$  of  $5.05^\circ$ . Including only the statistical and LHCb-related systematic uncertainties yields an uncertainty on  $\gamma$  of  $5.08^\circ$ , suggesting that the LHCb-related systematics contribute an uncertainty of  $0.6^\circ$ . This is a reduction compared to earlier analyses, where the contribution was about  $2^\circ$ . A significant contribution to the improvement is the efficiency-related systematic that has been avoided by promoting  $B^\pm \rightarrow D\pi^\pm$  to a signal channel. Including only the statistical and the strong-phase-related uncertainties leads to an uncertainty on  $\gamma$  of  $5.09^\circ$ , showing the strong-phase-related uncertainty to be  $0.6^\circ$ , somewhat lower than the expectation of  $1.2^\circ$  presented in Ref. [71]. This is partly because the uncertainty estimate of that paper does not take into account the use of the  $D \rightarrow K_S^0 K^+ K^-$  channel, and partly because the uncertainty estimate depends on the specific central values.

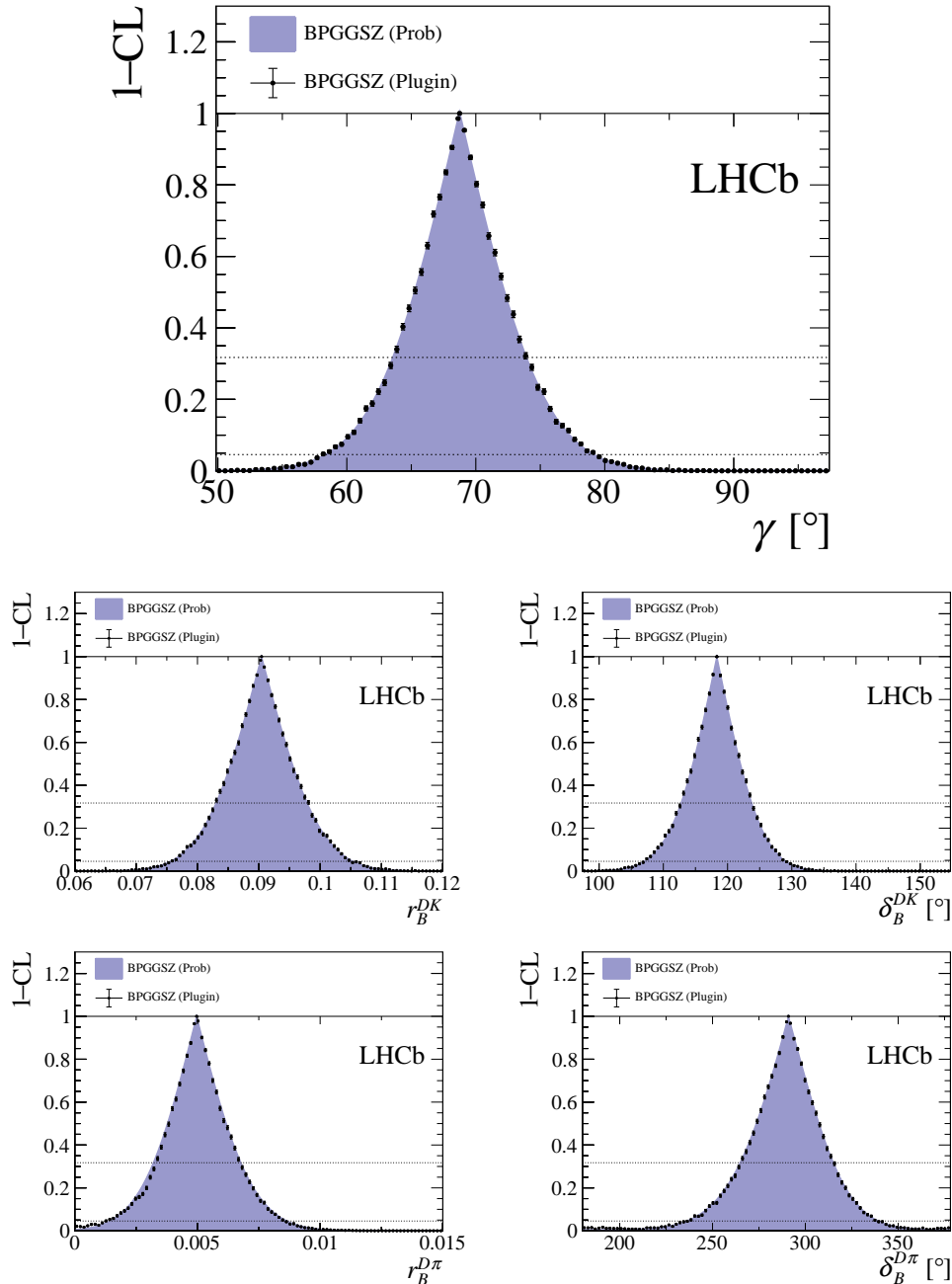


**Figure 5.57:** Confidence levels for the physics parameters of interest. The dotted horizontal lines correspond to the CL values 65 % and 95 %.

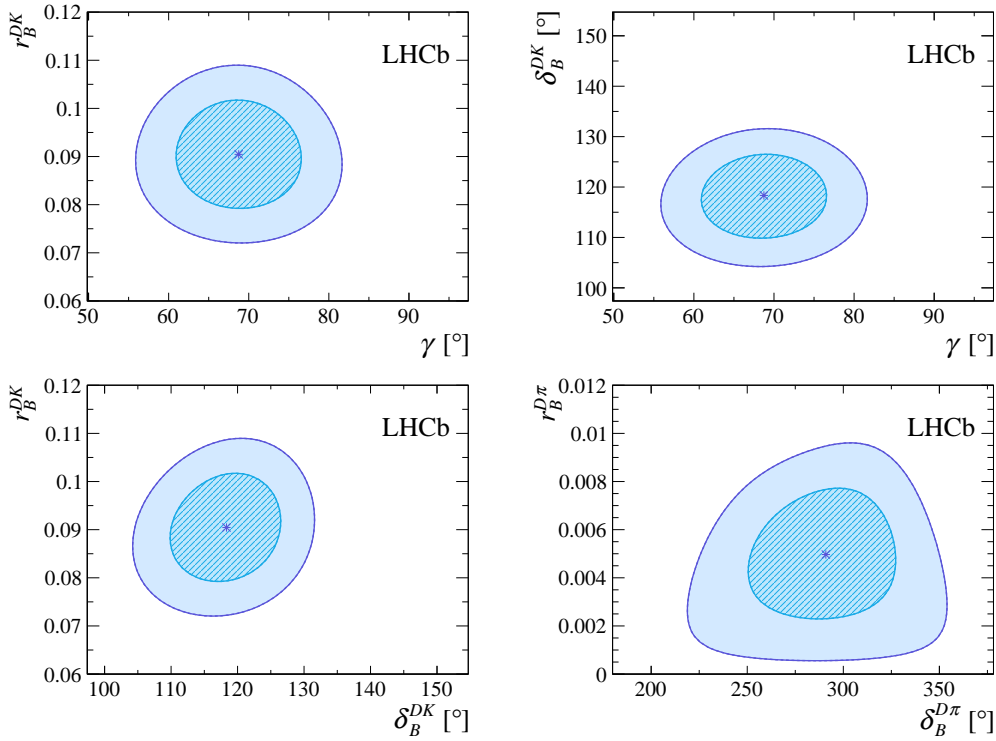


**Figure 5.58:** The 68 % and 95 % confidence regions for combinations of the physics parameters of interest, as obtained from the results of this measurement. The regions are calculated via the PROB method of gammacombo.

The obtained statistical uncertainty on  $\gamma$  is in excellent agreement with the expectation from pseudo experiments. The interpretation procedure outlined above has been performed for each of the pseudo experiments performed to establish the feasibility of the  $CP$  fit in Section 5.5.1 (including only statistical uncertainties on the observables) and the central 90 % interval of the obtained uncertainties is  $[4.4^\circ, 6.0^\circ]$ . Furthermore, the determination of  $\gamma$  is found to be unbiased, and the uncertainties on  $\gamma$  show the expected coverage properties. Similar studies have been carried out where no background decays are included in the generated data sets. In this case, the precision on  $\gamma$  is improved by about 30 %. The pseudo experiments do suggest small biases on  $r_B^{DK}$  and  $r_B^{D\pi}$  in the interpretation step, of 10 % and 25 % of the statistical uncertainty, respectively. In absolute terms, this corresponds to positive biases of  $\Delta r_B^{DK} = +0.0008$  (i.e. 1 % of the central value) and  $\Delta r_B^{D\pi} = +0.0004$  (about 8 % of the central value). These biases have been observed before [43], and have been determined to arise due to the constraint that  $r_B > 0$ . The results quoted in Eq. (6.5) have *not* been corrected for the bias and should be interpreted accordingly. The results from this thesis that will be used in combinations of  $\gamma$  measurements by LHCb (and others) is the measured observables,  $(x_\pm^{DK}, y_\pm^{DK}, x_\xi^{D\pi}, y_\xi^{D\pi})$ , and these were shown to be determined without a bias in Section 5.5.

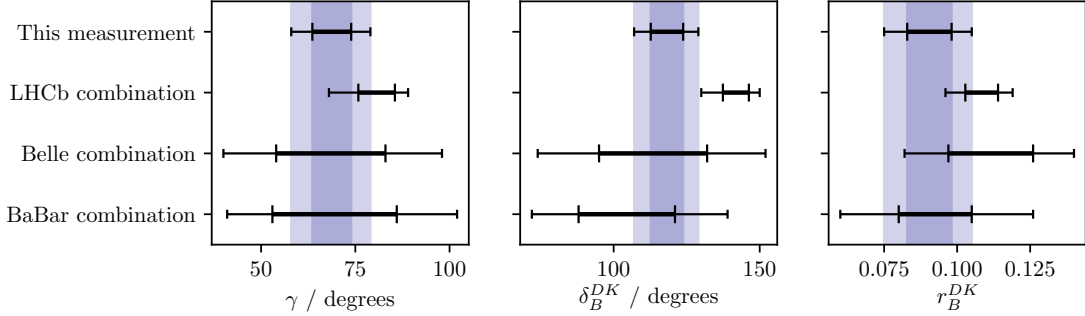


**Figure 5.59:** Comparison of the  $1\sigma$  and  $2\sigma$  confidence intervals obtained for  $\gamma$  and the physics parameters relating to  $B^\pm \rightarrow DK^\pm$  decays, with those from the combinations of  $\gamma$  measurements by the Belle [14] and BaBar [15] collaborations, and the 2018 combination of LHCb results [44] where the BPGBGSZ measurements have been excluded.

### 5.7.3 Compatibility with other measurements

It is worth comparing the obtained constraints on the physics parameters with the information available from other measurements, made at the  $B$  factories and by the LHCb collaboration using other decay channels. This comparison is made for  $\gamma$  and the hadronic parameters in the  $B^\pm \rightarrow DK^\pm$  decay in Fig. 5.59, comparing to the results of the combinations of  $\gamma$  measurements by the Belle [14] and BaBar [15] collaborations presented in 2013, and the 2018 combination of LHCb results [44]. For this purpose, the LHCb combination is re-performed, removing the input from earlier BPGBGSZ measurements that use  $B^\pm \rightarrow DK^\pm$  decays, because they were made using data that is re-analysed in the present thesis; thus they need to be excluded to make the results that are compared independent. The combination employs the same statistical method outlined above, with the exception that the likelihood now depends on observables measured in a number of different analyses. The included measurements are summarised in Table 5.22. It can be seen in Fig. 5.59 that the results obtained in this thesis agree well with the Belle and BaBar results, but are in some tension with the 2018 LHCb combination, especially for the  $\delta_B^{DK}$  parameter.

The level of compatibility can be quantified by calculating the three-dimensional  $\chi^2$  of the BPGBGSZ results and those of the LHCb combination (without the earlier BPGBGSZ measurements), with respect to the best fit values of  $(\gamma, r_B^{DK}, \delta_B^{DK})$  when all measurements are combined. The two-dimensional confidence regions obtained in these three cases are compared in Fig. 5.60, where some tension in  $r_B^{DK}$  and  $\delta_B^{DK}$  is visible again. The calculation is based on the PLUGIN uncertainties; for the LHCb combination these uncertainty estimates are slightly larger than the ones obtained via the PROB method. One obtains  $\chi^2 = \chi_{BPGBGSZ}^2 + \chi_{LHCb}^2 = 0.7 + 9.1 = 9.8$ ,

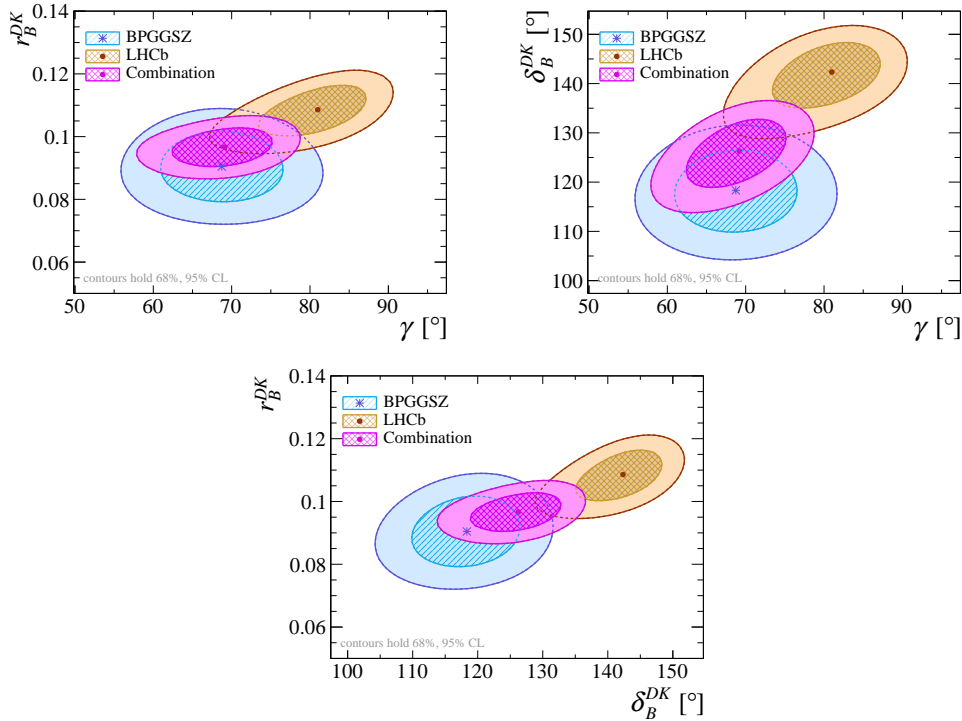


**Figure 5.60:** The 68 % and 95 % confidence regions for  $(\gamma, r_B^{DK})$ ,  $(\gamma, \delta_B^{DK})$ , and  $(\delta_B^{DK}, r_B^{DK})$  for this measurement, the 2018 LHCb combination [44] where the BPGGSZ results have been excluded, and the combination thereof, calculated via the PROB method of `gammapombo`.

which for 3 degrees of freedom correspond to a  $p$ -value of 2 %, or a  $2.3\sigma$  deviation. However, this tension is expected to be reduced when other measurements in the LHCb combination are updated to include results based on the full Run 1 and 2 data set. The most important update is that of the two-body ADS/GLW measurement in  $B^\pm \rightarrow DK^\pm$  decays because that measurement, and the BPGGSZ measurement presented in this thesis, have the largest impact in the combination.<sup>11</sup> The impact of the BPGGSZ measurement on the LHCb average can also be gauged by these studies: the 2018 LHCb combination [44] determines that  $\gamma = (81.0^{+4.5}_{-5.2})^\circ$  when the earlier BPGGSZ measurements are excluded; with the inclusion of the results presented here the favoured solution changes to  $\gamma = (69.1^{+4.1}_{-4.6})^\circ$ . The new central value is in excellent agreement with the expected value given other CKM measurements,  $\gamma = (65.66^{+0.90}_{-2.65})^\circ$  [?], and the uncertainties are reduced a fair amount.

The latest LHCb combination in which  $B^\pm \rightarrow D\pi^\pm$  parameters were determined is from 2016 [43]. Two solutions existed for  $(r_B^{D\pi}, \delta_B^{D\pi})$  which made the interpretation problematic. As can be seen in Fig. 5.61, the measurement presented in this thesis

<sup>11</sup>The ADS/GLW results based on the full Run 1 and 2 data set are not public at the time of writing, and can therefore not be included in the present discussion.

**Table 5.22:** List of the LHCb measurements used in the combination that the results obtained in the present thesis is compared to. These correspond to the 2018 LHCb combination [44], except that the earlier BPGGSZ results made with  $B^\pm \rightarrow DK^\pm$  decays have not been included in the comparison. In the method column, TD stands for "time-dependent", the ADS/GLW/BPGGSZ acronyms were defined in Chapter 2, and references are provided for the remaining methods.

| $B$ decay  | $D$ decay                          | Method           | Ref.  | Data set |
|--|------------------------------------|------------------|-------|----------|
| $B^+ \rightarrow DK^+$   | $D \rightarrow h^+h^-$             | GLW              | [153] | 2011-16  |
| $B^+ \rightarrow DK^+$   | $D \rightarrow h^+h^-$             | ADS              | [150] | 2011-12  |
| $B^+ \rightarrow DK^+$   | $D \rightarrow h^+\pi^-\pi^+\pi^-$ | GLW/ADS          | [150] | 2011-12  |
| $B^+ \rightarrow DK^+$   | $D \rightarrow h^+h^-\pi^0$        | GLW/ADS          | [165] | 2011-12  |
| $B^+ \rightarrow DK^+$   | $D \rightarrow K_S^0 K^+\pi^-$     | GLS [166]        | [167] | 2011-12  |
| $B^+ \rightarrow D^*K^+$   | $D \rightarrow h^+h^-$             | GLW              | [153] | 2011-16  |
| $B^+ \rightarrow DK^{*+}$  | $D \rightarrow h^+h^-$             | GLW/ADS          | [168] | 2011-16  |
| $B^+ \rightarrow DK^{*+}$  | $D \rightarrow h^+\pi^-\pi^+\pi^-$ | GLW/ADS          | [168] | 2011-16  |
| $B^+ \rightarrow DK^+\pi^+\pi^-$                                     | $D \rightarrow h^+h^-$             | GLW/ADS          | [169] | 2011-12  |
| $B^0 \rightarrow DK^{*0}$  | $D \rightarrow K^+\pi^-$           | ADS              | [170] | 2011-12  |
| $B^0 \rightarrow DK^+\pi^-$  | $D \rightarrow h^+h^-$             | GLW-Dalitz [171] | [152] | 2011-12  |
| $B^0 \rightarrow DK^{*0}$  | $D \rightarrow K_S^0 \pi^+\pi^-$   | BPGGSZ           | [63]  | 2011-12  |
| $B_s^0 \rightarrow D_s^\mp K^\pm$                                    | $D_s^+ \rightarrow h^+h^-\pi^+$    | TD               | [172] | 2011-12  |
| $B^0 \rightarrow D^\mp \pi^\pm$                                      | $D^+ \rightarrow K^+\pi^-\pi^+$    | TD               | [173] | 2011-12  |
| Measurements included in Ref. [44] but not in the present comparison |                                    |                  |       |          |
| $B^+ \rightarrow DK^+$   | $D \rightarrow K_S^0 h^+h^-$       | BPGGSZ           | [68]  | 2011-12  |
| $B^+ \rightarrow DK^+$   | $D \rightarrow K_S^0 h^+h^-$       | BPGGSZ           | [3]   | 2015-16  |

picks out one of these solutions, with which it is in excellent agreement. This solution agrees with the theoretically expected value of  $r_B^{D\pi} \sim 0.005$  [45]. Thus, the inclusion of the results presented here are expected to lead to a much less problematic inclusion of the  $B^\pm \rightarrow D\pi^\pm$  channel in future LHCb combinations.

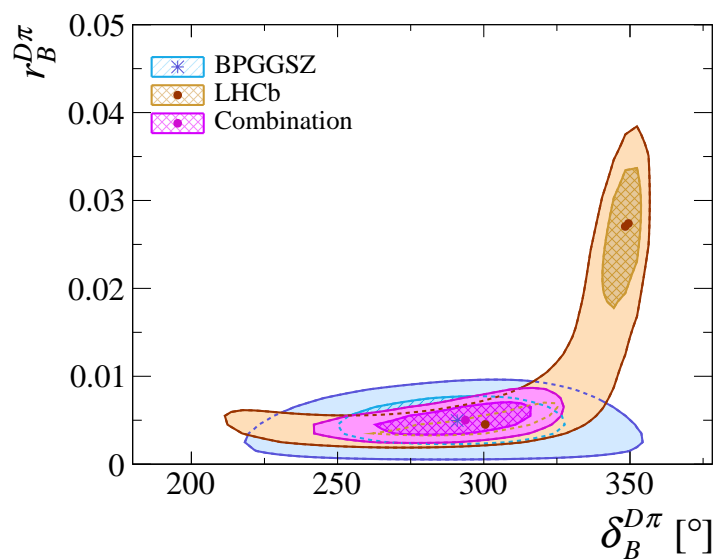


**Figure 5.61:** The 68 % and 95 % confidence regions for  $(\delta_B^{D\pi}, r_B^{D\pi})$  obtained from the results of this measurement, in the 2016 LHCb combination [43], and the combination thereof, calculated via the PROB method of `gammacombo`.

# 6

## Summary and outlook

The main result of the thesis is a measurement of the CKM angle  $\gamma$  using  $B^\pm \rightarrow DK^\pm$  and  $B^\pm \rightarrow D\pi^\pm$  decays, where  $D$  denotes a superposition of the  $D^0$  and  $\bar{D}^0$  states that decays to one of the final states  $K_S^0\pi^+\pi^-$  and  $K_S^0K^+K^-$ . Approximately 17,500  $B^\pm \rightarrow DK^\pm$  decays<sup>1</sup> and 230,000  $B^\pm \rightarrow D\pi^\pm$  decays are analysed, obtained from the  $pp$  collision data set collected by the LHCb experiment during Run 1 and 2 of the LHC. The total data set corresponds to an integrated luminosity of about  $8.7\text{ fb}^{-1}$  collected at centre-of-mass energies of  $\sqrt{s} = 7, 8,$  and  $13\text{ TeV}$ . The measurement relies on the phase-space distribution of signal decays, analysed using a model-independent method based on strong-phase measurements by the CLEO and BESIII collaborations; an approach known as the model-independent BPGGSZ method. The measured  $CP$ -violation observables are defined

$$x_\pm^{DK} = r_B^{DK} \cos(\delta_B^{DK} \pm \gamma), \quad y_\pm^{DK} = r_B^{DK} \sin(\delta_B^{DK} \pm \gamma), \quad (6.1)$$

and measured to be

$$\begin{aligned} x_-^{DK} &= (-5.68 \pm 0.96 \pm 0.20 \pm 0.23) \times 10^{-2}, \\ y_-^{DK} &= (-6.55 \pm 1.14 \pm 0.25 \pm 0.35) \times 10^{-2}, \\ x_+^{DK} &= (-9.30 \pm 0.98 \pm 0.24 \pm 0.18) \times 10^{-2}, \\ y_+^{DK} &= (-1.25 \pm 1.23 \pm 0.26 \pm 0.28) \times 10^{-2}, \end{aligned} \quad (6.2)$$

where the first uncertainty is statistical, the second arises due to systematic effects in the measurement, and the third is the propagated uncertainty on the strong-phase

---

<sup>1</sup>This number includes the approximately 13.5 % of  $B^\pm \rightarrow DK^\pm$  that are reconstructed as  $B^\pm \rightarrow D\pi^\pm$  decays in the analysis.

inputs from the CLEO and BESIII measurements. In addition, two nuisance parameters relating to  $B^\pm \rightarrow D\pi^\pm$  decays are measured. These are defined

$$x_\xi^{D\pi} = (r_B^{DK}/r_B^{D\pi}) \cos(\delta_B^{DK} - \delta_B^{D\pi}), \quad y_\xi^{D\pi} = (r_B^{DK}/r_B^{D\pi}) \sin(\delta_B^{DK} - \delta_B^{D\pi}), \quad (6.3)$$

and measured to be

$$\begin{aligned} x_\xi^{D\pi} &= (-5.47 \pm 1.99 \pm 0.32 \pm 0.14) \times 10^{-2}, \\ y_\xi^{D\pi} &= (0.71 \pm 2.33 \pm 0.54 \pm 0.18) \times 10^{-2}. \end{aligned} \quad (6.4)$$

Due to the measurement approach, the information on  $\gamma$  obtained from  $B^\pm \rightarrow D\pi^\pm$  decays is encoded in the  $(x_\pm^{DK}, y_\pm^{DK})$  parameters. The measured observables have been interpreted in terms of the underlying physics parameters, yielding the results

$$\begin{aligned} \gamma &= (68.7_{-5.1}^{+5.2})^\circ, \\ r_B^{DK} &= 0.0904_{-0.0075}^{+0.0077}, \\ \delta_B^{DK} &= (118.3_{-5.6}^{+5.5})^\circ, \\ r_B^{D\pi} &= 0.0050_{-0.0017}^{+0.0017}, \\ \delta_B^{D\pi} &= (291_{-26}^{+24})^\circ. \end{aligned} \quad (6.5)$$

This is the most precise stand-alone measurement of  $\gamma$  to date, with a precision comparable to that of all earlier measurements of  $\gamma$  combined. The measured value agrees with the expectation from global fits of all CKM parameters. For example, the CKMFitter group obtains  $\gamma = (65.66_{-2.65}^{+0.90})^\circ$  [33] in a global fit that excludes direct  $\gamma$  measurements, and the obtained values and uncertainties in other world averages are similar [24, 36].

The thesis presented the first BPGGSZ measurement by the LHCb collaboration to include  $B^\pm \rightarrow D\pi^\pm$  decays as a signal channel, and a series of feasibility studies that informed the analysis strategy has also been presented. While the impact on the  $\gamma$  precision from  $B^\pm \rightarrow D\pi^\pm$  decays is limited, the new strategy significantly simplified the treatment of the non-uniform phase-space acceptance in LHCb, and lead to a significant reduction of the systematic measurement uncertainty. This will become especially important in future measurements, where the precision will no longer be limited by the statistical uncertainty to the degree that it is now.

The thesis also presented a careful analysis of the impact of neutral kaon  $CP$  violation and material interaction on  $\gamma$  measurements based on the BPGGSZ method. This was a crucial step towards the promotion of the  $B^\pm \rightarrow D\pi^\pm$  channel to a signal channel: existing literature estimated the potential bias to be  $\mathcal{O}(1^\circ)$  in  $B^\pm \rightarrow DK^\pm$  decays *and to scale with*  $1/r_B$ . This suggested potentially

large biases for a  $B^\pm \rightarrow D\pi^\pm$  analysis, since  $r_B^{D\pi} \simeq 0.005$  is twenty times smaller than  $r_B^{DK} \simeq 0.1$ . However, the thesis argues that the actual impact is an order of magnitude smaller, as long as the determination of the  $CP$ -violation observables is based on the phase-space distribution of signal decays. This is demonstrated in a number of numerical studies that take the detector geometries of the LHCb and Belle II detectors into account; these studies are also used to assign a (reasonably small) systematic uncertainty on the measurement results discussed above.

## 6.1 A look towards the future

Precise measurements of  $\gamma$  play an important role in the physics programmes of both the LHCb and Belle II experiments, and the next 10–15 years will see huge improvements in the obtainable precision. Given the results of Chapter 5, it is clear that LHCb is well on course to reach, even surpass, the expected goal of determining  $\gamma$  with a precision of  $4^\circ$  using Run 1 and 2 data [174], when more analyses are performed with the full data set. In the longer run, LHCb is expecting to reach a precision of  $1^\circ$  in the combination of  $\gamma$  measurements by the end of Run 4 of the LHC, and on improving that to  $\sim 0.35^\circ$  in the planned (but not-yet approved or funded) Upgrade Phase II during the 2030’ies [37], with the BPGGSZ mode continuing to be an important contributor to the obtainable precision. The mode plays an even more significant role in the Belle II physics programme, being denoted the *golden mode* in the physics programme [127], due to a much higher  $K_S^0$  reconstruction efficiency in the experiment. When the planned data set corresponding to an integrated luminosity of  $50\text{ ab}^{-1}$  has been collected, the uncertainty on  $\gamma$  from the combination of all Belle II results is expected to be about  $1.6^\circ$  [127]; this is expected to happen in 2031 given the current schedule [175].

The main reason for the impressive expected improvement in precision is that current  $\gamma$  measurements are dominated by statistical uncertainties in all the major signal modes. This is expected to remain true for the BPGGSZ modes throughout the period described above. The current dominating systematic uncertainty on  $\gamma$  is due to the uncertainty on the measured strong-phase inputs, currently contributing an uncertainty of about  $\sim 1^\circ$ ; a number that represents a significant improvement compared to earlier analyses, due to the recently published measurements by the BESIII collaboration [71, 72]. These measurements are based on a data set corresponding to an integrated luminosity of  $2.9\text{ fb}^{-1}$ . The BESIII collaboration is planning to take data corresponding to an additional  $17\text{ fb}^{-1}$  at the  $\psi(3770)$  resonance energy during 2021–22 [75], which will allow for significantly improved

measurements. Therefore, is not expected that the strong-phase inputs will be a limiting systematic uncertainty in model-independent BPGGSZ measurements for the current generation of experiments.

It used to be the case that the dominating systematic uncertainty in LHCb measurements of  $\gamma$  with the BPGGSZ method was due to the non-trivial phase-space acceptance profile [3], contributing most of the  $\sim 2^\circ$  systematic uncertainty on  $\gamma$  related to experimental effects. This would have been the largest systematic uncertainty in the measurement presented in the thesis, and would potentially become the dominating uncertainty during the first upgrade phase of LHCb. However, as described in detail in the thesis, the uncertainty can be avoided altogether in a simultaneous analysis of  $B^\pm \rightarrow DK^\pm$  and  $B^\pm \rightarrow D\pi^\pm$  decays, allowing for maximal use of the large data sets to be collected by the LHCb experiment in the future.

With the results of this thesis, the world averages of  $\gamma$  measurements will move closer to the value preferred by global fits. The Standard Model passes yet another test. As such, the question remains open: does the CKM picture hold up to the increasingly stringent scrutiny of the next decades, or will signs of new physics start to appear?

# Appendices

# A

## Projections of the main fit to data

This appendix includes projections of the main fit to data described in Section 5.5.2, for each of the 160 subcategories in the fit. The projections for LL candidates where  $D \rightarrow K_S^0\pi^+\pi^-$  are shown in Figs. A.1 and A.2; the equivalent projections for DD candidates are shown in Figs. A.3 and A.4; finally the projections for candidates where  $D \rightarrow K_S^0K^+K^-$  are shown in Figs. A.5 and A.6.

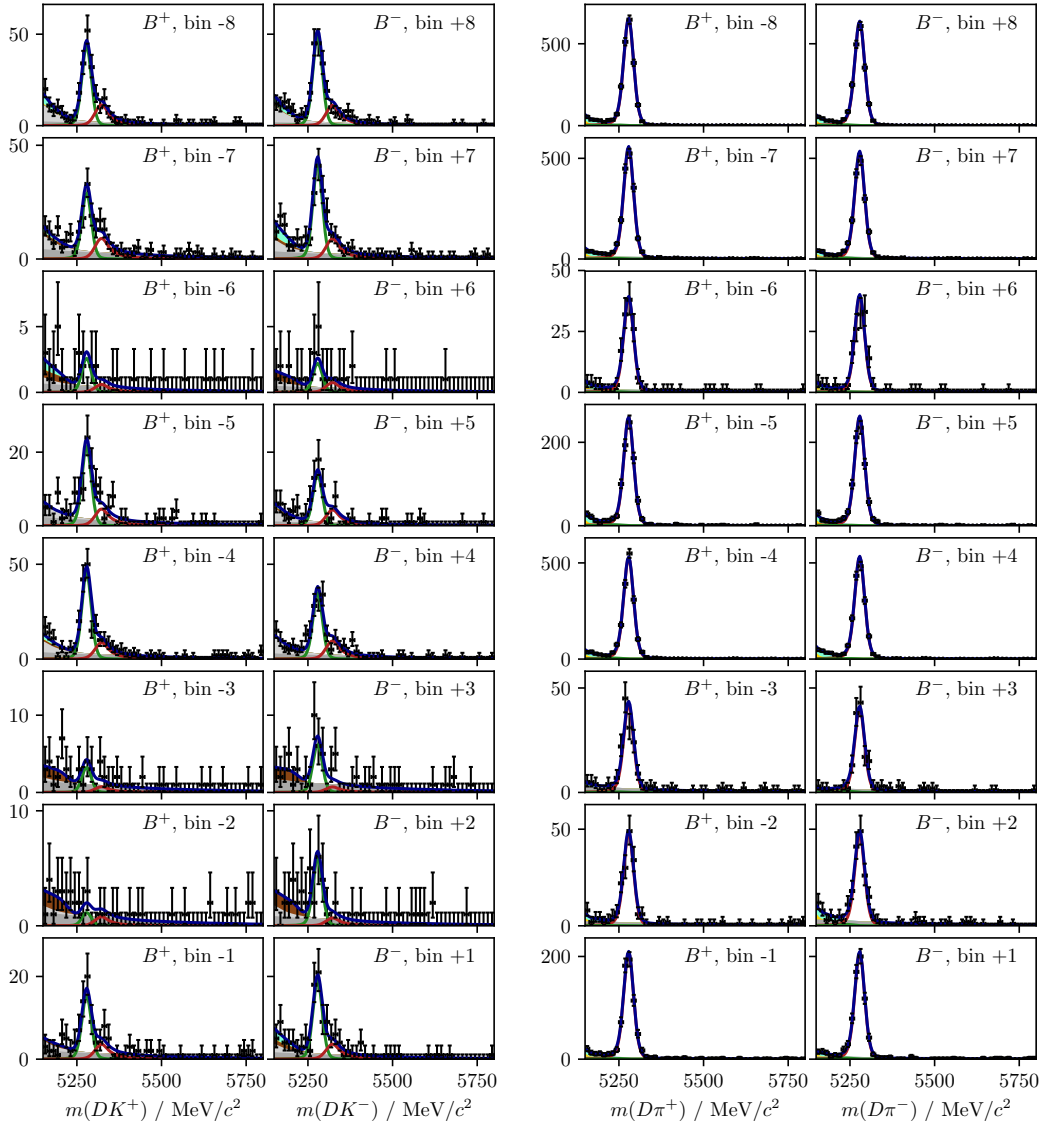


**Figure A.1:** Projections of the main fit to data described in Section 5.5. The two columns on the left show  $B^\pm \rightarrow DK^\pm$  candidates, split by charge, while the two columns on the right show  $B^\pm \rightarrow D\pi^\pm$  candidates. These projections are for the  $D \rightarrow K_S^0 \pi^+ \pi^-$  mode where the  $K_S^0$  meson is in the LL category.

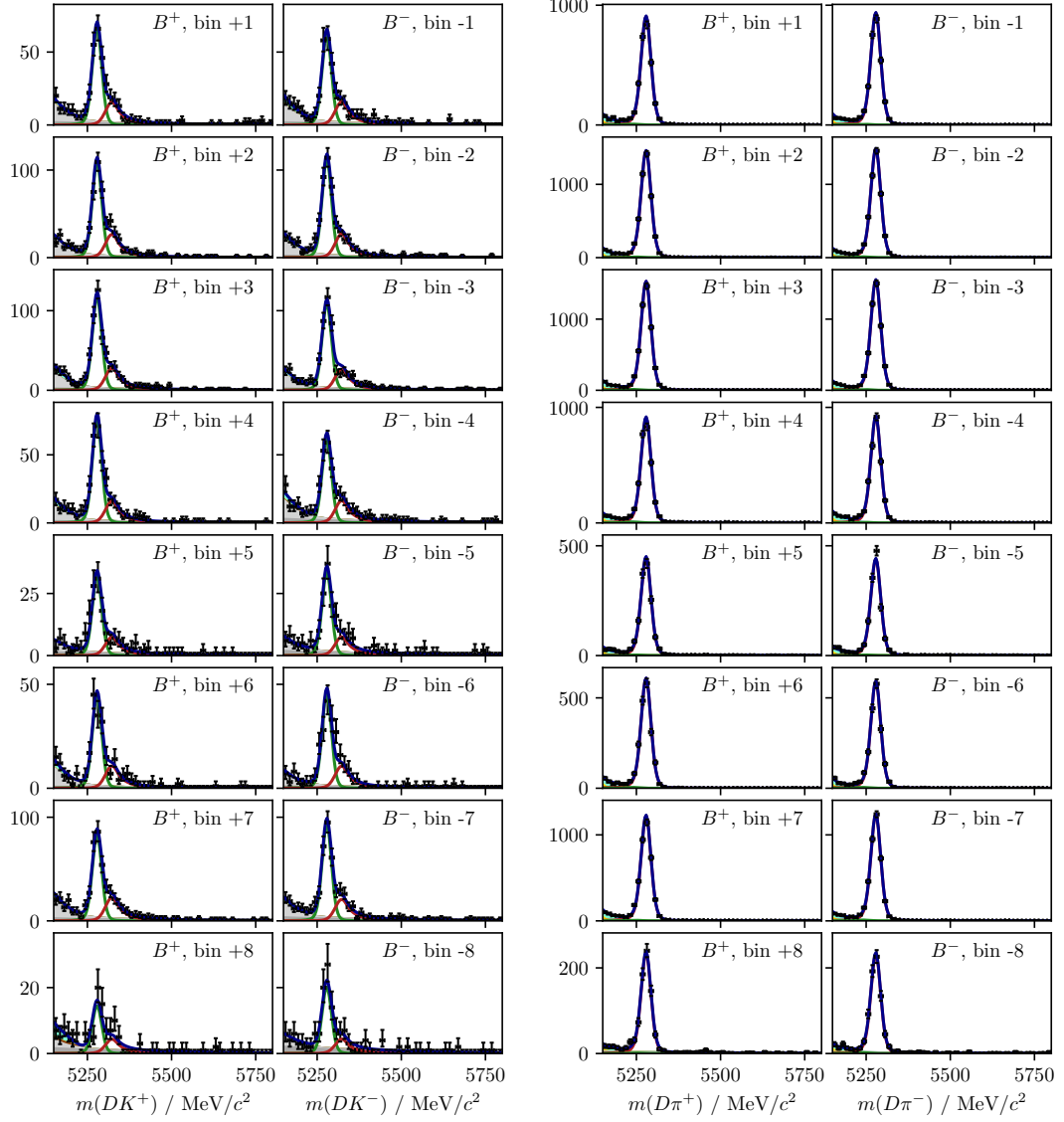


**Figure A.2:** Projections of the main fit to data described in Section 5.5. The two columns on the left show  $B^\pm \rightarrow DK^\pm$  candidates, split by charge, while the two columns on the right show  $B^\pm \rightarrow D\pi^\pm$  candidates. These projections are for the  $D \rightarrow K_S^0 \pi^+ \pi^-$  mode where the  $K_S^0$  meson is in the LL category.

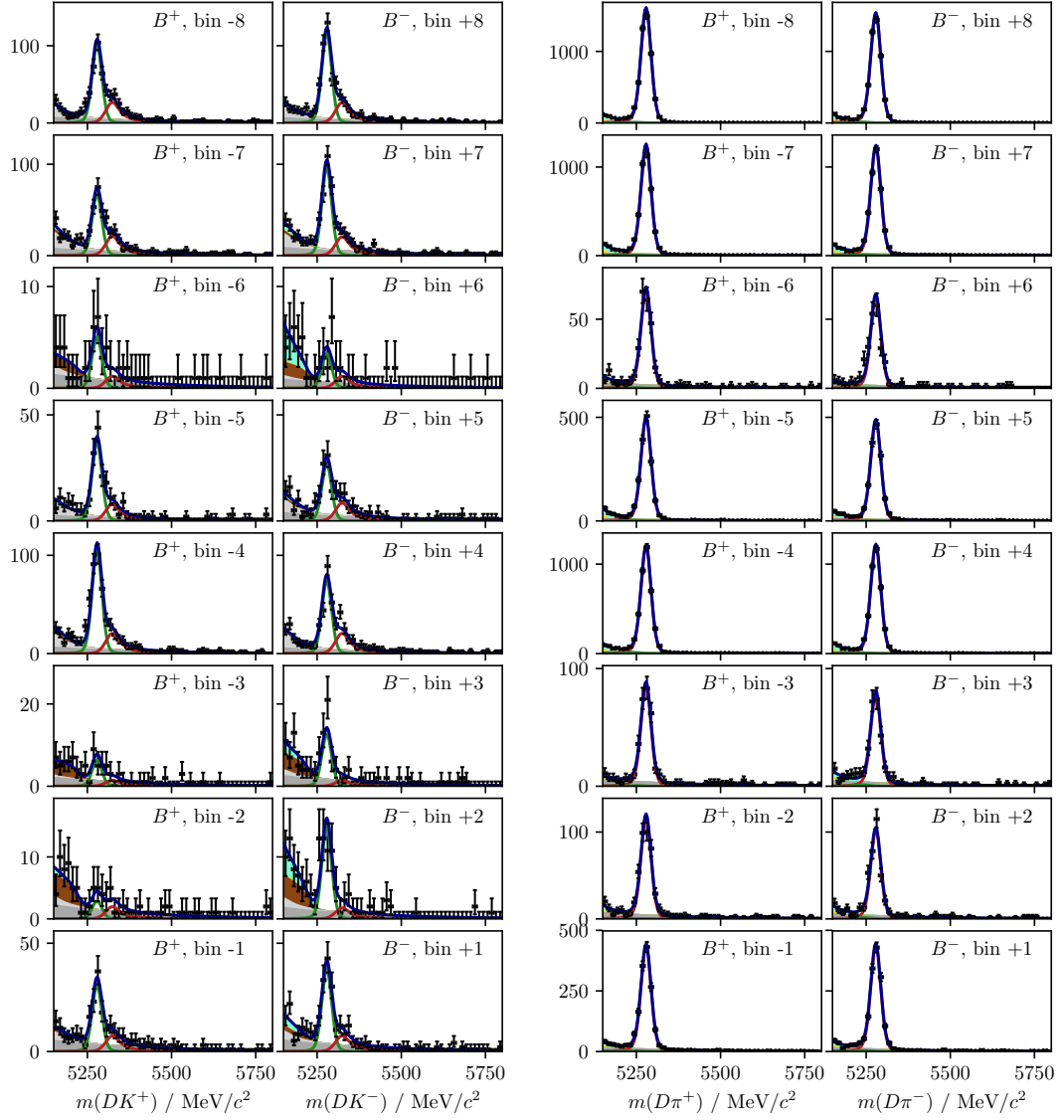


**Figure A.3:** Projections of the main fit to data described in Section 5.5. The two columns on the left show  $B^\pm \rightarrow DK^\pm$  candidates, split by charge, while the two columns on the right show  $B^\pm \rightarrow D\pi^\pm$  candidates. These projections are for the  $D \rightarrow K_S^0 \pi^+ \pi^-$  mode where the  $K_S^0$  meson is in the DD category.

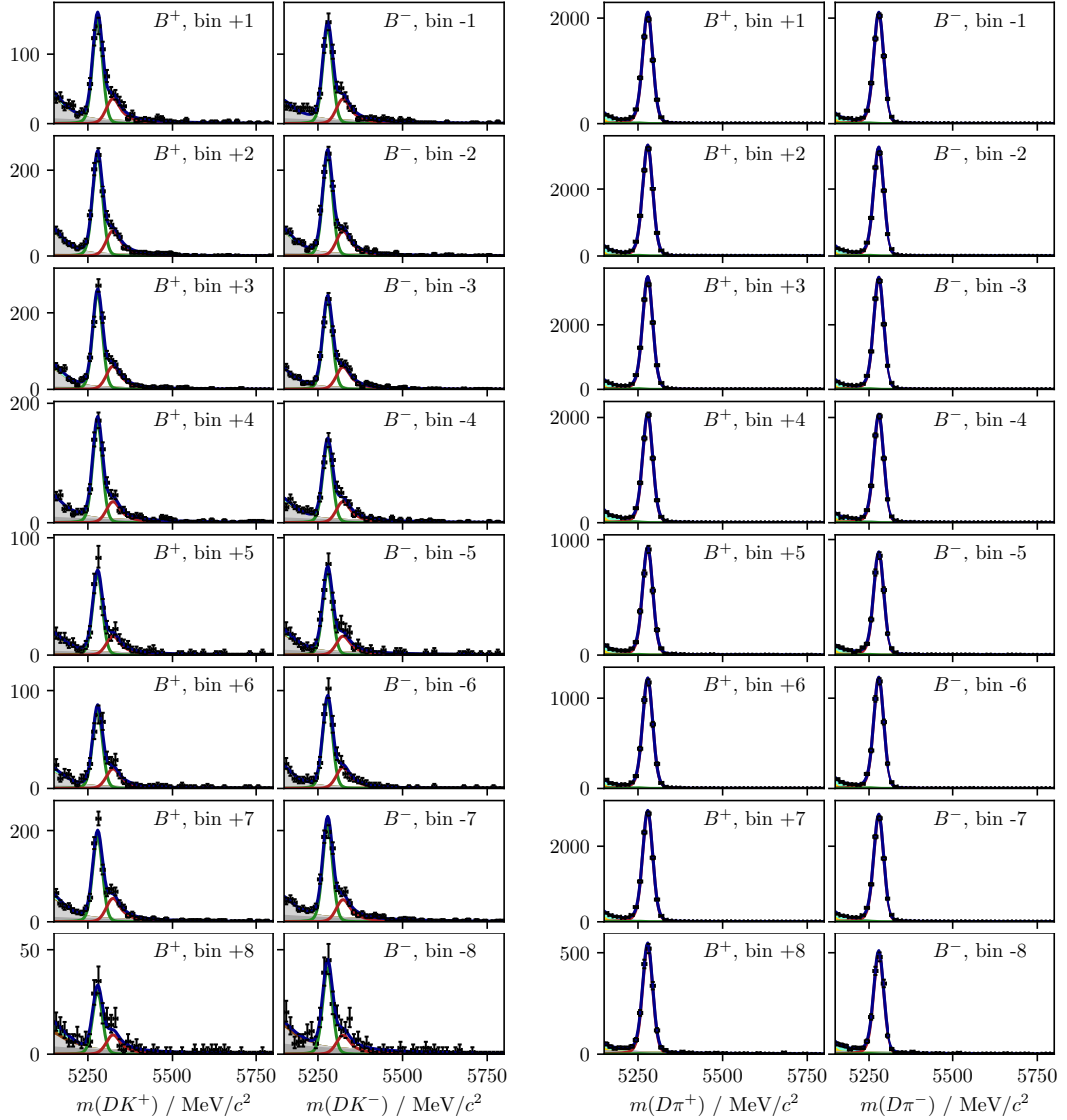


**Figure A.4:** Projections of the main fit to data described in Section 5.5. The two columns on the left show  $B^\pm \rightarrow DK^\pm$  candidates, split by charge, while the two columns on the right show  $B^\pm \rightarrow D\pi^\pm$  candidates. These projections are for the  $D \rightarrow K_S^0 \pi^+ \pi^-$  mode where the  $K_S^0$  meson is in the DD category.

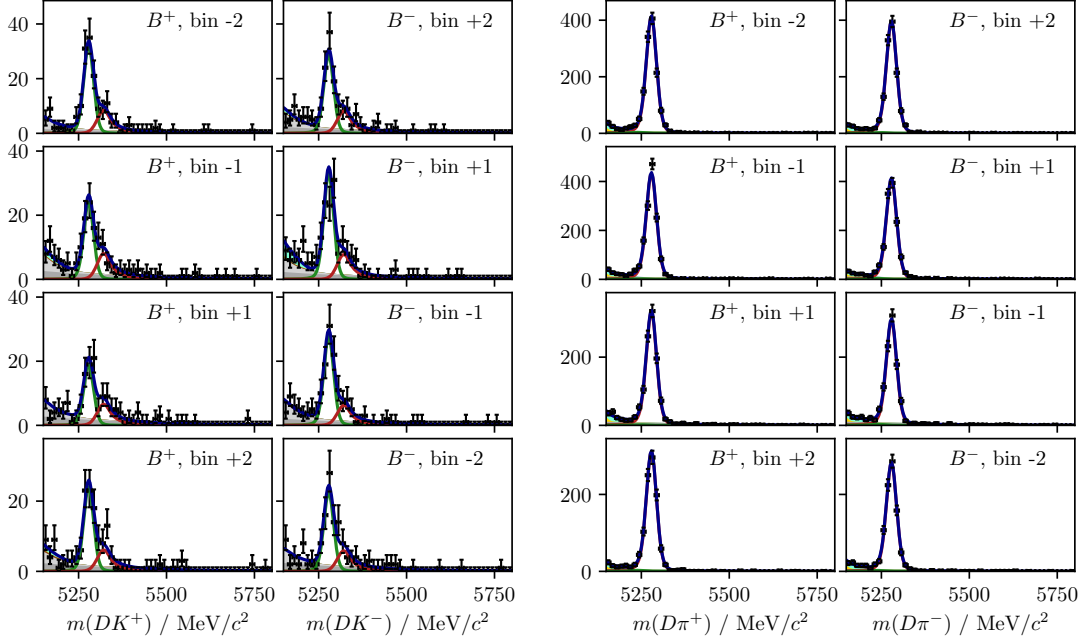


**Figure A.5:** Projections of the main fit to data described in Section 5.5. The two columns on the left show  $B^\pm \rightarrow DK^\pm$  candidates, split by charge, while the two columns on the right show  $B^\pm \rightarrow D\pi^\pm$  candidates. These projections are for the  $D \rightarrow K_S^0 K^+ K^-$  mode where the  $K_S^0$  meson is in the LL category.

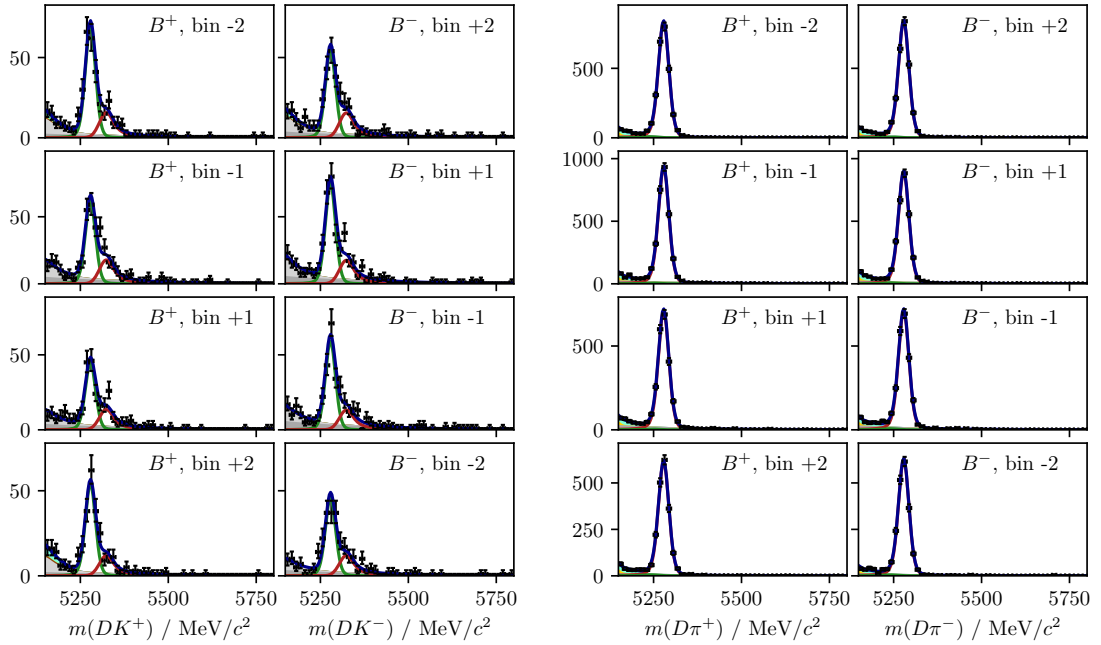


**Figure A.6:** Projections of the main fit to data described in Section 5.5. The two columns on the left show  $B^\pm \rightarrow DK^\pm$  candidates, split by charge, while the two columns on the right show  $B^\pm \rightarrow D\pi^\pm$  candidates. These projections are for the  $D \rightarrow K_S^0 K^+ K^-$  mode where the  $K_S^0$  meson is in the DD category.

# B

## Contributions for the LHCb collaboration

Beyond the data analysis and phenomenology work that I have performed, I have made numerous other contributions to the LHCb experiment. I have undertaken shift work as a RICH piquet and as a Data Manager. For two years, I was the liaison between the PID-performance working group and the *beauty-to-open-charm* (B2OC) physics working group, ensuring that relevant news and updates were communicated between the working groups. The exchange of this information is critical, since the PID calibration is updated regularly during data-taking, and reprocessed in case that issues are found. Furthermore, liaisons from different physics working groups come together in the performance working group, and therefore I was able to showcase ideas or problems from elsewhere in the collaboration for the benefit of analysts in the B2OC working group. As a part of this role, I performed validation work calibration for data samples collected during Run 2.

Preparations for Run 3 of the LHC are well under way. A major part of the LHCb upgrade is the evolution of the trigger system. With an average of  $7\text{ pp}$  interactions per bunch crossing in the upgrade, an event is very likely to have either a  $b\bar{b}$  or  $c\bar{c}$  pair produced. However, the bandwidth for data to be stored to disk is limited. Therefore, the role of trigger becomes that of separating *interesting* signal decays from other signal decays, rather than simply separating signal decays from background. This will be achieved by making the trigger entirely software-based, based on a readout of the whole detector in order to make even the first level of selections. Furthermore, the second layer of the software trigger will perform the full, offline-quality reconstruction, but still need to be fast enough to process the data before the disk buffer is exceeded. During Run 2, most analyses were based on

data selected via inclusive triggering, with the centralised stripping stage applied subsequently to select the signals of interest for specific analyses. In Run 3, the ambition is to run the equivalent of the stripping stage already in the second stage of the software trigger. This will allow for better selections in the trigger and for only saving information related to signal decays, rather than the full event information; both crucial points for optimising the signal rate given a limited band width.

Amongst the working groups, B2OC is unique in having a single code module that handles a large number of decay channels (approx 800 in total) in the stripping stage. I took the role as *migration coordinator*<sup>1</sup>, responsible for developing the equivalent functionality within the new trigger framework, to be run during the LHCb upgrade. The motivation behind a centralised selection module is to exploit the similarities between many B2OC selections to stay within timing and bandwidth limitations; for example, candidates for specific  $D$  decays are formed once and subsequently used in many different selections of  $B \rightarrow DX$  decay candidates. This fundamental design choice was kept in the new B2OC module, but apart from that it was redesigned and written from scratch, in order to follow the functional programming paradigm of the new trigger frame work and to simultaneously allow authors of individual selections to make use of the centrally defined candidates for performance reasons, while providing optimal flexibility for making analysis-specific choices without impacting other selections. I took a leading role in the initial design and testing of the new B2OC module, and helped the first analysts implement analysis-specific selections within it.

---

<sup>1</sup>Along with Alessandro Bertolin and Shunan Zhang.

## Bibliography

- [1] LHCb collaboration, R. Aaij *et al.*, *Measurement of the CKM angle  $\gamma$  in  $B^\pm \rightarrow DK^\pm$  and  $B^\pm \rightarrow D\pi^\pm$  decays with  $K_S^0 h^+ h^-$* , Submitted to JHEP (2020) [arXiv:2010.08483](https://arxiv.org/abs/2010.08483).
- [2] M. Bjørn and S. Malde, *CP violation and material interaction of neutral kaons in measurements of the CKM angle  $\gamma$  using  $B^\pm \rightarrow DK^\pm$  decays where  $D \rightarrow K_S^0 \pi^+ \pi^-$* , JHEP **19** (2019) 106, [arXiv:1904.01129](https://arxiv.org/abs/1904.01129).
- [3] LHCb collaboration, R. Aaij *et al.*, *Measurement of the CKM angle  $\gamma$  using  $B^\pm \rightarrow DK^\pm$  with  $D \rightarrow K_S^0 \pi^+ \pi^-$ ,  $K_S^0 K^+ K^-$  decays*, JHEP **08** (2018) 176, Erratum ibid. **10** (2018) 107, [arXiv:1806.01202](https://arxiv.org/abs/1806.01202).
- [4] G. W. S. Hou, *Flavor Physics and the TeV Scale*, Springer Tracts in Modern Physics, Berlin/Heidelberg, 2nd ed., 2019.
- [5] E. Noether, *Invariante Variationsprobleme*, Nachrichten von der Gesellschaft der Wissenschaften zu Göttingen, Mathematisch-Physikalische Klasse **1918** (1918) 235.
- [6] J. F. Donoghue, E. Golowich, and B. R. Holstein, *Dynamics of the Standard Model*, Cambridge University Press, Cambridge, 2014.
- [7] A. D. Sakarov, *Violation of CP Invariance, C Asymmetry, and Baryon Asymmetry of the Universe*, JETP Letters **5** (1966) 24.
- [8] G. Luders, *On the Equivalence of Invariance under Time Reversal and under Particle-Antiparticle Conjugation for Relativistic Field Theories*, Kong. Dan. Vid. Sel. Mat. Fys. Medd. **28N5** (1954) 1.
- [9] C. S. Wu *et al.*, *Experimental Test of Parity Conservation in Beta Decay*, Phys. Rev. **105** (1957) 1413.
- [10] T. D. Lee and C. N. Yang, *Question of Parity Conservation in Weak Interactions*, Phys. Rev. **104** (1956) 254.

- [11] J. H. Christenson, J. W. Cronin, V. L. Fitch, and R. Turlay, *Evidence for the  $2\pi$  Decay of the  $K_2^0$  Meson*, Phys. Rev. Lett. **13** (1964) 138.
- [12] BaBar collaboration, B. Aubert *et al.*, *Observation of CP Violation in the  $B^0$  Meson System*, Phys. Rev. Lett. **87** (2001) 091801, [arXiv:hep-ex/0107013](https://arxiv.org/abs/hep-ex/0107013).
- [13] Belle collaboration, K. Abe *et al.*, *Observation of large CP violation in the neutral B meson system*, Phys. Rev. Lett. **87** (2001) 091802, [arXiv:hep-ex/0107061](https://arxiv.org/abs/hep-ex/0107061).
- [14] Belle collaboration, K. Trabelsi, *Study of direct CP in charmed B decays and measurement of the CKM angle gamma at Belle*, [arXiv:1301.2033](https://arxiv.org/abs/1301.2033).
- [15] BaBar collaboration, D. Derkach, *Combination of gamma measurements from BaBar*, [arXiv:1301.3283](https://arxiv.org/abs/1301.3283).
- [16] LHCb collaboration, R. Aaij *et al.*, *Observation of CP violation in  $B^\pm \rightarrow DK^\pm$  decays*, Phys. Lett. **B712** (2012) 203, Erratum ibid. **B713** (2012) 351, [arXiv:1203.3662](https://arxiv.org/abs/1203.3662).
- [17] LHCb collaboration, R. Aaij *et al.*, *First observation of CP violation in the decays of  $B_s^0$  mesons*, Phys. Rev. Lett. **110** (2013) 221601, [arXiv:1304.6173](https://arxiv.org/abs/1304.6173).
- [18] LHCb collaboration, R. Aaij *et al.*, *Observation of CP violation in charm decays*, Phys. Rev. Lett. **122** (2019) 211803, [arXiv:1903.08726](https://arxiv.org/abs/1903.08726).
- [19] T2K collaboration, K. Abe *et al.*, *Constraint on the matter–antimatter symmetry-violating phase in neutrino oscillations*, Nature **580** (2020) 339, [arXiv:1910.03887](https://arxiv.org/abs/1910.03887).
- [20] L. K. Gibbons *et al.*, *Measurement of the CP-violation parameter  $\text{Re}(\varepsilon'/\varepsilon)$* , Phys. Rev. Lett. **70** (1993) 1203.
- [21] G. D. Barr *et al.*, *A new measurement of direct CP violation in the neutral kaon system*, Phys. Lett. **B317** (1993) 233.
- [22] NA48 collaboration, J. R. Batley *et al.*, *A precision measurement of direct CP violation in the decay of neutral kaons into two pions*, Phys. Lett. **B544** (2002) 97, [arXiv:hep-ex/0208009](https://arxiv.org/abs/hep-ex/0208009).
- [23] KTeV collaboration, A. Alavi-Harati *et al.*, *Measurements of direct CP violation, CPT symmetry, and other parameters in the neutral kaon system*, Phys. Rev. **D67** (2003) 012005, [arXiv:hep-ex/0208007](https://arxiv.org/abs/hep-ex/0208007).

- [24] HFLAV group, Y. S. Amhis *et al.*, *Averages of b-hadron, c-hadron, and  $\tau$ -lepton properties as of 2018*, arXiv:1909.12524, updated results and plots available at <https://hflav.web.cern.ch/>.
- [25] M. Kobayashi and T. Maskawa, *CP-Violation in the Renormalizable Theory of Weak Interaction*, Prog. Theor. Phys. **49** (1973) 652.
- [26] N. Cabibbo, *Unitary Symmetry and Leptonic Decays*, Physical Review Letters **10** (1963) 531.
- [27] L.-L. Chau and W.-Y. Keung, *Comments on the Parametrization of the Kobayashi-Maskawa Matrix*, Phys. Rev. Lett. **53** (1984) 1802.
- [28] Particle Data Group, P. A. Zyla *et al.*, *Review of particle physics*, Prog. Theor. Exp. Phys. **2020** (2020) 083C01.
- [29] L. Wolfenstein, *Parametrization of the Kobayashi-Maskawa Matrix*, Phys. Rev. Lett. **51** (1983) 1945.
- [30] Y. H. Ahn, H.-Y. Cheng, and S. Oh, *Wolfenstein parametrization at higher order: Seeming discrepancies and their resolution*, Phys. Lett. **B703** (2011) 571, arXiv:1106.0935.
- [31] A. J. Buras, M. E. Lautenbacher, and G. Ostermaier, *Waiting for the Top Quark Mass,  $K^+ \rightarrow \pi^+ \nu \bar{\nu}$ ,  $B_s^0 - \bar{B}_s^0$  Mixing, and CP asymmetries in B decays*, Phys. Rev. **D50** (1994) 3433, arXiv:hep-ph/9403384.
- [32] J. Charles *et al.*, *CP violation and the CKM matrix: Assessing the impact of the asymmetric B factories*, Eur. Phys. J. **C41** (2005) 1, arXiv:hep-ph/0406184.
- [33] CKMfitter group, J. Charles *et al.*, *Current status of the Standard Model CKM fit and constraints on  $\Delta F = 2$  new physics*, Phys. Rev. **D91** (2015) 073007, arXiv:1501.05013, updated results and plots available at <http://ckmfitter.in2p3.fr/>.
- [34] J. Brod and J. Zupan, *The ultimate theoretical error on  $\gamma$  from  $B \rightarrow DK$  decays*, JHEP **2014** (2014) 51, arXiv:1308.5663.
- [35] M. Blanke and A. J. Buras, *Emerging  $\Delta M_d$ -anomaly from tree-level determinations of  $|V_{cb}|$  and the angle  $\gamma$* , Eur. Phys. J. **C79** (2019) 159, arXiv:1812.06963.

- [36] UTfit collaboration, M. Bona *et al.*, *The unitarity triangle fit in the standard model and hadronic parameters from lattice QCD: A reappraisal after the measurements of  $\Delta m_s$  and  $BR(B \rightarrow \tau\nu_\tau)$* , JHEP **10** (2006) 081, arXiv:hep-ph/0606167, updated results and plots available at <http://www.utfit.org/>.
- [37] LHCb collaboration, I. Bediaga *et al.*, *Physics case for an LHCb Upgrade II - Opportunities in flavour physics, and beyond, in the HL-LHC era*, arXiv:1808.08865.
- [38] Y. Grossman and M. Savastio, *Effects of  $K^0 - \bar{K}^0$  mixing on determining  $\gamma$  from  $B^\pm \rightarrow DK^\pm$* , JHEP **2014** (2014) 8, arXiv:1311.3575.
- [39] M. Gronau and D. Wyler, *On determining a weak phase from charged B decay asymmetries*, Phys. Lett. **B265** (1991) 172.
- [40] M. Gronau and D. London, *How to determine all the angles of the unitarity triangle from  $B_d^0 \rightarrow DK_S^0$  and  $B_s^0 \rightarrow D\phi$* , Phys. Lett. **B253** (1991) 483.
- [41] D. Atwood, I. Dunietz, and A. Soni, *Enhanced CP Violation with  $B \rightarrow K D^0(\bar{D}^0)$  Modes and Extraction of the Cabibbo-Kobayashi-Maskawa Angle  $\gamma$* , Phys. Rev. Lett. **78** (1997) 3257, arXiv:hep-ph/9612433.
- [42] D. Atwood, I. Dunietz, and A. Soni, *Improved methods for observing CP violation in  $B^\pm \rightarrow K D$  and measuring the CKM phase  $\gamma$* , Phys. Rev. **D63** (2001) 036005, arXiv:hep-ph/0008090.
- [43] LHCb collaboration, R. Aaij *et al.*, *Measurement of the CKM angle  $\gamma$  from a combination of LHCb results*, JHEP **12** (2016) 087, arXiv:1611.03076.
- [44] LHCb collaboration, *Update of the LHCb combination of the CKM angle  $\gamma$* , LHCb-CONF-2018-002, 2018.
- [45] M. Kenzie, M. Martinelli, and N. Tuning, *Estimating  $r_B^{D\pi}$  as an input to the determination of the CKM angle  $\gamma$* , Phys. Rev. **D94** (2016) 054021, arXiv:1606.09129.
- [46] T. Evans, J. Libby, S. Malde, and G. Wilkinson, *Improved sensitivity to the CKM phase  $\gamma$  through binning phase space in  $B^- \rightarrow DK^-$ ,  $D \rightarrow K^+\pi^-\pi^-\pi^+$  decays*, Phys. Lett. **B802** (2020) 135188, arXiv:1909.10196.

- [47] P. K. Resmi, J. Libby, S. Malde, and G. Wilkinson, *Quantum-correlated measurements of  $D \rightarrow K_S^0 \pi^+ \pi^- \pi^0$  decays and consequences for the determination of the CKM angle  $\gamma$* , JHEP **01** (2018) 082, [arXiv:1710.10086](https://arxiv.org/abs/1710.10086).
- [48] S. Harnew *et al.*, *Model-independent determination of the strong phase difference between  $D_0$  and  $\bar{D}_0 \rightarrow \pi^+ \pi^- \pi^+ \pi^-$  amplitudes*, JHEP **2018** (2018) 144, [arXiv:1709.03467](https://arxiv.org/abs/1709.03467).
- [49] R. H. Dalitz, *CXII. On the analysis of  $\tau$ -meson data and the nature of the  $\tau$ -meson*, The London, Edinburgh, and Dublin Philosophical Magazine and Journal of Science **44** (1953) 1068.
- [50] BaBar and Belle collaborations, I. Adachi *et al.*, *Measurement of  $\cos 2\beta$  in  $B^0 \rightarrow D^{(*)} h^0$  with  $D \rightarrow K_S^0 \pi^+ \pi^-$  decays by a combined time-dependent Dalitz plot analysis of BaBar and Belle data*, Phys. Rev. **D98** (2018) 112012, [arXiv:1804.06153](https://arxiv.org/abs/1804.06153).
- [51] S. U. Chung *et al.*, *Partial wave analysis in K-matrix formalism*, Annalen der Physik **507** (1995) 404.
- [52] D. Aston *et al.*, *A study of  $K^- \pi^+$  scattering in the reaction  $K^- p \rightarrow \pi^+ n$  at 11 GeV/c*, Nucl. Phys. **B296** (1988) 493.
- [53] A. Bondar, *Proceedings of BINP special analysis meeting on Dalitz analysis, 24-26 Sep. 2002, unpublished*.
- [54] Belle collaboration, A. Poluektov *et al.*, *Measurement of  $\phi_3$  with Dalitz plot analysis of  $B^\pm \rightarrow D^{(*)} K^\pm$  decay*, Phys. Rev. **D70** (2004) 072003, [arXiv:hep-ex/0406067](https://arxiv.org/abs/hep-ex/0406067).
- [55] A. Giri, Y. Grossman, A. Soffer, and J. Zupan, *Determining  $\gamma$  using  $B^\pm \rightarrow D K^\pm$  with multibody  $D$  decays*, Phys. Rev. **D68** (2003) , [arXiv:hep-ph/0303187](https://arxiv.org/abs/hep-ph/0303187).
- [56] A. Ceccucci *et al.*, *Origins of the method to determine the CKM angle  $\gamma$  using  $B^\pm \rightarrow D K^\pm$ ,  $D \rightarrow K_S^0 \pi^+ \pi^-$  decays*, [arXiv:2006.12404](https://arxiv.org/abs/2006.12404).
- [57] BaBar collaboration, B. Aubert *et al.*, *Measurement of the Cabibbo-Kobayashi-Maskawa angle  $\gamma$  in  $B^\mp \rightarrow D^{(*)} K^\mp$  decays with a Dalitz analysis of  $D \rightarrow K_S^0 \pi^- \pi^+$* , Phys. Rev. Lett. **95** (2005) 121802, [arXiv:hep-ex/0504039](https://arxiv.org/abs/hep-ex/0504039).

- [58] BaBar collaboration, B. Aubert *et al.*, *Improved measurement of the CKM angle  $\gamma$  in  $B^\mp \rightarrow D^{(*)}K^{(*)\mp}$  decays with a Dalitz plot analysis of  $D$  decays to  $K_S^0\pi^+\pi^-$  and  $K_S^0K^+K^-$* , Phys. Rev. **D78** (2008) 034023, arXiv:0804.2089.
- [59] BaBar collaboration, P. del Amo Sanchez *et al.*, *Evidence for direct CP violation in the measurement of the Cabibbo-Kobayashi-Maskawa angle  $\gamma$  with  $B^\mp \rightarrow D^{(*)}K^{(*)\mp}$  decays*, Phys. Rev. Lett. **105** (2010) 121801, arXiv:1005.1096.
- [60] Belle collaboration, A. Poluektov *et al.*, *Measurement of  $\phi_3$  with Dalitz plot analysis of  $B^+ \rightarrow D^{(*)}K^{(*)+}$  decay*, Phys. Rev. **D73** (2006) 112009, arXiv:hep-ex/0604054.
- [61] Belle collaboration, A. Poluektov *et al.*, *Evidence for direct CP violation in the decay  $B^\pm \rightarrow D^{(*)}K^\pm$ ,  $D \rightarrow K_S^0\pi^+\pi^-$  and measurement of the CKM phase  $\phi_3$* , Phys. Rev. **D81** (2010) 112002, arXiv:1003.3360.
- [62] LHCb collaboration, R. Aaij *et al.*, *Measurement of CP violation and constraints on the CKM angle  $\gamma$  in  $B^\pm \rightarrow DK^\pm$  with  $D \rightarrow K_S^0\pi^+\pi^-$  decays*, Nucl. Phys. **B888** (2014) 169, arXiv:1407.6211.
- [63] LHCb collaboration, R. Aaij *et al.*, *Measurement of the CKM angle  $\gamma$  using  $B^0 \rightarrow DK^{*0}$  with  $D \rightarrow K_S^0\pi^+\pi^-$  decays*, JHEP **08** (2016) 137, arXiv:1605.01082.
- [64] A. Bondar and A. Poluektov, *Feasibility study of model-independent approach to  $\phi_3$  measurement using Dalitz plot analysis*, Eur. Phys. J. **C47** (2006) 347, arXiv:hep-ph/0510246.
- [65] A. Bondar and A. Poluektov, *The use of quantum-correlated  $D_0$  decays for  $\phi_3$  measurement*, Eur. Phys. J. **C55** (2008) 51, arXiv:0801.0840.
- [66] Belle collaboration, H. Aihara *et al.*, *First measurement of  $\phi_3$  with a model-independent Dalitz plot analysis of  $B^\pm \rightarrow DK^\pm$ ,  $D \rightarrow K_S^0\pi^+\pi^-$  decay*, Phys. Rev. **D85** (2012) 112014, arXiv:1204.6561.
- [67] LHCb collaboration, R. Aaij *et al.*, *A model-independent Dalitz plot analysis of  $B^\pm \rightarrow DK^\pm$  with  $D \rightarrow K_S^0h^+h^-$  ( $h = \pi, K$ ) decays and constraints on the CKM angle  $\gamma$* , Phys. Lett. **B718** (2012) 43, arXiv:1209.5869.

- [68] LHCb collaboration, R. Aaij *et al.*, *Measurement of the CKM angle  $\gamma$  using  $B^\pm \rightarrow DK^\pm$  with  $D \rightarrow K_S^0\pi^+\pi^-$ ,  $K_S^0K^+K^-$  decays*, JHEP **10** (2014) 097, [arXiv:1408.2748](https://arxiv.org/abs/1408.2748).
- [69] A. Poluektov, *Unbinned model-independent measurements with coherent admixtures of multibody neutral D meson decays*, Eur. Phys. J. **C78** (2018) 121, [arXiv:1712.08326](https://arxiv.org/abs/1712.08326).
- [70] CLEO collaboration, J. Libby *et al.*, *Model-independent determination of the strong-phase difference between  $D^0$  and  $\bar{D}^0 \rightarrow K_{S,L}^0 h^+h^-$  ( $h = \pi, K$ ) and its impact on the measurement of the CKM angle  $\gamma/\phi_3$* , Phys. Rev. **D82** (2010) 112006, [arXiv:1010.2817](https://arxiv.org/abs/1010.2817).
- [71] BESIII collaboration, M. Ablikim *et al.*, *Model-independent determination of the relative strong-phase difference between  $D^0$  and  $\bar{D}^0 \rightarrow K_{S,L}^0\pi^+\pi^-$  and its impact on the measurement of the CKM angle  $\gamma/\phi_3$* , Phys. Rev. **D101** (2020) 112002, [arXiv:2003.00091](https://arxiv.org/abs/2003.00091).
- [72] BESIII collaboration, M. Ablikim *et al.*, *Improved model-independent determination of the strong-phase difference between  $D^0$  and  $\bar{D}^0 \rightarrow K_{S,L}^0K^+K^-$  decays*, Phys. Rev. **D102** (2020) 052008, [arXiv:2007.07959](https://arxiv.org/abs/2007.07959).
- [73] C. Thomas and G. Wilkinson, *Model-independent  $D^0 - \bar{D}^0$  mixing and CP violation studies with  $D^0 \rightarrow K_S^0\pi^+\pi^-$  and  $D^0 \rightarrow K_S^0K^+K^-$* , JHEP **2012** (2012) 185, [arXiv:1209.0172](https://arxiv.org/abs/1209.0172).
- [74] LHCb collaboration, R. Aaij *et al.*, *Model-independent measurement of the CKM angle  $\gamma$  using  $B^0 \rightarrow DK^{*0}$  decays with  $D \rightarrow K_S^0\pi^+\pi^-$  and  $K_S^0K^+K^-$* , JHEP **06** (2016) 131, [arXiv:1604.01525](https://arxiv.org/abs/1604.01525).
- [75] C. Lin, *Hadronic Charm Meson Decays at BESIII*, In talk presented 28 July, 2020, at the ICHEP conference.
- [76] M. Nayak *et al.*, *First determination of the CP content of  $D \rightarrow \pi^+\pi^-\pi^0$  and  $D \rightarrow K^+K^-\pi^0$* , Phys. Lett. **B740** (2015) 1, [arXiv:1410.3964](https://arxiv.org/abs/1410.3964).
- [77] S. Malde *et al.*, *First determination of the CP content of  $D \rightarrow \pi^+\pi^-\pi^+\pi^-$  and updated determination of the CP contents of  $D \rightarrow \pi^+\pi^-\pi^0$  and  $D \rightarrow K^+K^-\pi^0$* , Phys. Lett. **B747** (2015) 9, [arXiv:1504.05878](https://arxiv.org/abs/1504.05878).
- [78] M. Gronau, *Improving bounds on  $\gamma$  in  $B^\pm \rightarrow DK^\pm$  and  $B^{\pm,0} \rightarrow DX_s^{\pm,0}$* , Phys. Lett. **B557** (2003) 198, [arXiv:hep-ph/0211282](https://arxiv.org/abs/hep-ph/0211282).

- [79] J. Garra Ticó, *A strategy for a simultaneous measurement of CP violation parameters related to the CKM angle  $\gamma$  in multiple B meson decay channels*, [arXiv:1804.05597](https://arxiv.org/abs/1804.05597).
- [80] J. G. Ticó *et al.*, *A study of the sensitivity to CKM angle  $\gamma$  under simultaneous determination from multiple B meson decay modes*, Phys. Rev. **D102** (2020) 053003, [arXiv:1909.00600](https://arxiv.org/abs/1909.00600).
- [81] C. De Melis, *The CERN accelerator complex. Complexe des accélérateurs du CERN*, <https://cds.cern.ch/record/2119882>, 2016.
- [82] ATLAS collaboration, *Luminosity determination in pp collisions at  $\sqrt{s} = 13$  TeV using the ATLAS detector at the LHC*, ATLAS-CONF-2019-021, 2019.
- [83] LHCb collaboration, A. A. Alves *et al.*, *The LHCb Detector at the LHC*, J. Inst. **3** (2008) S08005.
- [84] LHCb collaboration, C. Elsässer,  $\bar{b}b$  production angle plots, [https://lhcb.web.cern.ch/lhcb/speakersbureau/html/bb\\_ProductionAngles.html](https://lhcb.web.cern.ch/lhcb/speakersbureau/html/bb_ProductionAngles.html).
- [85] LHCb collaboration, P. R. Barbosa-Marinho *et al.*, *LHCb VELO (VErtex LOcator) - Technical Design Report*, LHCb-TDR-5, 2001.
- [86] LHCb VELO group, R. Aaij *et al.*, *Performance of the LHCb Vertex Locator*, J. Inst. **9** (2014) P09007, [arXiv:1405.7808](https://arxiv.org/abs/1405.7808).
- [87] LHCb Outer Tracker group, R. Arink *et al.*, *Performance of the LHCb Outer Tracker*, J. Inst. **9** (2014) P01002, [arXiv:1311.3893](https://arxiv.org/abs/1311.3893).
- [88] LHCb collaboration, R. Aaij *et al.*, *LHCb detector performance*, Int. J. Mod. Phys **A30** (2015) 1530022, [arXiv:1412.6352](https://arxiv.org/abs/1412.6352).
- [89] LHCb collaboration, S. Amato *et al.*, *LHCb RICH: Technical Design Report*, LHCb-TDR-3, 2000.
- [90] LHCb RICH collaboration, M. Adinolfi *et al.*, *Performance of the LHCb RICH detector at the LHC*, Eur. Phys. J. **C73** (2013) 2431, [arXiv:1211.6759](https://arxiv.org/abs/1211.6759).
- [91] LHCb RICH collaboration, A. Papanestis *et al.*, *Performance of the LHCb RICH detectors during the LHC Run II*, Nucl. Instrum. Meth **A876** (2017) 221, [arXiv:1703.08152](https://arxiv.org/abs/1703.08152).

- [92] LHCb collaboration, S. Amato *et al.*, *LHCb calorimeters: Technical Design Report*, LHCb-TDR-2, 2000.
- [93] LHCb ECAL group, I. Machikhiliyan, *The LHCb electromagnetic calorimeter*, J. Phys. Conf. Ser. **160** (2009) 012047.
- [94] LHCb collaboration, R. Aaij *et al.*, *Search for lepton-universality violation in  $B^+ \rightarrow K^+ \ell^+ \ell^-$  decays*, Phys. Rev. Lett. **122** (2019) 191801, [arXiv:1903.09252](https://arxiv.org/abs/1903.09252).
- [95] LHCb collaboration, R. Aaij *et al.*, *Measurement of CP-averaged observables in the  $B^0 \rightarrow K^{*0} \mu^+ \mu^-$  decay*, Phys. Rev. Lett. **125** (2020) 011802, [arXiv:2003.04831](https://arxiv.org/abs/2003.04831).
- [96] LHCb collaboration, R. Aaij *et al.*, *Measurement of the  $B_s^0 \rightarrow \mu^+ \mu^-$  branching fraction and effective lifetime and search for  $B^0 \rightarrow \mu^+ \mu^-$  decays*, Phys. Rev. Lett. **118** (2017) 191801, [arXiv:1703.05747](https://arxiv.org/abs/1703.05747).
- [97] LHCb collaboration, *LHCb muon system: second addendum to the Technical Design Report*, LHCb-TDR-4-add-2, 2005.
- [98] D. Hutchcroft, *VELO Pattern Recognition*, LHCb-2007-013, 2007.
- [99] M. Needham and J. Van Tilburg, *Performance of the track matching*, LHCb-2007-020, 2007.
- [100] M. Needham, *Performance of the Track Matching*, LHCb-2007-129, 2007.
- [101] O. Callot, *Downstream Pattern Recognition*, LHCb-2007-026, 2007.
- [102] R. Frühwirth, *Application of Kalman filtering to track and vertex fitting*, Nucl. Instrum. Meth. **A262** (1987) 444.
- [103] J. Van Tilburg, *Track simulation and reconstruction in LHCb*, CERN-THESIS-2005-040, 2005.
- [104] M. De Cian *et al.*, *Measurement of the track finding efficiency*, LHCb-PUB-2011-025, 2012.
- [105] LHCb collaboration, *PID performance plots*, <https://twiki.cern.ch/twiki/bin/view/LHCb/PIDConferencePlots>.
- [106] R. W. Forty and O. Schneider, *RICH pattern recognition*, LHCb-98-040, 1998.

- [107] J. R. T. De Mello-Neto and M. Gandelman, *Muon ID performance with the reoptimized LHCb detector*, LHCb-2003-089, 2003.
- [108] M. Gandelman and E. Polycarpo, *The Performance of the LHCb Muon Identification Procedure*, LHCb-2007-145, 2008.
- [109] H. Terrier and I. Belyaev, *Particle identification with LHCb calorimeters*, LHCb-2003-092, 2003.
- [110] LHCb collaboration, R. Aaij *et al.*, *The LHCb trigger and its performance in 2011*, J. Inst. **8** (2013) P04022, [arXiv:1211.3055](https://arxiv.org/abs/1211.3055).
- [111] LHCb collaboration, R. Aaij *et al.*, *Design and performance of the LHCb trigger and full real-time reconstruction in Run 2 of the LHC*, J. Inst. **14** (2019) P04013, [arXiv:1812.10790](https://arxiv.org/abs/1812.10790).
- [112] V. V. Gligorov and M. Williams, *Efficient, reliable and fast high-level triggering using a bonsai boosted decision tree*, J. Inst. **8** (2013) P02013, [arXiv:1210.6861](https://arxiv.org/abs/1210.6861).
- [113] I. Bird, *Computing for the Large Hadron Collider*, Annual Review of Nuclear and Particle Science **61** (2011) 99.
- [114] T. Sjöstrand, S. Mrenna, and P. Skands, *A brief introduction to PYTHIA 8.1*, Comput. Phys. Commun. **178** (2008) 852, [arXiv:0710.3820](https://arxiv.org/abs/0710.3820); T. Sjöstrand, S. Mrenna, and P. Skands, *PYTHIA 6.4 physics and manual*, JHEP **05** (2006) 026, [arXiv:hep-ph/0603175](https://arxiv.org/abs/hep-ph/0603175).
- [115] I. Belyaev *et al.*, *Handling of the generation of primary events in Gauss, the LHCb simulation framework*, J. Phys. Conf. Ser. **331** (2011) 032047.
- [116] D. J. Lange, *The EvtGen particle decay simulation package*, Nucl. Instrum. Meth. **A462** (2001) 152.
- [117] P. Golonka and Z. Was, *PHOTOS Monte Carlo: A precision tool for QED corrections in Z and W decays*, Eur. Phys. J. **C45** (2006) 97, [arXiv:hep-ph/0506026](https://arxiv.org/abs/hep-ph/0506026).
- [118] Geant4 collaboration, J. Allison *et al.*, *Geant4 developments and applications*, IEEE Trans. Nucl. Sci. **53** (2006) 270.
- [119] M. Clemencic *et al.*, *The LHCb simulation application, Gauss: Design, evolution and experience*, J. Phys. Conf. Ser. **331** (2011) 032023.

- [120] D. Müller, M. Clemencic, G. Corti, and M. Gersabeck, *ReDecay: A novel approach to speed up the simulation at LHCb*, Eur. Phys. J. **C78** (2018) 1009, [arXiv:1810.10362](https://arxiv.org/abs/1810.10362).
- [121] G. A. Cowan, D. C. Craik, and M. D. Needham, *RapidSim: An application for the fast simulation of heavy-quark hadron decays*, Comput. Phys. Commun. **214** (2017) 239, [arXiv:1612.07489](https://arxiv.org/abs/1612.07489).
- [122] LHCb collaboration, *LHCb performance numbers*, <https://lhcb.web.cern.ch/speakersbureau/html/PerformanceNumbers.html>.
- [123] LHCb collaboration, R. Aaij *et al.*, *Measurement of the  $B^\pm$  production cross-section in  $pp$  collisions at  $\sqrt{s} = 7$  and 13 TeV*, JHEP **12** (2017) 026, [arXiv:1710.04921](https://arxiv.org/abs/1710.04921).
- [124] A. Pais and O. Piccioni, *Note on the decay and absorption of the  $\theta^0$* , Phys. Rev. **100** (1955) 1487.
- [125] M. L. Good, *Relation between Scattering and Absorption in the Pais-Piccioni Phenomenon*, Phys. Rev. **106** (1957) 591.
- [126] W. Petscher *et al.*, *Regeneration of arbitrary coherent neutral kaon states: A new method for measuring the  $K^0 - \bar{K}^0$  forward scattering amplitude/forward scattering amplitude*, Z. Phys **C72** (1996) 543.
- [127] Belle II collaboration, E. Kou *et al.*, *The Belle II Physics Book*, Prog. Theor. Exp. Phys. **2019** (2019) 123C01, [arXiv:1808.10567](https://arxiv.org/abs/1808.10567).
- [128] I. I. Bigi and H. Yamamoto, *Interference between Cabibbo allowed and doubly forbidden transitions in  $D \rightarrow K_{S,L} + \pi$ 's decays*, Phys. Lett. **B349** (1995) 363, [arXiv:hep-ph/9502238](https://arxiv.org/abs/hep-ph/9502238).
- [129] CLEO collaboration, Q. He *et al.*, *Comparison of  $D \rightarrow K_S^0 \pi$  and  $D \rightarrow K_L^0 \pi$  decay rates*, Phys. Rev. Lett. **100** (2008) 091801, [arXiv:0711.1463](https://arxiv.org/abs/0711.1463).
- [130] Y. Grossman and Y. Nir, *CP violation in  $\tau^\pm \rightarrow \pi^\pm K_S \nu$  and  $D^\pm \rightarrow \pi^\pm K_S$ : the importance of  $K_S - K_L$  interference*, JHEP **2012** (2012) 2, [arXiv:1110.3790](https://arxiv.org/abs/1110.3790).
- [131] Y. Ohnishi *et al.*, *Accelerator design at SuperKEKB*, Prog. Theor. Exp. Phys. **2013** (2013) .
- [132] LHCb collaboration, *LHCb reoptimized detector design and performance: Technical Design Report*, LHCb-TDR-9, 2003.

- [133] J. Gassner, M. Needham, and O. Steinkamp, *Layout and Expected Performance of the LHCb TT Station*, LHCb-2003-140, 2004.
- [134] Belle collaboration, A. B. Kaliyar *et al.*, *Measurements of branching fraction and direct CP asymmetry in  $B^\pm \rightarrow K_S^0 K_S^0 K^\pm$  and a search for  $B^\pm \rightarrow K_S^0 K_S^0 \pi^\pm$* , Phys. Rev. **D99** (2019) 031102, [arXiv:1812.10221](https://arxiv.org/abs/1812.10221).
- [135] N. Hiroshi, *Search for new physics by a time-dependent CP violation analysis of the decay  $B \rightarrow K_S^0$  eta gamma using the Belle detector*, PhD thesis, Tohoku University, Senday, 2015.
- [136] A. Gsponer *et al.*, *Precise Coherent  $K_S^0$  Regeneration Amplitudes for C, Al, Cu, Sn, and Pb Nuclei from 20 to 140 GeV/c and Their Interpretation*, Phys. Rev. Lett. **22** (1979) 13.
- [137] R. A. Briere and B. Weinstein, *Determining the Phase of a Strong Scattering Amplitude from Its Momentum Dependence to Better Than 1°: The Example of Kaon Regeneration*, Phys. Rev. Lett. **75** (1995) 402.
- [138] B. R. Ko, E. Won, B. Golob, and P. Pakhlov, *Effect of nuclear interactions of neutral kaons on CP asymmetry measurements*, Phys. Rev. **D84** (2011) 111501, [arXiv:1006.1938](https://arxiv.org/abs/1006.1938).
- [139] LHCb collaboration, *LHCb VELO Upgrade Technical Design Report*, LHCB-TDR-013, 2013.
- [140] LHCb collaboration, *LHCb PID Upgrade Technical Design Report*, LHCB-TDR-014, 2013.
- [141] W. D. Hulsbergen, *Decay chain fitting with a Kalman filter*, Nucl. Instrum. Meth. **A552** (2005) 566, [arXiv:physics/0503191](https://arxiv.org/abs/physics/0503191).
- [142] L. Breiman, J. H. Friedman, R. A. Olshen, and C. J. Stone, *Classification and regression trees*, Wadsworth international group, Belmont, California, USA, 1984.
- [143] H. Voss, A. Hoecker, J. Stelzer, and F. Tegenfeldt, *TMVA - Toolkit for Multivariate Data Analysis with ROOT*, PoS **ACAT** (2007) 040; A. Hoecker *et al.*, *TMVA 4 — Toolkit for Multivariate Data Analysis with ROOT. Users Guide.*, [arXiv:physics/0703039](https://arxiv.org/abs/physics/0703039).
- [144] L. Anderlini *et al.*, *The PIDCalib package*, LHCb-PUB-2016-021, 2016.

- [145] M. Pivk and F. R. Le Diberder, *sPlot: A statistical tool to unfold data distributions*, Nucl. Instrum. Meth. **A555** (2005) 356, [arXiv:physics/0402083](https://arxiv.org/abs/physics/0402083).
- [146] A. N. Kolmogorov, *Sulla Determinazione Empirica di Una Legge di Distribuzione*, Giornale dell’Istituto Italiano degli Attuari **4** (1933) 83; N. Smirnov, *Table for Estimating the Goodness of Fit of Empirical Distributions*, Annals of Mathematical Statistics **19** (1948) 279.
- [147] R. Barlow, *Extended maximum likelihood*, Nucl. Instrum. Meth **A297** (1990) 496.
- [148] W. Verkerke and D. P. Kirkby, *The RooFit toolkit for data modeling*, eConf **C0303241** (2003).
- [149] T. Skwarnicki, *A study of the radiative cascade transitions between the Upsilon-prime and Upsilon resonances*, PhD thesis, Institute of Nuclear Physics, Krakow, 1986, DESY-F31-86-02.
- [150] LHCb collaboration, R. Aaij *et al.*, *Measurement of CP observables in  $B^\pm \rightarrow DK^\pm$  and  $B^\pm \rightarrow D\pi^\pm$  with two- and four-body D decays*, Phys. Lett. **B760** (2016) 117, [arXiv:1603.08993](https://arxiv.org/abs/1603.08993).
- [151] LHCb collaboration, R. Aaij *et al.*, *Dalitz plot analysis of  $B^0 \rightarrow \bar{D}^0\pi^+\pi^-$  decays*, Phys. Rev. **D92** (2015) 032002, [arXiv:1505.01710](https://arxiv.org/abs/1505.01710).
- [152] LHCb collaboration, R. Aaij *et al.*, *Constraints on the unitarity triangle angle  $\gamma$  from Dalitz plot analysis of  $B^0 \rightarrow DK^+\pi^-$  decays*, Phys. Rev. **D93** (2016) 112018, Erratum *ibid.* **D94** (2016) 079902, [arXiv:1602.03455](https://arxiv.org/abs/1602.03455).
- [153] LHCb collaboration, R. Aaij *et al.*, *Measurement of CP observables in  $B^\pm \rightarrow D^{(*)}K^\pm$  and  $B^\pm \rightarrow D^{(*)}\pi^\pm$  decays*, Phys. Lett. **B777** (2017) 16, [arXiv:1708.06370](https://arxiv.org/abs/1708.06370).
- [154] LHCb collaboration, R. Aaij *et al.*, *Dalitz plot analysis of  $B_s^0 \rightarrow \bar{D}^0K^-\pi^+$  decays*, Phys. Rev. **D90** (2014) 072003, [arXiv:1407.7712](https://arxiv.org/abs/1407.7712).
- [155] LHCb collaboration, R. Aaij *et al.*, *Measurement of b-hadron fractions in 13 TeV pp collisions*, Phys. Rev. **D100** (2019) 031102(R), [arXiv:1902.06794](https://arxiv.org/abs/1902.06794).
- [156] M. R. Chernick, *Bootstrap methods : a practitioner’s guide*, Wiley-Interscience publication, Wiley, New York ; Chichester, 1999.

- [157] A. Bondar, A. Poluektov, and V. Vorobiev, *Charm mixing in a model-independent analysis of correlated  $D^0\bar{D}^0$  decays*, Phys. Rev. **D82** (2010) 034033, [arXiv:1004.2350](https://arxiv.org/abs/1004.2350).
- [158] LHCb collaboration, R. Aaij *et al.*, *Measurement of CP violation in the three-body phase space of charmless  $B^\pm$  decays*, Phys. Rev. **D90** (2014) 112004, [arXiv:1408.5373](https://arxiv.org/abs/1408.5373).
- [159] LHCb collaboration, R. Aaij *et al.*, *Observation of several sources of CP violation in  $B^+ \rightarrow \pi^+\pi^+\pi^-$  decays*, Phys. Rev. Lett. **124** (2020) 031801, [arXiv:1909.05211](https://arxiv.org/abs/1909.05211).
- [160] M. Kenzie *et al.*, *Gammacombo user manual*, Can be obtained along with the code at: <https://gammacombo.github.io>.
- [161] J. Neumann, *Outline of a Theory of Statistical Estimation Based on the Classical Theory of Probability*, Phil. Trans. Royal Soc. London **A236** (1937).
- [162] E. L. Lehmann, *Elements of Large-Sample Theory*, Springer, 1998.
- [163] B. Sen, M. Walker, and M. Woodroffe, *On the Unified Method with Nuisance Parameters*, Statistica Sinica **19** (2009) 301.
- [164] C.-S. Chuang and T. L. Lai, *Resampling Methods for Confidence Intervals in Group Sequential Trials*, Biometrika **85** (1998) 317; C.-S. Chuang and T. L. Lai, *Hybrid Resampling Methods for Confidence Intervals*, Statistica Sinica **10** (2000) 1.
- [165] LHCb collaboration, R. Aaij *et al.*, *A study of CP violation in  $B^\mp \rightarrow Dh^\mp$  ( $h = K, \pi$ ) with the modes  $D \rightarrow K^\mp\pi^\pm\pi^0$ ,  $D \rightarrow \pi^+\pi^-\pi^0$  and  $D \rightarrow K^+K^-\pi^0$* , Phys. Rev. **D91** (2015) 112014, [arXiv:1504.05442](https://arxiv.org/abs/1504.05442).
- [166] Y. Grossman, Z. Ligeti, and A. Soffer, *Measuring  $\gamma$  in  $B^\pm \rightarrow K^\pm(KK^*)_D$  decays*, Phys. Rev. **D67** (2003) 071301, [arXiv:hep-ph/0210433](https://arxiv.org/abs/hep-ph/0210433).
- [167] LHCb collaboration, R. Aaij *et al.*, *A study of CP violation in  $B^\pm \rightarrow DK^\pm$  and  $B^\pm \rightarrow D\pi^\pm$  decays with  $D \rightarrow K_S^0 K^\pm \pi^\mp$  final states*, Phys. Lett. **B733** (2014) 36, [arXiv:1402.2982](https://arxiv.org/abs/1402.2982).
- [168] LHCb collaboration, R. Aaij *et al.*, *Measurement of CP observables in  $B^\pm \rightarrow DK^{*\pm}$  decays using two- and four-body D-meson final states*, JHEP **11** (2017) 156, Erratum ibid. **05** (2018) 067, [arXiv:1709.05855](https://arxiv.org/abs/1709.05855).

- [169] LHCb collaboration, R. Aaij *et al.*, *Study of  $B^- \rightarrow DK^-\pi^+\pi^-$  and  $B^- \rightarrow D\pi^-\pi^+\pi^-$  decays and determination of the CKM angle  $\gamma$* , Phys. Rev. **D92** (2015) 112005, [arXiv:1505.07044](https://arxiv.org/abs/1505.07044).
- [170] LHCb collaboration, R. Aaij *et al.*, *Measurement of CP violation parameters in  $B^0 \rightarrow DK^{*0}$  decays*, Phys. Rev. **D90** (2014) 112002, [arXiv:1407.8136](https://arxiv.org/abs/1407.8136).
- [171] T. Gershon, *On the measurement of the unitarity triangle angle  $\gamma$  from  $B^0 \rightarrow DK^{*0}$  decays*, Phys. Rev. **D79** (2009) 051301, [arXiv:0810.2706](https://arxiv.org/abs/0810.2706); T. Gershon and M. Williams, *Prospects for the measurement of the unitarity triangle angle  $\gamma$  from  $B^0 \rightarrow DK^+\pi^-$  decays*, Phys. Rev. **D80** (2009) 092002, [arXiv:0909.1495](https://arxiv.org/abs/0909.1495).
- [172] LHCb collaboration, R. Aaij *et al.*, *Measurement of CP asymmetry in  $B_s^0 \rightarrow D_s^\mp K^\pm$  decays*, JHEP **03** (2018) 059, [arXiv:1712.07428](https://arxiv.org/abs/1712.07428).
- [173] LHCb collaboration, R. Aaij *et al.*, *Measurement of CP violation in  $B^0 \rightarrow D^\pm \pi^\mp$  decays*, JHEP **06** (2018) 084, [arXiv:1805.03448](https://arxiv.org/abs/1805.03448).
- [174] LHCb collaboration, *Framework TDR for the LHCb Upgrade: Technical Design Report*, LHCB-TDR-012, 2012.
- [175] D. Kim, *CKM and CPV: Experimental Overview*, In talk presented 5 August, 2020, at the ICHEP conference.